Computational Study on the Role of Charge and Phonon Transport in Electronic and Thermoelectric Applications in a few Chalcogenides

A Thesis
Submitted for the Degree of
Doctor of Philosophy
In the Faculty of Science

by

Raju Kumar Biswas

Theoretical Sciences Unit
Jawaharlal Nehru Centre for Advanced Scientific Research,
(A Deemed University)
Bangalore-560064

April 2021

Dedicated to my Family...

DECLARATION

I hereby declare that the matter embodied in the thesis entitled "**Computational Study on the Role of Charge and Phonon Transport in Electronic and Thermoelectric Applications in a few Chalcogenides**" is the result of investigations carried out by me at the Theoretical Sciences Unit, Jawaharlal Nehru Centre for Advanced Scientific Research, Bangalore, India under the supervision of Prof. Swapan K. Pati and that it has not been submitted elsewhere for the award of any degree or diploma.

In keeping with the general practice in reporting scientific observations, due acknowledgement has been made whenever the work described is based on the findings of other investigators.

R. K. Biswas

Raju Kumar Biswas

CERTIFICATE

I hereby certify that the matter embodied in this thesis entitled "**Computational Study on the Role of Charge and Phonon Transport in Electronic and Thermoelectric Applications in a few Chalcogenides**" has been carried out by Mr. Raju Kumar Biswas at the Theoretical Sciences Unit, Jawaharlal Nehru Centre for Advanced Scientific Research, Bangalore, India under my supervision and that it has not been submitted elsewhere for the award of any degree or diploma.

SPati

Prof. Swapan K. Pati
(Research Supervisor)

Acknowledgements

”No one who achieves success does so without acknowledging the help of others. The wise and confident acknowledge this help with gratitude.” –Alfred North Whitehead

I take this opportunity to express my sincere gratitude to my PhD advisor Prof. Swapan K Pati for enormous freedom, constant motivation and excellent guidance throughout my Ph.D. Working with him has been a thoroughly enjoyable experience. His valuable comments and instructions in scientific communications have helped me immensely. I am extremely grateful for his kindness, endless support and encouragement during my stay at JNC. Initially, I was afraid of writing computational codes, but Sir convinced the importance of code writing as a computational physicist to me. I also convey my heartfelt gratitude for excellent computational resources he has provided for the group and the great help during writing this thesis.

My heartfelt gratitude to Prof. C. N. R. Rao for his vision about JNC. His presence speeches are truly very inspiring.

I would like to express my sincere gratitude to Prof. Bishwajyoti Dey (Savitribai Phule Pune University) and Prof. P. Durganandini (Savitribai Phule Pune

University) to orient myself towards research.

I am thankful my course instructors Prof. Waghmare, Prof. Shobhana Narasimhan, Prof. Balasubramanian, Prof. Vidhyadhiraja, and Prof. Meher K Prakash.

I would also like to thank Prof. Sundaresan, and Prof. Kanishka Biswas for the interesting and fruitful scientific discussions.

I thank to Dr. Bidhan Chandra Roy, Mr. Bikash Sasmal, Mrs. Basabdatta Bose, Mr. Dipesh Chanda, Mrs. Moumita Das, Mrs. Sanchita Barman, Mr. Soumya Sarkar, Mr. Sajal Basak and Mr. Partha Ghosh for teaching physics.

My special thanks to Dr. Swastika Banerjee, Dr. Dibyajyoti Ghosh, Dr. Shubhajit Das, Dr. Subhajit Roychowdhury, Dr. Pawan Kumar, Dr. Prasad Matukumilli VD, Dr. Rajdeep Banerjee, Dr. Debdipto Acharya, and Dr. Sudip Das for insightful discussions.

I would like to thank all the funding agencies like CSIR-UGC, JNCASR, Merit-cum-Means scholarship. Without their support, it would have never been possible to conduct research.

I am thankful to my present and past lab mates Dr. Pralok K Samanta, Dr. Swastika Banerjee, Dr. Dibyajyoti Ghosh, Dr. S R K Chaitanya Sharma Yamijala, Dr. Siam, Dr. Pallavi Bothra, Dr. Bradraj Pandey, Dr. Arkamita Bandyopadhyay, Dr. Somananda Sanyal, Dr. Sukanta Mondal, Dr. Navamani, Dr. Shubhajit Das, Dr. Abhiroop Lahiri, Dr. Neha Bothra, Madhulika, Pallavi Sarkar, Ashvini, Ganesh, Supriti, Bidhan, Dr. Paramita Banerjee, Anita, and Dr. Shazia for the scientific discussion.

I thank to Dr. Subhajit Roychowdhury, Paribesh, Pavitra, Moinak for scientific discussions during collaboration.

I would like to thank my friends Souvik, Ratan, Arka, Arabinda, Biswanath, Suman, Anaranya, Moinak.

I would like to thank all my friends in JNCASR, PRL, Pune University, TCIS-TIFR and Siliguri College-mates.

I am extremely thankful to my school friends Pulak, Animesh, Manash and Arnab for their support and company.

Thanks to JNCASR for providing all the facilities, Complab, CCMS colleague Anoop and Suresh, admin, academic office and health centre staffs.

I thank Anusooya ma'am and Sohan for their endless support, love & affection. I am grateful to Anusooya Ma'am for her kind guidance during the colloquium preparation as well as thesis writing along with my guide. She has spent her precious time to go through this thesis and make necessary corrections.

I am greatly thankful to Jethu (Nirmalendu Paul) and Boroma (Sipra Paul) for their love, affection and kind guidance. I also thank Prof. Dhurjati Prasad Datta (North Bengal University) for the help and motivation.

Last but not the least, my parents (Maa & Baba) for their unending support and encouragement. My Sister Shiny (Rita Biswas), without whom I can't think of my foot-steps since my childhood. They have always believed in me, and never tied me down in any of my endeavors. I thank Sresta who had been my friend and had advised in academic and non-academic affairs and supported me throughout.

Thank you ALL for making this thesis possible!

Synopsis

Transport properties of semiconductors are one of the major research areas in the 21st century. Three primary types of carrier action occur inside the semiconductors: drift, diffusion, and recombination processes. Drift happens due to the movement of charged particles under an electric field, which determines the current flow in photovoltaics cells and various Field Effect Transistors (FETs). On the other hand, the diffusion mechanism works when the particle moves due to concentration gradient or temperature gradient as the current flow in p-n junctions. The recombination processes are necessary to design light-emitting diodes (LED). Apart from the above transport phenomena, there is also an active research area where heat transport is studied to generate electric current, where scatterings and band engineering play a major role. Here we are mostly interested in studying charge carrier mobility driven by drift mechanisms and phonon and charge transport due to heat difference in layered as well as bulk semiconductors. In this thesis, we shall discuss various mechanisms and descriptors to enhance the thermoelectric performance of layered and bulk semiconductors, where one needs to increase also the magnitude of drift mobility and conductivity apart from a few other factors.

The first chapter of the thesis is the introduction chapter, which is followed by six work chapters. The thesis ends with a summary in the conclusion and outlook chapter. Chapter 2 discusses the mechanism to achieve ultrahigh carrier mobility in -TeO2 by application of strain. In chapter 3, we study vibrational spectra of MO (M=Sn/Pb) in their bulk and single-layer forms along with the signature of avoided crossing in their thermodynamic properties. Chapter 4 explores the superlattice of SnO-PbO which can be used as new oxide material for thermoelectric applications with a moderate zT value at high temperatures. In chapter 5, we demonstrate the role of Gd doping in bulk PbTe in terms of electronic as well as phonon transport properties for their thermoelectric applications. Chapter 6 aims to study the 3d-transition metal incorporated hexagonal phase of monolayer SnTe, which exhibits a relatively higher thermoelectric figure of merit at elevated temperatures. Finally, chapter 7 discusses the innovative approaches, such as, the Rashba effect and entropy engineering that enhance the thermoelectric performance in β-Ag_2Se at the near-room-temperature. Finally, chapter 8 summarizes all the major findings in the six work chapters.

In the Introduction chapter, we have discussed the recent energy crisis and the possible solutions in terms of the renewable sources. Both photovoltaic and thermoelectric applications generate electric current from renewable sources, such as, solar energy, heat energy, geothermal energy. To utilize this waste energy, we design new energy materials for such applications, which have been discussed comprehensively in this thesis. To understand the quantities accurately, we have solved Boltzmann transport equations (BTE) within deformation potential theory (DPT) to estimate Seebeck coefficients, relaxation time for electron and hole, charge carrier mobility, electrical conductivity, relaxation times for phonons, thermal conductivity. In fact, the scattering information including phonon-phonon, phonon-charge carrier, and charge carrier-charge carrier has been taken into consideration while calculating the transport coefficient. Furthermore, we have thoroughly described the computational methodology, which is based upon density functional theory (DFT) and density functional perturbation theory (DFPT) implemented in Quantum Espresso (QE) and Vienna Ab-initio Simulation Package (VASP). For finite temperature calculations, we have used ab-initio molecular dynamics (AIMD) simulation, which is implemented in VASP codes. All of these have been discussed in detail. Finally, the introduction chapter ends with a summary of the results of each of the subsequent chapters.

In Chapter 2, we have discussed the layered structure of β-TeO$_2$ that exhibits high carrier mobility together with a broad band gap, which could be a promising candidate for nanoelectronics applications. Suitable mechanical flexibility permits strain-engineering in such layered structures to manifest carrier transport anisotropy. In this context, we have used the ab-initio based density functional theory (DFT) method along with the Boltzmann transport equation (BTE) to explore the estimation of strain-induced charge carrier mobility. In fact, the lone pair associated with tellurium atoms leads to transport anisotropy in electron and hole mobility. Interestingly, we find that at some uniaxial compressive strain along a particular direction results in sudden enhancement in one type of carrier mobility, while for a certain uniaxial compressive strain in perpendicular direction results in sudden enhancement of exactly opposite carrier mobility. These findings have been rationalized based on carrier scattering information and carrier effective mass derived from the electronic dispersion curve. All these findings point towards layered β-TeO$_2$ as an emerging candidate for power electronics applications.

First-principle calculations of the phonon dispersion relation on the bulk and single layers of SnO and PbO have been studied in chapter 3. In agreement with experimental observations of Raman spectroscopy measurement, we find A$_1g$ mode is higher in frequency than that of E$_g$ mode. Moreover, the reason behind the shift of A$_2u$ mode to a higher frequency for the monolayer of both SnO and PbO is clearly understood from our calculations. In addition to the vibrational spectroscopy, we also find avoided crossing or Landau quasi-degeneracy between longitudinal acoustics (LA) and low energetic transverse optical (TO) modes in both bulk forms of SnO, PbO, and in a monolayer of SnO. The signature of such avoided crossing can be observed in the specific heat and vibrational entropy. While specific heat and entropy both decrease at the temperature corresponding to the avoided crossing region, the specific heat value shows a kink in that region. In contrast, such lowering/kink in thermodynamic variables do not appear in monolayer PbO. The reason behind the avoided crossing has been analyzed using the concept of Born effective charge and dielectric tensor.

Chapter 4 demonstrates the oxide materials which can be used in thermoelectric applications due to their low toxicity, environmentally friendly, high melting point, affordable cost, and good stability in the air. These materials play a significant role in the energy crisis that the world is facing today if they can be efficiently utilized as high-performance thermoelectric material in the 21st century. In this context, we have designed a layered oxide material, SnO-PbO, in its superlattice form. Our ab-initio calculations indicate that the layered crystal structure is dynamically and thermodynamically stable at ambient as well as at elevated temperatures. Furthermore, the lone pair associated with Sn and Pb atoms introduce crystallographic anisotropy which strongly scatters low energetic heat-carrying acoustics phonons and consequently reduces lattice thermal conductivity. On the other hand, degenerate bands and sharp peaks in the electronic density of states (DOS) give rise to higher Seebeck coefficients and the covalent bonding of Sn-O and Pb-O facilitate moderate electrical conductivity. In this work, deformation potential theory (DPT) coupled with Boltzmann transport formalism has been adopted to obtain carrier scattering information involving charge carrier mobility and hence carrier conductivity. As a consequence of this bonding hierarchy and crystallographic anisotropy, SnO-PbO could be considered as a next-generation oxide-based thermoelectric (TE) material.

Chapter 5 describes the role of Gd atoms in n-type PbTe which generally lacks behind due to the simplicity of its conduction band compared to the rich valence bands. In this study, we have shown the enhancement of the Seebeck coefficient and lowering of the lattice thermal conductivity of n-type PbTe by Gd doping. Gd doping in PbTe not only increases the electron effective mass via flattening of the conduction band but also introduces a non-interacting single band that exhibits non-dispersive feature at point along with dispersive nature in L $\longrightarrow$ Γ over the Brillouin zone. This non-dispersive flat band significantly improves the Seebeck coefficient. As a lanthanide, Gd prefers to attain a high coordination number, thereby remaining locally off-centered from the regular octahedral position of PbTe lattice, which introduces significant lattice anharmonicity. Due to Gd doping, a low energy nearly flat optical phonon mode originates in the phonon band structure. As a result of the flat optical phonon band, anharmonic phonon scattering strength drastically increases by several folds and subsequently lowers lattice thermal conductivity to a low value of 0.78 $\mathrm{Wm^{-1}K^{-1}}$ at 735 K. As a result, we obtain a high zT of 1.2 at 783 K for the Gd-doped PbTe system. The present results indicate that enhanced thermoelectric performance in n-type PbTe can be realized by synergistic integration of electronic structure modulation and enhanced phonon scattering.

Chapter 6 focuses on the newly explored hexagonal phase of 2D SnTe that has been shown to be thermodynamically stable and exhibits high thermoelectric performance. In this study, we mainly investigate the effect in terms of electrical as well as thermal transport properties due to the doping of 3d-transition metals (TM). Based on first-principles calculations and Boltzmann transport theory, our study encompasses that both V- and Mn- doped SnTe show moderate lowering of intrinsic carrier mobility due to lower elastic constant and higher carrier effective mass. Furthermore, V and Mn doping slightly enhance the Seebeck coefficient, while Fe and Co doping indicate semiconductor to metallic transition. Due to such metallic transition, the Seebeck coefficient drastically decreases for both Fe and Co doping, and in turn, the power factor diminishes. In the case of thermal transport, V and Mn doping show a reduction in lattice thermal conductivity than pristine 2D SnTe due to enhanced phonon-phonon scattering, and as a result, we achieve very high $zT \approx 2.24$ at 900 K for Mn-doped SnTe. The replacement of Sn by cost-effective and environmentally-friendly 3d-TM with enhanced thermoelectric performance would be beneficial for the energy crisis.

Chapter 7 aims to shed light on designing a near-room-temperature n-type thermoelectric material with high zT. Generally, pristine Ag2Se exhibits low thermal conductivity along with high electrical conductivity and Seebeck coefficient, which leads to high thermoelectric performance (n-type) at room temperature. We have reported in this chapter a pseudoternary phase, Ag2Se0.5Te0.25S0.25, which shows improved thermoelectric performance ($zT \approx 2.1$ at 400 K). Our study reveals that the Rashba type of spin-dependent band spitting, originated because of Te-doping, enhances the carrier mobility. Interestingly, locally off-centered S atoms and rising configurational entropy via substitution of Te and S atoms in Ag_2Se significantly reduce the lattice thermal conductivity (κ_{lat} κ 0.34 at 400 K). In order to accurately obtain electrical as well as thermal transport coefficient, we adopt deformation potential theory based on Boltzmann transport formalism. The combined consequence of the Rashba effect coupled with configurational entropy synergistically results in such high thermoelectric performance with the development of a new n-type thermoelectric material working at the near-room-temperature regime.

Finally, in chapter 8, which is actually the summary and outlook chapter, we have summarized all the main results of each of the six work chapters and their contributions toward electronic and thermoelectric applications. Since we have worked on both layered as well as bulk systems, we have described the correct descriptors to control carrier transport in device applications. In the near future, we are planning to predict new advanced materials with better thermoelectric efficiency using the high-throughput approaches together with other functionalities, namely, topological insulators and time-reversal symmetry breaking topological phases, etc.

List of publications

1. ”Achievement of Strain-Driven Ultrahigh Carrier Mobility in β-TeO_2”, **Raju K Biswas** and Swapan K Pati*, Materials Research Bulletin 141, 111343 (2021).

2. ”Vibrational spectra of MO (M= Sn/Pb) in their bulk and single-layer forms: role of avoided crossing in their thermodynamic properties”, **Raju K Biswas** and Swapan K Pati*, Bulletin of Materials Science 43(1), 1-10 (2020).

3. ”Exploring a Superlattice of SnO-PbO: A New Material for Thermoelectric Applications”, **Raju K Biswas** and Swapan K Pati*, ACS Applied Energy Materials 4(3), 2081-2090 (2021).

4. ”Discordant Gd and Electronic Band Flattening Synergistically Induce High Thermoelectric Performance in n-type PbTe”, Moinak Dutta, **Raju K Biswas** and Swapan K Pati and Kanishka Biswas*, ACS Energy Letters 6, 1625-1632 (2021).

5. ”Exploring the Thermoelectric Effect/Properties of 3d-Transition Metal Incorporated Two-dimensional SnTe: A Computational Study” **Raju K Biswas**,

Paramita Banerjee and Swapan K Pati*, (Submitted).

6. "Realizing high Near-Room-Temperature Thermoelectric Performance in n-type Ag_2Se through Rashba Effect and Entropy Engineering" **Raju K Biswas** and Swapan K Pati*, (Submitted).
7. "Phonon Localization and Entropy-Driven Point Defects Lead to Ultralow Thermal Conductivity and Enhanced Thermoelectric Performance in $(SnTe)_{1-2x}(SnSe)_x(SnS)_x$" S. Roychowdhury, **Raju K Biswas**, Moinak Dutta, Swapan K Pati and Kanishka Biswas*, ACS Energy Letters 4(7), 1658-1662 (2019).
8. "Broadband Colossal Dielectric Constant in the Superionic Halide $RbAg_4I_5$: Role of Intercluster Ag^+ Diffusion" Paribesh Acharyya, Tanmoy Ghosh, Shidaling Matteppanavar, **Raju K Biswas**, Premakumar Yanda, Srinivasa R. Varanasi, Dirtha Sanyal, A. Sundaresan, Swapan K Pati, and Kanishka Biswas*, The Journal of Physical Chemistry C 124(18), 9802-9809 (2020).
9. "Elusive Co_2O_3: A Combined Experimental and Theoretical Study" Pavitra N. Shanbhag, **Raju K Biswas**, S. K. Pati*, A. Sundaresan*, and C. N. R. Rao, ACS omega 5(45), 29009-29016 (2020).

List of Tables

Contents

List of Figures

1

Introduction

1.1 The energy crisis

At the start of 2021, the Energy industry continues to find itself in an ever shifting landscape. The last few years have been quite challenging for conventional energy sectors, such as oil & gas and mining and fossil fuel, while there has been great excitement around the new and innovative developments in green energy sectors. Furthermore, the dramatic impact that COVID-19 had on the global economy, the changing perspectives and accelerating trends on climate change and energy transition, all point to one direction: changes are needed with much vigor. Today, the energy industry finds itself in an incredibly exciting position. As researchers worldwide work towards a cleaner and greener future, the technology becomes more innovative, combining traditional fuels and resources with fresh and newer ideas.

Renaissance of interest have been to explore highly efficient electronic and thermoelectric materials as possible routes to address worldwide energy generations, utilizations, and managements. Along with these, there have been huge strides in the discovery of isolating newer materials with exotic transport properties leading to technological developments.

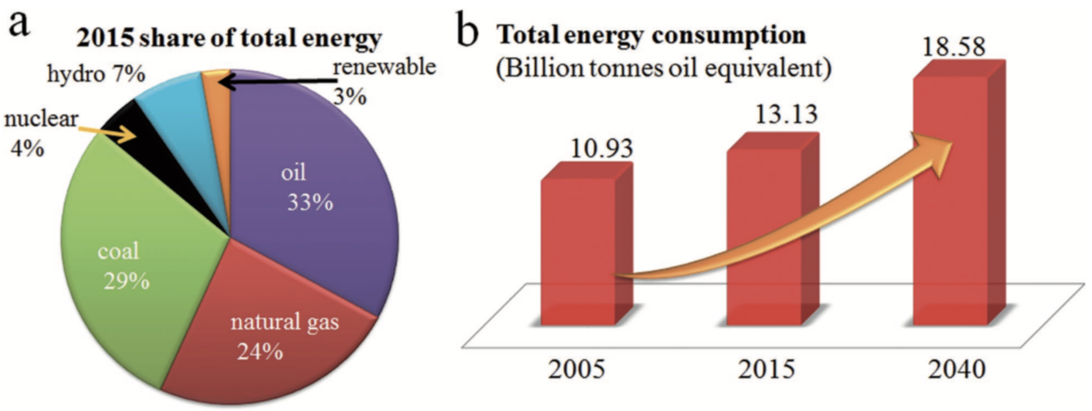

Figure 1.1: (a) 2015 share of total energy. (b) Statistic and estimated global energy consumption by source of 2005, 2015, and 2040. *Reproduced with permission from International Energy Outlook 2016, and U.S. Energy Information Administration 2016.*

1.2 The Past and the Future

Almost all the applications till today depend heavily on existing fuel resources which are diminishing at the fast pace and there have been many forums where the end of the fuel resources have been predicted. The world energy mostly consists of a variety of fossil fuels, mainly the variance of these three: oil, coal and natural gas. Many energy outlooks suggest that fossil fuel will remain dominant energy resources for next two to three decades. In fact, a report suggests that we are using different forms of fossil fuels-from solid (coal) to liquid (oil) to gas (natural gas)-as energy sources from the very beginning. Parallelly, the improved quality of life demands more consumption of fuels. According to British Petroleum statistical review of world energy, consumption of natural gas, global oil and coal has increased by 3%, 1.8% and 1% respectively. Figure 1.1(a) shows that almost 90% of the total power supply still depends upon conventional fossil fuels, and Figure 1.1(b) shows that the energy demand has been significantly rising.[1] Furthermore, $\approx$ 70% of the energy consumption of conventional fossil fuels[2] has been wasted in the form of heat by engines or factory systems, which was emitted with exhausted gas (300 K – 900 K) or taken up by the cooling systems. In fact, the magnitude of waste energy is tremendous, considering the total consumption of energy is equivalent to up to 13 billion tonnes of oil equivalent in 2015 (Figure 1.1(a)).[1] Therefore, it is urgently needed to seek alternative energy sources or to apply sustainable solutions to increase the energy efficiency of fossil fuels.

Furthermore, the processes of fossil fuels, consisting of extraction, transportation, and refining of fossil fuels as well as the medium of use have caused detrimental impacts on the world economy; both directly and indirectly. In fact, coal excavation in many places is banned due to many reasons; spills and leakages are common phenomena during withdrawal, carrying and storage of oil and gas leads to water and air pollution. Irrespective of the processes (heating, electricity production etc), the use of fossil fuels always involves combustion. Since carbon and hydrogen are the primary components of these fuels along with a few other elements (which were either present from the beginning or were added during refinement), most often, the byproducts are various gases (CH, CO_x, SO_x, NO_x), droplets of tar, soot, ash, and other organic compounds. These directly cause air pollution and soil pollution. Many studies have reported that through chemical reactions, these primary pollutants might be converted to secondary pollutants, like aerosol, ozone, peroxyacyl nitrates, various acids, etc causing acid rain (which disturbs the whole terrestrial and aquatic ecosystems) or ozone layer depletion (allowing ultra-violet ray to enter the earth surface) and many other adverse effects. The major by-products of these reactions are CO_2, CH_4, N_2O, $CHCl_3$ which are familiar as greenhouse gases, that effectively maintain an optimum world temperature, but excess abundant of these causes adverse effect in the environment, such as, rise in sea level, melting of ice caps, change in climate, leading to what is known as ‘greenhouse effects’.

Over time there is a general trend of one fossil fuel[3] surpassing another. For example, in the nineteenth century, coal overtook biomass as the biggest global energy supplier, but it was overthrown by petroleum in the 20th century; in fact, petroleum became the big energy supplier as coal. The limited quantities of these fuels pose a concern as the demand increases rapidly with the world population and economic growth in developing and under-developed countries. Statistics tell us that with the current consumption rates, we will run out of oil and gas in 20-30 years, and coal by 68 years.

The future lies in developing various forms of renewable resources, where most of the research in the world has been concentrating on. The renewable resources are too many, namely, solar spectrum, CO_2 reduction, Li, Na and Mg ion rechargeable batteries, light to electricity and heat to electricity conversions, to name a few. In fact, research works on each of these topics have been proceeding at an enormously fast pace worldwide. Renewable energy sources have come up as a promising remedy for the last few decades and a "transition from fossil fuels" is gaining prominence. Commonly known renewable energy sources are hydropower, biomass, geothermal, solar tidal, wind, hydrogen energy etc. However, engineering practicality, applicability, reliability, economy, scarcity of supply, public awareness, acceptability etc are issues which limits the utilization of renewable resources. Technological improvements have been a great concern for scientists over the years. With time, different groups have come up with new and revised strategies on the improvement of renewable energy techniques. For example, the following figure shows by 2050 how various countries would like to develop renewable resources (Shown in Figure 1.2).

We, however, will limit our discussion to various processes in which energy can be produced in terms of electricity. Three such applications will be discussed in detail. They are (i) Photovoltaic devices, which converts light energy to electrical energy, (ii) Field effect transistors, which convert electromagnetic field or electric field or bias to electrical current and finally (iii) Thermoelectric devices, which converts heat energy at a range of temperature to electrical energy.

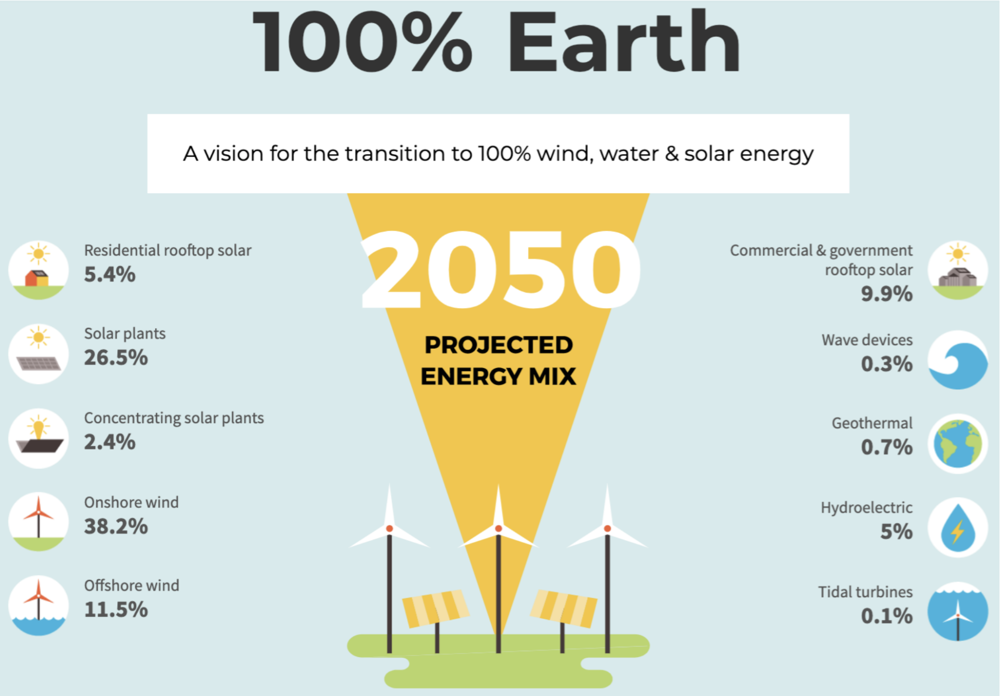

Figure 1.2: Projected energy consumption by 2050. This figure is taken from cleantecnica.com.

1.3 Photovoltaic, Field Effect Transistor and Thermoelectric Devices

The major devices which generate or produce electric energy are of three types (i) Thermoelectric, (ii) Photovoltaic and (iii) Transistor devices. While the first one converts heat energy to electrical energy at almost all temperature scales, the 2nd device converts light energy to electrical energy for almost all frequency light and the last device produces electric current either from electric field or electromagnetic field through a third electrode, called Gate. In all of these devices, electron and hole dynamics, phonon dynamics, innovative scatterings mechanism and band structure engineering with respect to electric field play major roles in applications. A good thermoelectric material requires band-like charge carrier transport and glass-like thermal transport. Like thermoelectric materials, photovoltaic solar cells should possess large electron-hole carrier mobility in combination

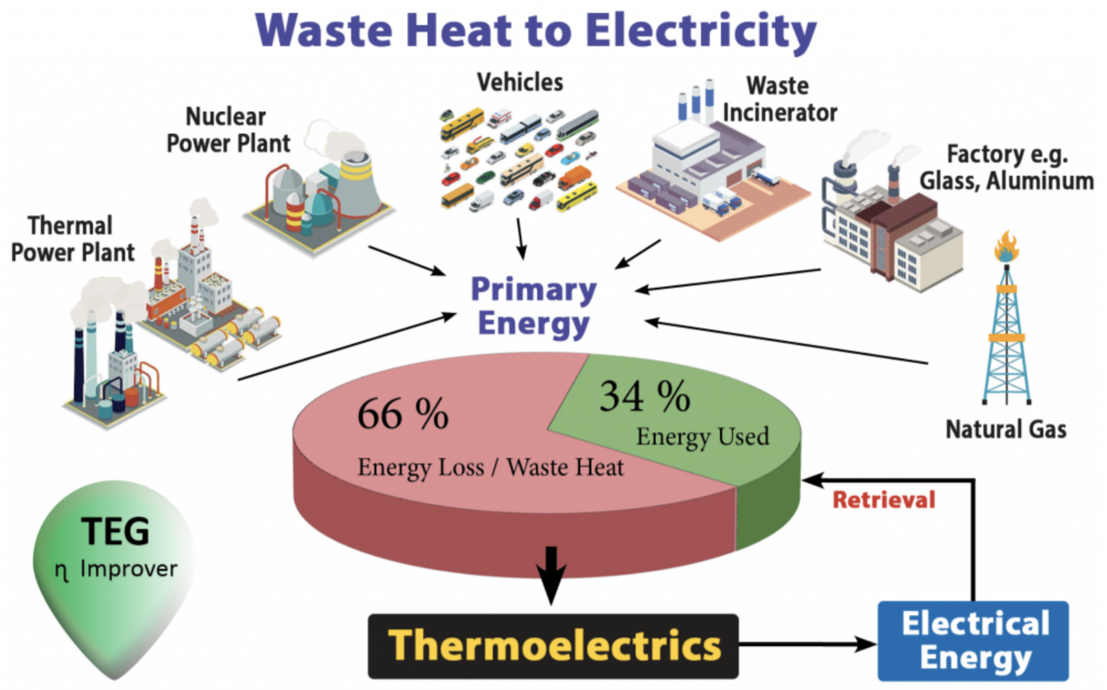

Figure 1.3: Sources of the waste heat energy. This figure is taken from https: //prometeon.it/.

with weak exciton (electron hole bound pair) binding energy.

Around 60-70% of the energy produced by fossil fuels burning or by fission nuclear power plants is lost mainly in the form of waste heat (Shown in Figure 1.3). High performance thermoelectric (TE) materials which can directly and reversibly convert heat energy to electrical energy have thus drawn much attention academically as well as economically in the last few decades. There is a huge scope to recover large quantities of thermal energy all over the world. Thermoelectric systems are an environment-friendly energy conversion technology, where various advantages can be envisaged; small size, adaptable shape, high reliability, no pollutants and feasibility in a wide temperature range. The only weak point of the currently available TEG (TE Generators) technologies is low efficiency. The effective efficiency of the best TEGs is based on the Seebek effect, currently available, in fact, doesn't exceed 5-6%. Moreover, also the cost/watt is still too high. Presently, the thermoelectric conversion efficiency is low due to the low perfor-

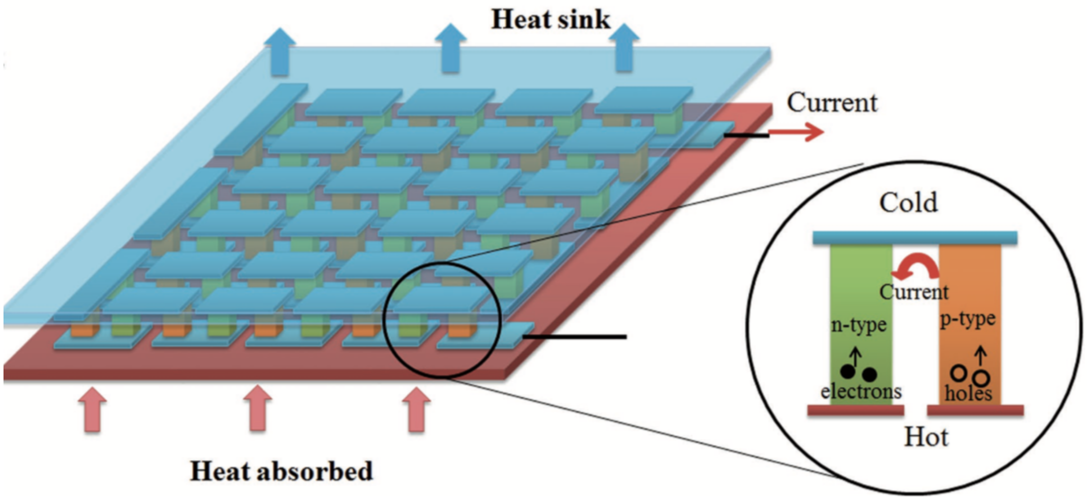

Figure 1.4: Schematic diagram of Thermoelectric device.

mance efficiency of the thermoelectric materials. The ecological benefits to the planet and the potential market of a new TEG technology offering high efficiency at affordable costs, are simply impressive.

Figure 1.4 shows a typical schematic diagram of a TE device, where both n- and p-type TE materials are connected and can be combined with electrodes to form TE generators (TEGs).[4] The advantages of using TEGs are that they can collect waste heat covering a very wide temperature range without any noise, vibration, or gas emission, and TEGs do not need refueling or maintenance for a very long period.[5–7] As a consequence, TEGs can improve the energy efficiency of fossil fuels and provide power supply simultaneously. Moreover, in many applications, specific power (power produced by per unit of mass, $\mathrm{Wkg^{-1}}$)[8] and power density[9] (power produced by per unit of area, $\mathrm{Wcm^{-2}}$) are introduced to evaluate the power output ability of TEGs in order to achieve high energy output with smaller size and weight. With the development of highly efficient TE materials, TEGs are expected to provide robust energy support in many fields and play very pivotal roles in reducing the consumption of fossil fuels.

1.4 Materials Selections

1.4.1 Photovoltaic Solar cell

The photovoltaic solar cells absorb light mainly coming from the sun in the visible range. The photons in light excite some of the electrons in the semiconductors to generate electron-hole (negative-positive) pairs or exciton pairs. These e-h pairs turn out to be long-lived exciton formation in line with weakly interacting bound states. Depending on the interactions between the electron and hole, there are strong and weak exciton formation. Strong and small volume exciton recombine to give rise to light, while the weak and large volume excitons can be separated. Since there is an internal electric field generated, these weakly bound electron-hole pairs are induced to separate. However, the recombination competes with the efficient separation of charge carriers. Once separated, the electrons move to the negative electrode while the holes move to the positive electrode with high equivalent electron-hole mobility. As a result, an electric current is generated to supply the external load. This is how photovoltaic effects work in a solar cell.

With rapid progress in a power conversion efficiency (PCE) to reach 25%, metal halide perovskite-based solar cells became a game-changer in a photovoltaic performance race. Many inorganic metal oxides, such as $BaTiO_3$, $PbTiO_3$, $SrTiO_3$, $BiFeO_3$, etc., were found to have the perovskite structure, so therefore, perovskite compounds are more commonly known as metal oxides, with formula ABO_3. Generally, oxide perovskites are in use in various ferroelectric, piezoelectric, dielectric, and pyroelectric applications. But except for some limited compositions, like in $LiNbO_3$, $PbTiO_3$, and $BiFeO_3$, which show weak but finite PV effect due to ferroelectric polarization (known as ferroelectric photovoltaics).[10] However, these metal oxide perovskites do not exhibit good semiconducting properties that would make them suitable for PV applications. Interestingly, there exists a class of halide perovskites, which differ from oxide perovskites such that there are halide anions in place of oxide anions (ABX_3; A = cation, B = divalent metal cation, X = halogen anion), which shows the semiconducting properties that are desired for PV applications. The discovery of such halide perovskites dates back to the 1890s. In 1893, Wells et al. performed a comprehensive study on the synthesis of lead halide compounds from solutions including lead halide and cesium, $CsPbX_3$ (X = Cl, Br, I),[11] ammonium (NH_4),[12] or rubidium, $RbPbX_3$.[13] Much later, in 1957, the Danish researcher, C. K. Møller found that $CsPbCl_3$ and $CsPbBr_3$ have the perovskite structure,[14,15] existing as a tetragonally distorted structure which undergoes a transition to a pure cubic phase at high temperature.[16]

In addition to $A_3Sb_2I_9$ class of materials, Sb_2S_3 with 1D chain structure and $A_2Sb_8S_{13}$ (A = Cs^+ , MA^+) with 2D layered structures, show semiconducting properties with band gap values, 1.72 eV, 1.85 eV, and 2.08 eV for Sb_2S_3, $Cs_2Sb_8S_{13}$, and $MA_2Sb_8S_{13}$, respectively.[17] From the electronic structures, the work function and ionization potential were also calculated, shedding light on possible contact materials for the PV applications.

Recently, it has been established that 3D layered structures work better as light harvesters than lower dimensional structures because of their lower band gap and lower exciton binding energy. Thus, attempts were made to form 3D structures consisting of Sb and Bi trivalent metal ions. This led to exploring the possibilities of heterovalent substitution of Pb^{2+} by incorporating trivalent metals (Bi, Sb) in combination with monovalent metals, such as, silver (Ag), gold (Au), copper (Cu), and potassium (K) into the perovskite structure, forming double perovskites possessing molecular structure of $A_2MM'X_6$ (A = Cs, MA; M = Bi, Sb; M = Ag, Au, Cu, K; X = I, Cl, Br).[18] Among many combinations of double-perovskite materials, $Cs_2BiAgBr_6$ and $Cs_2BiAgCl_6$ have been explored earnestly. Both $Cs_2BiAgBr_6$ [20,21] and $Cs_2BiAgCl_6$ [19] exhibit wide and indirect band gaps. Only a few studies have reported employment of $Cs_2BiAgBr_6$ for

PV device applications. Efficiencies of the cells of different architectures including $Cs_2BiAgBr_6$ as the absorber vary in the range 13%, depending on architecture and preparation conditions.[20-22] Even though these attempts[20,21] have shown that double perovskites based on AgBi combination can be a promising replacement for lead perovskites, Savory et al. reported its limitations to achieve high power conversion efficiency (PCE) (maximum limit is 10%), owing to its wide indirect band gap and large carrier effective masses. Theoretical investigation suggests that this limitation can be overcome by replacing Ag with indium (In) or thallium (Tl). Bi-In- and Bi-Tl-based double-perovskite materials possess direct band gap of $\approx$ 2 eV.[23] It has been found experimentally that the replacement of Ag with Tl in $(MA)_2AgBiBr_6$ also results in direct band gap of $\approx$ 2 eV. Unfortunately, in addition to such wide band gap ($\approx$ 2 eV) which is perfectly suitable for PV applications, higher toxicity of Tl (than Pb) limits use of BiTl perovskites in PSCs.[24]

1.4.2 Field Effect Transistors (FETs)

The charge carrier generation along with current modulated by gate voltage should drive higher electron-hole mobility on either side of source and drain in transistors. Despite the rapid advancement of optoelectronic applications, a big gap remains in understanding the fundamental transport properties of organo-lead halide perovskites, namely charge carrier character, mobility and charge transport mechanisms. To fill this gap, studies of basic field-effect transistor (FET) devices are urgently needed. Historically, related tin(II)-based 2D hybrid perovskites have attracted major interest for FET fabrication because of their attractive layered structure, with demonstrated field-effect mobilities up to 0.62 $cm^2V^{-1}s^{-1}$ and I_{on}/I_{off} ratio above 10^4 [25]. Improvement of mobility can be achieved by substitution of organic cation in hybrid perovskite, yielding FET saturation-regime mobility as high as 1.4 $cm^2V^{-1}s^{-1}$, and nearly an order of magnitude lower linear-regime mobility[26]. Further improvement was demonstrated through melt processed deposition technique, where saturation and linear mobilities of 2.6 and 1.7 $cm^2V^{-1}s^{-1}$ with I_{on}/I_{off} of 10^6 were achieved[27]. Conversely, only rare examples of 3D hybrid perovskites FETs can be found in the literature with limited hole mobility of the order of $\approx 10^{-5}$ $cm^2V^{-1}s^{-1}$ in the case of $CH_3NH_3PbI_3$ and strong hysteresis due to ionic transport, which so far have hindered the development of FET applications.

Moreover, two-dimensional (2D) transition metal di-chalcogenides (TMDCs) have emerged as excellent candidates for future low-power electronics and optoelectronics. Thanks to the sizable and thickness-dependent bandgaps in semiconducting 2H-phase crystals, TMDC field effect transistors (FETs) offer sufficient I_{on}/I_{off} ratio for logic applications. This attribute makes 2D TMDC FETs promising devices beyond graphene FETs which cannot be effectively switched off due to its zero bandgap. Molybdenum disulfide (MoS_2), a forerunner in the TMDCs family, has been extensively employed for making 2D FETs. Importantly, compared with other TMDCs, MoS_2 processes larger energy barriers against oxidation[28] and degradation[29] , making even its single-layer (1L) form stable in ambient, enabling persistent and robust 2D FETs. Various studies have been performed to demonstrate single-, few- and multilayer MoS_2 field effect transistors [30-31]. Although these studies reveal that MoS_2 FETs display a very high On/Off ratio (up to 10^6 - 10^8), most of these FETs suffer from relatively low mobility (especially compared to graphene FETs). Despite the demonstration of very high hall mobility of 34,000 $cm^2V^{-1}s^{-1}$ for six-layer MoS_2 at low temperature using careful contact engineering and dielectric encapsulation[32] , at room temperature, the highest field effect mobility is still around 500 $cm^2V^{-1}s^{-1}$ for multilayer MoS_2 FETs[33].

1.4.3 Thermoelectric Materials

Thermoelectrics is one of the major fields of study worldwide, where a temperature gradient can be converted to electrical power and vice versa. The efficiency of a thermoelectric material is directly proportional to its Figure of merit (zT), defined as $\frac{S^2\sigma}{\kappa}$T, where S is the Seebeck coefficient or thermopower, σ is the electrical conductivity ($S^2\sigma$ is called power factor), and κ is the thermal conductivity, including both from electrons (κ_e) and lattice vibrations (phonons, κ_{lat}) as heat carriers at a thermodynamic temperature, T. However, the optimization of these three parameters (S, σ, κ) to achieve high zT has become the key challenge due to their complicated interdependence. They are all strongly dependent on the material's band structure, transport properties and carrier concentration.

Table 1.1: Parameters which govern thermoelectric performance of a material.

Material	σ (S/m)	S (μV/K)	κ (W/mK)
Metal	Very high ($\simeq 10^7$)	Low ($\simeq 10$)	High ($\simeq 10^2$)
Insulator	Very low ($\simeq 10^{-10}$)	High ($\simeq 500 - 900$)	Low ($\simeq 10^{-3}$)
Semiconductor	Moderate ($\simeq 10^{-3}$)	High ($\simeq 120$)	Low ($\simeq 10$)

In literature, there are various approaches to improve zT, such as modifying band structure,[34,35] band convergence,[36,37] combination of flat bands (high effective mass) and dispersive bands (low effective mass) in electronic band structure to increase the power factor (PF). On the other side, several phonon-engineering strategies have been employed in semiconductors, such as, large anharmonicity,[38-39] large molecular weight,[40,41] complex crystal structure,[42] charge density distortion,[43] nanostructuring, (PbTe,[44-45] half-Heusler,[46-47]), rattling modes (skutterudites,[48,49] clathrates[50-53]), to name a few, to reduce thermal conductivity.

Many promising thermoelectric materials emerged in an endless stream till to-

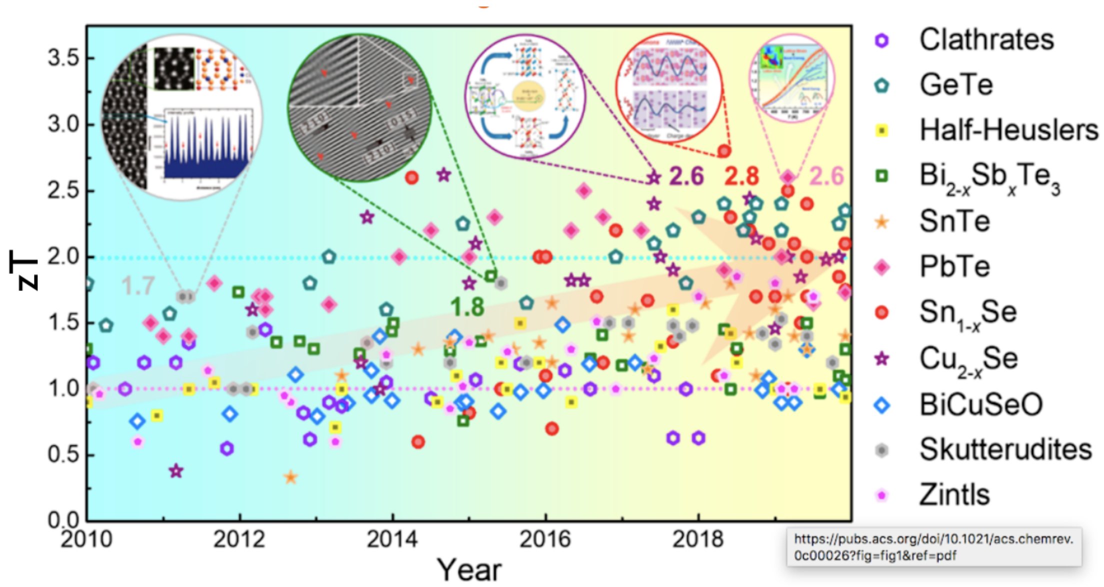

https://pubs.acs.org/doi/10.1021/acs.chemrev.0c00026?fig=fig1&ref=pdf

Figure 1.5: Status of Thermoelectric figure of merit.

day (Figure 1.5). Specifically, near room temperature (300–500 K) thermoelectrics include $(Bi,Sb)_2(Se,Te)_3$ based alloys and MgAgSb alloys.[54-55] Intermediate-temperature (500–900 K) thermoelectrics include Pb(Te, Se, S), Sn(Se, S),[56-62] SnTe,[63,64] GeTe,[65] Cu_2(Te, Se, S),[66,67] Mg_2(Si, Sn, Ge),[68-69] BiCuSeO,[70-71] Zn_4Sb_3,[72] In_4Se_3,[73] $Ba_8Ga_{16}Ge_{30}$,[74] skutterudites,[76-77] and tetrahedrites.[78] At high temperature (> 900 K), SiGe,[79] $(Pr, La)_3Te_4$,[80,81] $Yb_{14}MnSb_{11}$,[82] and half-Heusler (HH) alloys[83-85] are very promising thermoelectric candidates.

Although PbTe is a simple binary compound, its performance stands out among intermediate-temperature thermoelectrics. PbTe possesses several outstanding unique electronic band structures, superior electrical conductivity from high-symmetry cubic crystal structure, and low thermal conductivity caused by strong anharmonicity due to the Pb local off-centering.[86-88] To date, PbTe is still a research hot spot in the thermoelectric community. A large amount of achievements have been reported in PbTe-based thermoelectrics, which are evidenced by $zT_{max} \approx 2.2$ in p-type PbTe-SrTe in 2012,[89] $zT_{max} \approx 2.0$ in p-type PbTe-MgTe in 2013,[90] $zT_{max} > 2.0$ in p-type PbTe-PbS in 2014,[91] $zT_{max} \approx 2.5$ in p-type PbTe-SrTe in 2016,[92] $zT_{max} \approx 1.8$ in n-type PbTe-InSb,[93] and $zT_{max} \approx 1.8$ in n-type PbTe-Sb-I in 2017, etc. Therefore, it is essential to update these research progresses in PbTe-based thermoelectrics.

1.5 Theoretical formulation

Boltzmann transport equation method involves finding the transport parameters, such as, electronic conductivity, Seebeck coefficient and lattice thermal conductivity and associated terms (like mobility, relaxation time etc). Boltzmann transport equation (BTE) theory is a semi-classical theory and it includes different relaxation times for different scattering mechanisms like charge carrier-charge carrier scattering, charge carrier-phonon scattering, boundary scattering, defect scattering etc. All the relaxation times can be combined using Matthiessen rule, as

$$\frac{1}{\tau} = \frac{1}{\tau_{ch-ph}} + \frac{1}{\tau_{ch-ch}} + \frac{1}{\tau_{ph-ph}} + \frac{1}{\tau_{ch-imp}} + \frac{1}{\tau_{imp-imp}} + \frac{1}{\tau_{defect-defect}} + ... \tag{1.1}$$

1.5.1 Boltzmann Transport Theory

The intrinsic carrier mobility of a charged particle characterizes how quickly it can travel inside a material due to the external electric field. In fact, mobility strongly depends on the carrier scattering phenomena within the material. Predominantly, scattering caused by lattice vibrations determines intrinsic carrier mobility at high temperatures and constitutes the upper limit for free-standing defectless bulk and layered semiconducting materials. Besides phonons, the other scattering processes that contribute to the phenomenon are defects scattering, boundary scattering, impurity scattering which make it challenging to measure intrinsic mobility experimentally; as such, it is usually obtained theoretically.[94] Several methods available in the literature to calculate the carrier (electron/hole) mobility, such as the deformation potential theory (DPT)[95] using Boltzmann transport equation (BTE) theory. The BTE basically takes into account the electron-phonon coupling (EPC) matrix elements by which scattering rates and relaxation time are calculated from first principles.[96] The Boltzmann transport equation[97] (BTE) for electron distribution $f(\epsilon_{kn}) = f_{kn}$ reads

$$\frac{\partial f_{kn}}{\partial t} + v_{kn}.\nabla_r f_{kn} + \frac{F}{\hbar}.\nabla_k f_{kn} = (\frac{\partial f_{kn}}{\partial t})_{coll} \tag{1.2}$$

where the labels n and k denote the band index and k point, respectively. The velocity is defined as $v = \frac{1}{\hbar}\nabla_k \epsilon_{kn}$, and F = q(E + v × B) is the external force. The right-hand side of the above equation includes different scattering and dissipation processes that eventually drive the system to attain equilibrium. For a homogeneous system in a static electric field and zero magnetic fields, the BTE simplifies to

$$\frac{qE}{\hbar}.\nabla_k f_{kn} = (\frac{\partial f_{kn}}{\partial t})_{coll} \tag{1.3}$$

Considering $f_1 = f - f_0$ is linear in the applied electric field and for consistency, we neglect the term $\frac{1}{\hbar}.\nabla_k f_1(-eE)$, then BTE in the relaxation time approximation transforms to

$$\frac{\partial f}{\partial t} + v.\nabla f_1 - \frac{eE}{\hbar}.\nabla f_0 = -\frac{f_1}{f_0} \tag{1.4}$$

By solving the equation for relaxation time (τ), we obtain the intrinsic carrier mobility $\sigma = \frac{e\tau}{m^*}$. where e is the basic unit of charge; m* denotes the effective mass of carriers. However, to obtain intrinsic mobility that is more accurate and reliable, it is required to calculate the matrix elements of EPC for each scattering process over the full Brillouin zone. There are available methods such as solving the Boltzmann transport equation (BTE) using the carrier-phonon coupling (EPC) method by which we can estimate carrier scattering strength and relaxation time from first principles. The carrier relaxation time due to carrier-phonon scattering is given by Fermi's "golden rule" as[98],

$$\frac{1}{\tau_{ep}(k)} = \frac{2\pi}{\hbar}\Sigma_{k'}| < k'|\partial_q V|k > |^2[A+B](1-\frac{v_{k'}.v_k}{|v_{k'}||v_k|}) \tag{1.5}$$

$$A = (f_{k'} + n_q)\delta(E_k - E_{k'} + \hbar\omega_q)\delta_{k+q,k'+G} \tag{1.6}$$

$$B = (1 + n_q - f_{k'})\delta(E_k - E_{k'} - \hbar\omega_q)\delta_{k-q,k'+G} \tag{1.7}$$

where k, $k^{'}$, and q are wave vectors of the initial and final electronic states and the participating phonon state; E_k, $E_{k'}$, and ω_q are their respective energies; f_k, $f_{k'}$, and n_q are their equilibrium distribution functions; $< k'|\partial_q V|k >$ is the electron-phonon matrix element; G is a reciprocal lattice vector, and v_k and $v_{k'}$ are the group velocities of the initial and the final states. The factor $(1-\frac{v_{k'}.v_k}{|v_{k'}||v_k|})$ takes into account the momentum loss in the inelastic scattering processes, and thus the defined relaxation time is usually named "the momentum relaxation time" and used for calculating carrier mobility. Here, the challenging part is to calculate the electron-phonon matrix element, $< k'|\partial_q V|k >$. This term is computationally very expensive because it considers electrons can interact strongly with longitudinal as well as transverse optical phonon modes, which give rise to electron-phonon coupling matrix elements. Once the relaxation time is calculated throughout the Brillouin zone, we estimate the intrinsic carrier mobility accurately. Although the consideration of EPC matrix elements for each scattering process over the full Brillouin zone effectively determines accurate and reliable carrier mobility, it is computationally very expensive.

This complexity can be overcome by considering deformation potential theory (DPT) which is not only simple to understand but also computationally less expensive. Recently, it is extensively used to obtain intrinsic carrier mobility. Under DPT, the directional dependent carrier relaxation time,$\tau_\beta(i,k)$ can be derived considering the collision term in the Boltzmann Transport Equation (BTE)[99],

$$\frac{1}{\tau_\beta(i,k)} = k_B T \frac{4\pi^2 (E_\beta^c)^2}{hC_{3D}} \sum_{j,k' \in BZ} (1 - \frac{v_{jk'}}{v_{ik}}) \delta[E_{ik} - E_{jk'}] \tag{1.8}$$

where C_{3D} is elastic modulus. $\hbar$: Planck constant; k_B: Boltzmann constant; Here C_{3D} is expressed as,

$$2(E - E_0) = C_{3D} S_0 (\frac{\Delta l}{l_0})^2 \tag{1.9}$$

where E_0 and S_0 are the energy and lattice volume of the unit cell without strain and E is the energy of the strained system. The parabolic equation is used to calculate the value of C_{3D}. And the deformation potential constant, E_c^β is derived as,

$$E_\beta^c = \frac{\Delta E_{band}}{\frac{\Delta l}{l_0}} \tag{1.10}$$

where ΔE_{band} is a shift in energy level at the band edge position because of lattice strain $\frac{\Delta l}{l_0}$. To compute charge carrier mobility, we use Boltzmann transport formalism within deformation potential theory (DPT). Here, the band energies (ϵ_i) and carrier group velocities ($v_i = \frac{\nabla E_i(k)}{h}$) are obtained from the first-principle calculations. The carrier (electron and hole) mobility along the direction is defined as,

$$\mu_\beta^{e/h} = \frac{e}{k_B T} \frac{\sum_{i \in CB(VB)} \int \tau_\beta(i,k) v_\beta^2(i,k) b(k) dk}{\sum_{i \in CB(VB)} \int b(k) dk} \tag{1.11}$$

$$b(k) = exp[\mp \frac{E_i(k)}{k_B T}] \tag{1.12}$$

here, e and T are electronic charge and absolute temperature, respectively. In fact, Bardeen and Shockley in 1950 derived charge carrier mobility expression for three dimensional (3D) nonpolar semiconductors considering DPT.[100] Here, acoustics phonon limited intrinsic carrier mobility of a 3D non-polar semiconductor can be written as:

$$\mu = \frac{2^{3/2}\pi^{1/2}}{3} \frac{C_{3D}\hbar^4 e}{E_1^2 m^{*5/2}(k_B T)^{3/2}} \tag{1.13}$$

In 1969, Kawaji modified the theory mobility expression for 2D electron gas where the effect of anisotropic effective mass was incorporated into the theory. The 2D mobility expressions were written as[101-102]:

$$\mu_j = \frac{C_j \hbar^3 e}{E_j^2 m_j m_d k_B T} \tag{1.14}$$

where $j = x, y$, and $m_d = (m_x^* m_y^*)^{1/2}$ is the average effective mass along $x-$ and $y-$ directions while m_j^* is the direction-dependent carrier effective mass. C_j is the directional dependent elastic constant for 2D materials. Once mobility is obtained, we calculate electrical conductivity using the Drude formula $\sigma = ne\mu$. The thermopower or Seebeck coefficient (S) can be derived by solving BTE in the presence of a temperature gradient. Seebeck coefficient is enumerated using the following equation,[103]

$$S = -\frac{\pi^2}{3e} k_B^2 T \frac{\partial ln(DOS(E))}{\partial E} \tag{1.15}$$

here, k_B: Boltzmann constant and DOS(E): energy-dependent DOS. We also solve BTE to compute phonon relaxation time (τ_{iq}) is employed to calculate lattice thermal conductivity. The lattice thermal conductivity can be written as,

$$\kappa_{lat} = \sum_{i,i',q,q'} C_{iq} v_{iq} v_{i'q'} \tau_{iq} \tag{1.16}$$

where C_{iq} is the specific heat, v_{iq} is the phonon group velocity and τ_{iq} is the phonon relaxation time.

1.5.2 Electronic structure calculations

In quantum mechanics, all kind of characteristics of a system is stored in the corresponding wave function. Electronic information like energy, momentum etc can be derived with the help of corresponding operators from this wave function. It is denoted by a symbol Ψ, and written as $\Psi = \Psi$(R,r), where R and r represent the summarized spin and spatial coordinates of nuclei and electron respectively. The energy of each system can be obtained by applying Hamiltonian operator ($\hat{H}$) on Ψ(R,r) and the equation is widely known as Schrödinger equation,

$$\hat{H}\Psi(R,r) = E\Psi(R,r) \tag{1.17}$$

$$\hat{H} = -\frac{1}{2}\sum_{i=1}^{N}\nabla_i^2 - \sum_{k=1}^{K}\frac{1}{2M_k}\nabla_k^2 - \sum_{i=1}^{N}\sum_{k=1}^{K}\frac{Z_k}{|r_i - R_k|} + \frac{1}{2}\sum_{i\neq j}^{N}\frac{1}{|r_i - r_j|} + \frac{1}{2}\sum_{k\neq I}^{K}\frac{Z_k Z_I}{|R_k - R_I|} \tag{1.18}$$

$$\hat{H} = \hat{T_e} + \hat{T_n} + \hat{V_{en}} + \hat{V_{ee}} + \hat{V_{nn}} \tag{1.19}$$

In the above equation, the first term is the kinetic energy of N number of electrons, second term is kinetic energy of L number of nuclei, third, fourth and fifth terms are the potential energies corresponding to nuclei-electron, electron-electron, nuclei-nuclei interactions respectively.

1.5.3 Born-Oppenheimer Approximation

Born-Oppenheimer approximation, also familiar as adiabatic approximation, allows to decouple the dynamics of nuclei and electrons because the nuclei are almost 2000 times heavier than the electrons, so it can be assumed that nuclei remain static with respect to electrons movement. Hence time-independent Schrödinger equation (SE) can be written for electronic degrees of freedom in the presence of stationary nuclear part. The modified electronic Hamiltonian is,

$$\hat{H}_e = \hat{T}_e + \hat{V}_{en} + \hat{V}_{ee} \tag{1.20}$$

Over a period of time, various approaches with compatible approximations have been considered to solve the SE, which include Hartree-Fock (HF), configuration interaction (CI), coupled cluster, Moller-Plesset perturbation theory, to name a few. Along with HF theory, other methods are all wave-function based approach. Though these methods provide better results, the latter approaches demand high computational power.

1.5.4 Density Functional Theory

Density functional theory based method is a different approach to solve the SE, which replaces wave function with the electron density of the system to obtain the ground state electronic properties. This method was first proposed in 1960s in two seminar papers by Hohenberg-Kohn.[104] Later in two subsequent years, whose idea was mainly based upon Thomas-Fermi model. This *ab initio* (first principles) based method has gradually drawn attention as it is capable of mapping a complicated interacting problem to an easier non-interacting problem with replacement of the number of degrees of freedom, 3N (N is number of quantum particles) to only 3 spatial coordinates.

Hohenberg-Kohn Theory

This is based upon two theorem,

Theorem-I [Uniqueness] ”For any system of interacting particles in the presence of an external potential V$_{ext}$(r), the potential V$_{ext}$(r) can be uniquely determined, upto an additive constant, by the ground state density n$_0$(r).” In other words, the total ground state energy of a system is a unique functional of its density, E[n(r)], hence we can write:

$$E[n(r)] = \langle\Psi[n(r)]|H|\Psi[n(r)]\rangle \tag{1.21}$$

Theorem-II [Variational Theory] ”A functional which is universal for he energy E[n] in terms of density n(r) can be defined, valid for any external potential V$_{ext}$(r). For any particular V$_{ext}$(r), the exact ground state energy of the system defines the global minimum value for this functional, and the density which minimizes the functional is the exact ground state density n$_0$(r)”. The energy can be expressed as a sum of kinetic energy part (T[$n(r)$]), electrostatic energy part (U[$n(r)$]) and energy due to non-interacting electrons moving under external potential:

$$E[n(r)] = T[n(r)] + U[n(r)] + \int [V(\vec{r})n(\vec{r})d^3r] \tag{1.22}$$

Here the first two terms are independent of external potential and can be written in the form of universal functional of the electron density:

$$T = \int \frac{3}{10}[3\pi^2 n(r)]^{\frac{2}{3}} n(r)dr \tag{1.23}$$

$$U = \frac{1}{2}\int \frac{n(r)}{|r-r'|}dr'dr \tag{1.24}$$

The expression of kinetic energy is however inaccurate and moreover, the deduction of the functional of the interacting systems is not very clear. This is solved by Kohn-Sham approach, where they have proposed an indirect approximate approach to calculate energy functional E[n(r)].

Kohn-Sham Equations

Kohn and Sham considered a uniform electron density from 3d non-interacting electron gas and iteratively solved the Kohn-Sham equation. They considered, as a first approximation, a fictitious system of non-interacting electrons instead of a real system of interacting electrons having the same electron density. This theorem is enabled to calculate energy and other electronic properties of only the ground state. Having the same electron density leads to same ground state energies and other electronic properties. Since electrons are not affecting each other, Kohn-Sham equation can be considered as a set of single particle equations, which are simpler to handle than coupled Schrödinger equation, which gets more complicated with the increase of system size and hence number of electrons. The interacting part of the energies has been taken care of in terms of exchange-correlation and energy is written in terms of density:

$$E_{[\mathrm{n(r)}]} = T_{[\mathrm{n(r)}]} + E_{\mathrm{ext}[\mathrm{n(r)}]} + \frac{1}{2}\int \frac{n(r)}{|r-r'|} + v_{\mathrm{xc}[\mathrm{n(r)}]} \tag{1.25}$$

In the above equation, the first term is kinetic energy of only non-interacting electrons, second term is classical Coulomb interaction between nuclei and electron, third term is classical electron-electron interactions also known as Hartree interaction, the final term is exchange-correlation including the non-classical electrostatic interaction energy between electrons and the difference of energy between non-interacting and interacting kinetic energy of electron. The main idea behind this approach is that the first three terms can be dealt with simply and last term can be modified with better approximations.

Exchange-Correlation Functionals

The exchange-correlation functionals include two different kinds of electronic interactions; the exchange part comes because of fermionic nature of the electrons. The antisymmetrically paired electrons exchange with each other following Pauli exclusion principle. The other term i.e. correlation term arises from the effect of other electrons on kinetic and potential energy. The exact form of each interactions is still unknown, hence the mathematical expressions have been provided for both the terms. Hartree-Fock method was able to provide an exact form of exchange energy but it has not included correlation energy at all. Since the accuracy of calculation depends on the exchange-correlation functionals, various modifications have been done over the time.

Local density approximation: LDA is the simplest approximation, where the exchange correlation term can be expressed as a function of homogeneous electron gas i.e. uniform electron density.

$$E_{ex(n)}^{LDA} = \int e_{\mathrm{xc}}(n(r)n(r)dr \tag{1.26}$$

The mathematical form of exchange and correlation energy is:

$$e_{\mathrm{x}}(n) = -\frac{0.458}{r_{\mathrm{s}}} \tag{1.27}$$

$$e_{\mathrm{c}}(n) = -\frac{0.44}{r_{\mathrm{s}} + 7.8} \tag{1.28}$$

$\mathrm{r_s}$ is the radius of a sphere containing one electron. The correlation energy is deduced by quantum Monte-Carlo simulations, most commonly used one was proposed by Perdew and Zunger.[105] Inspite of being an extensive crude approximation, it works well for solid systems close to a homogeneous gas and explain a few physical properties like lattice parameters, vibrational frequencies, equilibrium geometries properly. However, it overestimates the binding energies and does not work well for inhomogeneous systems.

Generalized gradient approximation: To account for inhomogeneity of the system, GGA has modified LDA by including the gradient expansion term:

$$E_{\mathrm{ex(n)}} = \int e_{\mathrm{xc}}(n(r), |\partial n(r)|)n(r)dr \tag{1.29}$$

There are several approaches which can be included within GGA calculations, the commonly used ones is PBE[106]. The choice of functional is dependent upon the characteristics of the system. It has a tendency to underbind.

Several better modifications have been introduced to GGA resulting in meta-GGA, hybrid functionals. This functionals have been modified by considering both the electronic density and individual electronic wavefunctions to compute the energy and other properties.

Basis set and Pseudopotential

To do the calculations, the Kohn-Sham (KS) orbitals have to be expanded based on the nature of systems to solve the KS equation, like plane wave function[107] is used for periodic systems. According to Bloch's theorem, electron's wavefunction can be expressed as a product of plane wave and function correspond to the periodic lattice system:

$$\Psi_{\mathrm{nk}}(r) = e^{\mathrm{ik.r}}u^{\mathrm{nk}}(r) \tag{1.30}$$

here wave vector k is the crystal momentum vector.

It is well known that, the core electrons do not participate in the chemical reactions or have minimum role in exhibiting any physical or chemical properties; moreover since they are tightly bound and highly localized in nature hence all electron calculations are highly costly to calculate. The concept of pseudopotential approximation has arrived to deduct this computational cost by eliminating the core states calculations. Here instead of strong ionic potentials a weaker pseudo potentials which is a pseudo wavefunction of valence electrons only has been considered. The oscillation of valence electrons in the core region has not been taken into account, a pseudo wavefunction of the valence electrons has replaced the strong ionic potentials. There is a critical distance after nuclei, named as 'cut-off' radius beyond which the pseudo-wave function compares fairly well with the actual one. If this cut-off is high, then the pseudopotentials are called soft. The nature of PP approximation depends on its smoothness and transferability properties. There are three types of PP - norm-conserving, ultra-soft and projector-augmented wave.

1.5.5 Density Functional Perturbation Theory

Density Functional Perturbation Theory (DFPT) is a linear response technique for computing the second derivatives of the ground state energy with respect to external perturbation $\lambda \equiv \{\lambda_i\}$. The first and second derivatives of the ground-state energy are

$$\frac{\partial E}{\partial \lambda_i} = \frac{\partial E_{ion-ion}}{\partial \lambda_i} + \int dr \frac{\partial V_{ext}(r)}{\partial \lambda_i} \rho(r) \tag{1.31}$$

and

$$\frac{\partial^2 E}{\partial \lambda_i \lambda_j} = \frac{\partial^2 E_{ion-ion}}{\partial \lambda_i \lambda_j} + \int dr \frac{\partial^2 V_{ext}(r)}{\partial \lambda_i \lambda_j} \rho(r) + \int dr \frac{\partial \rho(r)}{\partial \lambda_i} \frac{\partial V_{ext}(r)}{\partial \lambda_j} \tag{1.32}$$

In Equation 1.32, $\frac{\partial \rho(r)}{\partial \lambda_i}$ is the induced charge-density by the first order perturbation, which is the new quantity to derive and defined as,

$$\frac{\partial \rho(r)}{\partial \lambda_i} = \sum_i \frac{\partial \phi_i^*(r)}{\partial \lambda} \phi_i(r) + \phi_i^*(r) \frac{\partial \phi_i(r)}{\partial \lambda} \tag{1.33}$$

In the linear approximation, $\frac{\partial\rho(r)}{\partial\lambda_i} = \Delta\rho(r)$ where, $\Delta\rho(r)$ can be expressed as,

$$\Delta\rho(r) = \sum_i^N \phi_i^*(r)\Delta\phi(r) \tag{1.34}$$

$$\left[-\frac{\hbar^2\nabla^2}{2m} + V_{KS}(r)\right]\phi_i(r) = \epsilon_i\phi_i(r) \tag{1.35}$$

$V_{KS}(r) = V_{loc}(r) + V_H(r) + V_{XC}(r).V_{KS}(r,\lambda)$,

V_{KS} depends on λ, as a result, $\phi_i(\mathbf{r},\lambda)$ and $\epsilon_i(\lambda)$ are the function of λ. Hence, after the first order derivative with respect to λ, we get,

$$\left[-\frac{\hbar^2\nabla^2}{2m} + V_{KS}(r) - \epsilon_i\right]\frac{\partial\phi_i}{\partial\lambda}\phi_i(r) = -\frac{\partial V_{KS}(r)}{\partial\lambda}\phi_i(r) + \frac{\partial\epsilon_i}{\partial\lambda}\phi_i(r) \tag{1.36}$$

where,

$$\frac{\partial V_{KS}(r)}{\partial\lambda_i} = \frac{\partial V_{local}(r)}{\partial\lambda_i} + \frac{\partial V_H(r)}{\partial\lambda_i} + \frac{\partial V_{XC}(r)}{\partial\lambda_i} \tag{1.37}$$

and

$$\frac{\partial V_H(r)}{\partial\lambda_i} = \int \frac{1}{|r-r'|}\frac{\partial\rho(r')}{\partial\lambda}d^3r' \tag{1.38}$$

So, the variation in Kohn-Sham potential is given by,

$$\frac{\partial V_{XC}(r)}{\partial\lambda_i} = \frac{dV_{XC}}{d\rho}\frac{\partial\rho(r)}{\partial\lambda} \tag{1.39}$$

$\Delta\epsilon_i = \langle\phi_i|\Delta V_{ext}(r)|\phi_i\rangle$

Hence, self-consistent solution of the set of linear equations, $\Delta\rho$ can be evaluated with reasonable accuracy. $\Delta\rho$ is used in Equation 1.32, to find the second derivative of the total energy. Following this procedure, DFPT method is applied to evaluate the phonon frequencies by evaluating the second derivatives of energy with respect to atomic positions (displacement of ions is the perturbation).

Advantages of the DFPT method are: (1) it avoids the use of supercell, (2) allows the calculation of phonon frequencies at arbitrary phonon wave vector (q), and (3) makes the intensity of the calculation independent of the phonon wavelength.

1.5.6 *ab initio* Molecular Dynamics

Predicting the material properties can be achieved quite accurately though usage of relativistic time-dependent Schrödinger equation. However, this method has serious limitation towards treating large and complex materials. To treat large systems, one need to find other suitable methods. In this regard, molecular dynamics (MD) simulations are quite reliable and computationally affordable to gain detailed structural and conformational aspects on a realistic time scale and atomic level. Simulating systems by MD, we can obtain ensemble-averaged properties, such as binding energy, relative stability of molecular conformations etc. by averaging over representative statistical ensembles of structures.

Basically, we need to obtain the numerical solution of Newton's equation of motion for all the nuclei within a system. In classical MD, the force (F_i) on a atom 'i' with mass M_i is formulated as follows,

$$\overrightarrow{F_i} = M_i \frac{\partial^2 \overrightarrow{r_i}}{\partial t^2} \tag{1.40}$$

The vector notations in forces F_i and positions r_i, *i.e.* in three dimensions the whole system is described by 3N coordinates. The forces on a atom 'i' is calculated as the negative derivative of the potential U, describing the interactions between the particles. And it can be written as,

$$\overrightarrow{F_i} = -\frac{\partial U}{\partial \overrightarrow{x_i}} \tag{1.41}$$

where, U, the inter-atomic potential, is a function of many degrees of freedom corresponding to all nuclei. The major challenge in MD simulations is calculating interatomic forces accurately. In classical MD, forces are calculated from "predefined potentials", which are either based on empirical data or on independent electronic structure calculations. Although, these empirical potentials have been modified over time to make them reliable, transferability is still the major issue. Moreover, classical MD cannot capture the bond-reformation processes taking place in many dynamic systems. To overcome these limitations, first-principle based approach *i.e.* ab-initio molecular dynamics (AIMD) has been developed by various groups. Here, the forces are calculated on-the-fly from accurate electronic structure calculations. However, the better accuracy and reliable predictive power of AIMD simulations demands significant increase in computational effort. Thus, till now, DFT is the most commonly applied method for electronic structure calculation during AIMD simulations. Notably, evaluation of interatomic forces in AIMD does not depend on any adjustable parameters but only on position of nuclei. Depending upon the way of solving the electronic structures in every AIMD steps, there are different approaches developed by the researchers. These are Ehrenfest molecular dynamics, Born-Oppenheimer molecular dynamics (BOMD), Carr-Parrinello molecular dynamics (CPMD) etc. For the works presented in this thesis, we have extensively used BOMD simulations to investigate structural evaluation of various low-dimensional as well as bulk systems at finite temperatures.

Born-Oppenheimer Molecular Dynamics

BOMD simulation is based on the direct solution of the static electronic structure problem in each molecular dynamics step, given the set of fixed nuclear positions at any instance of time. Hence, electronic structure part is tackled by solving the time-independent Schr*ö*dinger equation and then propagating the nuclei via classical molecular dynamics. Note that, unlike other AIMD methods, the time-dependence of the electronic structure is a consequence of nuclear motion for BOMD simulations. One can define the force ($F_i = M_i\ddot{R}_i(t)$) on a atom 'i' with mass M_i, as follows within the BOMD framework,

$$M_i\ddot{R}_i(t) = \nabla_i \underset{\psi_0}{min} < \psi_0|H_e|\psi_0 > \tag{1.42}$$

thus, the electronic ground state can be determined.

1.6 Softwares used:

To obtain the reported results in this thesis several packages have been used. We have considered periodic (bulk as well as layered) systems; all the electronic structure calculations were carried out with DFT method; geometry optimization, thermodynamic calculations, vibrational frequency analyses, were carried out using Quantum Espresso (QE) and Vienna Ab initio Simulation Package (VASP). The structures are constructed, visualized and analysed with the help of XCrySDen, VESTA, Xmgrace.

1.7 Computational Strategies

Over the years, various strategies have been adopted to enhance carrier transport properties which is an important parameter for advanced transport devices, photovoltaic and thermoelectric applications. The most effective approach to improve electronic transport properties is through carrier optimizations and band engineering; effectively to decouple electrical conductivity (σ) and Seebeck coefficient (S) and simultaneously increase their values to achieve higher thermoelectric power factor ($S^2\sigma$). Electrical conductivity is a product of mobility and number of charge carriers and interestingly, for advanced transport devices and photovoltaics, one has to increase the mobility to very high magnitudes. On the other hand, through nano-structuring, lattice thermal conductivity can be reduced without affecting electrical transport so that improved thermoelectric figure of merit can be achieved.

1.7.1 Optimizing Carrier Concentration

The parameters that affects thermoelectric performance, S, σ, and κ_e directly related via following relationship:

$$S = \frac{8\pi^2}{3}\frac{k_B^2}{eh^2}m^*T(\frac{\pi}{3n})^{2/3} \tag{1.43}$$

$$\sigma = \frac{ne^2\tau}{m^*} \tag{1.44}$$

$$\kappa_e = L\sigma T \tag{1.45}$$

m^* is the effective mass of carrier and as can be seen above, the m^* appears in the numerator for Seebeck coefficient while it is inversely proportional to electrical conductivity. Also while Seebeck coefficient is inversely proportional to carrier concentration (n), electrical conductivity is directly proportional to n. Their interdependent relationship limits the thermoelectric power factor. As a consequence, the appearance of heavy as well as light holes/electrons in the electronic band structure enhances the thermoelectric power factor significantly.

Moreover, such inter-relationships suggest that n needs to be compromised for high σ and S as well as low κ_e (Figure 1.6), making controlling n a crucial strategy to secure high zT values. Practically, n of materials can be modulated by tuning the extrinsic doping or intrinsic defects. Generally, carrier concentration

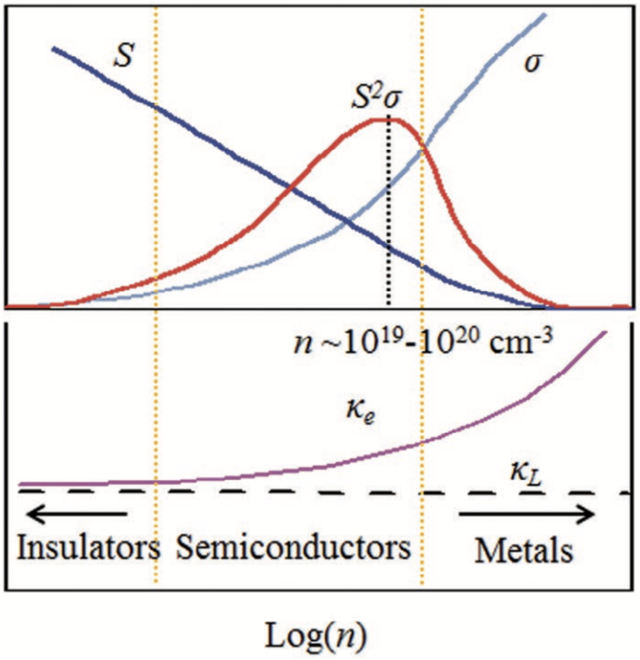

Figure 1.6: Schematic shows the n-dependent TE properties.

depends upon T and electronic nature of the materials.[108] To measure n, various theoretical as well as experimental procedures are available. According to single band model[109], $n = (m_d T)^{1.5}$ where m_d^* is the density of states effective mass which can be tuned by changing electronic band structure.

1.7.2 Band Engineering

The electrical transport properties of a material primarily governed by its band structure, so tuning the band structure can effectively modulate the overall TE performance. The key approaches towards band engineering includes (a) enlarge band gap to reduce bi-polar transport, (b) tune m*, (c) introduce resonant state near the Fermi level, (d) band convergence to enhance S.

Tuning the Bandgap

At high temperatures, thermal excitation occurs which can increase n and as a result zT reduces due to S reduction and κ_e enhancement according to Equations (1.43) and (1.45). Theoretical[110-111] and experimental[112] studies suggest that E_g of semiconductors can be efficiently tuned via doping, and the enlarged E_g can shift the thermal excitation temperature of minor charge carriers toward a higher temperature range to suppress the minor carriers. The minor charge carriers can behave as heat carriers, which causes bipolar thermal conductivity (κ_{bi}) [113-114] to contribute more κ that decreases zT. κ_{bi} is a function of E_g and T and is defined as[113] $\kappa_{bi} = exp[-E_g/2k_BT]$. As can be realised from the equation that κ_{bi} increases with increasing T, so that the impact of κ_{bi} at higher temperature can limit the zT value for the intermediate or high temperature TE materials.[113] On the other hand, κ_{bi} can be reduced via increasing E_g due to the reduced thermal excitation of minor carriers at high temperature.

Tuning carrier effective mass

For a given n, a high DOS effective mass (m_d^*) can lead to a high S according to Equation (1.43). The principle of increasing (m_d^*) by controlled doping is to increase the band effective mass of a single valley (m_b^*) as[115] $m_d^* = N_v^{2/3} m_b^*$; where N_v is the band degeneracy. However, increasing (m_b^*) will reduce μ since[115] $\mu \propto 1/m_b^*$. Therefore, $S^2\sigma$ can be reduced due to the σ reduction according to Equation (1.44), so that a high (m_d^*) does not always lead to an overall high zT. Therefore, to practically enhance σ of TE materials, it is important to tune the (m_d^*) so that the band structure has narrow and wide band at different k points (to obtain large and small m^* values). If not, one has to compromise with μ to obtain the optimized $S^2\sigma$.

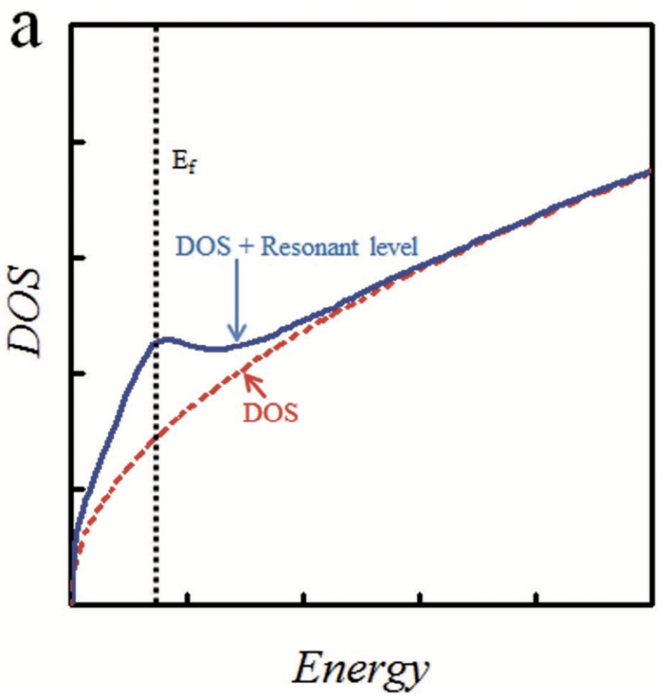

Figure 1.7: Schematic illustrates the resonant level on the DOS.

Introducing resonating states

Researchers have observed that in many situations, the energy level of dopants lies in the conduction or valence bands (depending upon the n- or p-type semiconductor material), introducing a “resonant” state due to a distortion on the host band (Figure 1.7(a)), and it is termed as resonant doping.[116] When the Fermi level moves close to the resonant state, m^* becomes significantly increased due to the increased DOS, thus, S increases according to Equation (1.43) without changing n.[116]

Band Convergence

According to equation (1.43), enhanced m_d^* due to large N_v could lead High zT of TE materials, but keep μ unaffected.[117] Nevertheless, N_v can also be increased when multiple electronic bands of materials converge via proper doping and in-

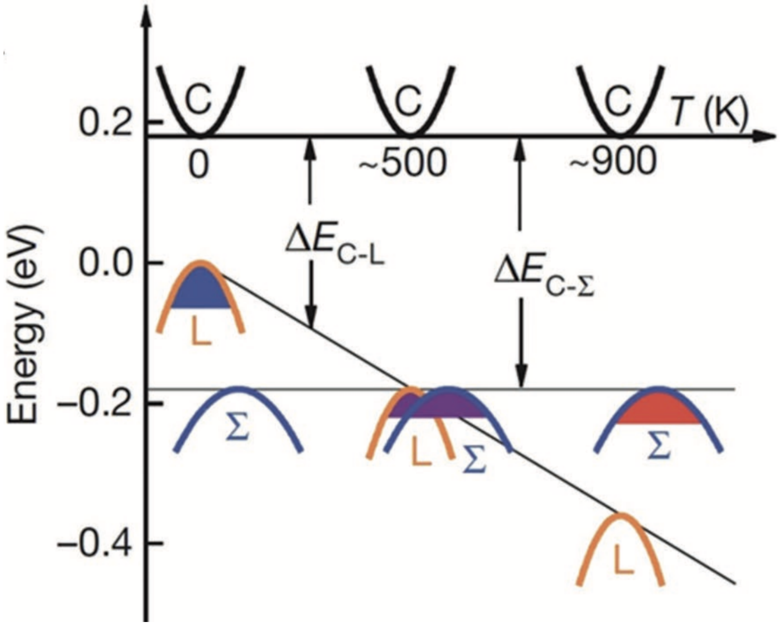

Figure 1.8: Schematic of band convergence in $\mathrm{PbTe_{0.85}Se_{0.15}}$. At 500 K, the two valence bands converge, resulting in transport contributions from both the L and Σ bands. Reproduced with permission.[125] Copyright 2018, Wiley Publishing Group.

creasing T (Figure 1.8).[118] Using PbTe as an example to demonstrate the band convergence, Figure 1.8 shows a two valence band model of PbTe, which includes a principle valence band (L band, located at the L point of the Brillouin zone) active at low temperature and a secondary valence band (Σ band, located at the Σ point of the Brillouin zone) dominating at the temperatures of $\simeq$ 450 K. There is a small energy separation ($\Delta E = E_{VL}{-}E_{V\Sigma}$) of $\simeq$ 0.2 eV (comparable to E_g) between these two valence bands, and the L band and Σ band have $N_v = 4$ and $N_v = 12$, respectively.[118] ΔE became smaller with increasing T and the band convergence of between the L band and Σ band was observed in Se-doped PbTe[118] at $\simeq$ 500 K (Se doping in PbTe increased the band convergence temperature[118]), as shown in Figure 1.8, providing an overall $N_v = 16$, and in turn leading to an increased m_d^* (Equation (1.43)) without explicitly reducing μ.[118] As a consequence, zT is greatly increased.

1.7.3 Nanostructure Engineering

It is clear from zT expression that thermal conductivity (κ) must be minimized to achieve high zT. Generally, when $S^2\sigma$ is increases via doping or alloying[119] with different elements, κ_{lat} simultaneously diminishes due to the increased phonon-phonon scattering by the introduced dopant atoms or ions.[120] However, such a lowering of κ_{lat} is usually compensated by the enhanced κ_e due to the increased n. For significantly reduction in κ_{lat}, and therefore, κ_{tot}, nanostructure engineering has been widely employed as an effective approach to obtain high zT mainly by two approaches: (a) developing low-dimensional nanomaterials[121] or (b) bulk materials containing nano-composites/nanoinclusions, which can ensure improved zT that benefits from the dimensional reduction of materials.[121] The enhancement of zT in low-dimensional TE materials is mainly due to the quantum confinement effect, while the bulk materials with nanocomposites/nanoinclusions involve complex phonon scattering mechanisms and low energy carrier filtering effects.

Low dimensional TE material

The low-dimensional or nanocrystalline materials can achieve a high zT through the quantum size effect and decreasing κ_{lat} by increasing the phonon scattering.[123] The decrement in dimensionality leads unique change the DOS and causes quantum confinements in the nano-structures,[122] which result in large S.

Nanocomposites/Nanoinclusions Engineering in Bulk systems

Experimentally, Nanocomposite TE materials[124] or materials containing nanoinclusions are relatively easy to fabricate and investigate compared to nanomaterials.[125] Bulk TE materials having nanosized substructures are being fabricated through various experimental techniques.[126] In fact, high density of interfaces (grain boundaries), lattice distortion, dislocations, and defects scattering originated due to introduction of nanostructures into bulk materials can influence phonon dynamics which in turn lowers κ_{lat}, thereby reducing κ. Figure 1.9 explains the scattering mechanisms between the carriers occurred due to nanoparticles in bulk materials that can scatter phonons of different wavelengths without disrupting charge carrier transport. Nanosized grains and grain boundaries predominantly scatter the phonons having medium and long wavelengths comparable to their wavelengths, while short wavelength phonons can be scattered by the point defects and dislocations. Such strong phonon scattering can reduce κ_{lat} to almost 50% which can lead to an increase in zT by a factor of 2. On the other hand, electrons with much shorter scattering wavelengths will not be scattered significantly, as a result, σ will not be affected due to the nature of nanocomposites. Recently, such strategies has been successfully adopted and become effective to enhance zT in many material systems including Cu_2Se,[127] Bi_2Te_3,[128] Bi_2Se_3,[129].

All-Scale Hierarchical Architectures

Generally, κ_{lat} depends upon their phonon dynamics including all ranges of wavelength (short, intermediate, and long), which can be effectively scattered by the features with comparable scales. Through innovative design, all-scale hierarchical architectures can be realized to provide full-spectrum phonon scattering which can dramatically improve the TE performance (Figure 1.9(b)). The principle of all-scale hierarchical architectures includes (1) point defects (including substitution atoms) which scatter phonons with short wavelengths; (2) grain boundaries, dislocations and lamellar/multilayer structures to scatter phonons with intermediate wavelengths; and (3) nanomeso-scale grains [127-128] or inclusions to scatter phonons with long wavelengths, so that the overall κ_{lat} can be reduced closer to the amorphous limit.

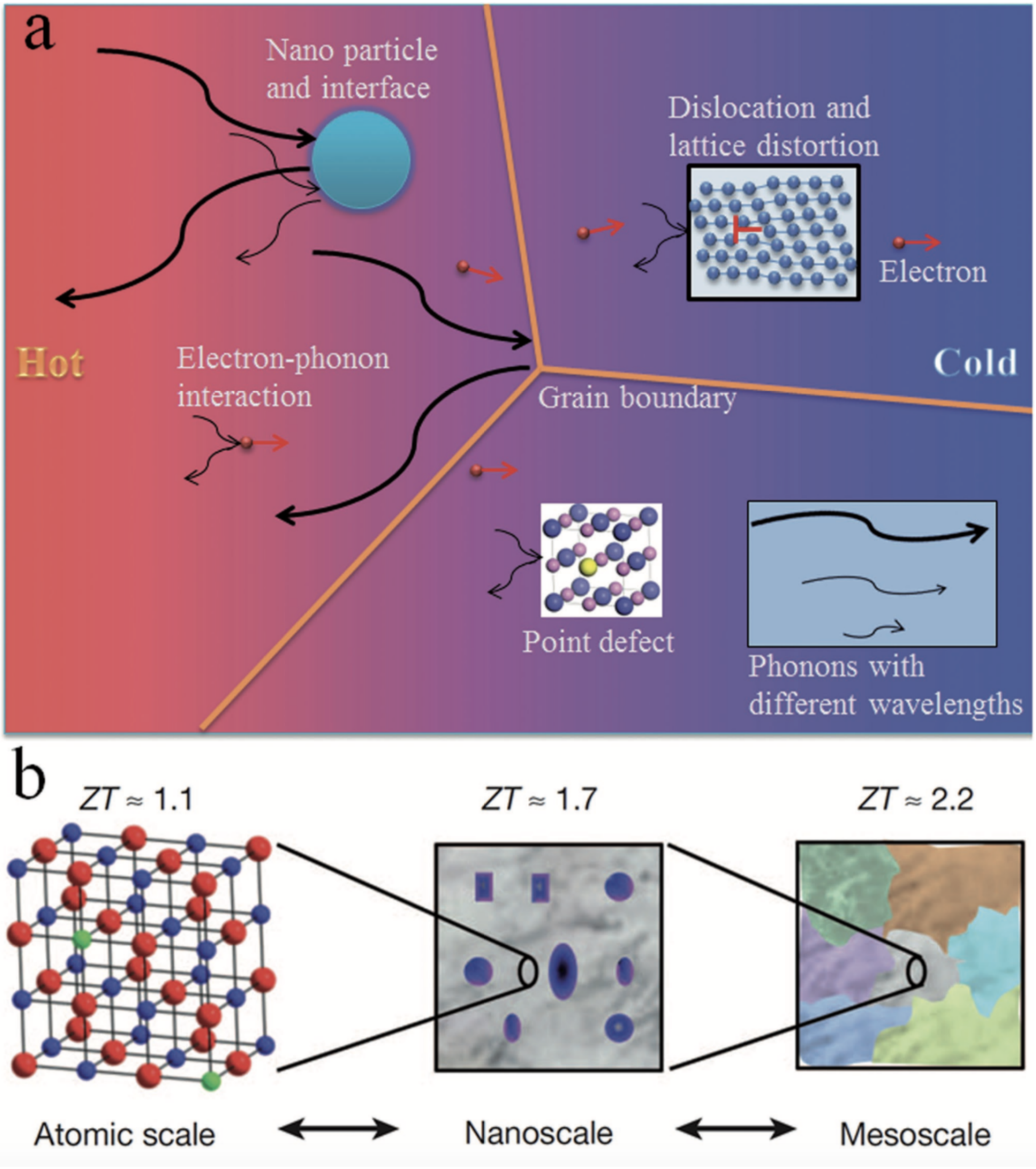

Figure 1.9: Schematic diagram of phonon scattering mechanisms and electronic transport within a thermoelectric material. Copyright 2012, Nature Publishing Group.

1.8 Scope of the thesis

The thesis commences with the study of the layered structure of β-TeO_2 that exhibits high carrier mobility together with a broad band gap, which could be a promising candidate for nanoelectronics applications. In chapter 3, we have analyzed the vibrational spectra of MO (M = Sn/Pb) and have also shown the role of avoided crossing in thermodynamic properties. In chapter 4, we have explored new layered superlattice (SnO-PbO) which is dynamically as well as thermodynamically stable and shown to be very good thermoelectric oxide material. Chapter 5 answers the underlying reason behind the appearance of unique electronic band structure and the reduction in lattice thermal conductivity due to Gd doping in PbTe. We have also modelled a new (hexagonal) phase of 2D SnTe and have explored thermoelectric properties because of 3d transition metal doped in 2D SnTe which will be discussed in chapter 6. Chapter 7 focuses on the pseudoternary phase, $Ag_2Se_{0.5}Te_{0.25}S_{0.25}$, which shows improved thermoelectric performance ($zT \simeq 2.1$ at 400 K) through Rashba effect and entropy engineering.

1.9 References

[1] Doman, L.E.; Arora, V.; Singer, L.E.; Zaretskaya, V.; Jones, A.; Huetteman, T.; Bowman, M.; Slater-Thompson, N.; Hojjati, B.; Peterson, D.; Gross, P. International energy outlook. US Energy Information, Administration 2016.

[2] Koumoto, K.; Terasaki, I.; Funahashi, R. Complex oxide materials for potential thermoelectric applications. MRS bulletin 2006, 31(3), 206-210.

[3] Administration UEI, 2017. International Energy Outlook 2017.

[4] Kim, H.S.; Liu, W.; Ren, Z. The bridge between the materials and devices of thermoelectric power generators. Energy Environmental Science 2017, 10(1), 69-85.

[5] Zhang, Q.H.; Huang, X.Y.; Bai, S.Q.; Shi, X.; Uher, C.; Chen, L.D. Thermoelectric devices for power generation: recent progress and future challenges. Advanced engineering materials 2016, 18(2), 194-213.

[6] Zebarjadi, M.; Esfarjani, K. MS Dresselhaus, ZF Ren, and Gang Chen. Perspectives on thermoelectrics: from fundamentals to device applications. Energy Environmental Science 2012, 5(1), 5147-5162.

[7] Zheng, X.F.; Liu, C.X.; Yan, Y.Y.; Wang, Q. A review of thermoelectrics research–Recent developments and potentials for sustainable and renewable energy applications. Renewable and Sustainable Energy Reviews 2014, 32, 486-503.

[8] Yang, J.; Caillat, T. Thermoelectric materials for space and automotive power generation. MRS bulletin 2006, 31(3), 224-229.

[9] Dunham, M.T.; Barako, M.T.; LeBlanc, S.; Asheghi, M.; Chen, B.; Goodson, K.E. Power density optimization for micro thermoelectric generators. Energy 2015, 93, 2006-2017.

[10] Yuan, Y.; Xiao, Z.; Yang, B.; Huang, J. Arising Applications of Ferroelectric Materials in Photovoltaic Devices. J. Mater. Chem. A 2014, 2, 60276041.

[11] Wells, H. L. U ber die Casium- und Kalium-Bleihalogenide. Zeitschrift fur anorganische Chemie 1893, 3, 195210.

[12] Weber, D. $CH_3NH_3PbX_3$, ein Pb(II)-System mit kubischer Perowskitstruktur/ $CH_3NH_3PbX_3$, a Pb(II)-System with Cubic Perovskite Structure. Z. Naturforsch., B: J. Chem. Sci. 1978, 33, 1443 1445.

[13] Weber, D. $CH_3NH_3SnBr_xI_{3-x}$ (x = 0 - 3), ein Sn(II)-System mit kubischer Perowskitstruktur/ $CH_3NH_3SnBr_xI_{3-x}$(x = 0 - 3), a Sn(II)- System with Cubic Perovskite Structure. Z. Naturforsch., B: J. Chem. Sci. 1978, 33, 862865.

[14] Møller, C. K. A Phase Transition in Cæsium Plumbochloride. Nature 1957, 180, 981982.

[15] Møller, C. K. Crystal Structure and Photoconductivity of Cæsium Plumbohalides. Nature 1958, 182, 14361436.

[16] Yang, R. X.; Butler, K. T.; Walsh, A. Assessment of Hybrid OrganicInorganic Antimony Sulfides for Earth-Abundant Photovoltaic Applications. J. Phys. Chem. Lett. 2015, 6, 50095014.

[17] Slavney, A. H.; Hu, T.; Lindenberg, A. M.; Karunadasa, H. I. A Bismuth-Halide Double Perovskite with Long Carrier Recombination Lifetime for Photovoltaic Applications. J. Am. Chem. Soc. 2016, 138, 21382141.

[18] McClure, E. T.; Ball, M. R.; Windl, W.; Woodward, P. M. Cs_2AgBiX_6 (X = Br, Cl): New Visible Light Absorbing, Lead-Free Halide Perovskite Semiconductors. Chem. Mater. 2016, 28, 1348 1354.

[19] Greul, E.; Petrus, M. L.; Binek, A.; Docampo, P.; Bein, T. Highly Stable, Phase Pure $Cs_2AgBiBr_6$ Double Perovskite Thin Films for Optoelectronic Applications. J. Mater. Chem. A 2017, 5, 19972 19981.

[20] Wu, C.; Zhang, Q.; Liu, Y.; Luo, W.; Guo, X.; Huang, Z.; Ting, H.; Sun, W.; Zhong, X.; Wei, S.; Wang, S. The dawn of lead-free perovskite solar cell: highly stable double perovskite $Cs_2AgBiBr_6$ film. Advanced Science 2018, 5(3), 1700759.

[21] Ning, W.; Wang, F.; Wu, B.; Lu, J.; Yan, Z.; Liu, X.; Tao, Y.; Liu, J.M.; Huang, W.; Fahlman, M.; Hultman, L. Long electron–hole diffusion length in high-quality lead-free double perovskite films. Advanced Materials 2018, 30(20), 1706246.

[22] Savory, C. N.; Walsh, A.; Scanlon, D. O. Can Pb-Free Halide Double Perovskites Support High-Efficiency Solar Cells? ACS Energy Lett. 2016, 1, 949955.

[23] Zhou, C.; Lin, H.; Lee, S.; Chaaban, M.; Ma, B. Organic inorganic Metal Halide Hybrids Beyond Perovskites. Mater. Res. Lett. 2018, 6, 552569.

[24] Kagan, C. R.; Mitzi, D. B.; Dimitrakopoulos, C. D. Organic-inorganic hybrid materials as semiconducting channels in thin-film field-effect transistors. Science 286, 945–947 (1999).

[25] Mitzi, D. B.; Dimitrakopoulos, C. D.; Kosbar, L. L. Structurally tailored organic inorganic perovskites: optical properties and solution-processed channel

materials for thin-film transistors. Chem. Mater. 2001, 13, 3728–3740.

[26] Mitzi, D.B.; Dimitrakopoulos, C.D.; Rosner, J.; Medeiros D.R.; Xu, Z.; Noyan, C. Hybrid field-effect transistor based on a low-temperature melt-processed channel layer. Advanced Materials 2002, 14(23), 1772-1776.

[27] Kc, S.; Longo, R.C.; Wallace, R.M.; Cho, K. Surface oxidation energetics and kinetics on MoS_2 monolayer. Journal of Applied Physics 2015, 117(13), 135301.

[28] Ataca, C.; Sahin, H.; Ciraci, S. Stable, single-layer MX_2 transition-metal oxides and dichalcogenides in a honeycomb-like structure. The Journal of Physical Chemistry C 2012, 116(16), 8983-8999.

[29] Radisavljevic, B.; Radenovic, A.; Brivio, J.; Giacometti, V.; Kis, A. Single-layer MoS_2 transistors. Nature nanotechnology 2011, 6(3), 147-150.

[30] Wang, H.; Yu, L.; Lee, Y.H.; Shi, Y.; Hsu, A.; Chin, M.L.; Li, L.J.; Dubey, M.; Kong, J.; Palacios, T. Integrated circuits based on bilayer MoS_2 transistors. Nano letters 2012, 12(9), 4674-4680.

[31] Das, S.; Chen, H.Y.; Penumatcha, A.V.; Appenzeller, J. High performance multilayer MoS_2 transistors with scandium contacts. Nano letters 2013, 13(1), 100-105.

[32] Cui, X.; Lee, G.H.; Kim, Y.D.; Arefe, G.; Huang, P.Y.; Lee, C.H.; Chenet, D.A.; Zhang, X.; Wang, L.; Ye, F.; Pizzocchero, F. Multi-terminal transport measurements of MoS_2 using a van der Waals heterostructure device platform. Nature nanotechnology 2015, 10(6), 534-540.

[33] Liu, H.; Peide, D.Y. MoS_2 Dual-Gate MOSFET With Atomic-Layer-Deposited Al_2O_3 as Top-Gate Dielectric. IEEE electron device letters 2012, 33(4), 546-548.

[34] Poudel, B.; Hao, Q.; Ma, Y.; Lan, Y.; Minnich, A.; Yu, B.; Yan, X.; Wang, D.; Muto, A.; Vashaee, D.; Chen, X. High-thermoelectric performance of nanostructured bismuth antimony telluride bulk alloys. Science 2008, 320(5876), 634-638.

[35] Harnwunggmoung, A.; Kurosaki, K.; Muta, H.; Yamanaka, S. High-temperature thermoelectric properties of thallium-filled skutterudites. Applied Physics Letters

2010, 96, 202107.

[36] Caillat, T.; Fleurial, J.P.; Borshchevsky, A. Preparation and thermoelectric properties of semiconducting Zn_4Sb_3. Journal of Physics and Chemistry of Solids 1997, 58, 1119-1125.

[37] Hsu, K.F.; Loo, S.; Guo, F.; Chen, W.; Dyck, J.S.; Uher, C.; Hogan, T.; Polychroniadis, E.K.; Kanatzidis, M.G. Cubic $AgPb_mSbTe_{2+m}$: bulk thermoelectric materials with high figure of merit. Science 2004, 303, 818-821.

[38] Ravich, I.I.; Efimova, B.A.; Smirnov, I.A. Semiconducting Lead Chalcogenides. Plenum Press, New York, 1970.

39 Girard, S.N.; He, J.; Zhou, X.; Shoemaker, D.; Jaworski C.M.; Uher, C.; Dravid, V.P.; Heremans, J.P.; Kanatzidis, M.G. High performance Na-doped PbTe–PbS thermoelectric materials: electronic density of states modification and shape-controlled nanostructures. Journal of the American Chemical Society 2011, 133, 16588-16597.

[40] Zhao, L.D.; Lo, S.H.; He, J.; Li, H.; Biswas, K.; Androulakis, J.; Wu, C.I.; Hogan, T.P.; Chung, D.Y.; Dravid, V.P.; Kanatzidis, M.G. High performance thermoelectrics from earth-abundant materials: enhanced figure of merit in PbS by second phase nanostructures. Journal of the American Chemical Society 2011, 133, 20476-20487.

[41] Morelli, D.T.; Jovovic, V.; Heremans, J.P. Intrinsically minimal thermal conductivity in cubic I-V-VI_2 semiconductors. Physical review letters 2008, 101, 035901.

[42] Zhou, T.; Lenoir, B.; Colin, M.; Dauscher, A.; Al Orabi; R.A.R.; Gougeon, P.; Potel, M.; Guilmeau, E. Promising thermoelectric properties in $Ag_xMo_9Se_{11}$ compounds ($3.4 \leq x \leq 3.9$). Applied Physics Letters 2011, 98, 162106.

[43] He, J.; Girard, S.N.; Zheng, J.C.; Zhao, L.; Kanatzidis, M.G.; Dravid, V.P. Strong phonon scattering by layer structured $PbSnS_2$ in PbTe based thermoelectric materials. Advanced Materials 2012, 24, 4440-4444.

[44] Clarke, D.R. Materials selection guidelines for low thermal conductivity thermal barrier coatings. Surface and Coatings Technology 2003, 163, 67-74.

[45] Wu, H.J.; Zhao, L.D.; Zheng, F.S.; Wu, D.; Pei, Y.L.; Tong, X.; Kanatzidis, M.G.; He, J.Q. Broad temperature plateau for thermoelectric figure of merit ZT > 2 in phase-separated $PbTe_{0.7}S_{0.3}$. Nature communications 2014, 5, 1-9.

[46] Gelbstein, Y.; Dashevsky, Z.; Dariel, M.P. In-doped $Pb_{0.5}Sn_{0.5}Te$ p-type samples prepared by powder metallurgical processing for thermoelectric applications. Physica B: Condensed Matter 2007, 396(1-2), 16-21.

[47] Gelbstein, Y.; Davidow, J. Highly efficient functional $Ge_xPb_{1-x}Te$ based thermoelectric alloys. Physical Chemistry Chemical Physics 2014, 16, 20120-20126.

[48] Xie, W.; Weidenkaff, A.; Tang, X.; Zhang, Q.; Poon, J.; Tritt, T.M. Recent advances in nanostructured thermoelectric half-Heusler compounds. Nanomaterials 2012, 2, 379-412.

[49] Kirievsky, K.; Shlimovich; M., Fuks, D.; Gelbstein, Y. An ab-initio study of the thermoelectric enhancement potential in nano-grained TiNiSn. Physical Chemistry Chemical Physics 2014, 16, 20023-20029.

[50] Kirievsky, K.; Gelbstein, Y.; Fuks, D. Phase separation and antisite defects in the thermoelectric TiNiSn half-Heusler alloys J. Solid State Chem. 2013, 203, 247–254.

[51] Terasaki, I.; Sasago, Y.; Uchinokura, K. Large thermoelectric power in $NaCo_2O_4$ single crystals. Physical Review B 1997, 56, 12685.

[52] Fujita, K.; Mochida, T.; Nakamura, K. High-temperature thermoelectric properties of $Na_xCoO_{2-\delta}$ single crystals. Japanese Journal of Applied Physics 2001, 40, 4644.

[53] Zhao, L.D.; Berardan, D.; Pei, Y.L.; Byl, C.; Pinsard-Gaudart, L.; Dragoe, N. $Bi_{1-x}Sr_xCuSeO$ oxyselenides as promising thermoelectric materials. Appl. Phys. Lett. 2010 , 97, 0921189.

[54] Kim, S.I.; Lee, K.H.; Mun, H.A.; Kim, H.S.; Hwang, S.W.; Roh, J.W.; Yang,

D.J.; Shin, W.H.; Li, X.S.; Lee, Y.H.; Snyder, G.J. Dense dislocation arrays embedded in grain boundaries for high-performance bulk thermoelectrics. Science 2015, 348(6230), 109-114.

[55] Poudel, B.; Hao, Q.; Ma, Y.; Lan, Y.; Minnich, A.; Yu, B.; Yan, X.; Wang, D.; Muto, A.; Vashaee, D.; Chen, X. High-thermoelectric performance of nanostructured bismuth antimony telluride bulk alloys. Science 2008, 320(5876), 634-638.

[56] Zhao, L.D.; Lo, S.H.; Zhang, Y.; Sun, H.; Tan, G.; Uher, C.; Wolverton, C.; Dravid, V.P.; Kanatzidis, M.G. Ultralow thermal conductivity and high thermoelectric figure of merit in SnSe crystals. Nature 2014, 508(7496), 373-377.

[57] Zhao, L.D.; Tan, G.; Hao, S.; He, J.; Pei, Y.; Chi, H.; Wang, H.; Gong, S.; Xu, H.; Dravid, V.P.; Uher, C. Ultrahigh power factor and thermoelectric performance in hole-doped single-crystal SnSe. Science 2016, 351(6269), 141-144.

[58] Wu, H.; Lu, X.; Wang, G.; Peng, K.; Chi, H.; Zhang, B.; Chen, Y.; Li, C.; Yan, Y.; Guo, L.; Uher, C. Sodium-doped tin sulfide single crystal: a nontoxic earth-abundant material with high thermoelectric performance. Advanced Energy Materials 2018, 8(20), 1800087.

[59] Chang, C.; Wu, M.; He, D.; Pei, Y.; Wu, C.F.; Wu, X.; Yu, H.; Zhu, F.; Wang, K.; Chen, Y.; Huang, L. 3D charge and 2D phonon transports leading to high out-of-plane ZT in n-type SnSe crystals. Science 2018, 360(6390), 778-783.

[60] Chen, Z.G.; Shi, X.; Zhao, L.D.; Zou, J. High-performance SnSe thermoelectric materials: Progress and future challenge. Progress in Materials Science 2018, 97, 283-346.

[61] Zhou, Y.; Zhao, L.D. Promising thermoelectric bulk materials with 2D structures. Advanced Materials 2017, 29(45), 1702676.

[62] Zhao, L.-D.; Chang, C.; Tan, G.; Kanatzidis, M. G. SnSe: a remarkable new thermoelectric material. Energy Environ. Sci. 9, 3044–3060 (2016).

[63] Zhao, L.D.; Zhang, X.; Wu, H.; Tan, G.; Pei, Y.; Xiao, Y.; Chang, C.; Wu, D.; Chi, H.; Zheng, L.; Gong, S. Enhanced thermoelectric properties in the

counter-doped SnTe system with strained endotaxial SrTe. Journal of the American Chemical Society 2016, 138(7), 2366-2373.

[64] Zhang, Q.; Liao, B.; Lan, Y.; Lukas, K.; Liu, W.; Esfarjani, K.; Opeil, C.; Broido, D.; Chen, G.; Ren, Z. High thermoelectric performance by resonant dopant indium in nanostructured SnTe. Proceedings of the National Academy of Sciences 2013, 110(33), 13261-13266.

[65] Wu, D.; Zhao, L.D.; Hao, S.; Jiang, Q.; Zheng, F.; Doak J.W.; Wu, H.; Chi, H.; Gelbstein, Y.; Uher, C.; Wolverton, C. Origin of the high performance in GeTe-based thermoelectric materials upon Bi_2Te_3 doping. Journal of the American Chemical Society 2014, 136(32), 11412-11419.

[67] He, Y.; Lu, P.; Shi, X.; Xu, F.; Zhang, T.; Snyder, G.J.; Uher, C.; Chen, L. Ultrahigh thermoelectric performance in mosaic crystals. Advanced Materials 2015, 27(24), 3639-3644.

[68] Liu, W.; Tan, X.; Yin, K.; Liu, H.; Tang, X.; Shi, J.; Zhang, Q.; Uher, C. Convergence of conduction bands as a means of enhancing thermoelectric performance of n-type $Mg_2Si_{1-x}Sn_x$ solid solutions. Physical review letters 2012, 108(16), 166601.

[69] Liu, W.; Kim, H.S.; Chen, S.; Jie, Q.; Lv, B.; Yao, M.; Ren, Z.; Opeil, C.P.; Wilson, S.; Chu, C.W.; Ren, Z. n-type thermoelectric material $Mg_2Sn_{0.75}Ge_{0.25}$ for high power generation. Proceedings of the National Academy of Sciences 2015, 112(11), 3269-3274.

[70] Zhao, L.D.; He, J.; Berardan, D.; Lin, Y.; Li, J.F.; Nan, C.W.; Dragoe, N. BiCuSeO oxyselenides: new promising thermoelectric materials. Energy Environmental Science 2014, 7(9), 2900-2924.

[71] Zhang, X.; Chang, C.; Zhou, Y.; Zhao, L.-D. BiCuSeO thermoelectrics: an update on recent progress and perspective. Materials 2017, 10, 198.

[72] Snyder, G. J.; Christensen, M.; Nishibori, E.; Caillat, T.; Iversen, B. B. Disordered zinc in Zn_4Sb_3 with phonon-glass and electron-crystal thermoelectric

properties. Nat. Mater. 2004, 3, 458–463.

[73] Rhyee, J.S.; Lee, K.H.; Lee, S.M.; Cho, E.; Kim, S.I.; Lee, E.; Kwon, Y.S.; Shim, J.H.; Kotliar, G. Peierls distortion as a route to high thermoelectric performance in $In_4Se_{3-\delta}$ crystals. Nature 2009, 459(7249), 965-968.

[74] Toberer, E. S.; Christensen, M.; Iversen, B. B.; Snyder, G. J. High temperature thermoelectric efficiency in $Ba_8Ga_{16}Ge_{30}$. Phys. Rev. B 2008, 77, 075203.

[75] Shi, X.; Yang, J.; Salvador, J.R.; Chi, M.; Cho, J.Y.; Wang, H.; Bai, S.; Yang, J.; Zhang, W.; Chen, L. Multiple-filled skutterudites: high thermoelectric figure of merit through separately optimizing electrical and thermal transports. Journal of the American Chemical Society 2011, 133(20), 7837-7846.

[76] Meng, X.; Liu, Z.; Cui, B.; Qin, D.; Geng, H.; Cai, W.; Fu, L.; He, J.; Ren, Z.; Sui, J. Grain boundary engineering for achieving high thermoelectric performance in n-type skutterudites. Advanced Energy Materials 2017, 7(13), 1602582.

77 Liu, W. S.; Zhang, B. P.; Li, J. F.; Zhao, L.-D. Effects of Sb compensation on microstructure, thermoelectric properties and point defect of $CoSb_3$ compound. J. Phys. D: Appl. Phys. 2007, 40, 6784–6790.

[78] Lu, X.; Morelli, D.T.; Xia, Y.; Zhou, F.; Ozolins, V.; Chi, H.; Zhou, X.; Uher, C. High performance thermoelectricity in earth-abundant compounds based on natural mineral tetrahedrites. Advanced Energy Materials 2013, 3(3), 342-348.

[79] Yu, B.; Zebarjadi, M.; Wang, H.; Lukas, K.; Wang, H.; Wang, D.; Opeil, C.; Dresselhaus, M.; Chen, G.; Ren, Z. Enhancement of thermoelectric properties by modulation-doping in silicon germanium alloy nanocomposites. Nano letters 2012, 12(4), 2077-2082.

[80] Cheikh, D.; Hogan, B.E.; Vo, T.; Von Allmen, P.; Lee, K.; Smiadak, D.M.; Zevalkink, A.; Dunn, B.S.; Fleurial, J.P.; Bux, S.K. Praseodymium telluride: a high-temperature, high-ZT thermoelectric material. Joule 2018, 2(4), 698-709.

[81] May, A. F.; Flage-Larsen, E.; Snyder, G. J. Electron and phonon scattering in the high-temperature thermoelectric $La_3Te_{4-z}M_z$(M=Sb,Bi). Phys. Rev. B 2010,

81, 125205.

[82] Toberer, E.S.; Cox, C.A.; Brown, S.R.; Ikeda, T.; May, A.F.; Kauzlarich, S.M.; Snyder, G.J. Traversing the metal-insulator transition in a Zintl phase: rational enhancement of thermoelectric efficiency in $Yb_{14}Mn_{1-x}Al_xSb_{11}$. Advanced Functional Materials 2008, 18(18), 2795-2800.

[83] Xin, J.; Tang, Y.; Liu, Y.; Zhao, X.; Pan, H.; Zhu, T. Valleytronics in thermoelectric materials. npj Quantum Materials 2018, 3(1), 1-10.

[84] Fu, C.; Bai, S.; Liu, Y.; Tang, Y.; Chen, L.; Zhao, X.; Zhu, T. Realizing high figure of merit in heavy-band p-type half-Heusler thermoelectric materials. Nature communications 2015, 6(1), 1-7.

[85] Yan, X.; Liu, W.; Chen, S.; Wang, H.; Zhang, Q.; Chen, G.; Ren, Z. Thermoelectric Property Study of Nanostructured p-Type Half-Heuslers (Hf, Zr, Ti)$CoSb_{0.8}Sn_{0.2}$. Advanced Energy Materials 2013, 3(9), 1195-1200.

[86] Božin, E.S.; Malliakas, C.D.; Souvatzis, P.; Proffen, T.; Spaldin, N.A.; Kanatzidis, M.G.; Billinge, S.J. Entropically stabilized local dipole formation in lead chalcogenides. Science 2010, 330(6011), 1660-1663.

[87] Delaire, O.; Ma, J.; Marty, K.; May, A.F.; McGuire, M.A.; Du, M.H.; Singh, D.J.; Podlesnyak, A.; Ehlers, G.; Lumsden, M.D.; Sales, B.C. Giant anharmonic phonon scattering in PbTe. Nature materials 2011, 10(8), 614-619.

[88] Chang, C.; Zhao, L.-D. Anharmoncity and low thermal conductivity in thermoelectrics. Mater. Today Phys. 2018, 4, 50–57.

[89] Biswas, K.; He, J.; Blum, I.D.; Wu, C.I.; Hogan, T.P.; Seidman, D.N.; Dravid, V.P.; Kanatzidis, M.G. High-performance bulk thermoelectrics with all-scale hierarchical architectures. Nature 2012, 489(7416), 414-418.

[90] Zhao, L.D.; Wu, H.J.; Hao, S.Q.; Wu, C.I.; Zhou, X.Y.; Biswas, K.; He, J.Q.; Hogan, T.P.; Uher, C.; Wolverton, C.; Dravid, V.P. All-scale hierarchical thermoelectrics: MgTe in PbTe facilitates valence band convergence and suppresses bipolar thermal transport for high performance. Energy Environmental Science

2013, 6(11), 3346-3355.

[91] Fu, L.; Yin, M.; Wu, D.; Li, W.; Feng, D.; Huang, L.; He, J. Large enhancement of thermoelectric properties in n-type PbTe via dual-site point defects. Energy Environmental Science 2017, 10(9), 2030-2040.

[92] Tan, G.; Shi, F.; Hao, S.; Zhao, L.D.; Chi, H.; Zhang, X.; Uher, C.; Wolverton, C.; Dravid, V.P.; Kanatzidis, M.G. Non-equilibrium processing leads to record high thermoelectric figure of merit in PbTe–SrTe. Nature communications 2016, 7(1), 1-9.

[93] Zhang, J.; Wu, D.; He, D.; Feng, D.; Yin, M.; Qin, X.; He, J. Extraordinary thermoelectric performance realized in n-type PbTe through multiphase nanostructure engineering. Advanced Materials 2017, 29(39), 1703148.

[94] Cheng, L.; Liu, Y. What Limits the Intrinsic Mobility of Electrons and Holes in Two Dimensional Metal Dichalcogenide. J. Am. Chem. Soc. 2018, 140, 1789517900.

[95] Mir, S. H. Exploring the electronic, charge transport and lattice dynamic properties of two-dimensional phosphorene. Phys. Rev. B 2019, 572, 8893.

[96] Cheng, L.; Liu, Y. What Limits the Intrinsic Mobility of Electrons and Holes in Two Dimensional Metal Dichalcogenide. J. Am. Chem. Soc. 2018, 140, 17895-17900.

[97] (a) Gunst, T.; Markussen, T.; Stokbro, K.; Brandbyge, M. First- principles method for electron-phonon coupling and electron mobility: Applications to two-dimensional materials. Phys. Rev. B: Condens. Matter Mater. Phys. 2016, 93 (3), 035414. (b) Sohier, T.; Calandra, M.; Park, C. H.; Bonini, N.; Marzari, N.; Mauri, F. Phonon- limited resistivity of graphene by first-principles calculations: Electron-phonon interactions, strain-induced gauge field, and Boltzmann equation. Phys. Rev. B: Condens. Matter Mater. Phys. 2014, 90 (12), 125414.

[98] Liao, B.; Zhou, J.; Qiu, B.; Dresselhaus, M.S.; Chen, G. Ab-initio study of electron-phonon interaction in phosphorene. Physical Review B 2015, 91(23),

235419.

[99] J. M. Ziman, Cambridge University Press (1972).

[100] Bardeen, J.; Shockley, W. Deformation potentials and mobilities in non-polar crystals. Physical review 1950, 80(1), 72.

[101] Xie, J.; Zhang, Z.Y.; Yang, D.Z.; Xue, D.S.; Si, M.S. Theoretical prediction of carrier mobility in few-layer BC2N. The journal of physical chemistry letters 2014, 5(23), 4073-4077.

[102] Lee, H. A theoretical model of thermoelectric transport properties for electrons and phonons. Journal of Electronic Materials 2016, 45, 1115-1141.

[103] Lee, H. Thermoelectrics: design and materials. John Wiley Sons, 2016.

[104] Hohenberg, P.; Kohn, W. Inhomogeneous electron gas. Physical review 1964, 136(3B), B864.

[105] Perdew, J.P.; Zunger, A. Self-interaction correction to density-functional approximations for many-electron systems. Physical Review B 1981, 23(10), 5048.

[106] Perdew, J.P.; Burke, K.; Ernzerhof, M. Generalized gradient approximation made simple. Physical review letters 1996, 77(18), 3865.

[107] Kresse, G.; Furthmüller, J. Efficient iterative schemes for ab-initio total-energy calculations using a plane-wave basis set. Physical review B 1996, 54(16), 11169.

[108] Pei, Y.; Gibbs, Z.M.; Gloskovskii, A.; Balke, B.; Zeier, W.G.; Snyder, G.J. Optimum carrier concentration in n-type PbTe thermoelectrics. Advanced energy materials 2014, 4(13), 1400486.

[109] Ioffe, A.F. Semiconductor Thermoelements, and Thermoelectric. Cool- ing-Infosearch Ltd. 1957: London, UK.

[110] Boukhris, N.; Meradji, H.; Ghemid, S.; Drablia, S.; Hassan, F.E.H. Ab-initio study of the structural, electronic and thermodynamic properties of $\mathrm{PbSe}_{1-x}\mathrm{S}_x$, $\mathrm{PbSe}_{1-x}\mathrm{Te}_x$ and $\mathrm{PbS}_{1-x}\mathrm{Te}_x$ ternary alloys. Physica Scripta 2011, 83(6), 065701.

[111] Hoang, K.; Mahanti, S.D.; Kanatzidis, M.G. Impurity clustering and impurity-

induced bands in PbTe-, SnTe-, and GeTe-based bulk thermoelectrics. Physical Review B 2010, 81(11), 115106.

[112] Hong, M.; Chen, Z.G.; Yang, L.; Zou, J. Enhancing thermoelectric performance of Bi_2Te_3-based nanostructures through rational structure design. Nanoscale 2016, 8(16), 8681-8686.

[113] Bahk, J.H.; Shakouri, A. Enhancing the thermoelectric figure of merit through the reduction of bipolar thermal conductivity with heterostructure barriers. Applied Physics Letters 2014, 105(5), 052106.

[114] Wang, S.; Yang, J.; Toll, T.; Yang, J.; Zhang, W.; Tang, X. Conductivity-limiting bipolar thermal conductivity in semiconductors. Scientific reports 2015, 5(1), 1-9.

[115] Pei, Y.; Shi, X.; LaLonde, A.; Wang, H.; Chen, L.; Snyder, G.J. Convergence of electronic bands for high performance bulk thermoelectrics. Nature 2011, 473(7345), 66-69.

[116]Heremans, J.P.; Jovovic, V.; Toberer, E.S.; Saramat, A.; Kurosaki, K.; Charoenphakdee, A.; Yamanaka, S.; Snyder, G.J. Enhancement of thermoelectric efficiency in PbTe by distortion of the electronic density of states. Science 2008, 321(5888), 554-557.

[117] Hicks, L.D.; Dresselhaus, M.S. Use of quantum-well superlattices to obtain a high figure of merit from nonconventional thermoelectric materials. MRS Online Proceedings Library 1993, 326(1), 413-418.

[118] Pei, Y.; Shi, X.; LaLonde, A.; Wang, H.; Chen, L.; Snyder, G.J. Convergence of electronic bands for high performance bulk thermoelectrics. Nature 2011, 473(7345), 66-69.

[119] Parrott, J.E. The thermal conductivity of sintered semiconductor alloys. Journal of Physics C: Solid State Physics 1969, 2(1), 147.

[120] Ahn, K.; Li, C.P.; Uher, C.; Kanatzidis, M.G. Thermoelectric properties of the compounds $AgPb_mLaTe_{m+2}$. Chemistry of Materials 2010, 22(3), 876-882.

[121] Safdar, M.; Wang, Q.; Mirza, M.; Wang, Z.; Xu, K.; He, J. Topological surface transport properties of single-crystalline SnTe nanowire. Nano letters 2013, 13(11), 5344-5349.

[122] Hicks, L.D.; Dresselhaus, M.S. Use of quantum-well superlattices to obtain a high figure of merit from nonconventional thermoelectric materials. MRS Online Proceedings Library 1993, 326(1), 413-418.

[123] Fan, X.A.; Yang, J.Y.; Xie, Z.; Li, K.; Zhu, W.; Duan, X.K.; Xiao, C.J.; Zhang, Q.Q. Bi_2Te_3 hexagonal nanoplates and thermoelectric properties of n-type Bi_2Te_3 nanocomposites. Journal of Physics D: Applied Physics 2007, 40(19), 5975.

[124] Lan, Y.; Minnich, A.J.; Chen, G.; Ren, Z. Enhancement of thermoelectric figure-of-merit by a bulk nanostructuring approach. Advanced Functional Materials 2010, 20(3), 357-376.

[125] Zhang, Q.; Ai, X.; Wang, L.; Chang, Y.; Luo, W.; Jiang, W.; Chen, L. Improved thermoelectric performance of silver nanoparticles-dispersed Bi_2Te_3 composites deriving from hierarchical two-phased heterostructure. Advanced Functional Materials 2015, 25(6), 966-976.

[126] Chen, Z.G.; Yang, L.; Ma, S.; Cheng, L.; Han, G.; Zhang, Z.D.; Zou, J. Paramagnetic Cu-doped Bi_2Te_3 nanoplates. Applied Physics Letters 2014, 104(5), 053105.

[127] Yang, L.; Chen, Z.G.; Han, G.; Hong, M.; Zou, J. Impacts of Cu deficiency on the thermoelectric properties of $Cu_{2-X}Se$ nanoplates. Acta Materialia 2016, 113, 140-146.

[128] Han, G.; Chen, Z.G.; Yang, L.; Hong, M.; Drennan, J.; Zou, J. Rational design of Bi_2Te_3 polycrystalline whiskers for thermoelectric applications. ACS applied materials interfaces 2015, 7(1), 989-995.

2

Strain Induced Ultrahigh Carrier Mobility in β-TeO$_2$

2.1 Introduction

Strain-engineering in multi-layered semiconductors is of great current interest, as these show great promise of increasing the charge carrier transport applications in combination with large bandgap and superior flexibility.[1-2] Recently, many fascinating high-performance transport properties of layered materials with large bandgap have been explored, which shows the significant impact in demonstrating advancement in applications in electronic and transport devices.[3-5] In this regard, semi-metallic graphene exhibits high carrier mobility, but unfortunately suffers a short carrier lifetime due to the gapless characteristics.[6-7] Most recently, air-stable black phosphorus with large bandgap and higher carrier mobility have been found to be quite promising for high-performance device applications.[8-9] In fact, phosphorene with moderate bandgap (2 eV) and ultrahigh hole carrier mobility (10^3-10^4 cm^{2}V^{-1}s^{-1}) around room temperature have already been explored in various transport devices.[10,11] Incidentally, out of all forms of phosphorenes, only a few show chemical stability, preventing their large scale general applications in ambient conditions.[12] On the other hand, binary layered materials, such as, a few-layer thick MoS_2 and encapsulated single-layer MoS_2 FETs have been shown to exhibit band-like transport with quite high mobility values (60–500 $cm^2V^{-1}s^{-1}$)[40,43-45]. Recently, two-dimensional (2D) AsP monolayer has been predicted to be a promising alternative for transport application due to its favourable direct bandgap, exceeding 14,000 $cm^2V^{-1}s^{-1}$ in mobility value.[42] Nonetheless, it is still of fundamental interest and technological importance to design a high bandgap binary layered material which not only shows chemical stability but also exhibits high carrier mobility, toward the device applications.

A most interesting and unique feature of layered material is the property of tunability, i.e., their physical as well as chemical properties can be modulated by varying number of layers in the stacking direction[13] or by applying external stimuli, such as, pressure or mechanical strain[14]. The role of strain is particularly significant in flexible and wearable technologies where the material is expected to bear a certain degree of variable strain. Various experimental techniques, such as, bending of flexible substrates, elongating an elastic substrate, piezoelectric stretching, substrate thermal expansion, and controlled wrinkling are currently employed in these layered materials for strain engineering.[15] In fact, there has been significant progress in understanding the underlying effect of strain engineering on such layered materials. In fact, there have been recent advances in the applications of strain technologies to explore anisotropy and related manifestaion of charge carrier transport properties. [16]

Interestingly, in recent years, among the most popular oxide materials, TeO_2 is a widely studied compound because of its unique features, like, complex crystal structure and broad electronic bandgap leading to its application in nonlinear optical properties[17]. In fact, tellurium oxide (TeO_2) and TeO_2-based glasses are used as a promising active material for optical switching devices because of their large nonlinear polarizability.[18] There are three crystalline phases of TeO_2, which have been explored experimentally as well as theoretically till recently.[19-20] Among the three phases, bulk TeO$_2$ exists in two stable polymorphs and one meta-stable form. The tetragonal phase, α-TeO$_2$ (paratellurite, P4$_1$2$_1$2)[21-23] is thermodynamically stable but rarely exists, while another stable phase, β-TeO$_2$ (tellurite, Pbca)[24-25] is found naturally. Recently, there has also been synthesis of a new metastable form of TeO$_2$, known as γ-TeO$_2$ (orthorhombic, P2$_1$2$_1$2$_1$).[26-27] Interestingly, all the three polymorphs are formed by corner-sharing TeO$_4$ trigonal bipyramidal units with different arrangements.

Out of the three phases, our interest lies in the naturally occurring tellurite layered crystal (β-TeO$_2$) of space group, Pbca, which has orthorhombic symmetry with eight formula units per unit cell. This layered structure with weak van der Waals interactions is dynamically and thermally quite stable as confirmed by large cohesive energy and positve energy vibrational spectra.[19] Furthermore, two dimensional (2D) TeO$_2$ structure not only has a large direct bandgap (3.32 eV), but also exhibits exceptionally high carrier mobility (10^4 cm^{2}V^{-1}s^{-1}).[28] These desirable properties motivate us to study β-TeO$_2$ as a promising layered semiconductor with high potential for novel applications in power electronics and advanced transport devices. In particular, the orthorhombic form of β-TeO$_2$ is interesting because of the layered structure which leads to spatial anisotropy in the charge distributions, which in turn may lead to anisotropy in the charge carrier transport properties. In this regard, we will highlight mostly strain-induced charge carrier mobility arising in this layered structure. The mechanical strain driven mobility will be analyzed in the context of acoustics phonon limited scattering models. We have adopted deformation potential theory (DPT) coupled with density functional theory (DFT) to compute strain-induced charge carrier mobility in the layered phase of TeO$_2$. The critical limit of uniaxial compressive strain leading to sudden amplification in carrier mobility will be discussed thoroughly based on carrier scattering processes. This would also help to understand the origin of anisotropy in electron and hole transport phenomena.

2.2 Theoretical Section

2.2.1 First principle simulations

The optimization of the crystal structure was performed using first-principles based density functional theory (DFT) in conjunction with projector augmented wave (PAW) potentials and Perdew Burke Ernzerted (PBE) generalized gradient approximation (GGA)[29-30] to the electronic exchange and correlation, as implemented in the Quantum Espresso (QE) package[31]. All of the atoms in the unit-cell are fully relaxed until the magnitude of Hellman-Feynman force on each atom is less than 0.025 $eV/\AA$. To describe long-range van der Waals (vdW) correction, we adopt Grimme's D2 dispersion interaction in our calculations. Our calculated lattice constants for bulk layered β-TeO_2 is a = 5.52 Å, b = 5.78 Å, and c = 12.15 Å, which are in good agreement with other theoretical calculations as well as with experimental results.[22,28] Our estimated PBE electronic structure band gap is 2.27 eV. As the PBE functional underestimates the bandgap of semiconductor, we use HSE06 functional[30] to estimate the exact bandgap of the optimized structure of bulk layered TeO_2 (which is 3.20 eV). The electronic wave function and charge density cutoff in a plane-wave basis are considered to be 70 Ry and 500 Ry, respectively. Brillouin zone integration of orthorhombic crystal structure is sampled on the grid of 24 x 24 x 10 k-points. The sharp discontinuity of the electronic states near the bandgap is smeared out with the Fermi-Dirac distribution function with a broadening of 0.003 Ry. To verify our results, a few calculations were carried out with higher number of k-points and higher cutoff values. However, these calculations also gave essentially the same results as obtained from smaller k-points and lower energy cutoff values.

The AIMD simulation is carried out in the unit cell containing 24 atoms. We run AIMD simulation considering the Nosé algorithm [46] up to 40 ps runtime with a time step of 1 fs and 40,000 SCF runs. All the calculations are performed by 4 × 4 × 2 k-mesh generated via the Monkhorst-Pack method [47]. For a better treatment of our weakly interacting (layered) systems, we have done the calculations by incorporating the van der Waals corrections using Grimme's DFT-D2 dispersion corrections [48], as implemented in VASP. The maximum allowed error in total energy (which is basically the optimization condition for the electronic self-consistent (SC)-loop) is 10^{-4} eV. The ground state geometries are optimized until the atomic forces acting on each atom (Hellman-Feynman forces) becomes less than 0.001 eV/Å. All the initial and optimized geometries have been visualized using the graphical software viz. VESTA [49].

2.2.2 The Boltzmann transport formalism

To compute charge carrier mobility, we use Boltzmann transport formalism within deformation potential theory (DPT).[33] Here, the band energies E_i and carrier group velocities ($v_\mathrm{i} = \frac{\nabla E_\mathrm{i}(k)}{h}$) are obtained from the first-principle calculations. The carrier (electron and hole) mobility along the β direction is defined as,

$$\mu_\beta^{e/h} = \frac{e}{k_B T} \frac{\sum_{i \in CB(VB)} \int \tau_\beta(i,k) v_\beta^2(i,k) b(k) dk}{\sum_{i \in CB(VB)} \int b(k) dk} \tag{2.1}$$

$$b(k) = exp[\mp \frac{E_i(k)}{k_B T}] \tag{2.2}$$

here, e and T are electronic charge and absolute temperature, respectively. The direction dependent carrier relaxation time, $\tau_\beta(i,k)$ can be derived considering the collision term in the Boltzmann Transport Equation (BTE)[33],

$$\frac{1}{\tau_\beta(i,k)} = k_B T \frac{4\pi^2 (E_\beta^c)^2}{hC_{3D}} \sum_{j,k' \in BZ} (1 - \frac{v_{jk'}}{v_{ik}}) \delta[E_{ik} - E_{jk'}] \tag{2.3}$$

where C_{3D} is elastic modulus; h: Planck constant; k_B: Boltzmann constant; Here C_{3D} is expressed as,

$$2(E - E_0) = C_{3D} S_0 (\frac{\Delta l}{l_0})^2 \tag{2.4}$$

where E_0 and S_0 are the energy and lattice volume of the unit cell without strain and E is the energy of the strained system. The parabolic equation is used to calculate the value of C_{3D}. And the deformation potential constant, E_c^β is derived as,

$$E_\beta^c = \frac{\Delta E_{band}}{\frac{\Delta l}{l_0}} \tag{2.5}$$

where ΔE_{band} is a shift in energy level at the band edge position because of lattice strain $\frac{\Delta l}{l_0}$. All the parameters are derived from the first-principles calculation. Finally, the transport calculations are done at room temperature (300 K).

2.3 Result and Discussions

The tellurite crystal, β-TeO$_2$ contains orthorhombic symmetry with eight formula units in the unit cell. Considering the layered structure, we optimize the structure via PBE + D2 calculations and found the bulk lattice parameters to be a = 5.52 $\AA$; b = 5.78 $\AA$; c = 12.15 $\AA$. These optimized lattice parameters are in good agreement with the earlier theoretical as well as experimental results.[19,24,25] Figure 2.1(a) represents the β-TeO$_2$ crystal structure viewed along the crystallographic a-direction. From the crystal structure, it is clear that TeO$_2$ crystal morphology encompasses rectangular lattice along the crystallographic b-direction. The

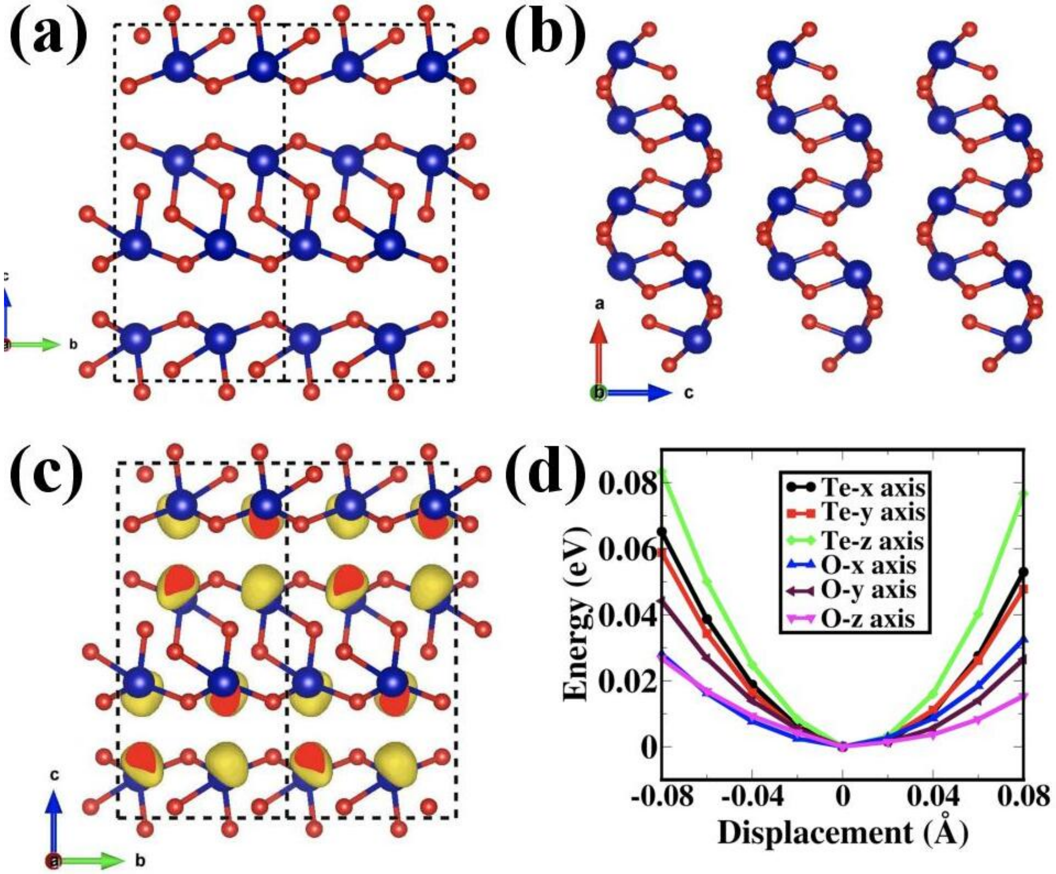

Figure 2.1: (a) Crystal structure viewed along the crystallographic a-direction. The atoms are indicated as follows: Te: Blue, O: red. (b) Crystal structure viewed along the crystallographic b-direction. Te-O bondings along crystallographic c-direction (a-direction) are considered as axial (equitorial) bonds. (c) Electron localization function (ELF) is plotted to show a 5s^2 lone pair associated with the Te atoms. ELF is virtualized using the package VESTA[39]. (d) Potential energy surface (PES) is plotted for both the atoms Te and O along each crystallographic direction. PES shows inhomogeneity in the bonding characteristics, which leads to anisotropy in the transport property.

consecutive rectangular lattices are bridged through Te–O covalent bonds. Moreover, the structural unit of β-TeO$_2$ contains TeO$_4$ trigonal pyramid, which forms a network by sharing vertices through bridging oxygen atoms. On the other hand, looking along the crystallographic b-direction, it is observed that each layer of TeO$_2$ forms a wavy like pattern along the crystallographic a-direction (shown in Figure 2.1(b)). Therefore, such unique features in the crystal topology with spatial anisotropy in the lattice structure are expected to play a major role in its transport property. The β-TeO$_2$ crystal has a layered structure with layers arranged perpendicular to the a-axis with an interlayer distance of 3 $\AA$.[20] The two consecutive interlayer interaction is dominated by weak long-range van der Waals (vdW) forces. In Figure 2.1(c), we plotted the Electron localization function (ELF) which indicates localized charge distribution associated with Te atom (isosurface value $\simeq 0.95$). These ELFs originate mainly from lone pairs of Te-5s orbitals, which are slightly tilted from the crystallographic c-axis within the interlayer space. These orientations of the lone pairs in turn drive the inhomogeneity in chemical bonding in the crystal environment that gives rise to further anisotropy in the crystal structure.

To address the chemical bonding inhomogeneity in more details, we plot the potential energy surface (PES) of each atom along the different crystallographic axis with atomic displacement from their equilibrium positions (see Figure 2.1(d)). The long-range Coulomb repulsion originating from 5s^2 lone pairs of tellurium atoms in consecutive layers along the z-directions results in a steep curve in the PES as a function of atomic displacement. In contrast, a comparatively shallow curve in PES is found for oxygen atoms. Along the in-plane direction, Te atoms are tightly bonded with the neighboring sites compared to the oxygen atoms. Since oxygen atoms act as bridges between the Te atoms, we carefully study their bonding characteristics. Importantly, oxygen atoms are strongly bonded with the lattice sites along the crystallographic y-direction (represented by maroon colour)

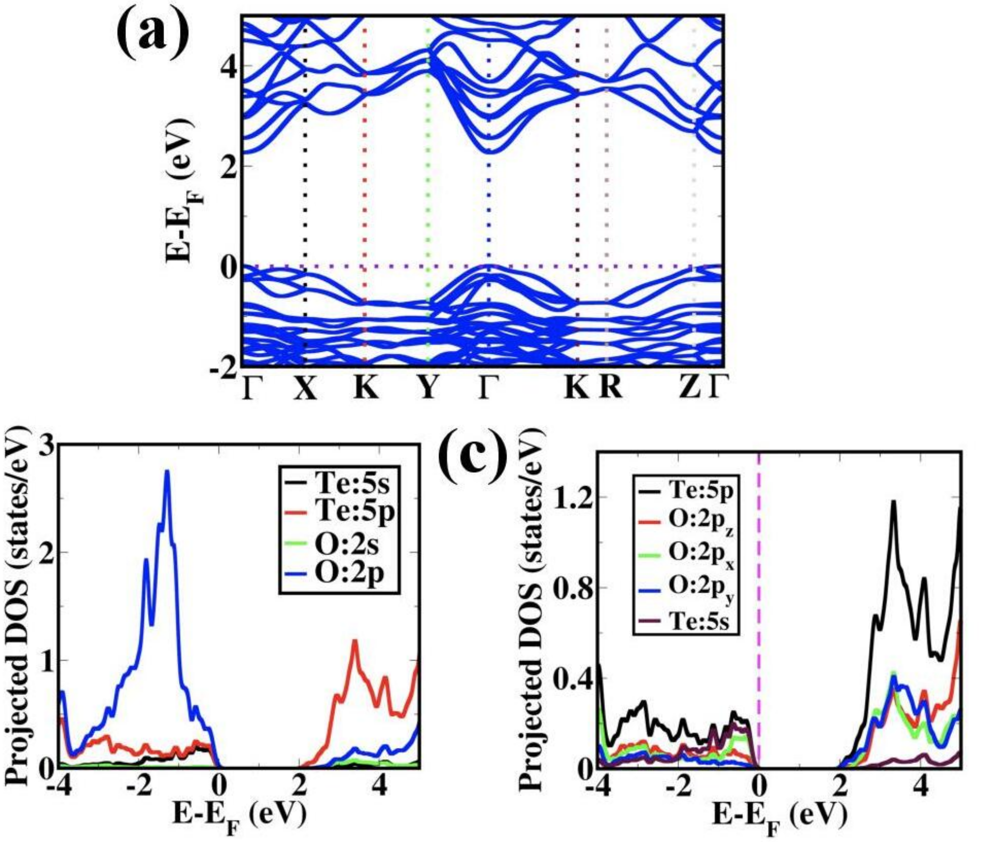

Figure 2.2: (a) Electronic band structure of β-TeO$_2$, plotted at the PBE level. The theoretically predicted direct band gap 2.27 eV at the high symmetry Γ point. (b) Atomic orbital projected density of states (pDOS) have been drawn. In the plot, it is observed that VBM is mainly contributed from Te-5p and O-2p with a reasonable contribution from Te:5s lone pair. Significantly, orbital contribution from O-2p is very high in the valence band. On the other hand, CBM is mostly dominated by Te-5p and O-2p with a small mixture of O-2s. (c) To highlight different oxygen p-orbital contributions to band structure, pDOS have been plotted as a function of energy. Interestingly, orbital O-2p$_x$ is responsible for hole conduction through the hybridization with Te-5p orbital and whereas O-2p$_y$ is responsible for electron conductions. Here, Fermi level is considered as reference level (0.0 eV) for all the figures.

compared to the x- and z-directions, which are indicated by blue and magenta colours, respectively. These bonding inhomogeneities in the structure motivates us to find whether these would influence anisotropy in the transport properties.

To shed light on the electronic structure-property, we investigate the electronic band structure of bulk β-TeO$_2$, which shows TeO$_2$ as a direct bandgap semiconductor of bandgap 2.27 eV at the PBE level (shown in Figure 2.2(a)). The band gap estimated with advanced HSE06 method [30] turns out to be 3.20 eV. The estimated bandgap at HSE06 level for bulk layered TeO$_2$ is lower than the monolayer counterpart.[28] Additionally, we also include the effect of spin-orbit coupling (SOC) to estimate the bandgap and interestingly we observe band gap correction is fairly negligible (0.09 eV). More importantly, the incorporation of spin-orbit coupling influences only the bandgap, not the overall band curvature which are the determining factors for carrier transport properties in the crystal.[28] Since the band dispersion does not change with costly functional, we carry out further transport calculations at the PBE level.

To understand the bond characteristics and orbital contribution to the specific bond, we calculate the atomic orbital projected density of states (pDOS) of TeO$_2$, which are shown in Figure 2.2(b). We observe that valence band maxima (VBM) are from Te-5p and O-2p with a fair mixture of Te-5s orbitals, whereas conduction band minima (CBM) is mostly dominated by Te-5p and O-2p, together with a small amount of O-2s orbital contribution. In fact, 5s^2 lone pairs from Tellurium has significant contribution to the valence band region, while it's contribution is negligibly small to the conduction band (see Figure 2.2(b)). Consequently, these orbital overlapping of lone pairs could give rise to electron and hole anisotropy in transport mechanisms. On the other hand, oxygen atoms act as the bridge between two tellurium atoms, and because of this, we focus on directional dependent p-orbitals to understand chemical bonding characteristics in the complex system. Interestingly, it has been found in Figure 2.2(c) that dominance of O-2p$_\mathrm{x}$ orbital is prevalent in VBM and thus mostly accountable for hole conduction through the hybridization with Te-5p orbital, while O-2p$_y$ orbital is responsible for electron conductions. Thus, bridged atomic orbital orientation mainly contributes to anisotropy in the electron and hole conductions. This important information gives us a hidden link about the the complex crystal structure along with the complex valence orbital orientation of the intervening oxygens with the anisotropy found in the transport characteristics.

It is well known that the layered materials often hold high mechanical stretchability and can reversibly withstand extreme structural deformations. Therefore, strain engineering has been considered as an effective method to modulate electronic structure properties of layered materials, which may further extend their application capabilities.[34-36] As illustrated in Figure 2.3(a), when biaxial strain (compressive/tensile) is applied along the in-plane direction, the variation of equatorial bond length is higher than the variation in axial Te-O bonds. The asymmetry in bond length alteration indicates chemical bonding inhomogeneity in the local environment in the crystal. In fact, this applied biaxial strain driven non-uniform bond length variations exerts quite high pressure in the unit cell. We observe biaxial strain-induced excessive pressure around 80 Kbar under the 4% compressive strain, while 120 Kbar in response of 4% tensile strain. As a consequence of excessive external pressure strived on the unit cell, the band dispersions are also affected. Here, we find that the applied biaxial strain further introduces anisotropy in the carrier effective mass. The hole effective mass drastically increases due to biaxial compressive strain (0-4%) and increment in the hole effective mass is even more prominent by the 0-4% tensile strain (Shown in Figure 2.3(b)). As a result of enhancement in hole effective mass, the hole mobility (calculated using equation (2.1)) decreases significantly as a function of biaxial strain which is plotted in Figure 2.3(c). On the other hand, the deterioration of electron mobility (shown in Figure 2.3(c)) occurs because of completely different reasons, i.e. due to electron-

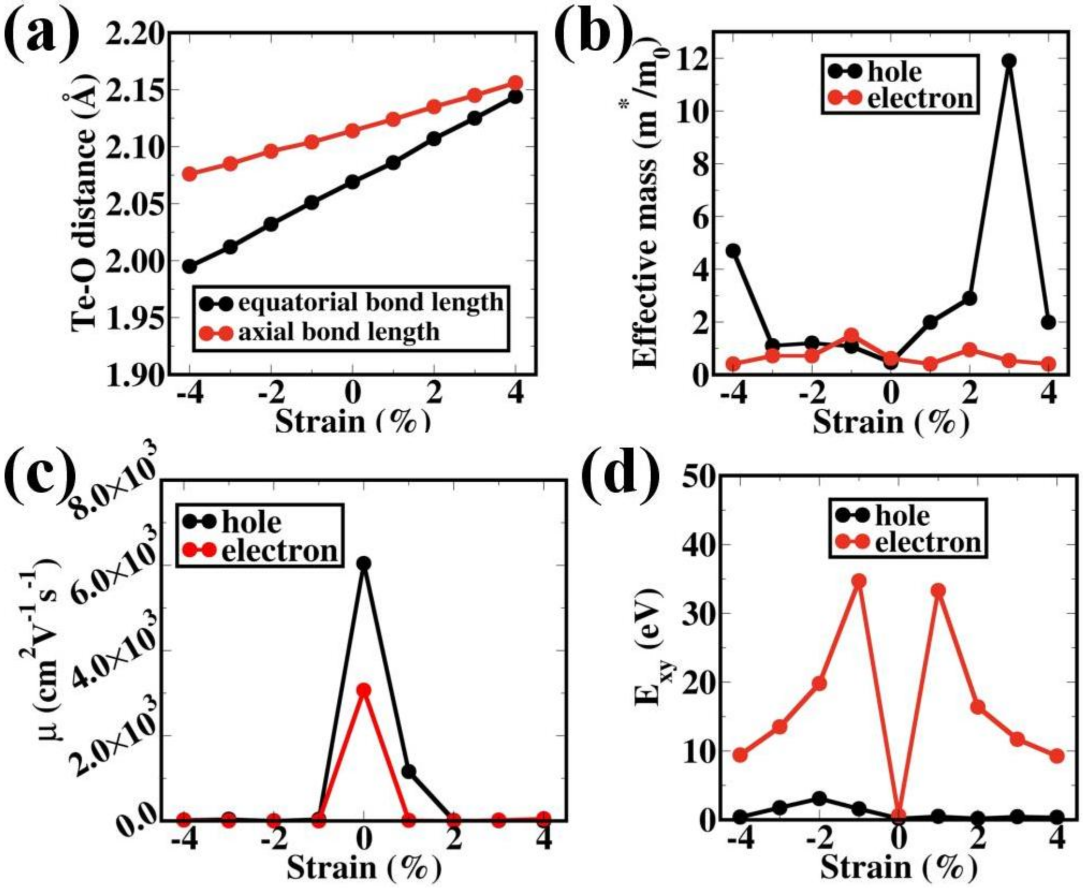

Figure 2.3: (a) Effect of bi-axial strain on Te-O bond length. Equatorial bonds are Te-O covalent chemical bonding along crystallographic a-direction, while axial bonds are Te-O bonding along the c-direction within a layer. (b) Carrier effective mass as a resultant of biaxial strain. Carrier effective mass is derived from curvature of band dispersion. (c) computed carrier mobility along x-direction in the band structure. Mobility has been calculated using the DPT formalism. (d) Deformation potential constant as a function of bi-axial strain has been plotted for charge carriers. The large value of deformation potential constant signifies carrier-phonon scattering strength in acoustic phonon limited scattering model.

acoustic phonon scatterings. The carrier and acoustic phonon coupling strength is characterized by E^c_{xy}, which increases due to applied biaxial strain. This electron-phonon scattering strength is shown in Figure 2.3(d). Finally, we conclude from the study that biaxial strain would not be beneficial for carrier transport in TeO$_2$ layered structure.

While probing the carrier mobility under the application of biaxial strain, which found to be futile, we moved to understand the effect due to the application of uniaxial strain in the in-plane directions. Importantly, the applied strain driven exerted pressure upon the unit cell is comparatively lower for uniaxial strain than in the case of applied biaxial strain. This is further verified from the calculation of strain-energy per atom, which is computed by (E-E$_0$), where E is the total energy of the unit cell with strain and E$_0$ is total energy without strain. The calculated strain energy per atom turns out to be 0.04 eV in case of uniaxial strain. Interestingly, we find that the computed strain energy is very low compared to other layered materials, which clearly brightens the application possibility of the layered phase of TeO$_2$ with applied uniaxial strain.[38]

The acoustics phonon limited scattering model has successfully been found to be extremely effective in studying transport properties in many layered materials for quite some time.[16,32-33] According to Boltzmann transport theory, the intrinsic carrier mobility (electron or hole) is proportional to both carrier relaxation time and carrier group velocity and inversely proportional to carrier effective mass. In fact, the carrier relaxation time mainly depends on three factors: (i) deformation potential constant or carrier-acoustics phonon scattering strength, (ii) elastic modulus, (iii) carrier-carrier scattering rates. Ideally, lower carrier-acoustics phonon scattering strength and carrier-carrier scattering rates along with higher elastic modulus enhances the carrier relaxation time and in turn, the intrinsic carrier mobility increases. To investigate the anisotropy in the transport property, we derive the descriptors, known as, deformation potential constant or carrier-phonon

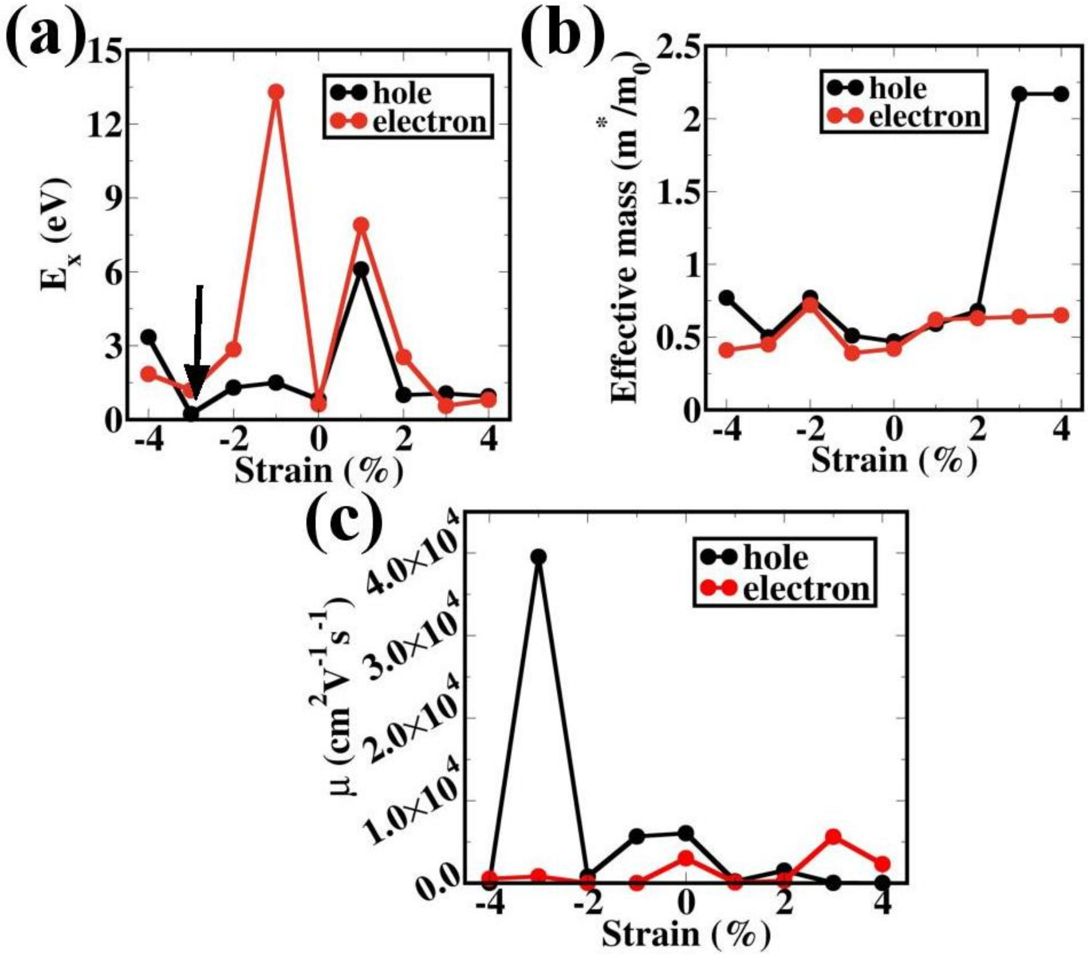

Figure 2.4: The effect of uniaxial strain along x-direction on (a) change carrier and phonon scattering strength (E_x). (b) charge carrier effective mass in units of m_0 where m_0 is bare mass of electron and (c) estimated carrier mobility along the x-direction. The sudden amplification of hole mobility (39500 cm^2 V^{-1}s^{-1}) is observed at 3% uniaxial compressive strain.

coupling strength E^c_β, which is calculated from the band edge shift in the band structure under the applied strain. Figure 2.4(a) illustrates carrier (electron/hole) scattering strength with acoustic phonons which shows higher values for strained systems. However, surprisingly, the deformation potential constant becomes lowest ($E^c_\beta \simeq 0.23$ eV) at 3% uniaxial compressive strain along x-direction. Interestingly, deformation potential constant, E^c_β, calculated for the layered TeO$_2$ is even lower than the same in two-dimensional Phosphorene.[16] Such a sudden lowering of deformation potential constant encourages us to look at carrier effective mass, which is derived from the electronic band curvature. Accordingly, we have computed carrier effective mass in response to the applied uniaxial strain along the x-direction and find that the hole effective mass is 0.5 m$_0$ (m$_0$: bare electron mass), which is quite low (shown in Figure 2.4(b)). The direction dependent deformation potential constants eventually determine the carrier relaxation time (see equation (2.3)). Finally, we estimate the carrier mobility which is shown in Figure 2.4(c), using the expression mentioned in equation (2.1). Most importantly, we achieve a sudden enhancement in hole mobility ≈ 39500 cm^{2}V^{-1}s^{-1} at the 3% applied uniaxial compressive strain. In contrast, compressive strain along x-direction does not increase electron mobility to a large extent. The sharp peak in terms of amplification of hole mobility is not only because of lower hole-phonon scattering strength but also lighter hole effective mass.

To further understand the effect upon the electronic structure due to applied uniaxial strain along the y-direction, we calculate the E^c_β and m* for both electron and hole. In this case, we also achieve lowest electron-phonon coupling strength ($E^c_\beta \simeq 0.9$ eV) and electron effective mass (m$^* \simeq 0.21$ m$_0$) under the 4% applied uniaxial compressive strain along y-direction. In fact, the further compressive strain along y-direction gives rise to higher carrier scattering strength which effectively reduces the mobility. The carrier-phonon scattering strength is plotted in Figure 2.5(a). In fact, we observe anisotropy in the carrier effective mass along

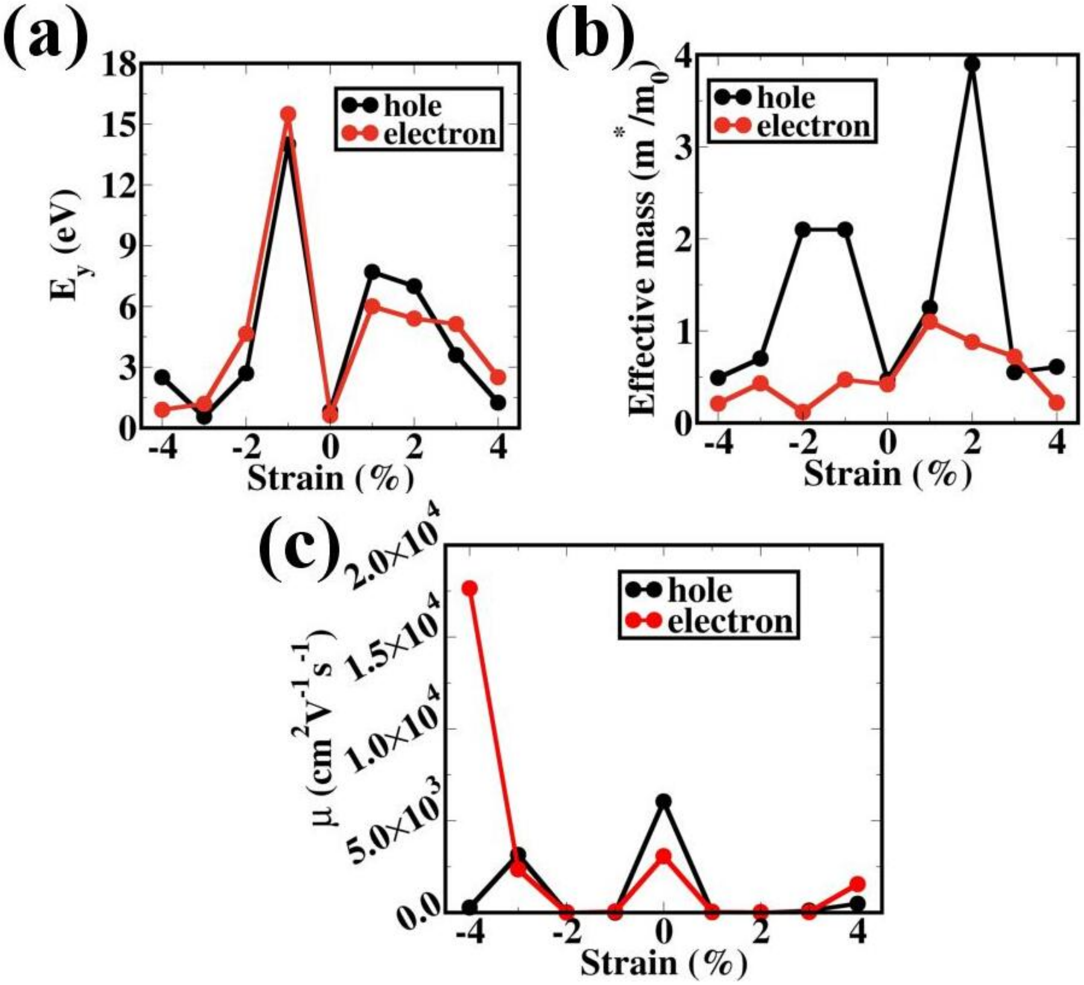

Figure 2.5: The effect of uniaxial strain along y-direction on (a) charge carrier and phonon scattering strength (E_y), (b) charge carrier effective mass in unit of m_0 and (c) predicted carrier mobility along the y-direction. The sudden amplification of electron mobility (17500 $cm^2V^{-1}s^{-1}$) is observed at 4% uniaxial compressive strain.

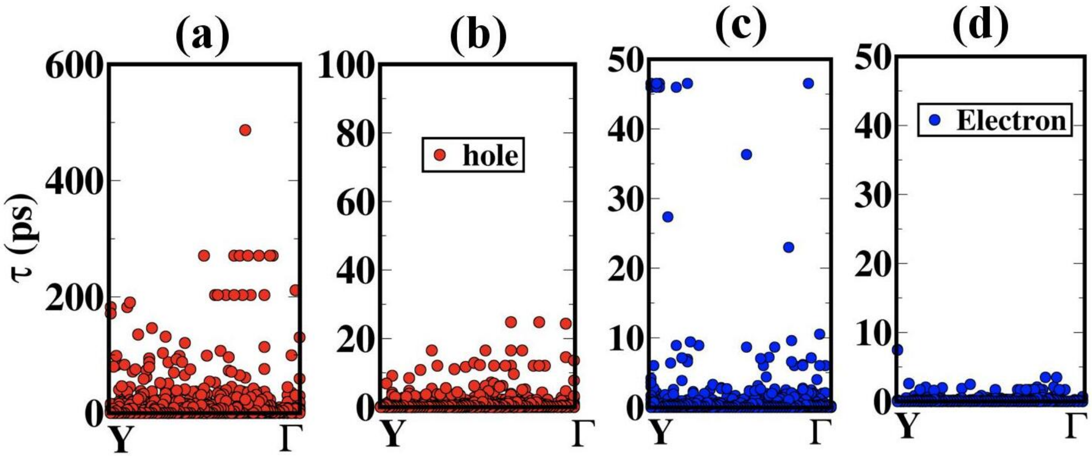

Figure 2.6: Relaxation time versus carrier-state along the Y-Γ k-path is shown for (a) uniaxial 3% compressive strain along x-direction, (b) without strain in case of holes mobility. Similar plots along the Y-Γ k-path are shown for (c) uniaxial 4% compressive strain along y-direction, (d) without strain in case of electron mobility. The number of points in the Brillouin zone corresponds to the number of carrier states (N_c) giving rise to the transport behavior dominated by the scattering relaxation time (τ).

the Γ-Y direction after the application of uniaxial strain along y-direction (see in Figure 2.5(b)). Our DFT based DPT formalism along with acoustics phonon limited scattering model estimates electron mobility which also shows a sudden peak in electron mobility at the 4% uniaxial compressive strain. Finally, the computed electron mobility is found to be of order 17500 $cm^2V^{-1}s^{-1}$ (shown in Figure 2.5(c)). Of particular interest is that TeO_2 has extremely high electron mobility, because of light electron effective mass and small deformation potential constant. To check thermal stability for the structure corresponding to the compressive stress which leads to the maximum change of carrier mobility, we perform ab-initio molecular dynamics (AIMD) simulation. During the AIMD simulation, we observe that layered TeO_2 crystal structure does not break chemical bonds at temperatures T = 300 K. In fact, we estimated Te-O bond length variation to be 0.02% and 1.2% at the 3% CS and 4% CS, respectively. From the AIMD study, we conclude that TeO_2 forms a thermally stable crystal structure even at higher temperatures (T=300 K) under compressive stress (CS).

In this context, analysis of the carrier-scattering process could give further microscopic realization toward transport mechanisms to achieve ultra-high charge carrier mobility. Figure 2.6 represents relaxation time (calculated using equation (2.3)) versus carrier scattering states along Γ-Y direction in the Brillouin zone. In Figures 2.6(a) and 2.6(b), we plot hole relaxation time along the Γ-Y direction in Brillouin zone. It is also found that the application of 3% uniaxial compressive strain increases the relaxation times (τ) by more than 10 fold than the case without strain. Eventually, higher hole lifetime contributes to enhancing large hole mobility. Moreover, the distribution of scattering states corresponding to holes over k-states is found to be significantly dense for a strained system compared to zero strain case. On the other hand, the distribution pattern of electron scattering states and the corresponding τ also increases in case of 4% uniaxial compressive strain along y-direction for electrons, which are shown in Figures 2.6(c) and 2.6(d), respectively. Interestingly, the dynamics of collision systems introduces new carrier scattering states of larger lifetimes over the broad range of k-states along the Γ-Y direction. In fact, the enhancement of electron relaxation time is predicted to be 5 fold higher for the strained system. The main point is that the emergence of a few scattering states with suppressing electron and hole recombination rates caused by lowering of deformation potential in combination with light carrier effective mass leads to the achievement of ultra-high carrier mobility in layered β-TeO$_2$.

2.4 Conclusion

In conclusion, we have described first-principles based deformation potential theory formalism to study strain-induced anisotropy in the carrier mobility of β-TeO$_2$. We have also analyzed carrier mobility at various compressive as well as tensile strain. At 3% compressive strain along the x-direction, we achieve a sudden enhancement in hole mobility (39500 cm^2 V^{-1}s^{-1}) that is because of the lowering of both hole-phonon coupling strength and hole effective mass. Because of the similar reasons for electrons, we also find a sharp peak in the electron mobility (17500 cm^2 V^{-1}s^{-1}) at 4% compressive strain along the y-direction. The enhancement of such large carrier mobility is attributed to the higher carrier relaxation time along the $\Gamma - Y$ direction. This wider bandgap material coupled with ultrahigh carrier mobility could be utilized for next-generation nano-electronics. Indeed, this flexible layered structure along with its unique strain-induced electron and hole dynamics would be beneficial for power electronics applications.

2.5 References

[1] Li, T.; Zhang, Z.; Zheng, W.; Lv, Y.; Huang, F. A possible high-mobility signal in bulk MoTe$_2$: Temperature independent weak phonon decay. AIP Advances 2016, 6(11), 115207.

[2] Sarwat, S.G.; Tweedie, M.; Porter, B.F.; Zhou, Y.; Sheng, Y.; Mol, J.; Warner, J.; Bhaskaran, H. Revealing strain-induced effects in ultrathin heterostructures at the nanoscale. Nano letters 2018, 18(4), 2467-2474.

[3] Wang, Q.H.; Kalantar-Zadeh, K.; Kis, A.; Coleman, J.N.; Strano, M.S. Electronics and optoelectronics of two-dimensional transition metal dichalcogenides. Nature nanotechnology 2012, 7(11), 699-712.

[4] Lei, S.; Lin, J., Jia, Y.; Gray, M.; Topp, A.; Farahi, G.; Klemenz, S.; Gao, T.; Rodolakis, F.; McChesney, J.L.; Ast, C.R. High mobility in a van der Waals layered antiferromagnetic metal. Science advances 2020, 6(6), eaay6407.

[5] Gillgren, N.; Wickramaratne, D.; Shi, Y.; Espiritu, T.; Yang, J.; Hu, J.; Wei, J.; Liu, X.; Mao, Z.; Watanabe, K.; Taniguchi, T. Gate tunable quantum oscillations in air-stable and high mobility few-layer phosphorene heterostructures. 2D Materials 2014, 2(1), 011001.

[6] Sun, Z.; Chang, H. Graphene and graphene-like two-dimensional materials in

photodetection: mechanisms and methodology. ACS nano 2014, 8(5), 4133-4156.

[7] Liu, Y.; Shivananju, B.N.; Wang, Y.; Zhang, Y.; Yu, W.; Xiao, S.; Sun, T.; Ma, W.; Mu, H.; Lin, S.; Zhang, H. Highly efficient and air-stable infrared photodetector based on 2D layered graphene–black phosphorus heterostructure. ACS applied materials interfaces 2017, 9(41), 36137-36145.

[8] Tan, S.J.R.; Abdelwahab, I.; Chu, L.; Poh, S.M.; Liu, Y.; Lu, J.; Chen, W.; Loh, K.P. Quasi-Monolayer Black Phosphorus with High Mobility and Air Stability. Advanced Materials 2018, 30(6), 1704619.

[9] Fei, R.; Yang, L. Strain-engineering the anisotropic electrical conductance of few-layer black phosphorus. Nano letters 2014, 14(5), 2884-2889.

[10] Li, L.; Yu, Y.; Ye, G.J.; Ge, Q.; Ou, X.; Wu, H.; Feng, D.; Chen, X.H.; Zhang, Y. Black phosphorus field-effect transistors. Nature nanotechnology 2014, 9(5), 372.

[11] Jiang, J.W.; Park, H.S. Negative poisson's ratio in single-layer black phosphorus. Nature communications 2014, 5(1), 1-7.

[12] Wood, J.D.; Wells, S.A.; Jariwala, D.; Chen, K.S.; Cho, E.; Sangwan, V.K.; Liu, X.; Lauhon, L.J.; Marks, T.J.; Hersam, M.C. Effective passivation of exfoliated black phosphorus transistors against ambient degradation. Nano letters 2014, 14(12), 6964-6970.

[13] Tosun, M.; Fu, D.; Desai, S.B.; Ko, C.; Kang, J.S.; Lien, D.H.; Najmzadeh, M.; Tongay, S.; Wu, J.; Javey, A. MoS_2 heterojunctions by thickness modulation. Scientific reports 2015, 5(1), 1-8.

[14] Shen, T.; Penumatcha, A.V.; Appenzeller, J. Strain engineering for transition metal dichalcogenides based field effect transistors. ACS nano 2016, 10(4), 4712-4718.

[15] Roldán, R.; Castellanos-Gomez, A.; Cappelluti, E.; Guinea, F. Strain engineering in semiconducting two-dimensional crystals. Journal of Physics: Condensed Matter 2015, 27(31), 313201.

[16] Banerjee, S.; Pati, S.K. Charge-transport anisotropy in black phosphorus: critical dependence on the number of layers. Physical Chemistry Chemical Physics 2016, 18(24), 16345-16352.

[17] Liu, X.; Mashimo, T.; Kawai, N.; Sekine, T.; Zeng, Z.; Zhou, X. Phase transition and equation of state of paratellurite (TeO_2) under high pressure. Materials Research Express 2016, 3(7), 076206.

[18] El-Mallawany R. A. Tellurite Glass Handbook 2002, Boca Raton.

[19] Ceriotti, M.; Pietrucci, F.; Bernasconi, M. Ab-initio study of the vibrational properties of crystalline TeO_2: The , , and phases. Physical Review B 2016, 73(10), 104304.

[20] Beyer, H. Verfeinerung der Kristallstruktur von Tellurit, dem rhombischen TeO_2. Zeitschrift für Kristallographie-Crystalline Materials 1967, 124(3), 228-237.

[21] Arlt, G.; Schweppe, H. Paratellurite, a new piezoelectric maternal. Solid State Communications 1968, 6(11), 783-784.

[22] Uchida, N.; Ohmachi, Y. Elastic and photoelastic properties of TeO_2 single crystal. Journal of Applied Physics 1969, 40(12), 4692-4695.

[23] Warner, A.W.; White, D.L.; Bonner, W.A. Acousto-optic light deflectors using optical activity in paratellurite. Journal of Applied Physics 1972, 43(11), 4489-4495.

[24] Beyer, H. Verfeinerung der Kristallstruktur von Tellurit, dem rhombischen TeO_2. Zeitschrift für Kristallographie-Crystalline Materials 1967, 124(3), 228-237.

[25] S.A. Malyutin, K.K. Samplavskaya, M.Kh. Karapet'yants, Russ J. Inorg. Chem. 1971, 16, 781.

[26] Blanchandin, S.; Marchet, P.; Thomas, P.; Champarnaud-Mesjard, J.C.; Frit, B.; Chagraoui, A. New investigations within the TeO_2-WO_3 system: phase equilibrium diagram and glass crystallization. Journal of materials science 1999, 34(17), 4285-4292.

[27] Champarnaud-Mesjard, J.C.; Blanchandin, S.; Thomas, P.; Mirgorodsky, A.;

Merle-Mejean, T.; Frit, B. Crystal structure, Raman spectrum and lattice dynamics of a new metastable form of tellurium dioxide: γ-TeO_2. Journal of physics and chemistry of solids 2000, 61(9), 1499-1507.

[28] Guo, S.; Zhu, Z.; Hu, X.; Zhou, W.; Song, X.; Zhang, S.; Zhang, K.; Zeng, H. Ultrathin tellurium dioxide: emerging direct bandgap semiconductor with high-mobility transport anisotropy. Nanoscale 2018, 10(18), 8397-8403.

[29] Hua, X.; Chen, X.; Goddard, W.A. Generalized generalized gradient approximation: An improved density-functional theory for accurate orbital eigenvalues. Physical Review B 1997, 55(24), 16103.

[30] Heyd, J.; Scuseria, G.E.; Ernzerhof, M. Hybrid functionals based on a screened Coulomb potential. The Journal of chemical physics 2003, 118(18), 8207-8215.

[31] Giannozzi, P.; Baroni, S.; Bonini, N.; Calandra, M.; Car, R.; Cavazzoni, C.; Ceresoli, D.; Chiarotti, G.L.; Cococcioni, M., Dabo, I.; Dal Corso, A. QUANTUM ESPRESSO: a modular and open-source software project for quantum simulations of materials. Journal of physics: Condensed matter 2009, 21(39), 395502.

[32] Banerjee, S.; Park, J.; Hwang, C.S.; Choi, J.H.; Lee, S.C.; Pati, S.K. Regulation of transport properties by polytypism: a computational study on bilayer MoS_2. Physical Chemistry Chemical Physics 2017, 19(32), 21282-21286.

[34] Cai, Y.; Ke, Q.; Zhang, G.; Feng, Y.P.; Shenoy, V.B.; Zhang, Y.W. Giant phononic anisotropy and unusual anharmonicity of phosphorene: interlayer coupling and strain engineering. Advanced Functional Materials 2015, 25(15), 2230-2236.

[35] Rodin, A.S.; Carvalho, A.; Neto, A.C. Strain-induced gap modification in black phosphorus. Physical review letters 2014, 112(17), 176801.

[36] Peng, X.; Wei, Q.; Copple, A. Strain-engineered direct-indirect band gap transition and its mechanism in two-dimensional phosphorene. Physical Review B 2014, 90(8), 085402.

[37] Kaur, S.; Kumar, A.; Srivastava, S.; Pandey, R.; Tankeshwar, K. Stability

and carrier transport properties of phosphorene-based polymorphic nanoribbons. Nanotechnology 2018, 29(15), 155701.

[38] Peng, Q.; Han, L.; Wen, X.; Liu, S.; Chen, Z.; Lian, J.; De, S. Mechanical properties and stabilities of -boron monolayers. Physical Chemistry Chemical Physics 2015, 17(3), 2160-2168.

[39] Momma, K.; Izumi, F. VESTA: a three-dimensional visualization system for electronic and structural analysis. Journal of Applied crystallography 2008, 41(3), 653-658.

[40] Cai, Y.; Zhang, G.; Zhang, Y.W. Polarity-reversed robust carrier mobility in monolayer MoS_2 nanoribbons. Journal of the American Chemical Society 2014, 136(17), 6269-6275.

[41] Schusteritsch, G.; Uhrin, M.; Pickard, C.J. Single-layered hittorf's phosphorus: a wide-bandgap high mobility 2D material. Nano letters 2016, 16(5), 2975-2980.

[42] Cai, X.; Chen, Y.; Sun, B.; Chen, J.; Wang, H.; Ni, Y.; Tao, L.; Wang, H.; Zhu, S.; Li, X.; Wang, Y. Two-dimensional Blue-AsP monolayers with tunable direct band gap and ultrahigh carrier mobility show promising high-performance photovoltaic properties. Nanoscale 2019, 11(17), 8260-8269.

[43] Bao, W.; Cai, X.; Kim, D.; Sridhara, K.; Fuhrer, M.S.; High mobility ambipolar MoS_2 field-effect transistors: Substrate and dielectric effects. Applied Physics Letters 2013, 102(4), 042104.

[44] Pradhan, N.R.; Rhodes, D.; Zhang, Q.; Talapatra, S.; Terrones, M.; Ajayan, P.M.; Balicas, L., Intrinsic carrier mobility of multi-layered MoS_2 field-effect transistors on SiO_2. Applied Physics Letters 2013, 102(12), 123105.

[45] Radisavljevic, B.; Kis, A. Mobility engineering and a metal–insulator transition in monolayer MoS_2. Nature materials 2013, 12(9), 815-820.

[46] Nosé, S. A unified formulation of the constant temperature molecular dynamics methods. The Journal of chemical physics 1984, 81(1), 511-519.

[47] Monkhorst, H.J.; Pack, J.D. Special points for Brillouin-zone integrations.

Physical review B 1976, 13(12), 5188.

[48] Grimme, S. Semiempirical GGA-type density functional constructed with a long-range dispersion correction. Journal of computational chemistry 2006, 27(15), 1787-1799.

[49] Momma, K.; Izumi, F. VESTA: a three-dimensional visualization system for electronic and structural analysis. Journal of Applied crystallography 2008, 41(3), 653-658.

3

Vibrational Spectra of MO (M=Sn/Pb) in Their Bulk and Single Layer Forms: Role of Avoided Crossing in their Thermodynamic Properties

3.1 Introduction

Recently, ab-initio based density functional theory (DFT) method has become well-established techniques to study vibrational and structural properties of various materials. For the last few decades, many studies on the dynamical property have been carried out on a number of three-dimensional as well as layered materials. Presently, several mechanical exfoliation techniques applied to various materials has lead to the synthesis of a large number of unique two dimensional systems. The most interesting among them is the two-dimensional material, graphene,[1] a hexagonal sheet of carbon atoms, which exhibits exotic physical properties, that

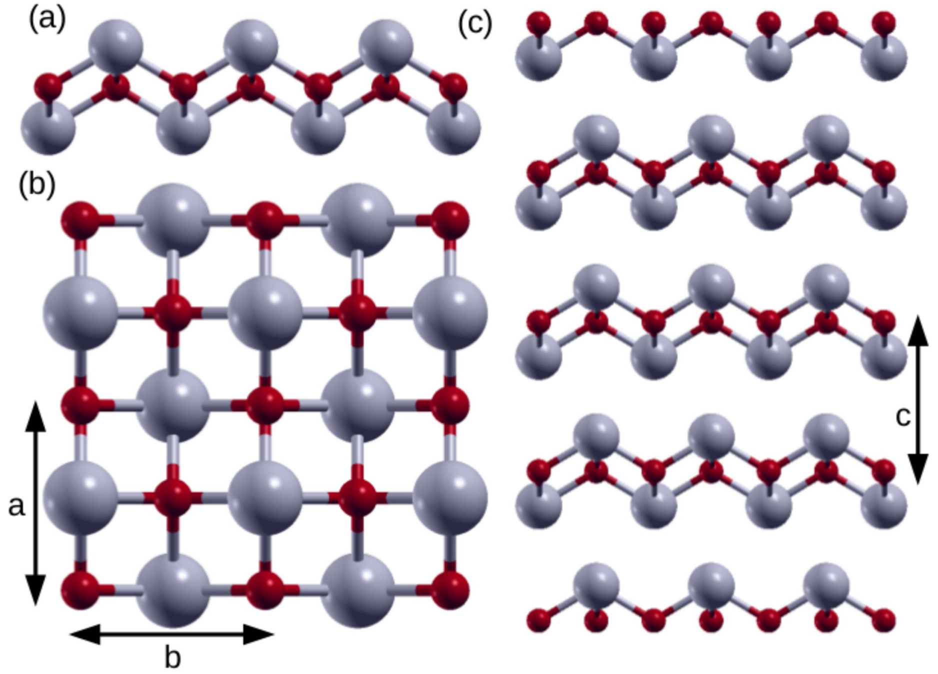

Figure 3.1: Crystal structure of MO (M=Sn/Pb). (a) monolayer, (b) viewed along z-axis, (c) bulk. The arrows in (b) depict lattice parameters a and b along the x and y directions, respectively. The interlayer distance is shown by an arrow in (c).

are not found in its bulk counterpart, graphite.[2] But the absence of a bandgap in graphene makes its application quite limited. On the other hand, there exist a large number of layered crystal structures, like BN-sheets[3], chalcogenides[4], oxides[5], sulfides[6], etc which show many fascinating properties for applications in electronic, optoelectronic, photovoltaic and thermoelectric devices.

Recently, atomic layers of MO (M=Sn/Pb) have been successfully fabricated using micromechanical and sonochemical exfoliation.[7,8,38] Because of the layer-dependent band gaps, these materials have attracted attention for their electronic, optoelectronic and thermoelectric applications.[9] Tin monoxide (SnO) is an interesting semiconductor which possesses a relatively small indirect band gap of 0.7 eV and optical gap of 2.7 eV in bulk.[10-12] However, the monolayer is an insulator and theoretically predicted band gap is 3.93 eV at the HSE06 level.[13]

On the other hand, for lead oxide, PbO, the fundamental gap is direct in case of monolayer (4.48 eV) and indirect for both bilayer (3.44 eV) and bulk (2.45 eV).[15] It has been observed in previous studies that the optical and electronic properties of these oxide materials are strongly dependent on their dimensions.[39] Recently, Umezawa et. al. have shown that the band gap in bulk-SnO can be tuned by reducing the dimension and by inducing biaxial strain quite effectively.[14]

Table 3.1: Optimized lattice parameters ($\mathring{A}$) [4,6,10] at which DFPT calculation were performed, optical dielectric constant and Born effective charge (e) for the tetragonal phase of bulk and monolayer of both SnO and PbO.

SnO			**PbO**		
Parameters	Bulk	Monolayer	Parameters	Bulk	Monolayer
a_{cell}	3.82	3.82	a_{cell}	3.97	3.97
a_{cell} (c-axis)	5.02	20.00	a_{cell} (c-axis)	5.02	20
ϵ_{xx}	7.47	2.18	ϵ_{xx}	6.26	2.06
ϵ_{yy}	7.47	2.18	ϵ_{yy}	6.26	2.06
ϵ_{zz}	6.86	1.32	ϵ_{zz}	5.76	1.26
$Z^*_{Sn(xy)}$	2.98	2.69	$Z^*_{Pb(xy)}$	3.08	3.26
$Z^*_{Sn(z)}$	2.67	0.51	$Z^*_{Pb(z)}$	2.06	0.44
$Z^*_{O(xy)}$	-3.00	-2.71	$Z^*_{O(xy)}$	-3.09	-3.27
$Z^*_{O(z)}$	-2.71	-0.54	$Z^*_{O(z)}$	-2.10	-0.46

Although, electronic, optical and transport properties of SnO as well as PbO have been studied in detail, the vibrational properties in terms of phonon spectra and their dynamics have not yet been studied properly for the two oxides in their layer as well as in bulk forms. The major outline of this chapter is to discuss full phonon spectra of MO (M=Sn/Pb), addressing Raman and IR modes with their associated atomic contributions. We have also performed density functional perturbation theory (DFPT) study to calculate self-force constants and interatomic force constants (IFCs). Interestingly, we obtain negative IFCs between M-M atoms belonging to adjacent layers for both SnO and PbO, because the charge on each metal atoms in two-dimensional layered materials is the same.[16]

In the phonon band structure, we encounter avoided crossing between longitudinal acoustic modes and transverse optical modes using the fine q (phonon wave vector) mesh calculations. Geurts et al. have obtained the vibrational spectrum of single-layer and multilayer SnO from Raman spectroscopy measurements.[17] They reported that Raman mode, A_{1g}, is higher in frequency than that of E_g mode, which is part of our spectral results. This anomalous behavior of Raman mode (A_{1g}) can successfully be explained by the concept of self-force constants and interatomic force constants. We have also explained the microscopic reason behind the avoided crossing between two degenerate phonon bands around the high symmetry points in the phonon dispersion curve.

In Sec. 3.2, we present a brief computational methodology for the calculation of phonon dispersion and the analysis of force constants in this chapter. In Sec. 3.3, we discuss the dielectric properties, Born effective charges and phonon dispersion in two parts for SnO and PbO single layer and bulk and compare with experimental data. In this section, we also explain self-force constants, interatomic force constants and Landau quasi degeneracy or avoided crossing. Finally, the chapter ends with an overall conclusion in Section 3.4.

3.2 Computational Methods

SnO and PbO are typical layered materials with the same crystal structure and tetragonal symmetry (D_{4h}).[18] To discuss the structure, we will use M, which will represent both Sn and Pb. The tetragonal litharge structure (space group P4/nmm) have 4-coordinated M and O atoms in the tetrahedral environment. The M atoms are bonded with four neighboring oxygen atoms, which forms the base of the square pyramid.[13,18-20] The asymmetric bonding arrangement gives rise to a layered structure which is stacked along the [001] crystal direction. Here, two consecutive MO layers are bound by weak van der Waals forces in bulk MO.

The geometry optimization is carried out with density functional theory (DFT) as implemented in the Quantum Espresso package within the plane waves and pseudopotential approach. For structure relaxation and energy calculation, we employ local gradient approximation (LDA) with norm-conserving pseudopotential[21]. The wave function cut-off is considered to be 70 Ry. The Monkhorst-Pack grid with 18 × 18 × 18 k-points for bulk MO and 18 × 18 × 1 for monolayer MO is used in sampling Brillouin zone integrations. The crystal structures are fully relaxed to minimize the energy until the magnitude of Hellman-Feynman force on each atom is less than 0.025 $eV/\mathring{A}$. The Gaussian spreading is considered to be 0.003 Ry.

Using first-principle based DFT calculation with van der Waals (vdW) forces, we find the optimized lattice parameters of bulk-SnO as a = b = 3.82 $\mathring{A}$ and c = 5.02 $\mathring{A}$. In the case of PbO, the lattice parameters are found to be a = b = 3.97 $\mathring{A}$ and c = 5.02 $\mathring{A}$. For monolayers, optimized lattice parameters are almost similar to the bulk but there is a vacuum of 20 Å along the crystallographic c-direction. The optimized lattice parameters for both SnO and PbO in their bulk and single-layer form are given in Table 3.1.

Recently, very efficient linear response techniques[22] have been proposed to obtain dynamical matrices at arbitrary wave vectors. Accurate phonon dispersion can be obtained on a fine grid of wave vectors covering the entire Brillouin zone along with the high symmetry points ($\Gamma \rightarrow$ X $\rightarrow$ M $\rightarrow \Gamma$). The optical dielectric constant, the Born effective charge and the force constants matrix have been computed at selected q-points in the Brillouin zone using ph.x code implemented in Quantum Espresso. The dynamical matrices has been calculated considering 4 x 4 x 4 grid in the Irreducible Brillouin zone (IBZ). Using a discrete Fourier transform, we get the short-range contribution to interatomic force constants (IFCs) in real space. Finally, the phonon dispersion curves can easily be obtained at any arbitrary q-point in the Brillouin zone from the reverse Fourier transform of

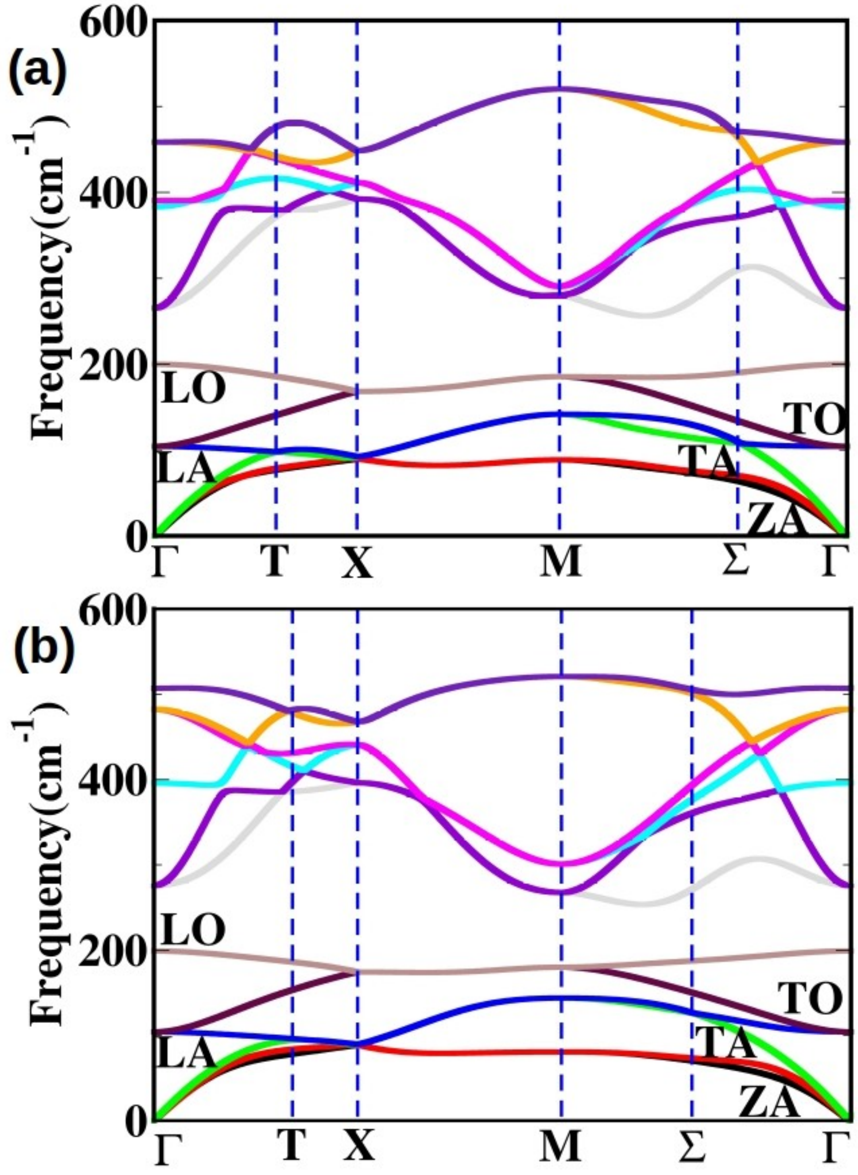

Figure 3.2: Phonon band structure of (a) bulk and (b) monolayer of SnO. Low energy acoustics and optical modes are indicated in the graph using different colors. The bands are represented in different colors like black: ZA, red: TA, green: LA, blue and maroon: TO (transverse optical), gray: LO (longitudinal optical).

interatomic force constants in real space.

Since SnO and PbO are polar semiconductors, the long-range character of the Coulomb forces give rise to the macroscopic electric field. This macroscopic electric field affects the longitudinal optical (LO) phonon modes in the limit of $q \rightarrow 0$, breaking the degeneracy of the LO modes with the transverse optical (TO) modes. In the long-wavelength limit, the matrix of the force constants can be written as the sum of analytic and non-analytic contributions of force constants.[23]

$$\widetilde{C}_{\alpha i,\beta j} = \widetilde{C}^{an}_{\alpha i,\beta j} + \widetilde{C}^{na}_{\alpha i,\beta j} \tag{3.1}$$

The analytic part, $\widetilde{C}^{an}_{\alpha i,\beta j}$, has been calculated from the response of zone-center phonon in zero macroscopic electric field condition. On the other hands, the non-analytic part, $\widetilde{C}^{na}_{\alpha i,\beta j}$, has a general expression

$$\widetilde{C}^{na}_{\alpha i,\beta j} = \frac{4\pi e^2}{\Omega} \frac{\sum_\gamma Z^\star_{i,\gamma\alpha} q_\gamma \sum_\nu Z^\star_{j,\nu\beta} q_\nu}{\sum_{\gamma\nu} q_\gamma \epsilon^\infty_{\gamma\nu} q_\nu} \tag{3.2}$$

where Ω is the volume of the unit cell. $\epsilon^\infty_{\gamma\nu}$ is the electronic contribution to static dielectric tensor and $Z^\star_{i,\gamma\alpha}$ is the Born effective charge tensor for ith atom in the unit cell. From equation 3.2, it is clear that non-analytic part of force constants contains macroscopic dielectric constant of the system and Born effective charge, whereas analytic part is calculated ignoring any macroscopic polarization associated with phonons. Once the IFCs are known, we calculate phonon band structure and phonon density of states (DOS) using matdyn.x code implemented in Quantum Espresso.

The computed phonon frequencies (ω_{qj}) calculated over the Brillouin zone can be utilized to enumerate thermodynamic quantity. Using thermodynamic relation, thermal properties, such as, specific heat at constant volume ($\mathrm{C_v}$) can be calculated from energy fluctuation equation (equation 3.3). On the other hand, vibrational entropy (S) can be computed from the internal energy and partition function (equation 3.6). The specific heat (C_v), internal energy (U) and partition function (Z) can be written as[36]:

$$C_v = \frac{< E^2 > - < E >^2}{k_B T^2} \tag{3.3}$$

$$U =< E >= \frac{\sum_{qj} E_{qj} exp(-\beta E_{qj})}{Z} \tag{3.4}$$

$$Z = \sum_{qj} exp(-\beta E_{qj}) \tag{3.5}$$

Phonon vibrational entropy depends upon the internal energy (U) and the partition function (Z) of the system. The vibrational entropy can be described as,

$$S = \frac{U}{T} + k_B lnZ \tag{3.6}$$

where T and k_B are temperature and Boltzmann constant respectively. Finally, phonon group velocity can be calculated by the following expression,

$$v_j(q) = \frac{\Delta E_j(q)}{h} \tag{3.7}$$

3.3 Result and Discussions

3.3.1 Born effective charge and dielectric properties

To describe long-range dipolar contribution to the lattice dynamics of polar material, it is essential to discuss the Born effective charge ($Z_k{}^*$) and optical dielectric tensor (ϵ_∞) [25]. It is well known from the previous literature[26] study that when Born effective charge corresponding to an element, deviates substantially from its nominal value of oxidation state, the bonding characteristics are no more purely ionic in nature. Our Born effective charge analysis also shows similar results that the associated charge for M and O deviates significantly from its expected oxidation state of +2 and -2 respectively, which reflects the partially covalent character of M-O bonds, both in bulk and monolayer form. It is shown in Table 3.1 that the Born effective charge differs more significantly for bulk SnO from its ionic oxidation state than for its monolayer. As a result, we conclude that Sn-O and Sn-Sn bonds are more covalent in nature in bulk compared to its monolayer counterpart. On the other hand, the magnitude of Born effective charges corresponding to Pb and O are higher in monolayer along the xy-plane than the stacking direction. It implies that the Pb-O bonds in monolayer are more covalent in nature than in the bulk. Also, the interlayer Pb-Pb bonds are comparatively weaker than interlayer Sn-Sn bonds. It has been observed that the interlayer Pb-Pb bonds are relatively weaker because of the presence of $6s^2$ lone pairs present in the interstitial positions between two layers.[33]

With the optimized geometry, we have calculated the electronic contribution to the dielectric tensor self-consistently. The calculated dielectric constant is larger for SnO in comparison to PbO. The larger value of dielectric constant signifies that the SnO can be polarized more due to the electric field created by their atomic (neighbours) displacements.[27] From the Born effective charge calculations, we find that the Sn-O bonds are more ionic in nature compared to the Pb-O, which gives rise to higher dielectric constant in their bulk and monolayer form for SnO. Weak inter-layer van der Waals interaction increases the dielectric constant along each crystallographic direction in bulk SnO, which is not possible in monolayer (shown in Table 3.1). Our density functional perturbation theory (DFPT) calculations estimated the dielectric constant to be 7.47 along the xy-direction and 6.86 along z-direction for bulk SnO, whereas the dielectric constant is 2.18 along the xy-direction and 1.32 along z-direction for monolayer SnO. Moreover, we have computed dielectric constant and Born effective charge for PbO that exhibits a

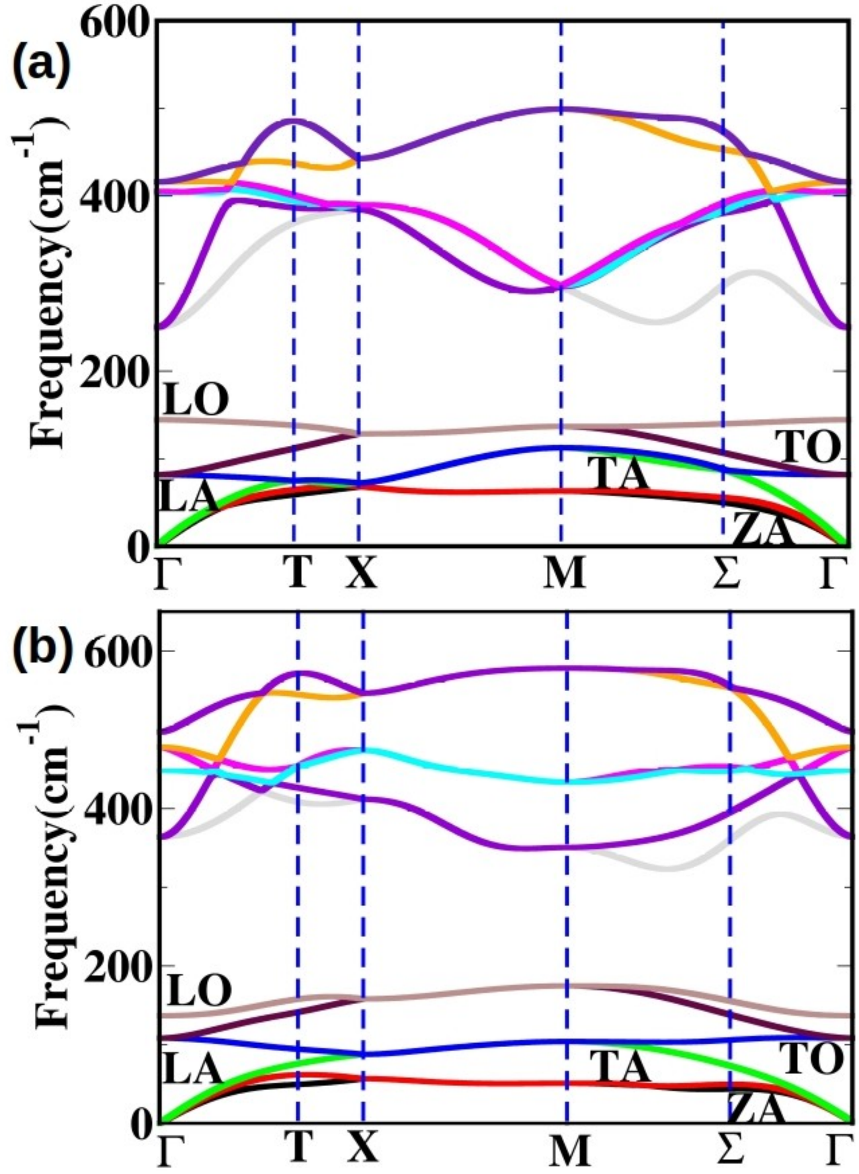

Figure 3.3: Phonon band structure of (a) bulk and (b) monolayer of PbO. Low energy acoustics and optical modes are indicated in the graph using several colors. The bands are represented in different colors like black: ZA, red: TA, green: LA, blue and maroon: TO (transverse optical), gray: LO (longitudinal optical).

Table 3.2: Phonon frequency (cm^{-1}) with optical character is described for bulk and monolayer SnO. The crystal plane is along ab-axis and out of plane is along c-axis. Atomic contribution to each mode is also given.

Bulk				**Monolayer**			
Frequency	Modes	Type	Atoms	Frequency	Modes	Type	Atoms
0.0	E_u	IR	Sn, O	0.0	E_u	IR	Sn, O
0.0	E_u	IR	Sn, O	0.0	E_u	IR	Sn, O
0.0	A_{2u}	IR	Sn, O	0.0	A_{2u}	IR	Sn, O
104.39	E_g	Raman	Sn, O	104.13	E_g	Raman	Sn, O
104.39	E_g	Raman	Sn, O	104.13	E_g	Raman	Sn, O
199.94	A_{1g}	Raman	Sn	199.06	A_{1g}	Raman	Sn
265.46	E_u	IR	Sn, O	275.81	B_{1g}	IR	Sn, O
265.46	E_u	IR	Sn, O	393.32	E_u	IR	Sn, O
383.36	B_{1g}	Raman	Sn, O	393.83	E_u	Raman	O
388.58	A_{2u}	IR	O	482.48	E_g	Raman	O
458.47	E_g	Raman	O	482.48	E_g	Raman	O
458.47	E_g	Raman	O	506.95	A_{2u}	IR	Sn, O

similar trend like SnO (see Table 3.1). This large difference in values for bulk and monolayer is an indicator that weak inter-layer van der Waals interactions play an important role in increasing the dielectric tensor and $Z_{\mathrm{k}}{}^{*}$ in both bulk SnO and PbO layered materials.

3.3.2 Phonon Dispersion

SnO

We begin our analysis of the vibrational properties with the description of the general features of the phonon dispersion of bulk and single-layer MO. We have compared our theoretical results with the experimental available data.[19,28-30] The overall agreement between theoretical lattice parameters and vibrational modes with experimental results motivates us to choose LDA functional for our further calculations (see Table 3.1, 3.2, 3.3). We have also verified theoretically predicted vibrational modes of bulk form of both SnO and PbO with the experimental results.[17,34,35]

The tetragonal unit cell of SnO consists of 4 atoms; so there are 12 normal modes of vibration (three acoustics modes and nine optical modes) at any q point in the Brillouin zone. At the zone center (Γ), three acoustics (ac) modes with $\Gamma_{ac} = 2E_u + A_{2u}$ symmetry have zero frequencies. The optical (op) modes are ($\Gamma_{op} = 4E_g + A_{1g} + 2E_u + B_{1g} + A_{2u}$) for bulk-SnO. Here g and u subscript represent symmetric and antisymmetric modes with respect to the center of inversion. The calculated eigenvectors allow us to visualize every mode in terms of motions of Sn and O atoms. The modes which vibrate in-plane [longitudinal acoustic (LA) and transverse acoustic (TA)] have dispersion higher than that of out of plane mode (ZA) which is shown in Figure 3.2. There are low energy optical modes found at 104 cm^{-1} and 199 cm^{-1}. As phonon wave vector (q) increases, longitudinal acoustic modes (LA) experience avoided scattering with the transverse optical modes (TO) along the high symmetry path Γ to X (T-point), which will be discussed later.

The high energy optical modes are separated from low energy optical modes by 65 cm^{-1} at Γ point. We have also identified the atomic displacement of Raman active modes, E_g, A_{1g}, B_{1g} and infrared active modes E_u and A_{2u} by studying the eigenvectors of each mode using XCrySDen programme[31]. The Raman and infrared (IR) modes are also tabulated in Table 3.2. We notice from Table 3.2 that the low energy Raman modes (E_g, A_{1g}) corresponding to bulk SnO are same as those of monolayer SnO, but this is not the case for PbO. This anomaly in the Raman modes will be discussed with the help of self-force constants and IFCs. We also notice that the IR mode, A_{2u}, is lower in frequency than the E_g Raman modes in bulk-SnO (see Table 3.2). But on the contrary, we find A_{2u} mode is higher in frequency than E_g mode for monolayer SnO, which is because of the lower dielectric constant (1.32) along the stacking directions. The interatomic force constants increase with lower dielectric constants (see equation 3.2) and in

Table 3.3: Phonon frequency (cm^{-1}) with optical character is described for bulk and monolayer PbO. The crystal plane is along ab-axis and out of plane is along c-axis. Atomic contribution to each mode is also given below.

Bulk				**Monolayer**			
Frequency	Modes	Type	Atoms	Frequency	Modes	Type	Atoms
0.00	E_u	IR	Pb, O	0.00	E_u	IR	Pb, O
0.00	E_u	IR	Pb, O	0.00	E_u	IR	Pb, O
0.00	A_{2u}	IR	Pb, O	0.00	A_{2u}	IR	Pb, O
81.79	E_g	Raman	Pb, O	108.25	E_g	Raman	Pb, O
81.79	E_g	Raman	Pb, O	108.25	E_g	Raman	Pb, O
144.56	A_{1g}	Raman	Pb	136.80	A_{1g}	Raman	Pb
249.99	E_u	IR	Pb, O	363.69	E_u	IR	Pb, O
249.99	E_u	IR	Pb, O	363.69	E_u	IR	Pb, O
402.54	B_{1g}	Raman	O	446.00	B_{1g}	Raman	O
403.66	E_g	Raman	Pb, O	477.68	E_g	Raman	O
415.74	E_g	Raman	O	477.68	E_g	Raman	O
415.74	A_{2u}	IR	O	497.10	A_{2u}	IR	Pb, O

turn increases the mode vibrations. Moreover, since we neglect the weak interlayer interaction in monolayer SnO, one IR mode, A_{2u}, shifts to higher frequency (from 388.58 cm^{-1} to 506.95 cm^{-1}).

The vibrational modes, particularly, the low energy modes are shown in the dispersion curve for bulk and monolayer SnO (see Figures 3.2a and 3.2b). There are 6 Raman modes tabulated along with atomic contribution in Table 3.2. There are also another 6 IR active modes including three acoustics modes. Frequencies of the first three Raman modes are almost the same for bulk and monolayer SnO (104 cm^{-1}, 104 cm^{-1}, 199 cm^{-1}). The reasons behind this will be discussed later in the IFCs part. Furthermore, phonon modes corresponding to monolayer are higher in magnitude with respect to its bulk counterpart, that is due to absence of interlayer vdW interactions. Overall, the monolayer and bulk SnO phonon dispersion show similar behavior. Nevertheless, we analyze all the above features in the next section with the help of self-force constant and the interatomic force constants (IFCs).

Table 3.4: Self-force constants for different atoms in the unit cell. B-MO represents bulk MO and M-MO represents monolayer MO in the table.

Atom	Direction	B-SnO	M-SnO	B-PbO	M-PbO
M	x/y	0.0808	0.0818	0.0816	0.1844
	z	0.2514	0.3080	0.2481	0.2784
O	x/y	0.1868	0.2124	0.1623	0.2436
	z	0.1920	0.2537	0.2132	0.2851

PbO

Figure 3.3 shows the phonon dispersion curve of both bulk and single-layer PbO. The general features are almost identical with SnO phonon dispersion curve. For a better comparison of SnO and PbO phonon bands in single layer and bulk, we have plotted phonon band structures in Figures 3.2 and 3.3 respectively. We observe that A_{1g} modes are lower in frequency for monolayer PbO than bulk-PbO. This peculiar feature can be understood using the concept of self-force constants and IFCs. The larger mass difference between Pb and Oxygen leads to higher frequency gap between low and high-frequency optical modes. The frequency gap between low and high energy optical modes for bulk and a single layer of SnO is around 66 cm^{-1} and 76 cm^{-1} respectively whereas for bulk and single-layer PbO, these gaps are around 105 cm^{-1} and 227 cm^{-1} respectively. The larger frequency gap for single layer PbO is the consequence of higher mass difference between Oxygen and Pb. Moreover, the frequency gap between low and high energy optical modes for monolayer PbO is further larger than bulk counterpart. This could be because of the absence of interlayer van der Waals interactions. All vibrational modes for PbO are mentioned in Table 3.3.

Table 3.5: Interatomic force constants between M (M=Sn/Pb) and oxygen atoms & interlayer M-M in tetragonal unit cell. B-MO represents bulk MO and M-MO represents monolayer MO in the table. IFC's are shown along x, y and z directions.

Bonds	Direction	B-SnO	M-SnO	B-PbO	M-PbO
M-O	x	-0.018	-0.011	-0.015	-0.002
	y	-0.041	-0.048	-0.039	-0.124
	z	-0.070	-0.129	-0.084	-0.130
M-M	z	-0.0098	-	-0.0077	-

3.3.3 Interatomic Force Constant

The interatomic force constants (IFCs) are considered as a fitting parameter in the vibrational problem of nonmetallic crystals. It is merely an expansion coefficient of an adiabatic potential with respect to the atomic displacements. The interatomic force constants (IFCs) are calculated in the construction of phonon dispersion relations. We consider that the IFCs matrix $C_{(\alpha,\beta)}(lk, l'k')$ which relates the force $F_\alpha(lk)$ on an atom k of unit cell l due to displacement $(l'k')$ of the atom k' in the cell, l', is defined through the following expression,

$$F_\alpha(lk) = C_{(\alpha,\beta)}(lk, l'k')\Delta\tau_\beta(l'k') \tag{3.8}$$

Initially, we examine self-force constants which specify the force on a single isolated atom at a unit displacement from its crystalline position. The values are tabulated in Table 3.4. The self-force constants are positive for all atoms in the two compounds both in bulk and monolayers. The positive value in self-force constant suggests that these two compounds are stable against isolated atomic displacement in their bulk and monolayer form.

In Table 3.2, we observe that there are three low energetic Raman modes (104 cm^{-1}, 104 cm^{-1} and 199 cm^{-1}) which are almost the same for both bulk and monolayer SnO. The eigenvectors corresponding to the Raman modes, E_g, have

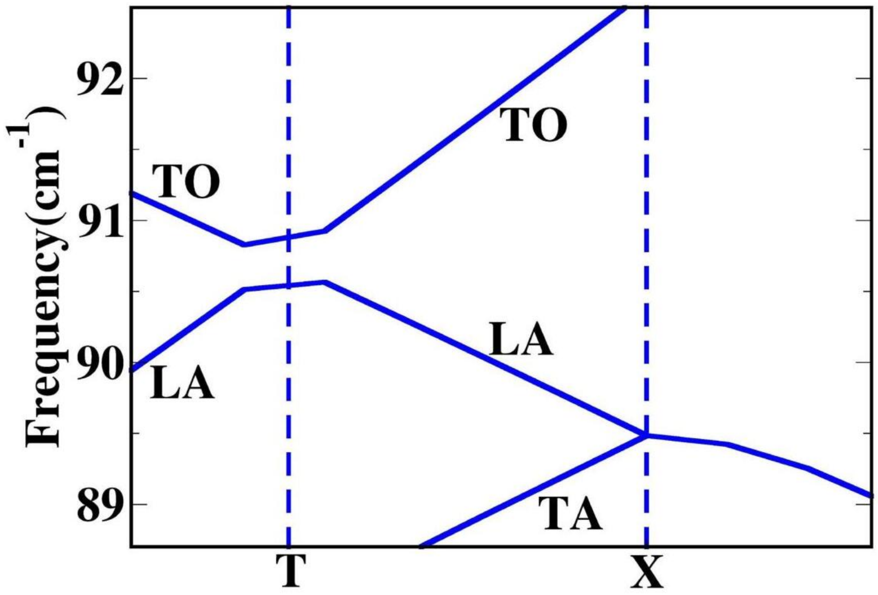

Figure 3.4: Avoided crossing occurred the point T at fine q-point. LA and TO bands cross each other at frequency 90.8 cm^{-1}. The inset crystal structures signify phonon eigenvectors (represented by arrows) corresponding to two bands at T-point. Both the phonon modes show same point group symmetry (Eu) at the vicinity of avoided crossing for SnO and only in bulk PbO.

main contributions from both Sn and O atomic displacement and the other Raman mode A_{1g} is originated solely from Sn displacement. Since self-force constant of Sn and O are the same for both bulk and monolayer SnO, E_g vibrations are also same. On the other hand, interatomic force constant between interlayer Sn atoms has negative value which leads to an increase in frequency (see Table 3.5). As a result, A_{1g} mode has higher frequency (199.94 cm^{-1}) in bulk SnO compared to its monolayer counterpart (199.06 cm^{-1}). Two IR modes E_u are also same in frequency (265.46 cm^{-1}) and they are associated with Sn and O oscillations. One IR mode A_{2u} and two other Raman modes E_g are mainly associated with Oxygen oscillations. Since O atoms are lighter in mass, these modes (A_{2u}, E_g) show higher vibrational frequencies.

Now we discuss phonon vibrational spectra through the analysis of real space force constants for monolayer SnO. In this case, one IR mode, A_{2u}, shifts higher in frequency for monolayer SnO which is because of the absence of interlayer van der Waals interaction along the z-direction (see Table 3.2). Another reason is due to the higher value of self-force constant along the stacking directions for monolayer with respect to bulk SnO. The self-force constants of Sn atom are more pronounced along the out of plane direction which leads to the higher frequency of mode A_{1u} with respect to E_g modes (see Table 3.4).

Unlike SnO, we observe that the first two Raman modes, E_g, are different in magnitude for bulk and monolayer PbO. The reason is that the self-force constant for Pb is higher for monolayer with respect to bulk in the in-plane direction (see Table 3.4). The three Raman modes (B_{1g}, $2E_g$) and three IR modes ($2E_u$, A_{2u}) are higher in frequency for monolayer compared to its bulk form. This is not only because of large self-force constant calculated using equation (3.2) but also due to the absence of interlayer interactions which give rise to higher vibrational frequencies.

3.3.4 Avoided Crossing

Avoided crossing or Landau quasi degeneracy occurs where two or more closely spaced energy levels do not cross, rather they avoid each other due to the the same symmetry.[32] On the other hand, energy levels with different symmetry may cross each other at any q point in the phonon band structure. The gap between these two avoided crossing bands depends upon the interaction strength in the vicinity of the avoided crossing point. Our calculations and subsequent analysis reveals that there is Landau quasi degeneracy or avoided crossing due to the coupling between the low lying optical (LLO) mode and longitudinal acoustic (LA) mode along the path Γ to M direction (Σ point) and Γ to K directions (T point) in the phonon dispersion curve (See Figure 3.2 and 3.3). We observe the avoided crossing in cases of single layer and bulk structure of SnO and in bulk PbO. Interestingly, we could not find any band crossing or avoided crossing in the phonon dispersion curve of monolayer PbO.

Figure 3.4 implies avoided crossing of two degenerate bands in the phonon dispersion band due to strong hybridization between the transverse optical (TO) and longitudinal acoustics (LA) modes. These hybridized vibrational modes are identified using the point group symmetry of each individual mode. To analyze the band crossing of the Landau degenerate bands in the vicinity of the avoided crossing point, the phonon eigenvectors are determined by diagonalizing the dynamical matrices. These phonon eigenvectors shown in Figure 3.4 indicate both phonon modes at the band crossing point have the same point group symmetry (E_u) and the magnitude of the eigenvectors signify equal contribution from TO and LA modes at particular q point (T & Σ points), where the avoided crossing occurs. The avoided crossing is further verified from the phonon density of states calculations shown in Figure 3.5. Since avoided crossing is absent in monolayer PbO, we observe finite density of states within the temperature range between 100 K to 150 K. Due to the avoided crossing between two degenerate bands in bulk and monolayer SnO and only in bulk PbO in the frequency range 90 cm^{-1} to 120 cm^{-1}, we find less density of states up to 150 cm^{-1} (see Figure 3.5).

As can be seen in Figure 3.4, the avoided crossing occurs at a frequency range from 90 cm^{-1} to 110 cm^{-1}. Note that, this frequency range is equivalent to temperature between 100 K to 120 K. As a consequence of avoided crossing in the phonon band structure, we observe a significant amount of effect on thermodynamic quantities. Figure 3.6 illustrates the specific heat and vibrational entropy at various temperatures from 0 K to 700 K, calculated using equations (3.3) and (3.6), respectively. We observe that the specific heat curve has a kink for both bulk and monolayer SnO and only in bulk PbO around T $\simeq$ 110 K, but in monolayer PbO these quantities remain smooth (see Figure 3.6). It is because of the avoided crossing, which is observed in both bulk and monolayer SnO along with bulk PbO.

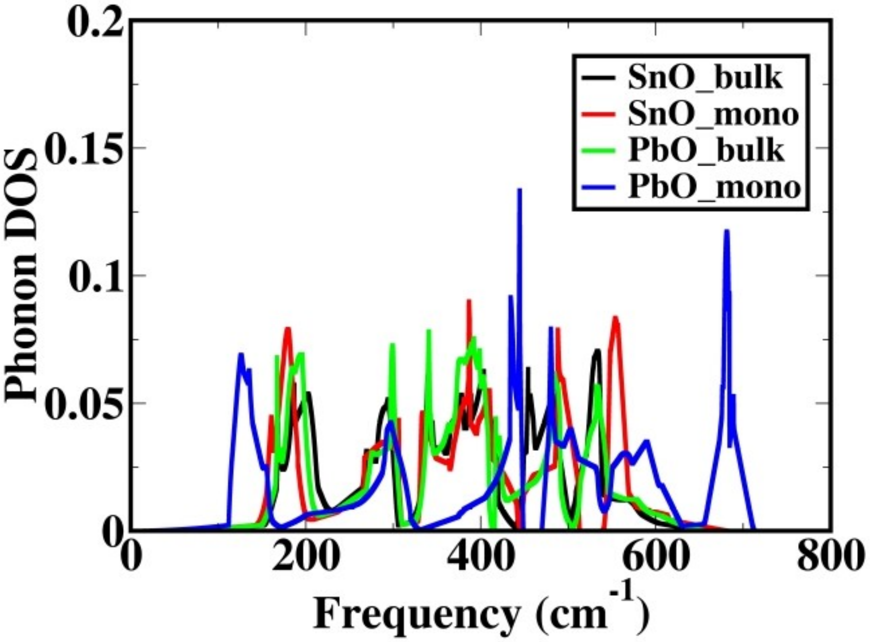

Figure 3.5: Projected phonon band structures are drawn for both bulk and monolayer of SnO and PbO. Here, phonon projected DOS of only monolayer PbO exhibiting significant contribution (blue line) in the low-frequency region around 150 cm^{-1}. This is because of the absence of avoided crossing in monolayer PbO.

Interestingly, we could not notice any avoided crossing for single layer PbO. This is due to the presence of higher vibrational mode E_g of 108.25 cm^{-1} in monolayer PbO in comparison to the same mode in bulk PbO at 81.79 cm^{-1}. However, in both bulk and monolayer SnO, this vibrational mode, E_g, has the same frequency of 104.39 cm^{-1}.

At higher temperatures, the specific heat is lower for PbO than for SnO due to the heavier mass of Pb compared to Sn. Heavier mass decreases the phonon frequency and as a result, specific heat and vibrational entropy also decreases at the higher temperatures. Our temperature dependent thermodynamic parameter study also shows that there is avoided crossing near the frequency, 91 cm^{-1}, for SnO and bulk PbO, which is manifested as a kink in specific heat and reduced vibrational entropy till T $\simeq$ 110 K.

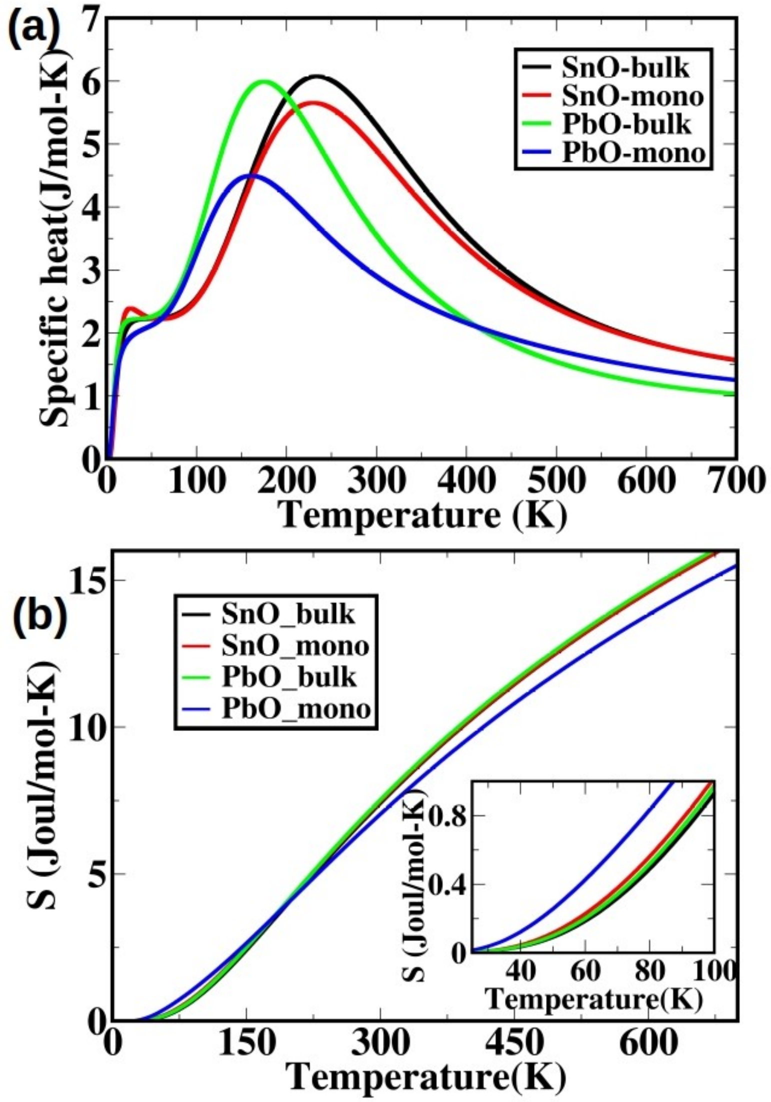

Figure 3.6: (a) Specific heat (C_v) and (b) vibrational entropy (S) are plotted with respect to temperature. We observe a kink in Specific heat for bulk-SnO, bulk-PbO and monolayer-SnO but not in single layer PbO at temperatures around 100 K. We also find vibrational entropy is higher for monolayer PbO than other three cases. At higher temperatures, C_v and S are lower for PbO than SnO because of the heavier mass of Pb. The inset of figure 3.6b shows vibrational entropy upto temperature 100 K (zoomed).

To further confirm the avoided crossing between two degenerate bands in bulk SnO, bulk PbO and monolayer SnO, we calculate the group velocity, v_{iq}, as a function of q for each phonon bands. Interestingly, we notice that the group velocity of the LA band suddenly decreases near T-point in bulk SnO phonon bands structure (see Figure 3.7(a)). To compensate for the energy conservation, the group velocity of the TO band sharply increases at the same q-point in the dispersion curve. Furthermore, we find similar discontinuity in $v(q)$ along the T to X point in the Brillouin zone for both monolayer of SnO and bulk PbO. This happens because of the avoided crossing at those q-points and consequently an abrupt change in phonon group velocity is manifested. This type of sudden change in group velocity is almost absent in monolayer PbO (see Figure 3.7(d)). These observations further confirm the appearance of avoided crossing between two degenerate bands in the dispersion curve around 100 K. Eventually, there are many more manifestations of similar Landau quasi degeneracies at other q-points like X and Σ points.

3.4 Conclusion

In conclusion, we have compared and contrasted phonon dispersions of SnO and PbO in their single layer and bulk forms using Density Functional Perturbation Theory (DFPT). We obtain good agreement of theoretical Raman and IR active modes with the available experimental data. We have shown some anomalous behavior of phonon dispersions which can be understood from the study of self-force constants and IFCs. Interestingly, we notice strong avoided crossing in both monolayer and bulk SnO and only in bulk PbO along the high symmetry points, which has a direct consequence in reducing the phonon contribution to vibrational entropy. Our study reveals the abrupt change in group velocity, which further confirms the appearance of Landau quasi degeneracy or avoided crossing in bulk

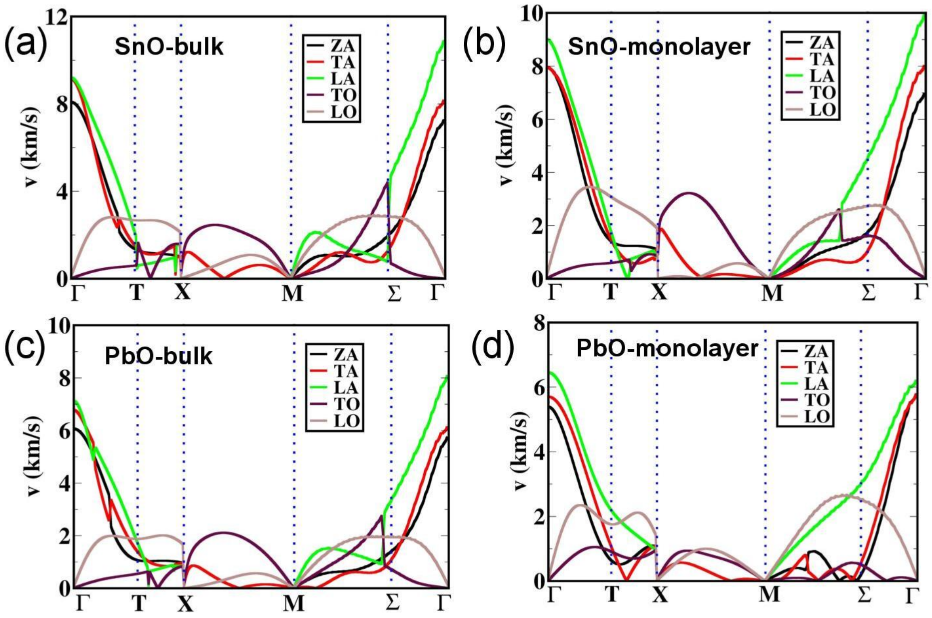

Figure 3.7: Group velocity (v) as a function of phonon wave vector (q) in (a) SnO-bulk, (b) SnO-monolayer, (c) PbO-bulk, (d) PbO-monolayer. There is sharp discontinuity in v between LA (green line) and TO (blue line) along the q-point. This abrupt discontinuity is a consequence of avoided crossing between the degenerate phonon bands.

and monolayer form of SnO and only in bulk PbO. Interestingly, we do not find any avoided crossing for monolayer PbO which is additionally validated by the appearance of kink in $C_v(T)$ dominated by the energy fluctuations. The main point is that because of the Landau quasi degeneracy and anti-crossing rule in the same symmetry, the specific heat and vibrational entropy will have similar behavior in the band dispersion. Our present work encompasses the comprehensive study on vibrational spectra of MO and provides new insight into the vibrational entropy and specific heat, which is crucial to the development of better thermoelectric materials.

3.5 References

[1] Geim, A.K.; Novoselov, K.S. The rise of graphene. In Nanoscience and technology: a collection of reviews from nature journals 2010, 11-19.

[2] Novoselov, K.S.; Geim, A.K.; Morozov, S.V.; Jiang, D.; Zhang, Y.; Dubonos, S.V.; Grigorieva, I.V.; Firsov, A.A. Electric field effect in atomically thin carbon films. science 2004, 306(5696), 666-669.

[3] Lin, C.H.; Fu, H.C.; Cheng, B.; Tsai, M.L.; Luo, W.; Zhou, L.; Jang, S.H.; Hu, L.; He, J.H. A flexible solar-blind 2D boron nitride nanopaper-based photodetector with high thermal resistance. npj 2D Materials and Applications 2018, 2(1), 1-6.

[4] Cahen, D.; Noufi, R., Surface passivation of polycrystalline, chalcogenide based photovoltaic cells. Solar Cells 1991, 30(1-4), 53-59.

[5] Miller, S.A.; Gorai, P.; Aydemir, U.; Mason, T.O.; Stevanović, V.; Toberer, E.S.; Snyder, G.J. SnO as a potential oxide thermoelectric candidate. Journal of Materials Chemistry C 2017, 5(34), 8854-8861.

[6] Molina-Sanchez, A.; Wirtz, L Phonons in single-layer and few-layer MoS_2 and WS_2. Physical Review B 2011, 84(15), 155413.

[7] Kumar, P.; Liu, J.; Ranjan, P.; Hu, Y.; Yamijala, S.S.; Pati, S.K.; Irudayaraj, J.; Cheng, G.J. Alpha lead oxide (α-PbO): a new 2D material with visible light sensitivity 2018. Small, 14(12), 1703346.

[8] Daeneke, T.; Atkin, P.; Orrell-Trigg, R.; Zavabeti, A.; Ahmed, T.; Walia, S.; Liu, M.; Tachibana, Y.; Javaid, M.; Greentree, A.D.; Russo, S.P. Wafer-scale synthesis of semiconducting SnO monolayers from interfacial oxide layers of metallic liquid tin. ACS nano 2017, 11(11), 10974-10983.

[9] D. Le Bellac, J. M. Kiat, P. Garnier, Journal of Solid State Chemistry, 1995, 114, 459-68.

[10] Ogo, Y.; Hiramatsu, H.; Nomura, K.; Yanagi, H.; Kamiya, T.; Hirano, M.;

Hosono, H. p-channel thin-film transistor using p-type oxide semiconductor, SnO. Applied Physics Letters 2008, 93(3), 032113.

[11] Li, Y.W.; Li, Y.; Cui, T.; Zhang, L.J.; Ma, Y.M.; Zou, G.T. The pressure-induced phase transition in SnO: a first-principles study. Journal of Physics: Condensed Matter 2007, 19(42), 425230.

[12] Govaerts, K.; Saniz, R.; Partoens, B.; Lamoen, D. van der Waals bonding and the quasiparticle band structure of SnO from first principles. Physical Review B 2013, 87(23), 235210.

[13] Seixas, L.; Rodin, A.S.; Carvalho, A.; Neto, A.C. Multiferroic two-dimensional materials. Physical review letters 2016, 116(20), 206803.

[14] Zhou, W.; Umezawa, N. Band gap engineering of bulk and nanosheet SnO: an insight into the interlayer Sn–Sn lone pair interactions. Physical Chemistry Chemical Physics 2015, 17(27), 17816-17820.

[15] Das, S.; Shi, G.; Sanders, N.; Kioupakis, E. Electronic and optical properties of two-dimensional α-PbO from first principles. Chemistry of Materials 2018, 30(20), 7124-7129.

[16] Gonze, X.; Charlier, J.C.; Allan, D.C.; Teter, M.P. Interatomic force constants from first principles: The case of -quartz. Physical Review B 1994, 50(17), 13035.

[17] Geurts, J.; Rau, S.; Richter, W.; Schmitte, F.J. SnO films and their oxidation to SnO_2: Raman scattering, IR reflectivity and X-ray diffraction studies. Thin solid films 1984, 121(3), 217-225.

[18] Meyer, M.; Onida, G.; Palummo, M.; Reining, L. Ab initio pseudopotential calculation of the equilibrium structure of tin monoxide. Physical Review B 2001, 64(4), 045119.

[19] Li, Y.W.; Li, Y.; Cui, T.; Zhang, L.J.; Ma, Y.M.; Zou, G.T. The pressure-induced phase transition in SnO: a first-principles study. Journal of Physics: Condensed Matter 2007, 19(42), 425230.

[20] Walsh, A.; Watson, G.W. Electronic structures of rocksalt, litharge, and

herzenbergite SnO by density functional theory. Physical Review B 2004, 70(23), 235114.

[21] Hamann, D.R.; Schlüter, M.; Chiang, C. Norm-conserving pseudopotentials. Physical Review Letters 1979, 43(20), 1494.

[22] Baroni, S.; Giannozzi, P.; Testa, A. Green's-function approach to linear response in solids. Physical review letters 1987, 58(18), 1861.

[23] Giannozzi, P.; De Gironcoli, S.; Pavone, P.; Baroni, S. Ab-initio calculation of phonon dispersions in semiconductors. Physical Review B 1991, 43(9), 7231.

[24] Cochran, W.; Cowley, R.A. Dielectric constants and lattice vibrations. Journal of Physics and Chemistry of Solids 1962, 23(5), 447-450.

[25] Molina-Sanchez, A.; Wirtz, L. Phonons in single-layer and few-layer MoS_2 and WS_2. Physical Review B 2011, 84(15), 155413.

[26] Gonze, X.; Lee, C. Dynamical matrices, Born effective charges, dielectric permittivity tensors, and interatomic force constants from density-functional perturbation theory. Physical Review B 1997, 55(16), 10355.

[27] Wang, X.; Zhang, F.X.; Loa, I.; Syassen, K.; Hanfland, M.; Mathis, Y.L. Structural properties, infrared reflectivity, and Raman modes of SnO at high pressure. physica status solidi (b) 2004, 241(14), 3168-3178.

[28] Moore Jr, W.J.; Pauling, L. The crystal structures of the tetragonal monoxides of lead, tin, palladium, and platinum. Journal of the American Chemical Society 1941, 63(5), 1392-1394.

[29] Born, M.; Huang, K. Dynamical theory of crystal lattices Oxford University Press 1954. London, New York.

[30] A. Kokalj, Journal of Molecular Graphics and Modelling, 1999, 17, 176-9.

[31] Devaquet, A. Avoided crossings in photochemistry. Pure Appl. Chem 1975, 41(4), 455-473.

[32] Walsh, A.; Watson, G.W. The origin of the stereochemically active Pb (II) lone pair: DFT calculations on PbO and PbS. Journal of Solid State Chemistry

2005, 178(5), 1422-1428.

[33] Semeniuk, O.; Csik, A.; Kökényesi, S.; Reznik, A. Ion-assisted deposition of amorphous PbO layers. Journal of Materials Science 2017, 52(13), 7937-7946.

[34] Baleva, M.; Tuncheva, V. Optical characterization of lead monoxide films grown by laser-assisted deposition. Journal of Solid State Chemistry 1994, 110(1), 36-42.

[35] Koval, S.; Burriel, R.; Stachiotti, M.G.; Castro, M.; Migoni, R.L.; Moreno, M.S.; Varela, A.; Rodriguez, C.O. Linear augmented-plane-wave frozen-phonon calculation, shell-model lattice dynamics, and specific-heat measurement of SnO. Physical Review B 1999, 60(21), 14496.

[36] Ziman, J. M. Principles of the Theory of Solids, Cambridge University Press 1972, London, 2nd edn, 211–229.

[37] Daeneke, T.; Atkin, P.; Orrell-Trigg, R.; Zavabeti, A.; Ahmed, T.; Walia, S.; Liu, M.; Tachibana, Y.; Javaid, M.; Greentree, A.D.; Russo, S.P. Wafer-scale synthesis of semiconducting SnO monolayers from interfacial oxide layers of metallic liquid tin. ACS nano 2017, 11(11), 10974-10983.

[38] Singh, M.; Della Gaspera, E.; Ahmed, T.; Walia, S.; Ramanathan, R.; van Embden, J.; Mayes, E.; Bansal, V. Soft exfoliation of 2D SnO with size-dependent optical properties. 2D Materials 2017, 4(2), 025110.

4

Superlattice of SnO-PbO: A New Material for Thermoelectric Applications

4.1 Introduction

The thermoelectric (TE) energy conversion technology has attracted much attention in the past decade.[1,2] The efficiency of thermoelectric devices can be described by a dimensionless quantity called figure of merit, $zT=\frac{S^2\sigma}{\kappa}T$, where S, σ, κ, T are the Seebeck coefficient, electrical conductivity, total thermal conductivity, and absolute temperature, respectively. The power factor is defined by the quantity, $S^2\sigma$. Ideally, to increase the figure of merit (zT), both the Seebeck coefficient and electrical conductivity must be increased, while thermal conductivity must be minimized simultaneously.[3-5] Interestingly, their interdependent relationship among the physical parameters makes challenging to develop an effective approach to enhance the zT value. Toward the development of efficient TE material, the crucial challenge is to balance those coupled parameters to optimize both electrical and thermal transport properties.[6,7]

In literature, there are various approaches to improve zT, such as modifying band structure,[8,9] band convergence,[10,11] combination of flat bands (high effective mass) and dispersive bands (low effective mass) in electronic band structure to increase the power factor (PF). On the other side, several phonon-engineering strategies have been employed in semiconductors, such as, large anharmonicity,[12-14] large molecular weight,[15,16] complex crystal structure,[17] charge density distortion,[18] nanostructuring, (PbTe,[19-21] half-Heusler,[22-24]), rattling modes (skutterudites,[25,26] clathrates[27]) to reduce thermal conductivity.

To date, there are numerous bulk materials with high zT value, which have been synthesized containing nano-structured alloys namely, BiSbTe,[28] filled skutterudites,[29] Tl doped PbTe[30] etc. However, they lose chemical and thermal stability in air. Also, most of the developments are centered on the p-type materials, while n-type thermoelectric materials are only a few with quite low thermoelectric efficiency. For p-type semiconductors, it is easy to tune in the band structure so that there are heavy hole and light hole regions due to weak bonding features in these classes of systems. Nano-structuring gives rise to lower thermal conductivity either due to entropic or enthalpic routes,[31] however, long term use of the materials remains a challenge.

On the other hand, there exist a large number of oxide materials with an exponentially large number of crystal structures, which have been used in various devices and phenomena, namely, solid-state devices, p-n junctions, electrical, magnetic, electromagnetic, multiferroic to magneto-resistance and superconductivity. These oxides are robust in respect of large-scale application due to their low toxicity, affordable cost and good stability in air. As a result, thermoelectric (TE) oxides would play an important role in extensive applications to convert wasted heat into electricity over heavy metallic alloys due to their superior chemical and thermal robustness. Many oxides are also light in weight and eco-friendly which are suitable for commercial applications for energy harvesting devices.

However, in general, TE oxides are known to exhibit low figure of merit (zT) because of the light atomic weight of oxygen leading to large lattice thermal conductivity. Interestingly, high ionic character of oxygen also induces lower carrier mobilities and conductivities.[32,33] Till now, several promising families of TE oxide materials have been discovered, including $Sr_{0.9}La_{0.1}TiO_{3\text{-}\delta}$ ($\kappa_{lat} \simeq 3.0$ W/mK, $zT \simeq 0.21$ at 750 K),[34] $In_{1.8}Ge_{0.2}O_3$($\kappa_{lat} \simeq 2.0$ W/mK, $zT \simeq 0.46$ at 1273 K),[35] $Ca_{0.9}Yb_{0.1}$ MnO_3($\kappa_{lat} \simeq 1.6$ W/mK, $zT \simeq 0.16$ at 1000 K), BiCuSeO ($\kappa_{lat} \simeq 0.4$ W/mK, $zT \simeq 0.5$ at 900 K)[27]. These materials still show very low zT value which is mainly either due to moderate electrical conductivity or high thermal conductivity. In addition, LaAgSO forms a layered crystal structure with conductive AgS layers and LaO as a charge reservoir, both being mutually separated. Due to less carrier concentration, this oxide material does not show a good thermoelectric figure of merit.[36] However, metal oxide has recently been shown great achievement as thermoelectric material due to the complex crystal structure or lattice anharmonicity driven by lone pairs.[32,33]

On the basis of crystal symmetry and lattice anharmonicity driven by the stereoactive lone pairs along the crystallographic c-direction, we propose a new layered oxide material: superlattice of SnO and PbO (SnO-PbO) as a thermoelectric complex. Experimentally, Kwestroo et al.[37] was able to synthesize up to 40% mole fraction Sn content in SnO-PbO solid solution in the liquid phase. However, we consider the composition of SnO-PbO superlattice ($Sn_{0.5}Pb_{0.5}O$) in our theoretical model and optimize the lattice parameters. In fact, we explored other possible configurations with random occupation of Sn and Pb atoms at particular crystallographic sites. The adopted optimized crystal was not only energetically the lowest one, rather other possible configurations were dynamically unstable. These complex forms crystal structure like layered ZrCuSiAs type with tetragonal unit cell a = b = 3.87 $\mathring{A}$, c = 10.05 $\mathring{A}$ and the space group P4/nmm. It exhibits a two-dimensional layered structure containing Sn and Pb layers connected by Oxygen atoms. Each Sn and Pb atom bonded with oxygen atoms makes a prism-like structure. The stereoactive lone pair associated with $Sn^{2+}(5s^2)$ and $Pb^{2+}(6s^2)$ induces charge distribution anisotropy in the system along the stacking direction. As we will describe below, these inhomogeneous bonding characteristics along the in-plane direction and weak van der Waals interactions along the out of plane direction is the key reason to achieve high zT value in such oxide materials.

4.2 Theoretical Section

4.2.1 First principle simulations

We perform first-principles based density functional theory calculations as implemented in the Quantum Espresso package[38] that employs the pseudopotential model considering the interaction between ionic core and valence electrons in an atom. We use scalar relativistic norm-conserving pseudopotentials as exchange-correlation energy of the electrons with generalized gradient approximated (GGA)[39] functional parametrized by Perdew, Burke, Erzenhoff (PBE).[40] The electronic wave function and charge density cutoff in plane-wave basis are considered to be 70 Ry and 280 Ry, respectively. Brillouin zone integration of tetragonal crystal structure is sampled on the uniform grid of 20 x 20 x 10 k-points. The sharp discontinuity of the electronic states near the bandgap is smeared out with the Fermi-Dirac distribution function with broadening of 0.003 Ry.

We consider two layers of SnO in the tetragonal unit cell where two Sn sublayers are connected by a covalent bond with the oxygen atoms within a single layer forming bi-prism like structure. Then we substitute Pb in place of Sn at the two adjacent layers and optimize the crystal structure until the magnitude of Hellman-Feynman force on each atom is less than 0.025 $\frac{eV}{\mathring{A}}$. Then, we determine the electronic band structure with the optimized lattice parameter a = 3.87 $\mathring{A}$, b

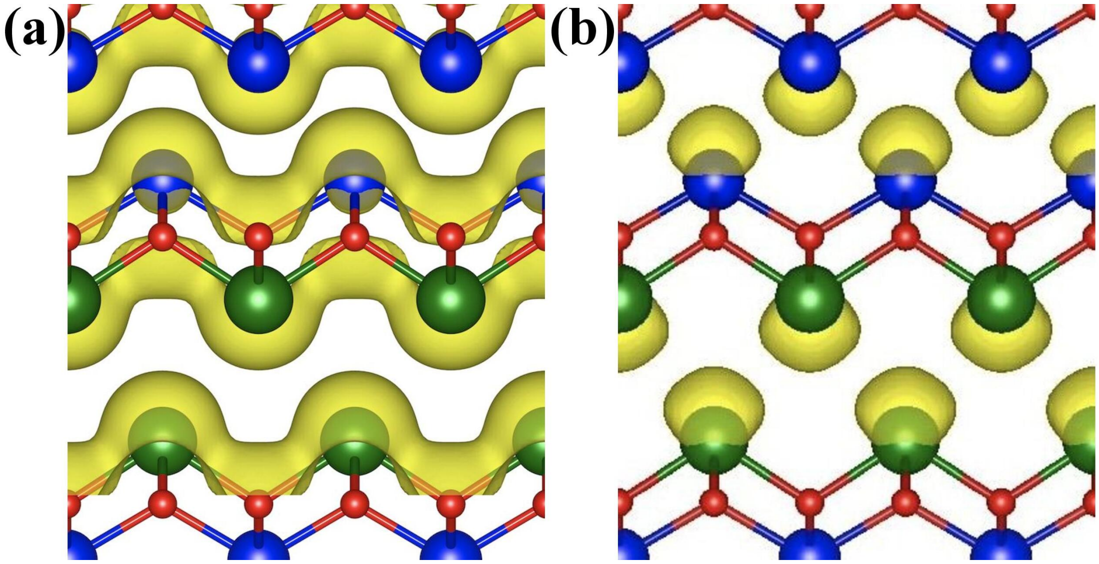

Figure 4.1: Crystal structure of SnO-PbO. (a) Total charge density plot. (b) Electron localization function (ELF) calculated with DFT visualized at the iso-surface value of 0.9, reveals the presence of lone pairs around Sn and Pb atoms. Here, colour coding of the atoms are as follows, Blue: Sn, Green: Pb and Red: O atoms.

$= 3.87\ \mathring{A}$ and c $= 10.05\ \mathring{A}$ considering 20 x 20 x 10 Monkhorst-Pack *k*-mesh. Our SnO-PbO unit cell contains 8 atoms in it where 2 Sn, 2 Pb, 4 O atoms are present in the unit cell. The incorporation of PBE-D2(3) van der Waals (vdW) corrections reduces lattice parameters along the stacking direction by 0.07 Å. In fact, the calculations using the PBE functional along with D3 van der Waals corrections reproduced the experimental cell parameters within acceptable deviations.[37] To justify our theoretical parameters, we have compared optimized lattice parameter for SnO and PbO with their experimental value and we observe equilibrium lattice parameter matches fairly well with experiments. After testing the theoretical parameters for SnO and PbO, we devise similar parameters for SnO-PbO superlattice. Finally, to observe the effect of spin-orbit coupling (SOC) in band structure, we adopt SOC in our calculations. Interestingly, we find that the effect of SOC in band dispersion is negligibly small. As a consequence, the band dispersion curve does not get much affected because of the inclusion of spin-orbit coupling.

4.2.2 Ab-initio Molecular dynamics simulation

To access the thermal stability, we have also performed ab-initio molecular dynamics (AIMD) simulations at 300 K, 500 K, and 700 K as implemented in Vienna Ab initio Simulation Package (VASP)[67-68]. We consider generalized gradient approximated (GGA) exchange-correlation functional[69] with a uniform grid of 6 × 6 × 6 *k*-mesh and an energy cutoff of 50 Ry. We also consider 2 x 2 x 2 supercell (32 atoms) for molecular dynamics studies. The plane-wave basis set, scalar relativistic pseudopotentials, and projected augmented wave (PAW)[70] methods were adopted for molecular dynamics simulations. The Nose–Hoover thermostat and barostat[71-72] were used to evaluate the equilibrium dynamics under the NPT ensemble. Equilibrium dynamics were maintained for 50 ps with a time step of 1 fs after the equilibrium spanning of the first 10 ps.

4.3 Results and Discussion

We use first-principles density functional theory (DFT) to study thermoelectric properties of a new oxide material, SnO-PbO superlattice in layered crystal form. The tetragonal crystal structure of SnO-PbO (shown in Figure 4.1) consists of both ionic and covalent bonding features like other oxide materials.[32] The oxidation state of Sn, Pb, O are +2, +2, -2, respectively, which makes the compound valence balanced and we find that it possesses small finite band gap near the Fermi level.

Total charge density plot in Figure 4.1(a) shows overlapping of charge clouds between Sn-O atoms and Pb-O atoms, implying the presence of covalent bonding in the ab-plane. The charge associated with Sn, Pb atoms in out of plane direction (in $5s^2$ and $6s^2$ lone pairs, respectively), leads to weak van der Waals (vdW) interaction between two adjacent layers. This weakly interacting vdW forces between the adjacent layers along c-direction motivate us to analyze the bonding characteristics more rigorously.

To investigate accurately the chemical bonding nature, we introduce a real space descriptor of charge density calculated using density functional theory. The total charge density plot (Shown in Figure 4.1(a)) shows overlapping of charge clouds within the layer, resulting in covalent bonding between Sn-O and Pb-O. On the other hand, the electron localization function (ELF) reveals lone pairs around the Sn and Pb atoms. Interestingly, we find that the lone pair associated with Sn^{2+} and Pb^{2+} ions occupy interstitial spaces between adjacent layers (Shown in Figure 4.1(b)). These lone pairs interact weakly within the layers and induce lattice anharmonicity which can be explained by projected DOS calculations.

For understanding the bonding characteristics and atomic level dynamics more rigorously, we perform potential energy surface calculations (Figure 4.2(a)) for each atom by displacing them along each crystallographic direction from their equilibrium position. The deep energy well of Sn and Pb along out of plane (z-axis) direction suggests that they are tightly bound to the crystallographic sites, whereas shallow potential curve of Sn and Pb along the in-plane direction (xy-plane) indicates that they are relatively loosely bonded and can vibrate more easily and scatter heat-carrying acoustics phonons. In contrast, oxygens are relatively uniformly bonded with the surrounding atoms, making the layered crystal structure stabilized. The inhomogeneity in bonding characteristics arising due to non-uniformity among the bound heavy metals influences adversely the phonon dynamics and in turn reduces lattice thermal conductivity significantly.

The crystal orbital Hamiltonian population (COHP)[46] analysis method allows us to consider band energies as a pairwise orbital contribution from various pairs of chemical bonds. To study the chemical bonding nature of different pairs, we perform COHP analysis using the LOBSTER code[47] as a post-processing tool along with the Quantum Espresso package. Our calculation shows that COHP value (Figure 4.2(b)) associated with nearest-neighbour Sn-O bonding is higher

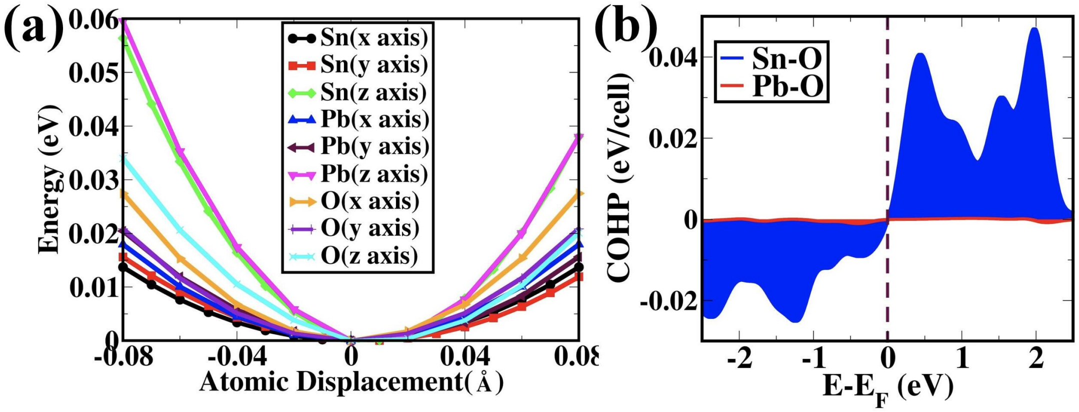

Figure 4.2: (a) Potential energy surface of individual constituent atoms as a function of displacement from an equilibrium position along with the three crystallographic directions. (b) COHP plot for Sn-O bonding (blue) and Pb-O bonding (red). The negative value of (COHP) signifies orbital overlapping between two atoms that are bonding in nature below the Fermi level and stabilizes the crystal structure.

with respect to nearest-neighbour Pb-O bonding. This leads to more orbital overlapping between Sn:5p and O:2p than between Pb:6p and O:2p orbitals near the Fermi level. The relatively large COHP value between Sn-O bonding below the Fermi level confirms the fairly strong chemical bonding strength for Sn-O interaction than for Pb-O. We have further verified the bonding strength between the metal-oxygen bonding by calculating Integrated COHP (ICOHP). The parameter (ICOHP) measures degree of covalency or bonding strength, which has been computed by integrating COHP within the integration limit below the Fermi level from -2.5 eV to Fermi energy (0.0 eV; scaled). Our computed ICOHP values turned out higher for Sn-O than Pb-O that suggests bonding strength between Sn-O orbitals is reasonably stronger than Pb-O. The dissimilar degree of covalency appearing due to variability in bonding strengths, which in turn leads to the decrease in lattice thermal conductivity of SnO-PbO superlattice.

Furthermore, SnO-PbO is found to be a multiband material with an indirect bandgap of 0.2 eV in the bulk. Interestingly, the top of the valence band consists of multiple hole pockets located along K ⟶ Z symmetry group direction (shown in

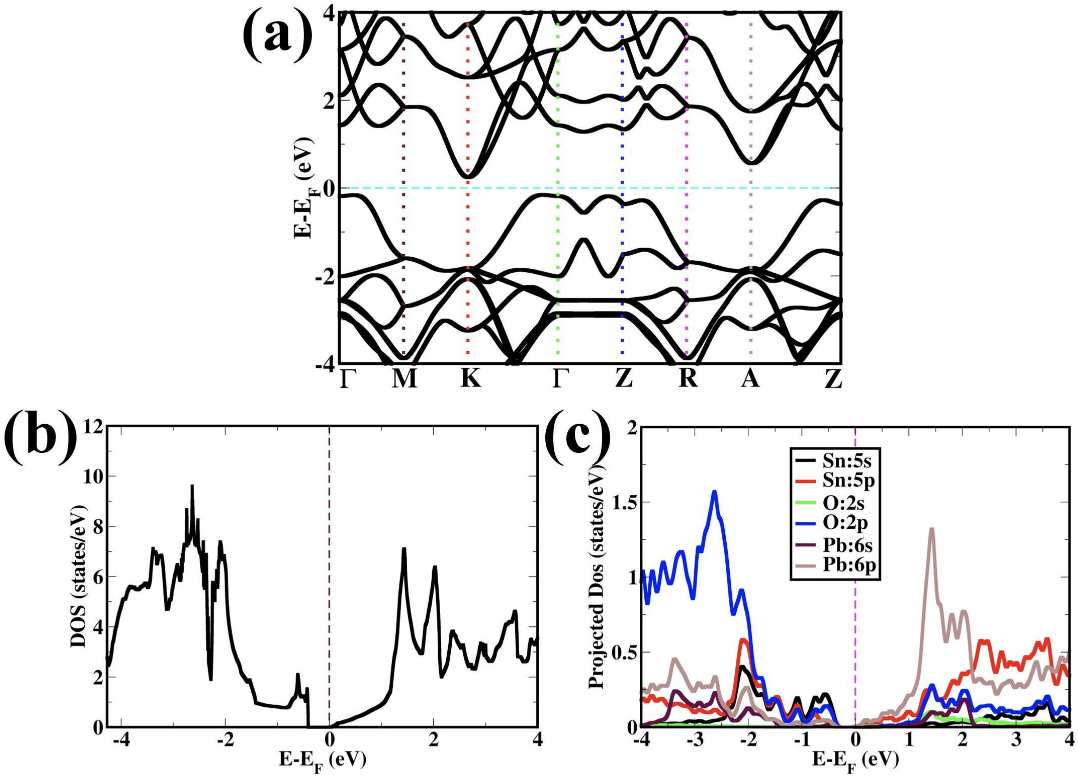

Figure 4.3: (a) Calculated electronic band structure along the special k-point in the Brillouin zone. The DFT band gap turns to be 0.2 eV. The multivalley degenerate valence band is dispersive in nature along the $\Gamma \longrightarrow K$ and $Z \longrightarrow R$ direction. (b) The total DOS is drawn. The sharp peak in the valence band signifies the bands to be flat and non-dispersive in nature that is required to increase Seebeck coefficient. (c) The atom projected density of states (pDOS) shows the valence band edges are dominated by Sn:5s lone pair orbital and O:2p, while conduction band edge consists of states derived from Pb:6p and Sn:5p orbitals.

Figure 4.3(a)) near the Fermi level. A large number of band valleys N_v present in electronic band dispersion is another strategy to obtain a high power factor in such materials. Here, N_v is the effective total number of carrier pockets or valleys in the Brillouin zone containing both orbital and symmetry-related degeneracy. Such materials consisting of multi-valley bands exhibit higher electrical conductivity, while Seebeck coefficients remain the same.[48]

To achieve high Seebeck coefficient at a given carrier concentration, one has to increase band effective mass value (m_b^*) which is obtained as the second derivative of the energy dispersion curve. Thus, the band effective mass can be enhanced by an increase in the number of degenerate bands or by flat or nearly flat bands near the Fermi level. Interestingly, the DOS effective mass and band effective mass are related via $m_d^* = N_v^{\frac{2}{3}} m_b^*$, where N_v is the number of band valleys and subscripts in mass indicate DOS (d) or band (b) effective mass.

The DOS for the SnO-PbO is shown in Figure 4.3(b) where we observe the sharp peak in DOS in the valence band, which appears due to the flat band at Γ point. Moreover, the electronic DOS is highly asymmetry in nature near the Fermi level, resulting in the large value of Seebeck coefficient.[49] According to pisarenko plot in the degenerate limit, the relationship between Seebeck coefficient (S) and DOS effective mass (m_d^*) can be described as $S = \frac{2k_B^2 T}{3e\hbar^2}(\frac{\pi}{3n})^{\frac{2}{3}} m_d^*$. The presence of multiple nondispersive bands in the valence band below the Fermi level are responsible for high Seebeck coefficient in p-type (Pb,Sn)S solid solution.[50] Likewise, we also observe flat bands along with asymmetry nature in DOS near Fermi level that helps to enhance Seebeck coefficient in SnO-PbO superlattice.

Bilc et al.[51] have demonstrated that high power factor (PF) along the band dispersion direction can be expected when flat and dispersive bands present together. In this case, the flat band is found at Γ point and highly dispersive bands are present along with $\Gamma \longrightarrow K$ and $\Gamma \longrightarrow M$ directions in the Brillouin zone (see Figure 4.3(a)). Because of such a unique nature of band dispersion relation, SnO-PbO could be considered as an efficient thermoelectric oxide material.

To further understand the orbital contribution toward the band dispersion, we analyze projected DOS (pDOS) in Figure 4.3(c). It is found from the pDOS that valence bands are mostly contributed from O:2p and Sn:5s orbitals. Effective contribution from Pb orbitals is minimum to valence band below the Fermi level. We also identify that the bottom of the conduction bands is dominated by Sn:5p and Pb:6p orbitals. Due to such dispersive nature of the valence bands, hole conductivity is expected to be higher in the SnO-PbO complex. Moreover, we find that overlapping of the lone pair orbital with of Sn:5s^2 and Pb:6s^2 have different bonding nature with nearby O-2p orbital. In fact, there is significant orbital overlapping of Sn:5s^2 with O-2p in the valence band region below Fermi level, while Pb:6s^2 does not have orbital overlapping with O-2p. The dissimilar orbital overlapping introduces bonding inhomogeneity inside the crystal which leads to lattice anharmonicity at high temperatures.

It is a widely known fact in DFT formalism that the GGA exchange-correlation functional underestimate the bandgap of the material. Therefore, we use hybrid functionality along with GGA to obtain the correct value of the bandgap. We determine the bandgap of SnO-PbO to be 1.13 eV using hybrid functional calculations (HSE06).[52,53] Since the bandgap calculated within hybrid functional overestimate to some extent, we can expect the actual bandgap to be within GGA and HSE06 predicted values. The moderate to high electronic bandgap is an essential procedure to suppress bipolar thermal conductivity, especially at elevated temperatures. Previously, it was found that bipolar thermal conductivity plays a significant role in Bi_2Te_3,[54] PbTe,[55] SnTe,[56] etc. which not only increases the total thermal conductivity, it deteriorates the Seebeck coefficient as well. The sole reason behind the large bipolar diffusion conductivity is because of their narrow electronic bandgap. That's the reason, one effective approach to enlarge the bandgap would be to alloy high bandgap candidate, PbO, within narrow bandgap material, SnO, which is the case here. Likewise, similar studies have also been performed in the literature as MnTe alloying in SnTe,[57] PbS alloying in PbSe,[58] MgTe alloying in PbTe,[59] to name a few.

To uncover the origin of relatively low thermal conductivity, we carry out first-principles density functional perturbation theory (DFPT) to calculate phonon dispersion in the first Brillouin zone. Our phonon dispersion study reveals that SnO-PbO is dynamically stable layered three-dimensional material (see Figure 4.4(a)). To further check the stability of SnO-PbO superlattice, We compute formation energy ($F.E$) using the equation ($F.E = E(SnO-PbO) - E(SnO) - E(PbO)$) which

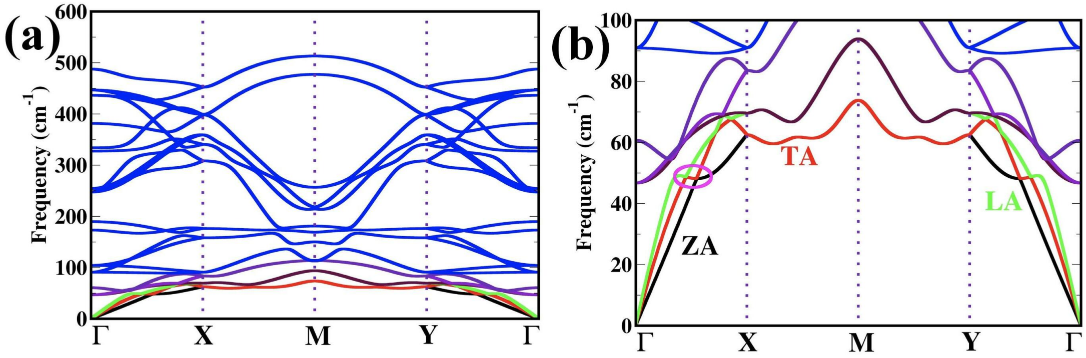

Figure 4.4: (a) Calculated phonon dispersion of SnO-PbO. Here, positive phonon frequencies suggest the complex is dynamically stable with regards to small atomic displacement. (b) Highlighted acoustics phonon modes along with a few low energetic optical phonons. The circle shown in the figure indicates avoided crossing among the acoustics branches and sometimes with optical branches.

turns out to be -0.097 eV per formula unit. The negative value of formation energy additionally confirms the stability of the SnO-PbO complex system. Additionally, we further check the thermal stability of the adopted SnO-PbO crystal structure. Therefore, we perform AIMD simulation at various temperatures (T=300 K, 500 K, 700 K). Equilibrium dynamics were maintained for 50 ps with a time step of 1 fs after the equilibrium spanning of the first 20 ps. Thermodynamic parameters, such as, temperature (T), Gibbs free energy (G), Total energy (E), and potential energy (V) have been plotted as a function of AIMD time steps. During the AIMD simulation, we observe that SnO-PbO superlattice does not break chemical bonds with the increasing temperatures. Actually, it only varies the lattice parameters along with atomic bond length and bond angles. Our AIMD simulation reveals that SnO-PbO superlattice is thermally stable.

In the phonon spectrum, there are three acoustics modes (shown in Figure 4.4(b)), which are mainly accountable for heat conduction and which have frequencies around 48 cm^{-1} along the X and Y (a,b-axis). The low-frequency acoustics mode indicates small group velocity at the zone center Γ-point (Shown in Table 4.1) and low Debye temperature, which in turn facilitates low thermal conductivity, κ_{lat}, along the in-plane direction (e.g., according to Debye-Callaway (DC) model[60]). The predicted Debye characteristic temperature turns out to be 24 K for SnO-PbO. Comparatively, the very low value of Debye temperature indicates the presence of Umklapp inelastic scattering along with normal scattering, which generates thermal resistance, reducing thermal conductivity. In addition, we also observe avoided crossing between the acoustics phonons in the dispersion curve (shown by magenta color ellipse in Figure 4.4(b)).[73] The Landau quasi-degeneracy or avoided crossing leads to adverse effects on the phonon dynamics. In fact, the lattice thermal conductivity κ_{lat} is related to phonon group velocity via $\kappa \simeq \frac{1}{3}Cv_g^2\tau$, where C is the specific heat at constant volume, v_g is phonon group velocity, and τ is relaxation time of phonons. Since the average phonon group velocity is small, κ_{lat} is expected to be very low along the in-plane directions.

Table 4.1: Average phonon group velocity (v_m), Debye temperature (Θ_D) calculated using the equation from Ref. 74.

Materials	$v_m(m/s)$	$\Theta_D(K)$
SnO	920	65
PbO	724	50
SnO-PbO	423	24

According to DC model,[60] the point defect in a solid solution emanates from (a) the mass differences $\simeq$ 88.49 amu of constituent elements (Sn $\simeq$ 118.71 amu and Pb $\simeq$ 207.2 amu) and (b) interatomic coupling force differences due to size variations i.e 0.4 (Sn $\simeq$ 1.4 $\mathring{A}$ and Pb $\simeq$ 1.8 $\mathring{A}$). These point defects scatter low energy acoustics phonons, which further reduces thermal conductivity.

4.3.1 Transport coefficient calculations

The performance of semiconducting materials is not only governed by the electronic band gap, but also controlled by carrier mobility. In this regard, we employ

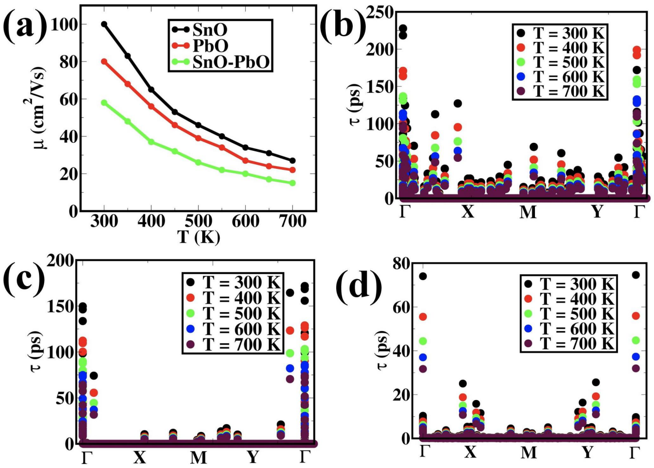

Figure 4.5: (a) Temperature-dependent mobility for layered form of bulk SnO, bulk PbO and bulk SnO-PbO. (b) Phonon lifetime of SnO (c) Phonon lifetime of PbO at various temperatures is shown. (d) Mode phonon lifetime for SnO-PbO. Comparing phonon relaxation time of SnO, PbO, SnO-PbO, calculated using DPT based BTE formalism, it has been observed that phonon lifetime τ for SnO-PbO is comparatively lower than that of SnO and PbO, although carrier scattering states are more for SnO. The lower value of phonon lifetime is the reason to achieve ultralow lattice thermal conductivity in SnO-PbO.

a phonon limited scattering model to correctly predict charge carrier mobility in layered material. Similarly, we have also determined temperature dependent phonon transport coefficients using Boltzmann Transport Equation (BTE) within constant relaxation time approximation (RTA). Our adopted deformation potential theory (DPT) coupled with Boltzmann transport theory is reasonably good to envisage transport coefficient for linearly dispersive layered materials.[41] In fact, many researchers have been studying DPT to calculate transport coefficient in various 3D layered systems. In addition, we also have verified our computationally predicted results with the pre-existing experimental as well as other theoretical results of both bulk forms of SnO and PbO, separately. The charge carrier mobility obtained using DPT along the in-plane directions for bulk layered form of SnO and PbO compare fairly well with the experimental results.[61-64] This validation motivates us to study DPT based BTE formalism for newly explored SnO-PbO layered crystal structure as thermoelectric applications.

Table 4.2: Deformation potential constant (eV) and elastic constant (10^{11} Jm^{-3}) parameters for hole. Effective mass in unit of m_0 for hole calculated from band curvatures along $\Gamma \longrightarrow K$ directions in the reciprocal space.

Materials	SnO	PbO	SnO-PbO
E_1	3.77	2.57	2.51
C_{3D}	85.5	56.7	35.5
m*	0.07	0.08	0.14

Carrier mobility calculations of electrons and holes have been carried out using equation (1.13) and plotted as a function of temperatures (Shown in Figure 4.5(a)). While performing mobility calculations, we only consider charge-phonon scattering. Ideally, there are various scattering mechanisms involved in the real material such as charge carrier-charge carrier scattering, scattering from impurity and crystal defects, scattering of charges from thermal vibrations of the ions or charge carrier-phonon scattering and boundary scattering. However, at high temperature, the charge carrier-phonon scattering is the dominating one in the case of semiconductors. Because of that, we neglect impurity scattering, boundary scattering and carrier-carrier scattering which has much smaller contribution to the overall scattering compared to the thermal vibration of the ions. Especially, the mobility expression requires information about direction dependent carrier effective mass ($m^*_{\frac{e}{h}}$) and deformation potential constant ($\mathrm{E_1}$) along with elastic constant ($\mathrm{C_{3D}}$). Using the parameters mentioned in Table 4.2, we compute carrier mobility for the layered structure of bulk SnO, bulk PbO and bulk SnO-PbO superlattice along the in-plane directions. Interestingly, the carrier mobility for SnO-PbO superlattice is lower in magnitude than the same in SnO and in PbO individually, due to the carrier-carrier scatterings and higher carrier effective mass in the former (Shown in Table 4.2). Once carrier mobility values are known, we have used the Drude model $\sigma = ne\mu^{\frac{e}{h}}$ to evaluate charge carrier electrical conductivity (σ) along the $\Gamma \longrightarrow K$ direction. Figure 4.5(a) represents the variation of total charge carrier mobility for bulk SnO, bulk PbO, and bulk SnO-PbO layered complexes as a function of temperatures. The temperature dependent mobility values eventually determine the charge carrier electrical conductivity of TE materials.

We have also incorporated DPT based BTE to quantify lattice thermal conductivity κ_{lat} using the equation (1.16). Here, lattice thermal conductivity depends on specific heat (C), phonon group velocity (v_g) and phonon relaxation time (τ). Phonon group velocities are calculated via formula $v_{iq} = \frac{\nabla E_{iq}}{h}$. Finally, we have calculated lattice thermal conductivity (κ_{lat}) for bulk SnO, bulk PbO and bulk SnO-PbO. Interestingly, the estimated κ_{lat} for SnO calculated within RTA is well consistent with previous theoretically predicted results as well as experimental results.[64,65] The phonon lifetime which are needed to evaluate lattice thermal conductivity for bulk SnO, bulk PbO and bulk SnO-PbO, are shown in Figure 4.5(b), 4.5(c) and 4.5(d), respectively. Using the phonon group velocity along with phonon-phonon scattering rates, we estimate lattice thermal conductivity of SnO, PbO and SnO-PbO. Interestingly, lattice thermal conductivity obtained using DPT based BTE formalism compares fairly closely with the lattice thermal conductivity values determined through an iterative method. Eventually, our adopted methodology opens up a new simple mechanism to enumerate complex lattice thermal conductivity for layered materials in an efficient way. Finally, κ_{lat} for SnO, PbO and SnO-PbO have been calculated and plotted in Figure 4.6(c) at room temperature till up to 700 K. In this regard, κ_{lat} reaches minimum value 0.71 W/mK at 700 K. The reason behind the ultralow thermal conductivity, even smaller than the PbO, is in fact due to the presence of heavy metal, occurrence of avoided crossing in the phonon dispersion curve and presence of point defect due to lattice mismatch.

Another important parameter which determines the efficiency of good thermoelectric material is Seebeck coefficient (S). The temperature dependent Seebeck coefficient for SnO, PbO and SnO-PbO are drawn in Figure 4.6(a). In this con-

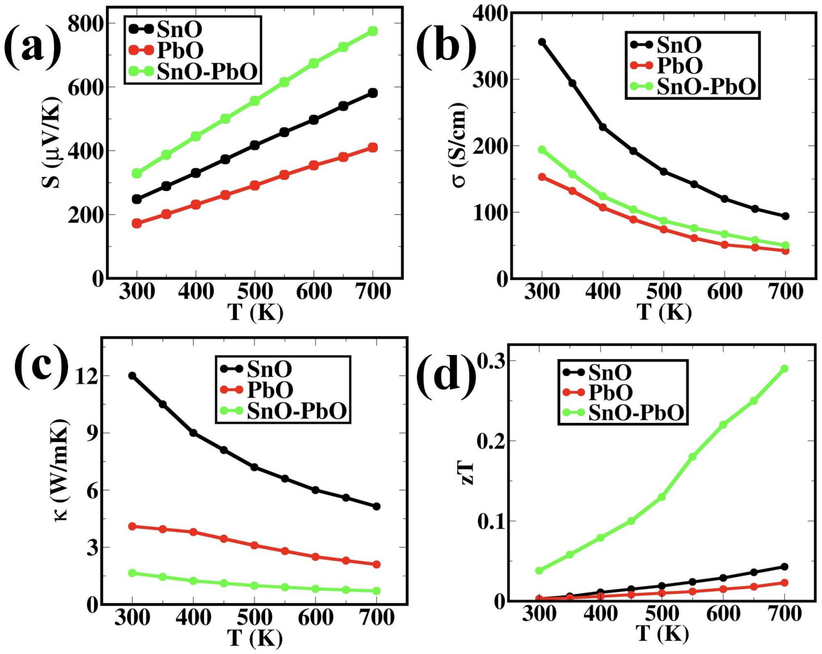

Figure 4.6: (a) Seebeck coefficient, (b) electrical conductivity, (c) lattice thermal conductivity, (d) zT, as a function of temperatures have been drawn. The sharp rise in value of $zT \simeq 0.3$ at temperature 700K has been achieved in SnO-PbO layered material.

text, S has been calculated using the equation, (1.15). Seebeck coefficient for SnO-PbO increases with the temperature at a much higher rate than for SnO and PbO individually, which is attributed due to the sharp peak in the valence band of DOS.

Figure of merit, zT, has been calculated based on the electrical and thermal transport properties at different temperatures (Figure 4.6(d)). Interestingly, our theoretically predicted zT value for SnO is well consistent with previous results.[64,66] In fact, we achieved the increasing trend in zT 0.3 value at 700 K for SnO-PbO superlattice. The main point of the attainment of such higher zT values for SnO-PbO compared to SnO and PbO respectively, signifies towards the cooperativity and such cooperativity may be exploited by making stable superlattice of various other oxide materials. After all, any oxide material with high zT value would be a boon for mankind.

4.4 Conclusions

In this chapter, we have described that a superlattice of SnO-PbO could be a TE oxides depending upon the doping type and compositions. Our results also indicate that this complex is dynamically as well as thermodynamically stable at both ambient and higher temperatures. All the calculations have been carried out based on first principles lattice dynamics and DPT based Boltzmann transport equations within RTA. It shows high Seebeck coefficient and low thermal conductivity, compared to its component oxides. We also use Boltzmann transport theory to calculate lattice thermal conductivity at various temperatures. The localized lone pair induced charge anisotropy and bonding inhomogeneity are the reason for reduction of the lattice thermal conductivity in this air-stable TE oxide. Our methodology to predict transport coefficient at various temperatures provides a new mechanism (DPT based BTE) to understand thermoelectricity rigorously and directs to design oxide superstructures as next generation thermoelectric materials.

4.5 References

[1] Tan, G.; Zhao, L. D.; Kanatzidis, M. G. Rationally designing high-performance bulk thermoelectric materials. Chemical reviews 2016, 116, 12123-12149.

[2] Zhu, T.; Liu, Y.; Fu, C.; Heremans, J. P.; Snyder, J. G.; Zhao, X. Compromise and synergy in high-efficiency thermoelectric materials. Advanced materials 2017, 29, 1605884.

[3] Zhao, L.D.; Lo, S.H.; Zhang, Y.; Sun, H.; Tan, G.; Uher, C.; Wolverton, C.; Dravid, V.P.; Kanatzidis, M.G. Ultralow thermal conductivity and high thermoelectric figure of merit in SnSe crystals. Nature 2014, 508, 373-377.

[4] Zhao, W.; Liu, Z.; Sun, Z.; Zhang, Q.; Wei, P.; Mu, X.; Zhou, H.; Li, C.; Ma, S.; He, D.; Ji, P. Superparamagnetic enhancement of thermoelectric performance.

Nature 2017, 549, 247-251.

[5] Chang, C.; Wu, M.; He, D.; Pei, Y.; Wu, C.F.; Wu, X.; Yu, H.; Zhu, F.; Wang, K.; Chen, Y.; Huang, L. 3D charge and 2D phonon transports leading to high out-of-plane ZT in n-type SnSe crystals. Science 2018, 360, 778-783.

[6] Zhao, W.; Wei, P.; Zhang, Q.; Peng, H.; Zhu, W.; Tang, D.; Yu, J.; Zhou, H.; Liu, Z.; Mu, X.; He, D. Multi-localization transport behaviour in bulk thermoelectric materials. Nature communications 2015, 6, 1-7.

[7] Zhao, W.; Liu, Z.; Wei, P.; Zhang, Q.; Zhu, W.; Su, X.; Tang, X.; Yang, J.; Liu, Y.; Shi, J.; Chao, Y. Magnetoelectric interaction and transport behaviours in magnetic nanocomposite thermoelectric materials. Nature nanotechnology 2017, 12, 55-60.

[8] Poudel, B.; Hao, Q.; Ma, Y.; Lan, Y.; Minnich, A.; Yu, B.; Yan, X.; Wang, D.; Muto, A.; Vashaee, D.; Chen, X. High-thermoelectric performance of nanostructured bismuth antimony telluride bulk alloys. Science 2008, 320, 634-638.

[9] Harnwunggmoung, A.; Kurosaki, K.; Muta, H.; Yamanaka, S. High-temperature thermoelectric properties of thallium-filled skutterudites. Applied Physics Letters 2010, 96, 202107.

[10] Caillat, T.; Fleurial, J.P.; Borshchevsky, A. Preparation and thermoelectric properties of semiconducting Zn_4Sb_3. Journal of Physics and Chemistry of Solids 1997, 58, 1119-1125.

[11] Hsu, K.F.; Loo, S.; Guo, F.; Chen, W.; Dyck, J.S.; Uher, C.; Hogan, T.; Polychroniadis, E.K.; Kanatzidis, M.G. Cubic $AgPb_{(m)}SbTe_{(2+m)}$: bulk thermoelectric materials with high figure of merit. Science 2004, 303, 818-821.

[12] Ravich, I.I.; Efimova, B.A.; Smirnov, I.A. Semiconducting Lead Chalcogenides. Plenum Press, New York, 1970.

[13] Girard, S.N.; He, J.; Zhou, X.; Shoemaker, D.; Jaworski C.M.; Uher, C.; Dravid, V.P.; Heremans, J.P.; Kanatzidis, M.G. High performance Na-doped PbTe–PbS thermoelectric materials: electronic density of states modification and

shape-controlled nanostructures. Journal of the American Chemical Society 2011, 133, 16588-16597.

[14] Zhao, L.D.; Lo, S.H.; He, J.; Li, H.; Biswas, K.; Androulakis, J.; Wu, C.I.; Hogan, T.P.; Chung, D.Y.; Dravid, V.P.; Kanatzidis, M.G. High performance thermoelectrics from earth-abundant materials: enhanced figure of merit in PbS by second phase nanostructures. Journal of the American Chemical Society 2011, 133, 20476-20487.

[15] Morelli, D.T.; Jovovic, V.; Heremans, J.P. Intrinsically minimal thermal conductivity in cubic I–V–VI_2 semiconductors. Physical review letters 2008, 101, 035901.

[16] Zhou, T.; Lenoir, B.; Colin, M.; Dauscher, A.; Al Orabi; R.A.R.; Gougeon, P.; Potel, M.; Guilmeau, E. Promising thermoelectric properties in $Ag_xMo_9Se_{11}$ compounds ($3.4 \leq x \leq 3.9$). Applied Physics Letters 2011, 98, 162106.

[17] He, J.; Girard, S.N.; Zheng, J.C.; Zhao, L.; Kanatzidis, M.G.; Dravid, V.P. Strong phonon scattering by layer structured $PbSnS_2$ in PbTe based thermoelectric materials. Advanced Materials 2012, 24, 4440-4444.

[18] Clarke, D.R. Materials selection guidelines for low thermal conductivity thermal barrier coatings. Surface and Coatings Technology 2003, 163, 67-74.

[19] Wu, H.J.; Zhao, L.D.; Zheng, F.S.; Wu, D.; Pei, Y.L.; Tong, X.; Kanatzidis, M.G.; He, J.Q. Broad temperature plateau for thermoelectric figure of merit ZT > 2 in phase-separated $PbTe_{0.7}S_{0.3}$. Nature communications 2014, 5, 1-9.

[20] Gelbstein, Y.; Dashevsky, Z.; Dariel, M.P. In-doped $Pb_{0.5}Sn_{0.5}Te$ p-type samples prepared by powder metallurgical processing for thermoelectric applications. Physica B: Condensed Matter 2007, 396(1-2), 16-21.

[21] Gelbstein, Y.; Davidow, J. Highly efficient functional $Ge_xPb_{1-x}Te$ based thermoelectric alloys. Physical Chemistry Chemical Physics 2014, 16, 20120-20126.

[22] Xie, W.; Weidenkaff, A.; Tang, X.; Zhang, Q.; Poon, J.; Tritt, T.M. Recent advances in nanostructured thermoelectric half-Heusler compounds. Nanomateri-

als 2012, 2, 379-412.

[23] Kirievsky, K.; Shlimovich; M., Fuks, D.; Gelbstein, Y. An ab initio study of the thermoelectric enhancement potential in nano-grained TiNiSn. Physical Chemistry Chemical Physics 2014, 16, 20023-20029.

[24] Kirievsky, K.; Gelbstein, Y.; Fuks, D. Phase separation and antisite defects in the thermoelectric TiNiSn half-Heusler alloys. J. Solid State Chem. 2013, 203, 247–254.

[25] Terasaki, I.; Sasago, Y.; Uchinokura, K. Large thermoelectric power in $NaCo_2O_4$ single crystals. Physical Review B 1997, 56, 12685.

[26] Fujita, K.; Mochida, T.; Nakamura, K. High-temperature thermoelectric properties of $Na_xCoO_{2-\delta}$ single crystals. Japanese Journal of Applied Physics 2001, 40, 4644.

[27] Zhao, L.D.; Berardan, D.; Pei, Y.L.; Byl, C.; Pinsard-Gaudart, L.; Dragoe, N. $Bi_{1-x}Sr_xCuSeO$ oxyselenides as promising thermoelectric materials. Appl. Phys. Lett. 2010 , 97, 0921189.

[28] Poudel, B.; Hao, Q.; Ma, Y.; Lan, Y.; Minnich, A.; Yu, B.; Yan, X.; Wang, D.; Muto, A.; Vashaee, D.; Chen, X. High-thermoelectric performance of nanostructured bismuth antimony telluride bulk alloys. Science 2008, 320, 634-638.

[29] Harnwunggmoung, A.; Kurosaki, K.; Muta, H.; Yamanaka, S. High-temperature thermoelectric properties of thallium-filled skutterudites. Applied Physics Letters 2010, 96, 202107.

[30] Heremans, J.P.; Jovovic, V.; Toberer, E.S.; Saramat, A.; Kurosaki, K.; Charoenphakdee, A.; Yamanaka, S.; Snyder, G.J. Enhancement of thermoelectric efficiency in PbTe by distortion of the electronic density of states. Science 2008, 321, 554-557.

[31] Roychowdhury, S.; Biswas, R.K.; Dutta, M.; Pati, S.K.; Biswas, K. Phonon Localization and Entropy-Driven Point Defects Lead to Ultralow Thermal Conductivity and Enhanced Thermoelectric Performance in $(SnTe)_{1-2x}(SnSe)_x(SnS)_x$.

ACS Energy Letters 2019, 4, 1658-1662.

[32] Lamontagne, L.K.; Laurita, G.; Gaultois, M.W.; Knight, M.; Ghadbeigi, L.; Sparks, T.D.; Gruner, M.E.; Pentcheva, R.; Brown, C.M.; Seshadri, R. High thermopower with metallic conductivity in p-type Li-substituted $PbPdO_2$. Chemistry of Materials 2016, 28, 3367-3373.

[33] Miller, S.A.; Gorai, P.; Aydemir, U.; Mason, T.O.; Stevanović, V.; Toberer, E.S.; Snyder, G.J. SnO as a potential oxide thermoelectric candidate. Journal of Materials Chemistry C 2017, 5, 8854-8861.

[34] Liu, J.; Wang, C.L.; Su, W.B.; Wang, H.C.; Zheng, P.; Li, J.C.; Zhang, J.L.; Mei, L.M. Enhancement of thermoelectric efficiency in oxygen-deficient $Sr_{1-x}La_xTiO_{3-\delta}$ ceramics. Applied Physics Letters 2009, 95, 162110.

[35] Bérardan, D.; Guilmeau, E.; Maignan, A.; Raveau, B. In2O3: Ge, a promising n-type thermoelectric oxide composite. Solid State Communications 2008, 146, 97-101.

[36] Palazzi, M.; Jaulmes, S. Structure du conducteur ionique (LaO) AgS. Acta Crystallographica Section B: Structural Crystallography and Crystal Chemistry 1981, 37, 1337-1339.

[37] Kwestroo, W.; van den Biggelaar, J.H.; Langereis, C. The formation of PbO-SnO solid solutions. Materials Research Bulletin 1970, 5, 307-313.

[38] Giannozzi, P.; Baroni, S.; Bonini, N.; Calandra, M.; Car, R.; Cavazzoni, C.; Ceresoli, D.; Chiarotti, G.L.; Cococcioni, M.; Dabo, I.; Dal Corso, A. QUANTUM ESPRESSO: a modular and open-source software project for quantum simulations of materials. Journal of physics: Condensed matter 2009, 21, 395502.

[39] Hua, X.; Chen, X.; Goddard, W.A. Generalized generalized gradient approximation: An improved density-functional theory for accurate orbital eigenvalues. Physical Review B, 55, 16103.

[40] Perdew, J.P.; Burke, K.; Ernzerhof, M. Generalized gradient approximation made simple. Physical review letters 1996, 77, 3865.

[41] Banerjee, S.; Pati, S.K. Charge-transport anisotropy in black phosphorus: critical dependence on the number of layers. Physical Chemistry Chemical Physics, 18, 16345-16352.

[42] Ziman, J.M. Principles of the Theory of Solids, Cambridge University Press, London, 2nd edn, 1972, 211–229.

[43] Lang, H.; Zhang, S.; Liu, Z. Mobility anisotropy of two-dimensional semiconductors. Physical Review B 2016, 94, 235306.

[44] Lee, H. A theoretical model of thermoelectric transport properties for electrons and phonons. Journal of Electronic Materials 2016, 45, 1115-1141.

[45] Lee, H. Thermoelectrics: design and materials. John Wiley Sons, 2016.

[46] Deringer, V.L.; Tchougréeff, A.L.; Dronskowski, R. Crystal orbital Hamilton population (COHP) analysis as projected from plane-wave basis sets. The journal of physical chemistry A 2011, 115, 5461-5466.

[47] Maintz, S.; Deringer, V.L.; Tchougréeff, A.L.; Dronskowski, R. LOBSTER: A tool to extract chemical bonding from plane-wave based DFT. Journal of computational chemistry 2016, 37, 1030-1035.

[48] Zhang, G.; Zhang, Y.W. Thermoelectric properties of two-dimensional transition metal dichalcogenides. Journal of Materials Chemistry C 2017, 5, 7684-7698.

[49] Samanta, M.; Pal K.; Pal, P.; Waghmare, U.V.; Biswas, K. Localized vibrations of bilayer leading to ultralow lattice thermal conductivity and high thermoelectric performance in weak topological insulator n-type BiSe. Journal of the American Chemical Society 2018, 140, 5866-5872.

[50] Hao, S.; Dravid, V.P.; Kanatzidis, M.G.; Wolverton, C. Research Update: Prediction of high figure of merit plateau in SnS and solid solution of (Pb, Sn) S. APL Materials 2016, 4, 104505.

[51] Bilc, D.I.; Hautier, G.; Waroquiers, D.; Rignanese, G.M.; Ghosez, P. Low-dimensional transport and large thermoelectric power factors in bulk semiconductors by band engineering of highly directional electronic states. Physical review

letters 2015, 114, 136601.

[52] Heyd, J.; Scuseria, G.E.; Ernzerhof, M. Hybrid functionals based on a screened Coulomb potential. The Journal of chemical physics 2003, 118, 8207-8215.

[53] Paier, J.; Marsman, M.; Hummer, K.; Kresse, G.; Gerber, I.C.; Ángyán, J.G.; Screened hybrid density functionals applied to solids. The Journal of chemical physics 2006, 124, 154709.

[54] Goldsmid, H.J. Bismuth telluride and its alloys as materials for thermoelectric generation. Materials 2014, 7, 2577-2592.

[55] Xiao, Y.; Wu, H.; Cui, J.; Wang, D.; Fu, L.; Zhang, Y.; Chen, Y.;, He, J.; Pennycook, S.J.; Zhao, L.D. Realizing high performance n-type PbTe by synergistically optimizing effective mass and carrier mobility and suppressing bipolar thermal conductivity. Energy Environmental Science 2018, 11, 2486-2495.

[56] Zhao, L.D.; Zhang, X.; Wu, H.; Tan, G.; Pei, Y.; Xiao, Y.; Chang, C.; Wu, D.; Chi, H.; Zheng, L.; Gong, S. Enhanced thermoelectric properties in the counter-doped SnTe system with strained endotaxial SrTe. Journal of the American Chemical Society 2016, 138, 2366-2373.

[57] Tan, G.; Shi, F.; Hao, S.; Chi, H.; Bailey, T.P.; Zhao, L.D.; Uher, C.; Wolverton, C.; Dravid, V.P.; Kanatzidis, M.G. Valence band modification and high thermoelectric performance in SnTe heavily alloyed with MnTe. Journal of the American Chemical Society 2015, 137, 11507-11516.

[58] Androulakis, J.; Todorov, I.; He, J.; Chung, D.Y.; Dravid, V.; Kanatzidis, M. Thermoelectrics from abundant chemical elements: high-performance nanostructured PbSe–PbS. Journal of the American Chemical Society 2011, 133, 10920-10927.

[59] Zhao, L.D.; Wu, H.J.; Hao, S.Q.; Wu, C.I.; Zhou, X.Y.; Biswas, K.; He, J.Q.; Hogan, T.P.; Uher, C.; Wolverton, C.; Dravid, V.P. All-scale hierarchical thermoelectrics: MgTe in PbTe facilitates valence band convergence and suppresses bipolar thermal transport for high performance. Energy Environmental Science

2013, 6, 3346-3355.

[60] Callaway, J.; von Baeyer, H.C. Effect of point imperfections on lattice thermal conductivity. Physical Review 1960, 120, 1149.

[61] Liang, L.Y.; Liu, Z.M.; Cao, H.T.; Pan, X.Q. Microstructural, optical, and electrical properties of SnO thin films prepared on quartz via a two-step method. ACS applied materials interfaces 2010, 2, 1060-1065.

[62] Caraveo-Frescas, J.A.; Alshareef, H.N. Transparent p-type SnO nanowires with unprecedented hole mobility among oxide semiconductors. Applied Physics Letters 2013, 103, 222103.

[63] Mondal, P.S.; Okazaki, R.; Taniguchi, H.; Terasaki, I. Photo-Seebeck effect in tetragonal PbO single crystals. Journal of Applied Physics 2013, 114, 173710.

[64] Kuwahara, S.; Tanusilp, S.A.; Ohishi, Y.; Muta, H.; Yamanaka, S.; Kurosaki, K. Synthesis of High-Density Bulk Tin Monoxide and Its Thermoelectric Properties. Materials Transactions 2018, 59, 1022-1029.

[65] Wan, W.; Ge, Y.; Liu, Y. Strong phonon anharmonicity and low thermal conductivity of monolayer tin oxides driven by lone-pair electrons. Applied Physics Letters 2019, 114, 031901.

[66] Miller, S.A.; Gorai, P.; Aydemir, U.; Mason, T.O.; Stevanović, V.; Toberer, E.S.; Snyder, G.J. SnO as a potential oxide thermoelectric candidate. Journal of Materials Chemistry C 2017, 5, 8854-8861.

[67] Kresse, G.; Hafner, J. Ab initio molecular dynamics for liquid metals. Phys. Rev. B 1993, 47, 558561.

[68] Kresse, G.; Hafner, J. Ab initio molecular-dynamics simulation of the liquid-metal–amorphous-semiconductor transition in germanium. Phys. Rev. B 1994, 49, 1425114269.

[69] Perdew, J. P.; Burke, K.; Ernzerhof, M. Generalized gradient approximation made simple. Phys. Rev. Lett. 1996, 77, 3865.

[70] Kresse, G.; Joubert, D. From ultrasoft pseudopotentials to the projector

augmented-wave method. Phys. Rev. B 1999, 59, 1758 1775.

[71] Nose, S. A unified formulation of the constant temperature molecular dynamics methods. J. Chem. Phys. 1984, 81, 511519.

[72] Hoover, W. Canonical dynamics: method for simulations in the canonical ensemble. Phys. Rev. A 1985, 31, 16951697.

[73] Biswas, R.K; Pati, S.K. Vibrational spectra of MO (M= Sn/Pb) in their bulk and single-layer forms: role of avoided crossing in their thermodynamic properties. Bulletin of Materials Science 2020, 43, 1-10.

[74] Rathore, E.; Juneja, R.; Culver, S.P.; Minafra, N.; Singh, A.K.; Zeier, W.G.; Biswas, K. Origin of Ultralow Thermal Conductivity in n-Type Cubic Bulk $AgBiS_2$: Soft Ag Vibrations and Local Structural Distortion Induced by the Bi-$6s^2$ Lone Pair. Chemistry of Materials 2019, 31, 2106-2113.

5

Enhancing Thermoelectric Performance in n-type PbTe via Gd doping

5.1 Introduction

A major part ($\simeq 65\%$) of energy in the world gets wasted as heat during conversion. The current technological development allows us to convert this waste heat energy into electricity through the machanism, called thermoelectricity. Thermoelectric materials can directly and reversibly convert waste heat into electricity.[1] Generally, thermoelectric materials are characterized by its dimensionless quantity, figure of merit, zT, which is described as $zT = \frac{S^2\sigma}{\kappa}T$; σ, S and κ are electrical conductivity, Seebeck coefficient, and total thermal conductivity, respectively. While σ is governed by charge carriers mobility in a material, the thermal conductivity is controlled due to both charge carriers (κ_{el}) and lattice vibrations (κ_{lat}). In fact, the thermoelectric descriptors (σ, S, and κ) have a complicated relationship with various material parameters, which limits improvement of zT. Interestingly, most of the improvements in optimizing thermoelectric parameters have primarily been focused on balancing these interdependent descriptors.[1] Several innovative computational strategies, like, electronic band flattening,[2] band convergence,[3] charge carrier optimization,[4] resonant states,[5] band alignment,[6] mobility enhancement,[7] effective mass engineering,[8] slight symmetry reduction[9] etc. have been effectively carried out to enhance the power factor ($S^2\sigma$) of a material.[10] Similarly, lowering the κ_{lat} of materials is achieved through several novel approaches, e.g. phonon scattering by point defects,[11] nano-precipitates,[12] all scale hierarchical phonon scattering,[13] to name a few.

Generally, PbTe as rock-salt structure is well known for its unprecedented p-type thermoelectric performance in the temperature range of 700 – 950 K. In fact, p-type PbTe shows high thermoelectric performance due to its intrinsic low thermal conductivity arising from significant lattice anharmonicity and presence of unique electronic band structure.[14] The valence band (VB) of PbTe comprises of two neighboring bands L and Σ which have very little energy off-set ($\Delta E_{L-\Sigma} =$ 0.15 – 0.20 eV)[14] and thus effective valence band convergence has been achieved in p-type PbTe to improve upon its thermoelectric performance.[3] In contrast, conduction band of PbTe comprises of only a single L band and thus lags behind in comparison to its p-type counterpart.[14] The presence of lower degenerate valleys in the conduction band (CB) as compared to the valence band (VB) generates intrinsically low Seebeck coefficient values and thus poses a greater challenge to improve its n-type thermoelectric performance.[14]

Currently, research on n-type PbTe primarily focuses on optimizing charge carrier concentration and mobility,[15] simultaneously modulating the electronic and thermal properties of a material as seen in PbTe-Cu_2Te, PbTe-AgSbSe_2[16]; enhancing effective mass as in case of $Pb_{0.988}Sb_{0.012}$Te-GeTe, $Pb_{0.98}$ $Ga_{0.02}$Te-GeTe and PbTe-MnTe. Similarly, nano-structuring to reduce κ_{lat} and simultaneously improving electronic structure properties is also observed in In and Sb co-doped PbTe, PbTe-PbS etc.[17] However, simplicity of the conduction band and a large band offset between two neighboring conduction band ($\Delta E_{L-\Sigma} \simeq 0.45$ eV) prohibited n-type PbTe to be as efficient thermoelectric materials as its p-type counterpart.[14]

In this chapter, we emphasize Gd doped PbTe can be used as n-type thermoelectric material in the temperature range of 295 – 823 K.

Experimentally, Gd doped PbTe was synthesized and they have obtained its crystal structure and have carried out thermoelectric measurements. They found that the Gd doping on PbTe increases the n-type carrier concentration to 1.46 x 10^{19} cm^{-3}.

We have carried out a detailed theoretical study on the Gd doped PbTe crystal system. Our density functional theory (DFT) calculations on the electronic structure properties shows that on Gd doping, the principal bandgap at L point opens up along with formation of a non-interacting flat conduction band which increases the band effective mass (m^*). Atom projected electronic density of states (pDOS) reveals that the non-interacting band is contributed from the hybridized state of Gd, which enhances the Seebeck coefficient in Gd doped PbTe. Furthermore, Gd is observed to be preferred in off-centered position in the PbTe lattice due to discordant nature of Gd in the octahedral coordination, which creates significant lattice anharmonicity. Using density functional perturbation theory, we show that phonon dispersion spectra has the presence of low frequency nearly flat optical Kondo like phonon mode. Both these effects, i.e., the presence of locally off-centered Gd in PbTe and the formation of low energy localized Kondo like phonon mode synergistically enhances the scattering of acoustic phonons. This significantly lowers the κ_{lat} to 0.79 W/mK at 735 K. Ultralow κ_{lat} in n-type Gd doped PbTe coupled with the electronic structure modification results in superior thermoelectric performance.

5.2 Theoretical Calculations

First principle based density functional theory (DFT) calculations have been performed to study structural relaxation and electronic structure-property calculations using the Quantum Espresso package.[18] The Kohn-Sham equations are solved using a 70 Ry plane wave basis states with the projected augmented wave (PAW) method[19] and the generalized gradient approximation[20] is employed. The total energy and the ionic forces are converged to within 10^{-8} eV and 0.025 eV/$\mathring{A}$, respectively. A uniform grid of k-mesh in the Brillouin zone of 4000 k-points has been considered for electronic structure calculations. The sharp discontinuity of the electronic states near the Fermi level are smeared out with the Fermi-Dirac distribution function with broadening of 0.003 Ry. We consider 3 x 3 x 3 supercell of PbTe containing 54 atoms ($Pb_{27}Te_{27}$) and one Pb substituted with Gd atom ($Pb_{26}Gd_1Te_{27}$) for electronic structure calculation. In order to incorporate relativistic effects because of the presence of heavy metals in the supercell, we include the spin-orbit coupling (SOC) term in the band structure calculations. Our calculated electronic band dispersion obtained using PBE-SOC functional compares fairly well and is consistent with previous DFT results on controlled PbTe.[21] To access the bond strength and bonding interaction, we execute crystal orbital Hamiltonian population (COHP) analysis between the pairwise orbitals corresponding to Te-Gd atoms in the crystal structure of Gd doped PbTe.

The phonon dispersion calculation of PbTe and Gd-doped PbTe unit cells have been carried out using density functional perturbation theory (DFPT) formalism implemented in Quantum Espresso suite of codes. A strict energy convergence of 10^{-10} eV has been used to obtain phonon frequencies accurately. We calculate phonon group velocity (v_{iq}) using the equation, $v_{iq} = \frac{\nabla E_{iq}}{h}$. For phonon calculations, we have considered a 2 x 2 x 1 supercell (primitive cell of PbTe contains 2 atoms). Therefore, we have obtained the phonon dispersion curve for 8 atoms in

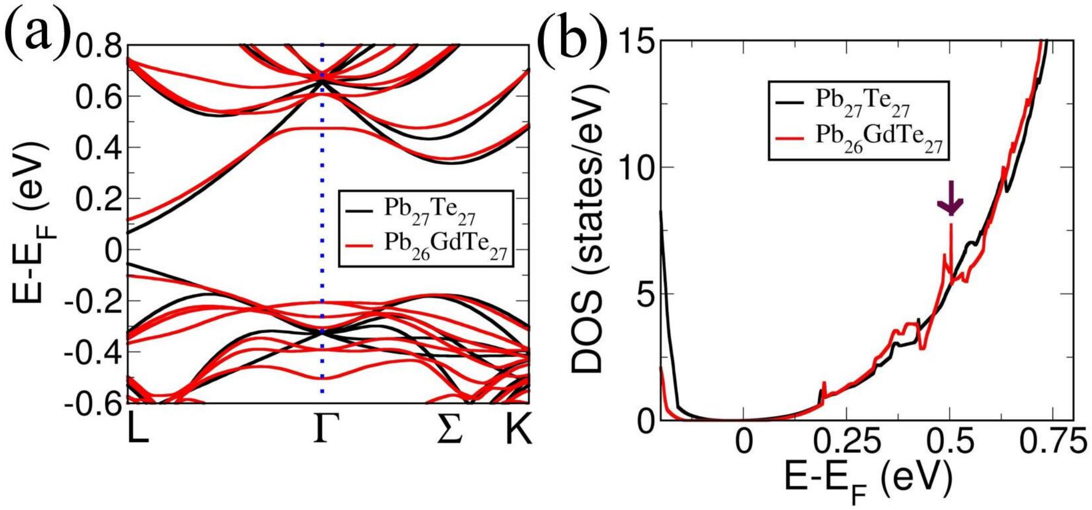

Figure 5.1: (a) Electronic band structure of PbTe (black) and Gd-doped PbTe (red), containing 54 atoms in the 3 × 3 × 3 supercell. (b) Electronic DOS of PbTe and Gd-doped PbTe. The relatively flat nature in the conduction band is further confirmed by a sharp peak in DOS, marked by a maroon arrow.

the constructed 2 x 2 x 1 supercell. It contains 24 phonon modes at each q-point: out of the 24 phonon modes, there are 3 acoustic phonon modes and 21 optical phonon modes present.

5.3 Results and discussion

Gd is an n-type donor with a common oxidation state of +3, and upon substituting it with Pb^{2+}, it would impart an additional electron into the lattice. To understand how Gd doping influences the electronic transport properties of PbTe, we have performed a detailed DFT analysis of electronic structure. Figure 5.1(a) represents the electronic band structures of PbTe and Gd-doped PbTe plotted together for comparison. It is evident that upon Gd incorporation, the band gap at L point increases from 0.15 to 0.25 eV. Experimentally, the pristine PbTe has a band gap of $\simeq$ 0.27 eV that increases to 0.29 eV for Pb_{1-x} Gd_xTe (x = 0.75%).

Furthermore, doping with Gd atoms introduces a few new features in the elec-

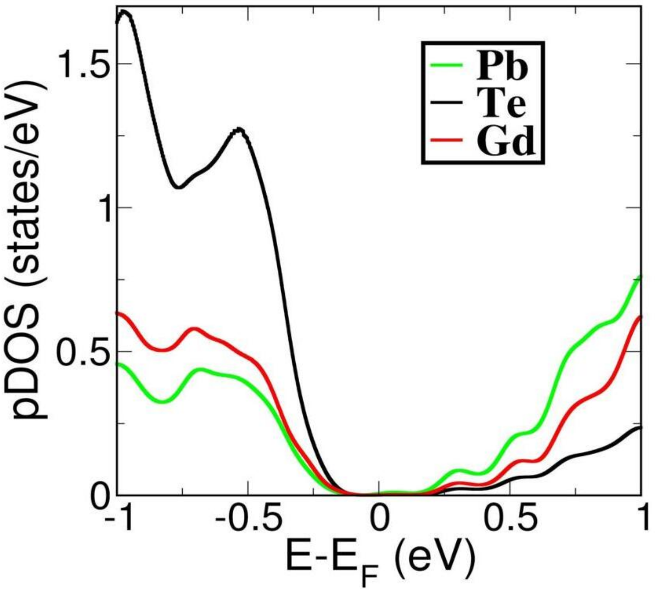

Figure 5.2: Atom projected electronic density of states (pDOS). Fermi level (E_F) is considered as reference.

tronic band structure, which is beneficial for thermoelectric power factor. Herein, we observe a noninteracting single band just above the Fermi level in the conduction band that is nearly dispersionless around the Γ point and relatively dispersive along the L $\longrightarrow$ Γ direction (red lines, Figure 5.1(a). In fact, the flat nature is further verified through the sharp peak observed in the electronic DOS plot, which is shown by the maroon arrow in Figure 5.1(b) and resembles that of Sb- and I-codoped PbTe.[22] Here, this nondispersive band leads to a higher Seebeck coefficient.[23-24] This band flattening is accompanied by an increase in the effective mass (m^*) of the conduction band. Pristine PbTe has an effective mass of $\simeq 0.3m_e$, which increases to $\simeq 0.42m_e$ for Gd-doped PbTe. On the other hand, due to band convergence, electrical conductivity increases to $\simeq$ 1020 S/cm at 300 K. In fact, due to Gd doping in PbTe, Seebeck coefficient also increases from 240 to 261 μV/K at 870 K.

Atom projected electronic density of states (pDOS) for Gd doped PbTe revealed that the conduction band levels have main contributions from the hybridized states

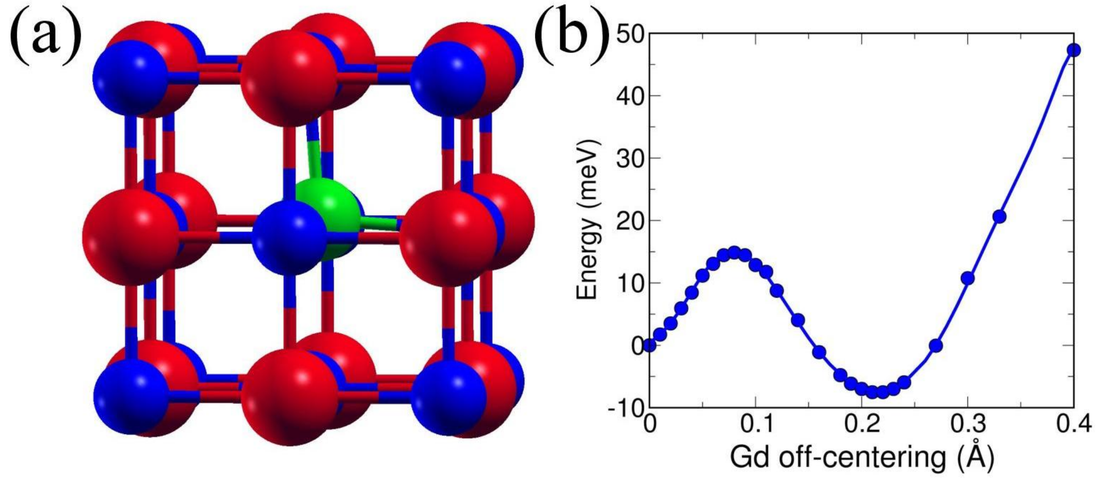

Figure 5.3: (a) Off-centered Gd atom at the distorted octahedral position in PbTe. Colour codes are represented as follows: Pb: red; Te: blue; Gd: green. (b) Energy vs. Gd off-centering plot showing a minimum energy when Gd is off-centered by $\simeq 0.21\ \AA$ along the [111] direction.

of Te – Gd and Te – Pb bonding, with maximum contribution from Pb (Figure 5.2). The electronic structures are calculated on the basis of the energetically most favorable configuration where Gd atoms are displaced along the crystallographic direction [111] from their ideal octahedral positions (Figure 5.3(a)). The off-centering of the Gd atom from the regular octahedral site is around 0.21 $\AA$. This tendency of Gd to off-center from the parent Pb position actually arise due to the discordant nature of Gd, which prefers to attain a higher coordination number (CN) (CN $>$ 6) than possible for rock-salt PbTe (CN = 6).[25] Through the off-centering configuration of Gd in Gd-doped PbTe, the structure further reduces their total energy significantly by 13 meV, which is shown in Figure 5.3(b).

To further understand the chemical aspect of such Gd off-centering, we perform crystal orbital Hamiltonian population (COHP) analysis between the orbitals of Te and Gd. COHP is calculated by considering the DOS multiplied by the Hamiltonian matrix element and it indicates degree of covalency and nature of bonding interactions. A negative value of COHP signifies bonding nature while a positive value implies antibonding or unstable nature. Figures 5.4(a) and 5.4(b) repre-

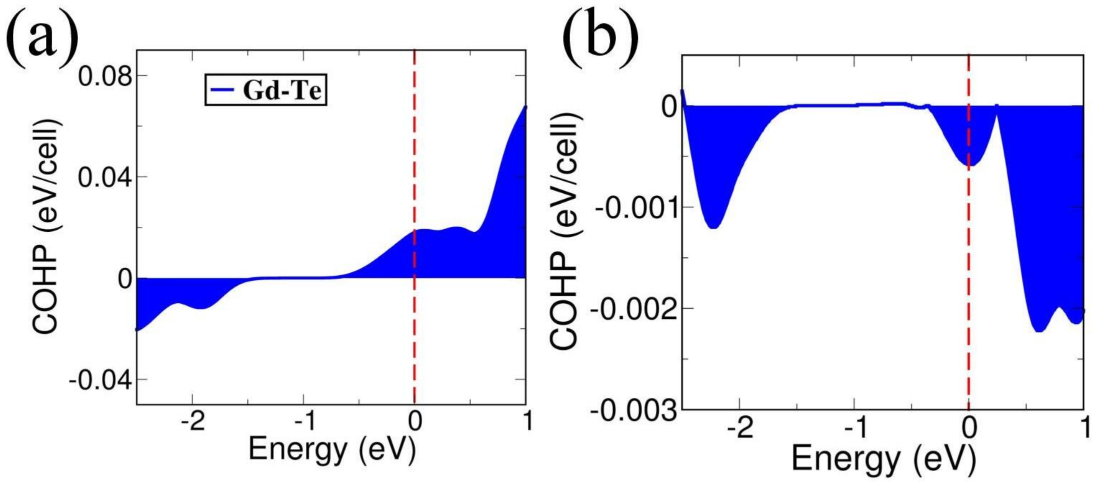

Figure 5.4: Crystal orbital Hamiltonian population (COHP) is plotted for Gd doped PbTe with (a) undistorted and (b) off-centered Gd atom from the equilibrium octahedral position.

sent the COHP between the orbital of Te and Gd for both the undistorted (Gd at the regular octahedral site) and off-centered site of the Gd atom in the PbTe lattice, respectively. Interestingly, the interaction between Te and Gd orbitals is antibonding in nature close to the Fermi level (and above the Fermi level) when Gd atoms are placed at their undistorted octahedral site. However, through the off-centering, the GdTe interaction becomes bonding and thereby stable in nature, which is energetically more favorable than the undistorted case. This locally off-centered Gd atom increases the lattice anharmonicity and subsequently plays an important role in reducing the lattice thermal conductivity of n-type PbTe significantly (discussed later).[26]

To comprehend the nature of thermal transport in these materials, we have calculated the phonon dispersion of pristine PbTe and Gd-doped PbTe (Figures 5.5(a) and 5.5(b)). We find that the Gd atom introduces nearly a flat band around the frequency $\simeq 38$ cm^{-1} along $\Gamma \longrightarrow \text{Z} \longrightarrow \text{R} \longrightarrow \text{X}$ directions over the Brillouin zone of phonon dispersion (Figure 5.5(b)). The low energy nearly dispersionless optical mode reflects a weak interatomic force constant (IFC) and thereby reflects weak bonding between the associated atoms. These disentangled nondispersive

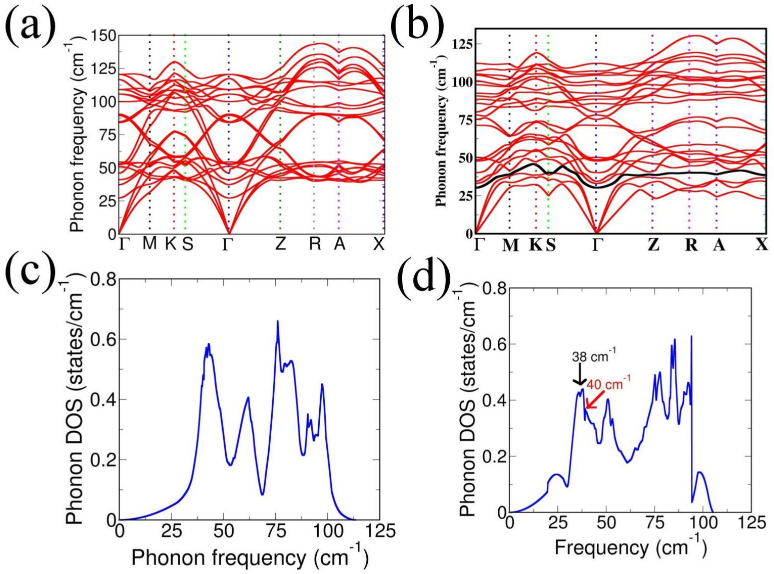

Figure 5.5: Phonon dispersion for (a) PbTe and (b) Gd-doped PbTe. Appearance of a special band, which is represented by black colour, reveals nearly nondispersive nature along $\Gamma \longrightarrow Z \longrightarrow R \longrightarrow X$ directions due to Gd doping. Phonon DOS for (c) PbTe and (d) Gd-doped PbTe. Here, a sudden enhancement in DOS at 38 cm^{-1} , which is indicated by a black arrow, appears because of Gd doping in PbTe. This increment in DOS originated because of a low-energy nearly flat band (shown in black color in Figure 5.5(d)) in the Gd-doped PbTe.

optical phonon mode behave similar to the Kondo-like phonon mode, as seen previously for type-I clathrates with Ce and La as guests, and are doubly degenerate in nature.[27] For microscopic understanding of the nearly flat phonon band, we carefully analyze phonon dispersion over the full Brillouin zone. In this regard, the vibrational frequencies have been accurately calculated using density functional perturbation theory (DFPT) as implemented in Quantum Espresso (QE).[18] In fact, we compute vibrational Eigenvalues at the particular irreducible q-points depending upon the crystal symmetry. Some of the important vibrational modes for particular q-points are tabulated in Table 5.1. While doping with Gd atom in place of Pb, we encounter two sets of possible degenerate Einstein modes (ω_1 and ω_2) at the non-zero $q-$points. Interestingly, the Gd atom at the 4a crystallographic site constitutes a non-interacting hybridized state with Te and Pb atoms and constructs phonon mode which is flat in nature over the Brillouin zone along $\Gamma \longrightarrow Z$

$\longrightarrow$ R $\longrightarrow$ X directions. These non-dispersive vibrational modes are degenerate in energy due to specific crystal symmetry for some particular irreducible $q-$points. These degenerate vibrational modes are identified as pseudospins in the Kondo model.[28] In the context of the spin Kondo model,[29] pseudospins represent spin up and spin down states. Similar to the spin systems, the vibrational Eigenvectors associated to the degenerate Eigenvalues are orthogonal to each other. These nearly non-dispersive Kondo-like degenerate optical phonon modes strongly scatter extended acoustics modes, similar to the spin Kondo system, where localized spin scatters free electrons and in turn reduces the carrier conductivity.

Table 5.1: List of some irreducible $q-$points and corresponding degenerate vibrational Eigen values. The q-points are in the unit of $\frac{2\pi}{l}$; where l is lattice constant.

q_x	q_y	q_z	$\omega_1(cm^{-1})$	$\omega_2(cm^{-1})$
0.00	-0.57	-0.20	38	38
0.00	-0.57	-1.02	41	41

Moreover, we observe an avoided crossing between the longitudinal acoustic (LA) mode and the low energetic optical mode at 40 cm^{-1} near the high-symmetry S point in the phonon dispersion curve (Figure 5.5(d)). Such an avoided crossing is a signature for strong scattering of heat-carrying acoustic phonons. Figures 5.5(c) and 5.5(d) represent phonon DOS for PbTe and Gd doped PbTe. A sharp peak in the density of states near 38 cm^{-1} (black arrow, Figure 5.5(d)) is evidenced due to the appearance of nondispersive flat optical phonon mode.

To uncover how this localized optical phonon mode affects the thermal transport, we have calculated the atom-projected phonon DOS (Figure 7.6(a)). The atom-projected phonon DOS of Gd overlaps significantly with Pb atoms and hybridizes less with Te atoms at $\simeq$ 38 cm^{-1}. Furthermore, the Eigen mode visualization of this flat phonon mode shows significant contribution from the Gd atoms, indicating that the chemical origin of this flat phonon mode arises due to the

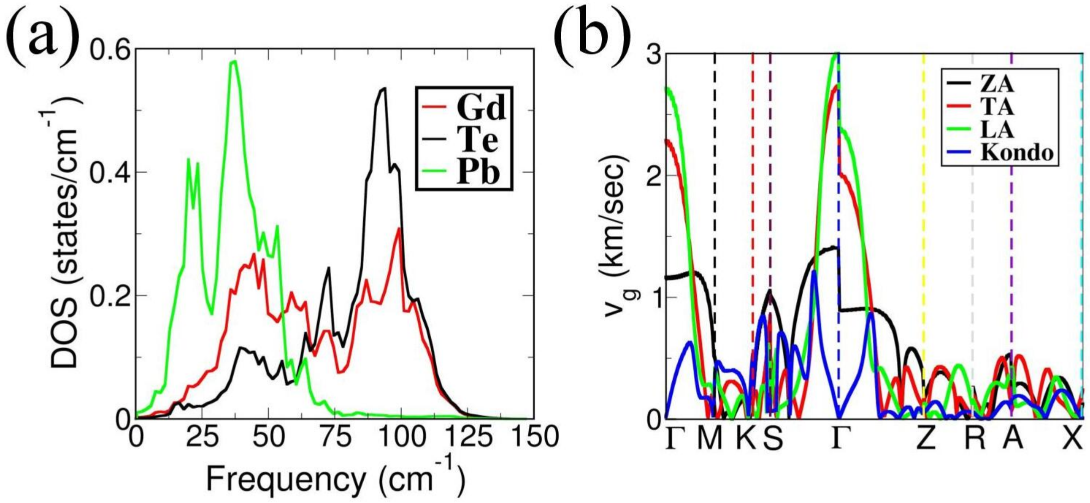

Figure 5.6: (a) Atom projected phonon DOS. (b) Phonon group velocity vs. q-points. The avoided crossing is further verified from the phonon group velocity plot where sharp changes in phonon group velocity is observed in S point. Please note the group velocity is low for flat low energy Kondo-like optical phonon band (shown in blue color).

doping of Gd atom in PbTe. These hybridized modes effectively scatter acoustic phonons and reduce lattice thermal conductivity significantly. Moreover, this localized optical mode displays very low group velocity $\simeq$ 230 m/s along $\Gamma \longrightarrow$ Z $\longrightarrow$ R $\longrightarrow$ X directions (Figure 7.6(b)). The low group velocity driven by the low-energy localized optical mode is the primary reason to achieve low lattice thermal conductivity in Gd-doped PbTe. Gd doping further decreases the speed of sound along one of the transverse directions (v_{t2}) from 1690 to 1160 m/s (Table 5.2). This reduction in v_{t2} decreases the overall mean speed of sound of the acoustic phonons from 1570 m/s for Gd-doped PbTe compared to 2035 m/s for pristine PbTe. This reduction in the mean speed of sound along with the presence of low energy flat optical phonon mode and lattice anharmonicity induced via Gd off-centering plays a pivotal role in lowering the κ_{lat} of Gd-doped PbTe. As a result, we achieve ultralow lattice thermal conductivity, $\kappa_{lat} \simeq 0.78$ W/mK at 735 K.

The signature of the appearance of the Kondo like non-dispersive mode has also been verified from the phonon contribution to the theoretical specific heat (Figure

Table 5.2: Speed of sound of the acoustic phonons.

Compounds	v_l (m/s)	v_{t1} (m/s)	v_{t2} (m/s)	v_{mean} (m/s)
PbTe	2680	2180	1690	2035
PbGdTe	2700	2290	1160	1570

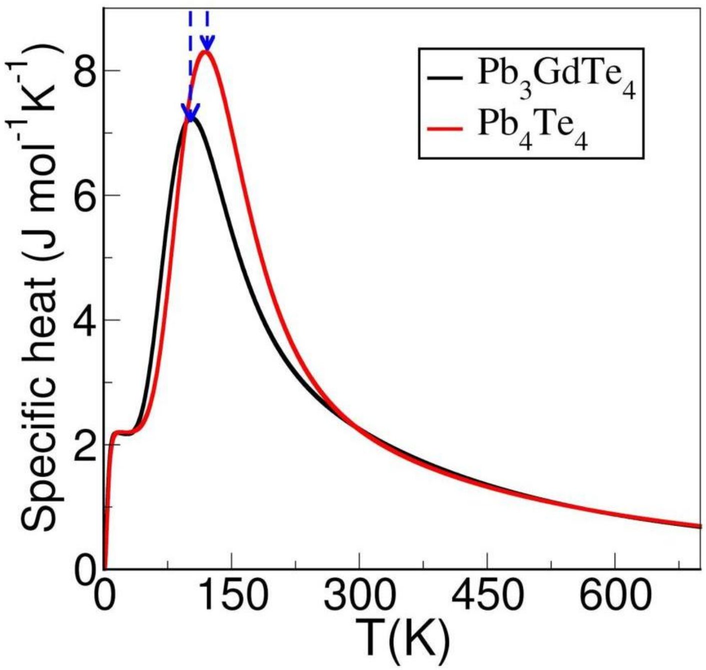

Figure 5.7: Phonon contribution to the specific heat as a function of temperature for pristine and Gd doped PbTe.

5.7). In fact, a broad maximum of specific heat curve appears around 121 K which is actually near to the Debye temperature of PbTe system.[30-31] Interestingly, it is observed that the broad maximum of the specific heat is sharpened and shifted towards the lower temperatures as a result of Gd doping. Such behaviors can be explained in terms of the temperature scales where these effects are controlled; it is not by Debye temperature, rather governed by some reduced energy scale due to Kondo type phonon mode [32]. Thus, reduced temperature scale strongly enhances Umklapp scattering that results in limiting the lattice thermal conductivity.

Finally, with so low thermal conductivity dominated by the discordant nature of Gd and low group velocity along with high electronic conductivity because of band convergence and high Seebeck coefficients due to higher m^*, the Gd doped PbTe exhibits a zT of $\simeq 1.2$ at 783 K, which was estimated experimentally.

5.4 Conclusions

In conclusion, Gd doping introduces a non-interacting flat conduction band in n-type PbTe which increases its m^*. The presence of this nearly dispersionless conduction band distorts the electronic DOS near the conduction band which is found to be beneficial for enhancing the Seebeck coefficient of the material. Gd is found to be favorable when it is off-centered from its parent position by $\simeq 0.21$ $\AA$ along [111] crystallographic direction in the PbTe lattice. DFT based phonon dispersion revealed the presence of low frequency nearly flat optical phonon mode which resembles to that of phonon-Kondo mode and plays a pivotal role in scattering the heat-carrying acoustic phonons, thus lowering its κ_{lat}. The high thermoelectric performance of Gd doped PbTe is resultant of high power factor arising due to distortion of electronic DOS and simultaneous low thermal conductivity due to Gd off-centering and enhanced scattering due to formation of Kondo-like low energy phonon modes. Finally, due to such reasons, Gd doped PbTe exhibits zT to be 1.2 at 783 K.

5.5 References

[1] Tan, G.; Zhao, L.-D.; Kanatzidis, M. G., Rationally Designing High-Performance Bulk Thermoelectric Materials. Chem. Rev. 2016, 116, 12123-12149.

[2] Xiao, Y.; Wu, H.; Cui, J.; Wang, D.; Fu, L.; Zhang, Y.; Chen, Y.; He, J.; Pennycook, S. J.; Zhao, L.-D., Realizing high performance n-type PbTe by syn-

ergistically optimizing effective mass and carrier mobility and suppressing bipolar thermal conductivity. Energy Environ. Sci. 2018, 11, 2486-2495.

[3] Pei, Y.; Shi, X.; LaLonde, A.; Wang, H.; Chen, L.; Snyder, G. J., Convergence of electronic bands for high performance bulk thermoelectrics. Nature 2011, 473, 66-69.

[4] Sarkar, D.; Ghosh, T.; Banik, A.; Roychowdhury, S.; Sanyal, D.; Biswas, K., Highly Converged Valence Bands and Ultralow Lattice Thermal Conductivity for High-Performance SnTe Thermoelectrics. Angew. Chem. Int. Ed. 2020, 59, 11115-11122.

[5] Heremans, J. P.; Jovovic, V.; Toberer, E. S.; Saramat, A.; Kurosaki, K.; Charoenphakdee, A.; Yamanaka, S.; Snyder, G. J., Enhancement of Thermoelectric Efficiency in PbTe by Distortion of the Electronic Density of States. Science 2008, 321, 554.

[6] Biswas, K.; He, J.; Zhang, Q.; Wang, G.; Uher, C.; Dravid, V. P.; Kanatzidis, M. G., Strained endotaxial nanostructures with high thermoelectric figure of merit. Nat. Chem. 2011, 3, 160.

[7] Xiao, Y.; Wu, H.; Li, W.; Yin, M.; Pei, Y.; Zhang, Y.; Fu, L.; Chen, Y.; Pennycook, S. J.; Huang, L.; He, J.; Zhao, L.-D., Remarkable Roles of Cu To Synergistically Optimize Phonon and Carrier Transport in n-Type PbTe-Cu_2Te. J. Am. Chem. Soc. 2017, 139, 18732-18738.

[8] Luo, Z.-Z.; Zhang, X.; Hua, X.; Tan, G.; Bailey, T. P.; Xu, J.; Uher, C.; Wolverton, C.; Dravid, V. P.; Yan, Q.; Kanatzidis, M. G., High Thermoelectric Performance in Supersaturated Solid Solutions and Nanostructured n-Type PbTe-GeTe. Adv. Funct. Mater. 2018, 28, 1801617.

[9] Li, J.; Zhang, X.; Chen, Z.; Lin, S.; Li, W.; Shen, J.; Witting, I. T.; Faghaninia, A.; Chen, Y.; Jain, A.; Chen, L.; Snyder, G. J.; Pei, Y., Low-Symmetry Rhombohedral GeTe Thermoelectrics. Joule 2018, 2, 976-987.

[10] Dutta, M.; Ghosh, T.; Biswas, K., Electronic structure modulation strategies

in high-performance thermoelectrics. APL Mater. 2020, 8, 040910.

[11] Roychowdhury, S.; Biswas, R. K.; Dutta, M.; Pati, S. K.; Biswas, K., Phonon Localization and Entropy-Driven Point Defects Lead to Ultralow Thermal Conductivity and Enhanced Thermoelectric Performance in $(SnTe)_{1-2x}(SnSe)_x(SnS)_x$. ACS Energy Lett. 2019, 4, 1658-1662.

[12] Biswas, K.; He, J.; Wang, G.; Lo, S. H.; Uher, C.; Dravid, V. P.; Kanatzidis, M. G., High thermoelectric figure of merit in nanostructured p-type PbTeMTe (M = Ca, Ba). Energy Environ. Sci. 2011, 4, 4675.

[13] Biswas, K.; He, J.; Blum, I. D.; Wu, C. I.; Hogan, T. P.; Seidman, D. N.; Dravid, V. P.; Kanatzidis, M. G., High-performance bulk thermoelectrics with all-scale hierarchical architectures. Nature 2012, 489, 414-418.

[14] Xiao, Y.; Zhao, L.-D., Charge and phonon transport in PbTe-based thermoelectric materials. npj Quantum Mater. 2018, 3, 55.

[15] Pei, Y.; Gibbs, Z. M.; Gloskovskii, A.; Balke, B.; Zeier, W. G.; Snyder, G. J., Optimum Carrier Concentration in n-Type PbTe Thermoelectrics. Adv. Energy Mater. 2014, 4, 1400486.

[16] Yang, Z.; Wang, S.; Sun, Y.; Xiao, Y.; Zhao, L.-D., Enhancing thermoelectric performance of n-type PbTe through separately optimizing phonon and charge transport properties. J. Alloys Compd. 2020, 828, 154377.

[17] Pei, Y.; Lensch-Falk, J.; Toberer, E. S.; Medlin, D. L.; Snyder, G. J., High Thermoelectric Performance in PbTe Due to Large Nanoscale Ag_2Te Precipitates and La Doping. Advanced Functional Materials 2011, 21, 241-249.

[18] Giannozzi, P.; Baroni, S.; Bonini, N.; Calandra, M.; Car, R.; Cavazzoni, C.; Ceresoli, D.; Chiarotti, G. L.; Cococcioni, M.; Dabo, I.; Dal Corso, A.; de Gironcoli, S.; Fabris, S.; Fratesi, G.; Gebauer, R.; Gerstmann, U.; Gougoussis, C.; Kokalj, A.; Lazzeri, M.; MartinSamos, L.; Marzari, N.; Mauri, F.; Mazzarello, R.; Paolini, S.; Pasquarello, A.; Paulatto, L.; Sbraccia, C.; Scandolo, S.; Sclauzero, G.; Seitsonen, A. P.; Smogunov, A.; Umari, P.; Wentzcovitch, R. M., QUANTUM

ESPRESSO: a modular and open-source software project for quantum simulations of materials. J. Phys.: Condens. Matter 2009, 21, 395502.

[19] Blöchl, P. E., Projector augmented-wave method. Phys. Rev. B: Condens. Matter Mater. Phys. 1994, 50, 17953-17979.

[20] Perdew, J. P.; Burke, K.; Ernzerhof, M., Generalized gradient approximation made simple. Phys. Rev. Lett. 1996, 77, 3865.

[21] Xiao, Y.; Wu, H.; Cui, J.; Wang, D.; Fu, L.; Zhang, Y.; Chen, Y.; He, J.; Pennycook, S. J.; Zhao, L.-D., Realizing high performance n-type PbTe by synergistically optimizing effective mass and carrier mobility and suppressing bipolar thermal conductivity. Energy Environ. Sci. 2018, 11, 2486-2495.

[22] Fu, L.; Yin, M.; Wu, D.; Li, W.; Feng, D.; Huang, L.; He, J. Large enhancement of thermoelectric properties in n-type PbTe via dual-site point defects. Energy Environ. Sci. 2017, 10, 20302040.

[23] Isaacs, E. B.; Wolverton, C. Remarkable thermoelectric performance in $BaPdS_2$ via pudding-mold band structure, band convergence, and ultralow lattice thermal conductivity. Phys. Rev. Mater. 2019, 3, 015403.

[24] Mori, K.; Sakakibara, H.; Usui, H.; Kuroki, K. Ideal band shape in the potential thermoelectric material $CuAlO_2$: Comparison to $NaxCoO_2$. Phys. Rev. B: Condens. Matter Mater. Phys. 2013, 88, 075141.

[25] Sastri, V. S.; Bunzli, J.-C.; Rao, V. R.; Rayudu, G. V. S.; Perumareddi, J. R. Structural Chemistry of Lanthanide Complexes. Modern Aspects of Rare Earths and Their Complexes; Elsevier: Amsterdam, 2003; Chapter 5, pp 375422.

[26] Luo, Z.-Z.; Cai, S.; Hao, S.; Bailey, T. P.; Su, X.; Spanopoulos, I.; Hadar, I.; Tan, G.; Luo, Y.; Xu, J.; Uher, C.; Wolverton, C.; Dravid, V. P.; Yan, Q.; Kanatzidis, M. G. High Figure of Merit in GalliumDoped Nanostructured n-Type PbTe-xGeTe with Midgap States. J. Am. Chem. Soc. 2019, 141, 1616916177.

[27] Ikeda, M. S.; Euchner, H.; Yan, X.; Tomes, P.; Prokofiev, A.; Prochaska, L.; Lientschnig, G.; Svagera, R.; Hartmann, S.; Gati, E.; Lang, M.; Paschen, S.

Kondo-like phonon scattering in thermoelectric clathrates. Nat. Commun. 2019, 10, 887.

[28] Schrieffer, J. R.; Wolff, P. A., Relation between the Anderson and Kondo Hamiltonians. Phys. Rev. 1966, 149, 491-492.

[29] (12) Nozières, P.; Blandin, A., Kondo effect in real metals. J. Phys. France 1980, 41, 193-211.

[30] Zhang, Y., First-principles Debye–Callaway approach to lattice thermal conductivity. J. Materiomics 2016, 2, 237-247.

[31] Zhang, Y.; Ke, X.; Chen, C.; Yang, J.; Kent, P. R. C., Thermodynamic properties of PbTe, PbSe, and PbS: First-principles study. Phys. Rev. B: Condens. Matter Mater. Phys. 2009, 80, 024304.

[32] Ikeda, M. S.; Euchner, H.; Yan, X.; Tomeš, P.; Prokofiev, A.; Prochaska, L.; Lientschnig, G.; Svagera, R.; Hartmann, S.; Gati, E.; Lang, M.; Paschen, S., Kondo-like phonon scattering in thermoelectric clathrates. Nat. Commun. 2019, 10, 887.

6

Exploring the Thermoelectric Properties of 3d-Transition Metal doped Two-dimensional SnTe: A Computational Study

6.1 Introduction

In today's increasing demand of renewable energy [1-4] scenario, thermoelectric (TE) materials [5-6] are playing a pivotal role. They can produce renewable energy, such as, electricity from the solar heat as well as from the waste heat generated via different industrial and chemical processes [7-8]. Such conversion of energy follows the Seebeck effect [9] which is a clean and environment-friendly process with benefit of zero-emission. The efficiency of a TE material has been evaluated by the dimensionless figure of merit zT [10], defined as $zT = \frac{\sigma S^2 T}{\kappa_{tot}}$, where σ represents the electrical conductivity, S represents the Seebeck coefficient, T represents the temperature in Kelvin and κ_{tot} represents the total thermal conductivity which is the sum of lattice thermal conductivity (κ_{lat}) and electronic thermal conductivity

(κ_{elec}). The higher the value of zT, the better is the efficiency of a thermoelectric material at a given temperature [11-12]. A high zT value can be achieved by enhancing the Seebeck coefficient (S) and electrical conductivity (σ) and reducing the thermal conductivity κ_{tot}, so that the temperature difference generating the Seebeck coefficient can be retained. The Seebeck coefficient can be enhanced by engineering the electronic band structure, thereby achieving the band convergence or by generating the resonant state near the Fermi level [13-16]. In fact, Seebeck coefficient increases when carrier effective mass increases whereas the charge carrier conductivity is inversely proportional to effective mass. Thus, the materials should contain both dispersive as well as non-dispersive band curvature, which may arise for systems with inhomogeneity in chemical bonding features. On the other hand, the thermal conductivity can be reduced by maximizing the all-length-scale phonon scatterings.[17-18] Another strategy to achieve high-efficiency thermoelectric energy conversion is to employ materials with intrinsically low thermal conductivity and enhanced vibrational anharmonicity [19-20].

In the last few years, the two-dimensional (2D) group IV-VI mono chalcogenide materials (e.g., SnSe, GeTe etc.) have drawn considerable attention as possible candidates for thermoelectric energy conversion [21-24]. They are reported to exhibit better thermoelectric efficiency as compared to their bulk counterparts. This is attributed to the quantum confinement effects, which cause unique structural and electronic properties leading to the reduction of their intrinsic lattice thermal conductivity. Besides, low-dimensional tin-chalcogenides are reported to achieve an enhanced value of the Seebeck coefficient due to the higher electronic density of states near the Fermi level.

More recently, the successful fabrication of 2D (atomic-thick) SnTe on the graphitized 6H-SiC (0001) substrate by Chang et al.[25] via molecular beam epitaxial technique, motivated the researchers to explore its applicability as the thermoelectric material. The density of intrinsic Sn vacancies in this atomically thick

2D SnTe, as reported both experimentally and computationally (using density functional theory i.e., DFT), is almost two to three orders of magnitude lower than that of the bulk SnTe [26-27]. Hence, 2D SnTe is also expected to follow a similar trend as the other 2D group IV-VI mono chalcogenide materials and act as an efficient candidate for thermoelectric energy conversion. However, only a very few computational reports [28-30] are there explaining the structural, electronic, or thermoelectric properties of pure and various variants of SnTe monolayer and 2D SnTe. In 2017, Xu et al. [28] investigated the electronic and optical properties of SnTe monolayer by DFT and many-body perturbation theory. In another report, Liu et al. [29] computationally explored the coexistence of magnetism and ferroelectricity in 3d transition-metal (3d-TM) doped SnTe monolayer. However, the thermoelectric behavior of the transition metal (TM) doped SnTe monolayer remained unexplored. Recently, Guo et al. [30] investigated the electronic properties of SnTe monolayer using DFT by substituting the Sn atom with different group III/IV and V elements. They observed that the substitution of Sn atoms in SnTe monolayer by the group V elements (P/As/Sb/Bi) transformed it into n-type degenerate semiconductors possessing an excess number of free electrons which could contribute to electronic conduction. As a consequence, these group V elements doped SnTe monolayers have been predicted to show higher electrical conductivity as compared to that of the pristine one. Moreover, its smaller carrier effective mass indicates higher carrier mobility and conductivity. Therefore, the possibility of higher thermoelectric conversion efficiency than the pristine SnTe monolayer may possibly be expected although they did not evaluate the thermal conductivity and Seebeck coefficients. Thus, a systematic investigation and a clear understanding of the electronic and thermoelectric behavior of hetero-atom doped 2D SnTe is still elusive. This could be due to the several phase transitions of 2D SnTe at different pressures and temperatures.

In 2019, Li et al. [31] first reported the thermoelectric properties of orthorhombic SnTe monolayer using DFT and Boltzmann transport equation theory and predicted a significantly high zT value (> 2). However, recently, a new hexagonal phase of 2D SnTe, known as β'-SnTe with P$\bar{3}$m1 symmetry (space group no. 164), is reported by Dong et al. [32] as the most stable among all the possible 2D phases of SnTe, including the currently available orthogonal and other phases. This has been confirmed via the Universal Structure Predictor: Evolutionary Xtallography (USPEX) method combined with the density functional calculations.

In fact, earlier the hexagonal 2D phase with P$\bar{3}$m1 symmetry was identified both experimentally and theoretically for GeTe [33-34] and SiTe [35] as a two-component $(\mathrm{GeTe})_2(\mathrm{Sb_2Te_3})_\mathrm{m}$ and $(\mathrm{SiTe})_2(\mathrm{Sb_2Te_3})_\mathrm{m}$ (where m is an integer) superlattices respectively. In 2016, Sa et al. [36] explained that in these $(\mathrm{GeTe})_2(\mathrm{Sb_2}$ $\mathrm{Te_3})_\mathrm{m}$ and $(\mathrm{SiTe})_2(\mathrm{Sb_2}\ \mathrm{Te_3})_\mathrm{m}$ superlattices, the GeTe or SiTe structures, and the corresponding $\mathrm{Sb_2Te_3}$ layers are connected via weak Te–Te van der Waals forces. This aspect indicates the independence of the GeTe and SiTe building blocks from the overall superlattice structures. Hence, there is a high possibility of finding these 2D GeTe, SiTe, or some other similar type of group IV-VI monochalcogenides independently without the presence of $\mathrm{Sb_2}\ \mathrm{Te_3}$ layers. Furthermore, Sa et al. [36] confirmed the high stability of these 2D $(\mathrm{AX})_2$ structures (A = Si, Ge, Sn, and Pb, and X = Se and Te) by energy evaluations, lattice dynamical studies (calculating the phonon dispersion), and chemical bonding analysis.

Motivated by the most recent development of finding a stable hexagonal SnTe monolayer in 2019, in this work, we have investigated the geometrical and electronic structure, stability, and thermoelectric efficiency of pristine as well as 3d-TM doped 2D hexagonal SnTe monolayer using first-principles DFT based calculations and Boltzmann transport theory. Furthermore, the reason behind choosing the 3d-TM atoms as the substitutional dopant elements are their non-toxicity, cost-effectiveness, and lighter weight as compared to that of Sn. In this study, we solve Boltzmann transport equation (BTE) within relaxation time approximation

(RTA) to obtain electrical as well as thermal transport co-efficients. To verify our in-house codes, using our programs, we have computed Seebeck coefficient, lattice thermal conductivity and zT to be 456 $\mu V/K$, 1.47 $Wm^{-1}K^{-1}$ and 2.12, respectively at 900 K for 2D SnTe. Dong et al.[32] also estimated Seebeck co-efficient, lattice thermal conductivity and zT by solving BTE at 900 K for 2D SnTe and that eventually turns out to be 450 $\mu V/K$, 1.38 $Wm^{-1}K^{-1}$ and 2.17 respectively. These findings motivated us to comprehensively study the thermoelectric performance of 3d-TM doped 2D SnTe.

The prime objective of the present work is to understand how the various thermoelectric parameters of pristine 2D SnTe changes upon 3d-TM substitutions. We have investigated the dynamical and thermal stability of these 3d-TM doped systems via phonon dispersion calculation and ab-initio Molecular Dynamics (AIMD) simulation up to 900 K. Our results indicate that the doped systems that are considered by us are dynamically as well as thermodynamically stable. Our main aim is to understand the dependence of various parameters for finding the electrical and thermal transport coefficients, and thereby estimating the trend for achieving 3d-TM doped 2D SnTe as the high-performance thermoelectric material.

6.2 Theoretical Section

6.2.1 First-principle formalism

We perform the first-principle based density functional theory (DFT) method implemented in the Quantum Espresso (QE) package to obtain a relaxed crystal structure. For structural relaxation, we use projected augmented wave (PAW) pseudopotential as exchange-correlation energy of the electrons with generalized gradient approximation (GGA) functional parametrized by Perdew, Burke, Erzenhoff (PBE).[43] The energy cutoff of wavefunction and charge density on a plane-wave basis is considered as 50 Ry and 200 Ry, respectively. A uniform grid of 4 x 4 x 1 $k-$points is used for Brillouin space integration and 12 x 12 x 1 $k-$mesh is considered to accurately calculate the electronic density of states (DOS). We optimize the crystal structure until the magnitude of Hellman-Feynman force on each atom is less than 0.025 eV/$\mathring{A}$. Once the pristine SnTe monolayer is relaxed, we doped 3d transition metal (TM= V/Mn/Fe/Co) in the Sn site and optimize the lattice parameters. In fact, during optimization, we consider Hubbard U $\simeq$ 2.5 eV to incorporate electron-electron correlation effects for 3d TM doped systems. To justify the U value chosen, we have verified electronic structure calculations by considering other U values (U $\simeq$ 1.5, 3.5, 4.5, 5.5 in eV) as well. Interestingly, we observe that the incorporation of U only modifies the electronic bandgap to some extent, while band dispersion remains unaltered with U values above U $\simeq$ 2.5 eV. Usually, it is a well known fact that the electronic band curvature is the determining factor for carrier transport calculations. After the optimization, the electronic structure calculations have been performed considering the unit cells of various sizes (e.g. 1 x 1, 2 x 1).

Density functional perturbation theory (DFPT) is a well established method to analyze vibrational spectra for understanding dynamical stability. We consider 3 x 3 x 1 $q-$mesh to calculate the phonon band structure. The SnTe monolayer consists of 8 atoms in the unit cell which is considered for phonon frequency calculations. The phonon spectra, calculated for SnTe monolayer (1 x 1 unit cell), correctly reproduce the result obtained by Dong et al. [32]. The phonon transport calculations have also been performed considering 2 x 1 unit cells. To compute the lattice thermal conductivity in pristine as well as in TM doped SnTe systems, we further focus on various underlying branches in the phonon dispersion spectra.

To perform the Bader charge analysis [37] and AIMD simulation, we have used the DFT-based [38-39] code Vienna Ab-initio Simulation Package (VASP) [40-41] which is associated with the projector augmented plane-wave basis set. Projected-augmented wave method (PAW) [42] potentials are employed to characterize all the constituent elements viz. Sn, V, Mn, Fe, Co, and Te. Generalized gradient approximation (GGA) is incorporated to treat the exchange-correlation functional of Perdew-Burke-Ernzerhof (PBE) [43]. The AIMD simulation is carried out by following the Nosé algorithm [44] up to 20 ps runtime with a time step of 1 fs and 20,000 SCF runs. All the calculations are performed by $4 \times 4 \times 1$ $k-$mesh generated via the Monkhorst-Pack method [45]. For a better treatment of our weakly interacting (layered) systems, we have carried out the calculations by incorporating the van der Waals corrections using Grimme's DFT-D2 dispersion corrections [46], as implemented in VASP. The maximum allowed error in total energy (which is basically the optimization condition for the electronic self-consistent loop) is 10^{-4} eV. The ground state geometries are optimized until the atomic forces acting on each atom (Hellman-Feynman forces) becomes less than 0.001 eV/$\AA$. All the initial and optimized geometries have been visualized using the graphical software viz. VESTA[47].

6.3 Results and Discussion

6.3.1 Structure and stability

Initially, we have considered two different phases/structures of 2D SnTe. One is the most extensively studied orthorhombic phase [25,27,30] and the other one is the recently reported hexagonal β'-SnTe phase [32,36]. After the full geometry optimization, we found that the unit cell of the hexagonal β'-SnTe phase is energetically lower by 0.11 eV as compared to that of the orthorhombic phase. This is in agreement with the earlier reported results [32]. Moreover, the experimental feasibility of this β' phase is predicted earlier by Sa et al. [36]. Hence, we proceed further with our calculations by considering the hexagonal phase of 2D SnTe. The

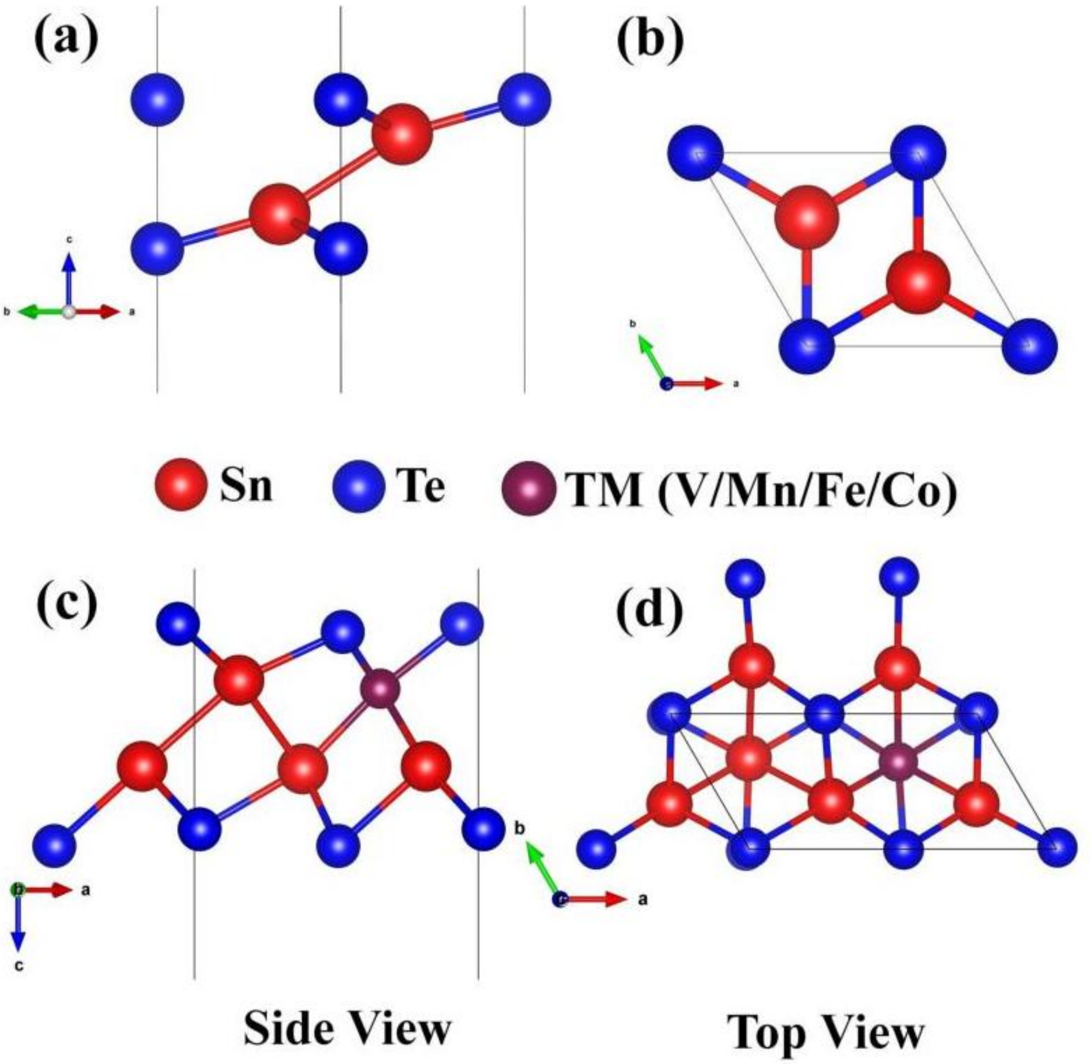

Figure 6.1: (a) side view and (b) top view of the ground state optimized geometry for the unit cell of hexagonal β' phase of 2D-SnTe. (c) side view and (d) top view of the model structures of 3d-TM doped 2D β'-SnTe systems.

ground state geometry optimized structure of this hexagonal β'-SnTe is shown in Figure 6.1. From Figure 6.1, it is clear that the unit cell of 2D SnTe consists of four atoms among which two are Sn atoms and the other two are Te atoms. The hexagonal phase of 2D SnTe, as shown in Figure 6.1, has a layered structure. The unit cell consists of two sublayers, each of which contains one Sn atom and one Te atom which are strongly bonded by an Sn-Te covalent bond. The two centrally symmetric Sn-Te sub-layers are bonded by a comparatively weaker (van der Waals) Sn-Sn bond [32,36]. The lattice parameter of this 2D β'-SnTe is found to be a = 4.32 Å. This value compares fairly well with the earlier reported [32,36] lattice parameter values of 2D β'-SnTe system. The formation energy (F.E) of the 2D β'-SnTe is estimated as -11.60 eV by using the following equation:

$$F.E = E(SnTe) - mE(Sn) - nE(Te) \tag{6.1}$$

where, E(SnTe) represents the total energy of the unit cell of 2D β'-SnTe, E(Sn) and E(Te) represent the total energy of an isolated Sn and Te atom respectively in the gas phase, m and n represent the total number of Sn and Te atoms in the unit cell of 2D β'-SnTe.

To explore the thermoelectric properties of the 2D β'-SnTe, we have considered a 2 × 1 supercell which consists of four Sn and four Te atoms and a vacuum of 12 $\AA$ along the z direction. In the optimized structure, the Sn-Te and Sn-Sn bond lengths are found to be $\simeq 2.95$ $\AA$ and $\simeq 3.33$ $\AA$, respectively, which are in agreement with the earlier reports. In order to be sure of the stability of dynamical lattice, the 2D β'-SnTe, we have estimated the phonon dispersion curves for both the unit cell and the 2 × 1 supercell through the density functional perturbation theory (DFPT) based methods, which are illustrated in Figure 6.2 as blue solid lines. Figure 6.2 clearly indicates the lattice dynamical stability without any negative or imaginary frequency for both the unit cell as well as for the 2 × 1 supercell.

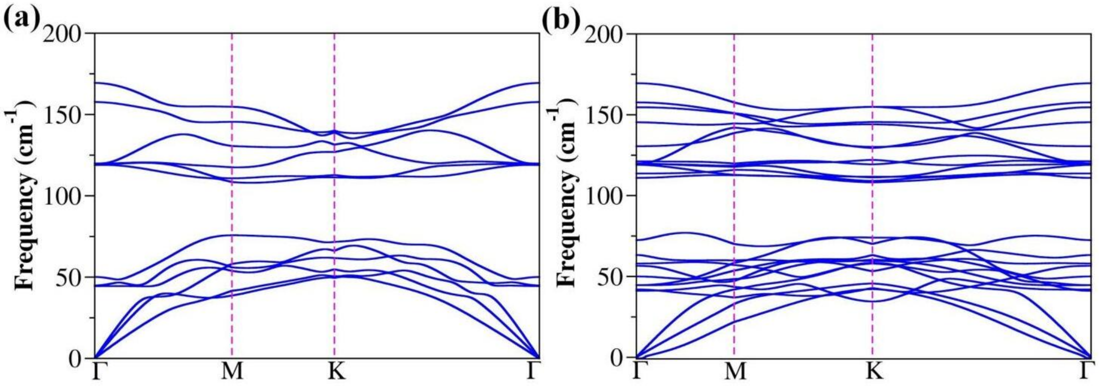

Figure 6.2: The phonon dispersion curves of 2D β'-SnTe for (a) unit cell and (b) 2 × 1 supercell. All positive/real frequency values indicate good dynamical stabilities of both the unit cell and 2 x 1 supercell.

Furthermore, the nature of the phonon dispersion spectra for the unit cell (Figure 6.2(a)) is in full agreement with the earlier reported findings.

After investigating the lattice dynamical stability of the pristine systems, we have substitutionally doped 3d-TM atom e.g., V, Mn, Fe, and Co on this 2 × 1 supercell of 2D β'-SnTe by replacing one of the Sn atoms and adopted energetically lowered crystal structure. This is equivalent to 12.5 % doping concentration of the 3d-TM atom. Figures 6.1 (c) and (d) represent the model structures of 3d-TM doped 2D β'-SnTe systems. The V, Mn, Fe, and Co-doped 2D β'-SnTe are designated as V@SnTe, Mn@SnTe, Fe@SnTe, and Co@SnTe respectively. Table 6.1 gives the formation energy of the pristine as well as the 3d-TM doped 2D β'-SnTe systems, and the binding energy of the TM atom on the 3d-TM doped 2D β'-SnTe systems. The formation energy of the 3d-TM doped 2D β'-SnTe systems are estimated with respect to the pristine 2D SnTe by using the following equation:

$$F.E = E(TM@SnTe) + E(Sn) - E(SnTe) - E(TM) \tag{6.2}$$

where E(TM@SnTe) and E(SnTe) represent the total energy of the 3d-TM doped 2D β'-SnTe and the 2 × 1 supercell of pristine 2D β'-SnTe systems respectively.

Table 6.1: Formation energy ($F.E$), and binding energy ($B.E$) of various TM atom on the 3d-TM doped 2D β'-SnTe systems.

Systems	Sn_4Te_4	Sn_3VTe_4	Sn_3MnTe_4	Sn_3FeTe_4	Sn_3CoTe_4
$F.E$	-11.60	-4.03	-7.01	-1.37	-1.90
$B.E$	0.00	-8.92	-12.06	-6.20	-6.78

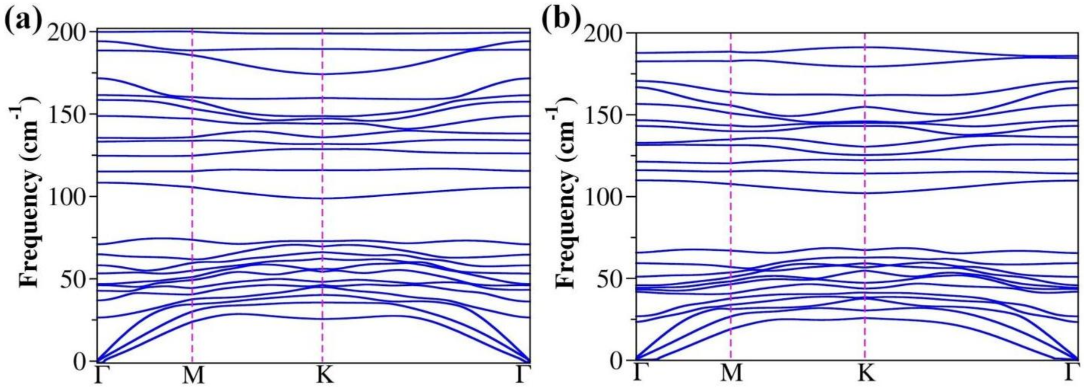

Figure 6.3: The phonon dispersion curves of (a)V@SnTe and (b)Mn@SnTe systems.

E(Sn) and E(TM) represents the total energy of an isolated Sn and TM atom respectively in the gas phase. Table 6.1 clearly shows that all the 3d-TM doped SnTe systems have negative formation energy, which indicates good energy stability. Mn@SnTe system shows the lowest formation energy (highest negative value) which indicates the highest stability and is followed by the V@SnTe, Co@SnTe, and Fe@SnTe systems. The perfect lattice dynamical stability of the V and Mn doped 2D β'-SnTe systems have also been realized by estimating their phonon dispersion curves (shown in Figure 6.3). The binding energy (B.E) of the TM atom on the 3d-TM doped 2D β'-SnTe systems are evaluated by using the following equation:

$$B.E. = E(Sn_{p-x}TM_xTe) - E(Sn_{p-x}Te) - xE(TM) \tag{6.3}$$

where $E(Sn_{p-x}TM_xTe)$ represents the total energy of the 3d-TM doped 2D β'-

SnTe system which is equal to the $E(TM@SnTe)$ mentioned in equation (6.2). p and x represent the total number of Sn and TM atoms in the 2×1 supercell of pristine 2D β'-SnTe and the 3d-TM doped 2D β'-SnTe systems respectively. In the present report, p and x are always equal to four and one respectively. $E(Sn_{p-x}Te)$ represents the 2D β'-SnTe system with x number of Sn vacancies. E(TM) is similar to the equation (6.3). From Table 6.1 it is clear that the binding energy of the TM atoms follows a similar trend as that of the formation energy of the 3d-TM doped 2D β'-SnTe systems. Also, the binding energy values of V and Mn are significantly higher as compared to that of the Co and Fe. Hence, the V-Te and Mn-Te bond lengths are expected to remain more stable as compared to that of the Fe-Te and Co-Te at a higher temperature. Moreover, if we expand the 3d-TM doped 2D β'-SnTe systems, we find that the minimum TM-TM separation in the periodically repeating structures of all the four 3d-TM doped 2D β'-SnTe systems becomes > 4 $\mathring{A}$. These TM-TM distances are significantly higher as compared to that in the bulk structures of the corresponding TM atom, thereby ruling out the possibility of cluster formation between these TM atoms in our systems.

Since most of the applications of the thermoelectric materials are at higher temperatures, we wanted to gain some knowledge about the stability of these 3d-TM doped 2D β'-SnTe systems at higher temperatures. To find it, we have performed ab-initio molecular dynamics (AIMD) simulations as implemented in VASP with the four 3d-TM doped systems. The AIMD simulation is carried out up to 20 ps runtime with 1 fs time step, 20000 SCF runs, and varying the temperature from 0 to 900 K. Our AIMD results indicate that all the four 3d-TM doped 2D β'-SnTe systems remain stable even after 20 ps runtime at around 900 K without any kind of cluster formation or agglomeration between the doped TM atoms. The degree of change in bond length at 900 K after 20 ps runtime as compared to that at the 0 K (ground state optimized structure) is shown in Figure 6.4. The results in Figure 6.4 indicate that the maximum change in bond lengths is $< 5\%$ which

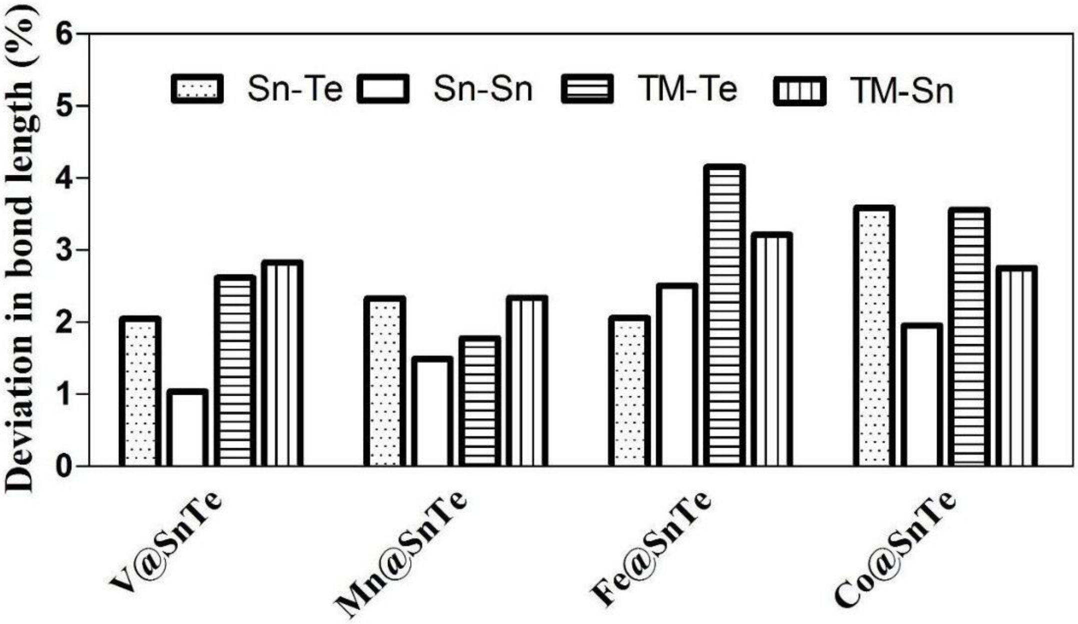

Figure 6.4: The % of deviation in bond length at 900 K after 20 ps runtime via AIMD simulation as compared to that at the 0 K (ground state optimized structure). The maximum change in bond lengths is $< 5\%$ which can be considered negligible in terms of stability of the systems.

can be considered as a negligible difference to the stability of the systems.

6.3.2 Nature of bonding and Bader charge transfer

After ensuring the overall structural integrity and stability of the 3d-TM doped 2D β'-SnTe systems, we try to explore the nature of TM-Te and TM-Sn bindings in these systems. As mentioned earlier in section 6.3.1, our DFT based results indicate a small deviation in bond lengths after doping with the 3d-TM atoms as compared to that of the pristine system. According to the analysis of the Cambridge Structural Database [53], covalent radii of Sn, V, Mn, Fe, Co, and Ti are 1.39 $\AA$, 1.53 $\AA$, 1.39 $\AA$, 1.32 $\AA$, 1.26 $\AA$, and 1.38 $\AA$ respectively. So, it is clear that the estimated Sn-Te and TM-Te bond lengths in the 3d-TM doped 2D β'-SnTe systems are quite close to the corresponding ideal covalent bond lengths. These findings indicate that both Sn and TM atoms are bonded with Te atoms in the same sublayer by the covalent bonds. However, the estimated Sn-Sn bond lengths are found to be much longer than the ideal covalent bond length values, thereby indicating the characteristics of weak van der Waals interaction rather than pure covalent bonding. For the TM-Sn bindings, we found that the V-Te and Mn-Te bond length values in the V@SnTe and Mn@SnTe systems indicate the van der Waals type weak interactions. However, the Fe-Te and Co-Te bond length values in the Fe@SnTe and Co@SnTe systems indicate the characteristics of covalent bondings.

Table 6.2: Bader charges of atoms on the pristine and the 3d-TM doped 2D β'-SnTe systems.

Atoms	Sn_4Te_4	Sn_3VTe_4	Sn_3MnTe_4	Sn_3FeTe_4	Sn_3CoTe_4
Sn	+0.45	+0.38	+0.42	+0.42	+0.44
Te	-0.45	-0.60	-0.61	-0.35	-0.19
TM	-	+0.72	+0.63	+0.28	+0.11

Furthermore, to obtain a quantitative picture about the nature of bonding of the TM atoms in the 3d-TM doped 2D β'-SnTe systems, we have carried out Bader charge analysis. Table 6.2 represents the Bader charge of Sn, TM and Te atoms for the pristine as well as for the 3d-TM doped 2D β'-SnTe systems. In the 3d-TM doped systems, the charge of Sn and Te atoms which are only the nearest neighbor of the doped 3d-TM atoms are considered here. From Table 6.2, it is evident that a significantly small amount of charge is transferred from both the Sn and TM atoms to the neighboring Te atoms. This small amount of charge transfer does not change the covalent nature of the Sn-Te and TM-Te bonds. The charge transfer mechanism is further explained by the iso-surface plotting of charge density (Figure 6.5) for the 3d-TM doped 2D β'-SnTe systems with an iso-surface value of 0.037 eV/$\AA^3$. Here in Figure 6.5, the light green color represents the accumulation or distribution of electronic charge density. The comparatively higher amount of charge density around the Sn-Te and TM-Te bonds indicates the

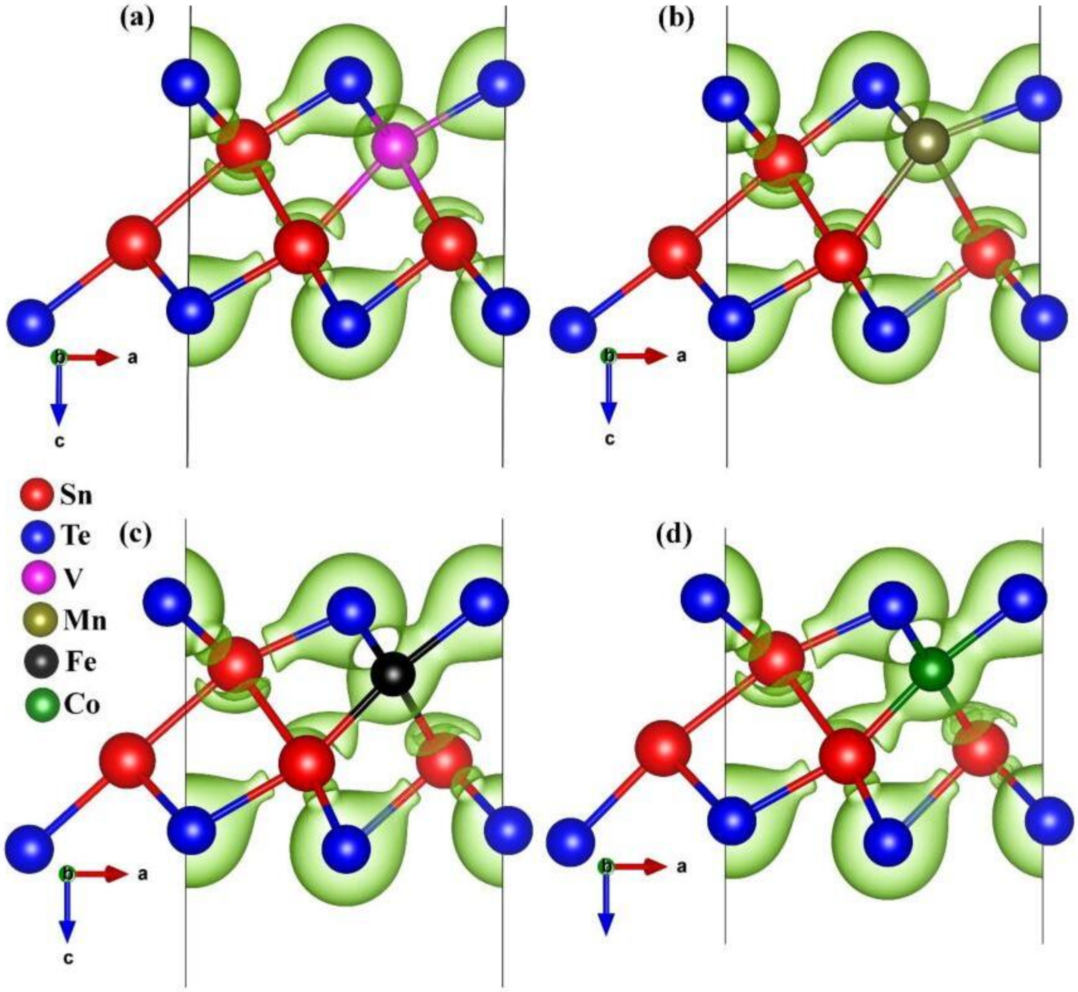

Figure 6.5: Iso-surface plotting of charge density for (a) V@SnTe, (b) Mn@SnTe, (c) Fe@SnTe, and (d) Co@SnTe systems. Here, the light green color indicates the accumulation or distribution of charges. The iso-surface value for these four systems is 0.037 eV/$\AA^3$.

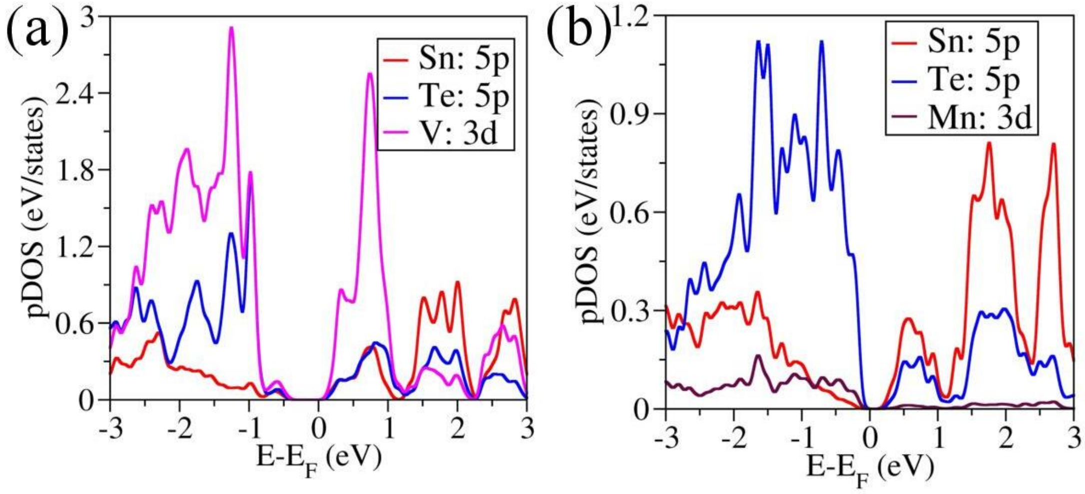

Figure 6.6: Partial density of states (pDOS) of (a) V@SnTe and (b) Mn@SnTe systems. It has been observed that V:3d orbital (shown in magenta color) has a significant contribution in both valence and conduction band near Fermi level, while Mn:3d orbital (maroon color) has a very little contribution in the conduction band. The Fermi level (E_F) is set to zero.

covalent nature of these bonds in all the four 3d-TM doped 2D β'-SnTe systems. On the other hand, the significantly smaller amount of charge density present between the Sn and TM atoms represent the weak van der Waals characteristics of Sn-Sn bonds on all the four 3d-TM doped 2D β'-SnTe systems and TM-Te bonds on the V@SnTe and Mn@SnTe systems. However, in Figures 6.5(c) and 6.5(d), the higher accumulation of charge density again indicates the covalent nature of the Fe-Te and Co-Te bonds in the Fe@SnTe and Co@SnTe systems. So, our results in Figure 6.5 justifies the explanation given earlier in this section by the bond length values.

6.3.3 Electronic structure analysis

After understanding the structural characteristics, stability, and the nature of bonding of the 3d-TM doped 2D β'-SnTe systems, we now analyze the electronic structures of these systems. Figure 6.6 represents the partial density of states (pDOS) of the V@SnTe and Mn@SnTe systems. Furthermore, the pDOS of the

Fe@SnTe and Co@SnTe are found to be metallic in nature. The nature of pDOS represents the covalent characteristics of the Sn-Te and TM-Te bonds, thereby corroborating the justification mentioned in section 6.3.1. In fact, we observe that the significant contribution of V:3d orbital in both the valence and conduction bands near the Fermi level, whereas Mn:3d orbital has comparatively less contribution in the conduction band region in case of Mn@SnTe. Figures 6.7 (a)-(c) represents the electronic band dispersion for 2 × 1 supercell of pristine 2D β'-SnTe systems and also for the V@SnTe and Mn@SnTe systems. The band structures for both the pristine and the 3d-TM (V and Mn) doped 2D β'-SnTe systems indicate that these systems have an indirect bandgap (E_g). In the pristine 2D β'-SnTe systems, the estimated E_g value is 0.55 eV for 2 × 1 supercell. These computed E_g values are significantly higher as compared to that of the bulk SnTe. The nature of the band structure for the unit cell is in full agreement with the earlier reported findings. From Figure 6.7 it is clear that the estimated E_g values increase further in the V@SnTe (1.16 eV) and Mn@SnTe (0.8 eV) systems that are eventually effective to suppress bipolar thermal conductivity, especially at elevated temperatures.[54] Interestingly, the band structure calculations for Fe@SnTe and Co@SnTe systems show that they are metallic in nature. We will comment on their thermoelectric behavior later.

6.3.4 Electrical transport properties

Figure 6.8 depicts the charge carrier transport properties at finite temperatures for SnTe thin layer and 3d transition metal (TM) doped monolayer SnTe. The carrier mobility is evaluated using equation (1.14). The determining factors to estimate carrier mobility are deformation potential constant or carrier-acoustics phonon scattering strength, elastic modulus, carrier effective mass and effective carrier-carrier scatterings in terms of band deformation. And the carrier effective mass

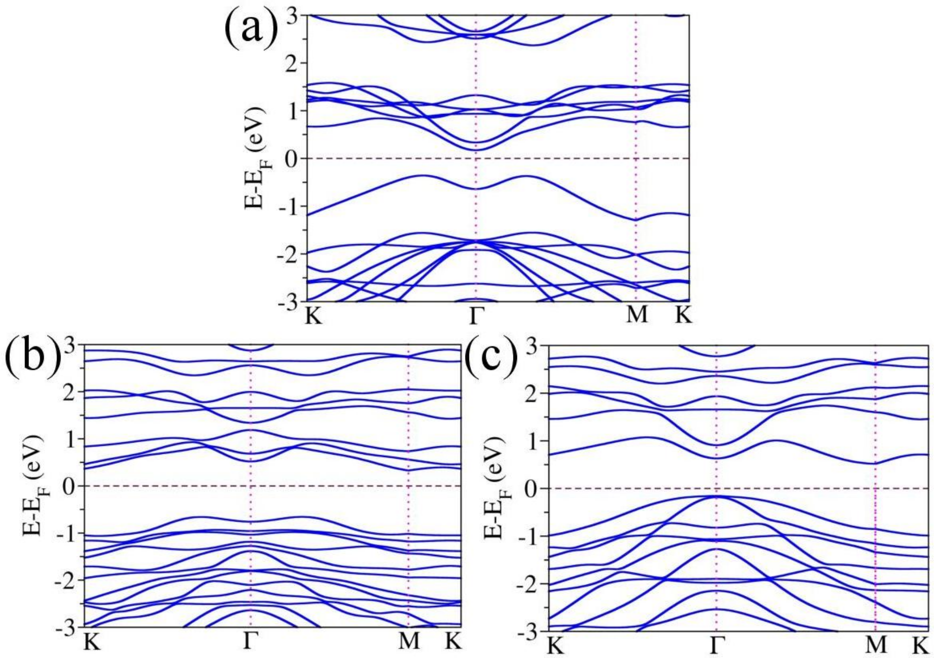

Figure 6.7: Electronic band structures of (a) 2D β'-SnTe, (b) V@SnTe, (c) Mn@SnTe systems, along the high symmetry points in the Brillouin zone. We consider a 2 x 1 supercell to plot the electronic dispersion curve. The reference level is set as Fermi level (zero energy level).

has been estimated from the inverse of the band dispersion curve ($m^* = \frac{\hbar^2}{\frac{d^2E}{d^2k}}$). The carrier phonon scattering strength and elastic modulus are calculated to be 1.72 eV and 12 J/m^2, respectively for pristine monolayer SnTe. While doping V and Mn upon Sn site, E_1 decreases to 1.32 eV and 1.26 eV, respectively. On the other hand, elastic modulus decreases from 12 J/m^2 to 9 J/m^2 for V doping but slightly increases to 12.19 J/m^2 for Mn doping. The decreasing hole-phonon scattering strength along with slightly higher elastic modulus is the reason to achieve higher hole mobility in Mn-doped SnTe.

Analogously, in the case of 3d TM doping (Fe and Co), we achieve significantly higher intrinsic carrier mobility. Here, the parameters required to determine hole mobility due to Fe and Co doping in SnTe thin layers are tabulated in Table 6.3. Similarly, the electron mobility is also obtained using equation (1.14). We have also reproduced hole and electron mobility with the data given in the article by

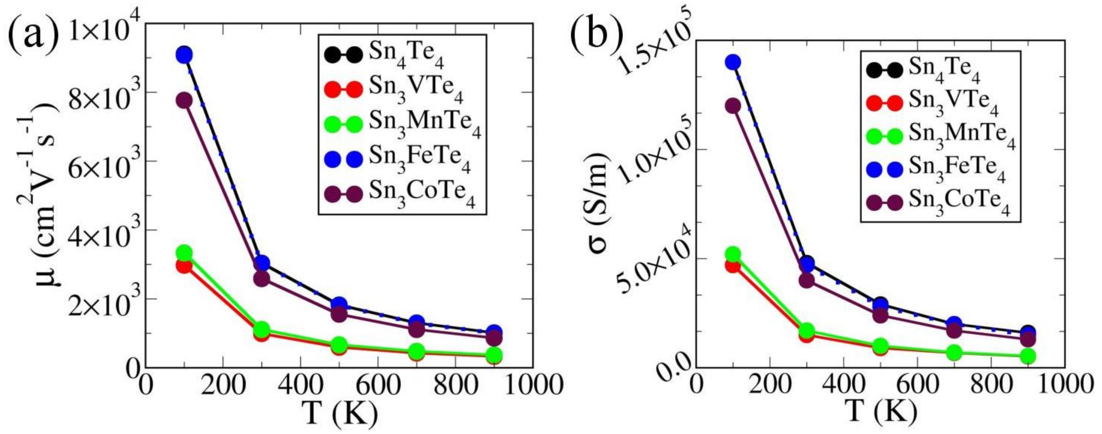

Figure 6.8: (a) charge carrier mobility , (b) electrical conductivity at the temperature range (100-900K).

Dong et al. [32] Now, we estimate the total (hole and electron) mobility for pure and 3d TM doped SnTe and shown in Figure 6.8(a). Although carrier-phonon coupling strength decreases because of V and Mn doping, still mobility decreases due to increased carrier effective mass. In fact, localized d orbital originating from V and Mn atoms arises near the Fermi level which eventually decreases the carrier mobility. In contrast, it is very important to note that elastic modulus increases for Fe and Co doping, and as a result, total mobility increases for the Fe and Co doped cases. As a consequence, mobility reaches the same order of mobility as monolayer SnTe in Fe doped case. Once we obtain intrinsic carrier mobility for pristine as well as doped SnTe, we can easily determine electrical conductivity, σ, using the well known Drude formula $\sigma = ne\mu$. To estimate the electrical conductivity, we have calculated the hole concentration (since it is a p-type material) to be the order of 10^{12} cm^{-2}. Figure 6.8(b) represents the temperature-dependent electrical conductivity for pristine and transition metal doped SnTe. Interestingly, we observe that the electrical conductivity decreases due to V and Mn doping, whereas increases in magnitude for Fe and Co doped SnTe monolayers.

Seebeck coefficient is considered as another important parameter to determine the thermoelectric properties. Ideally, the Seebeck coefficient or thermoelectric

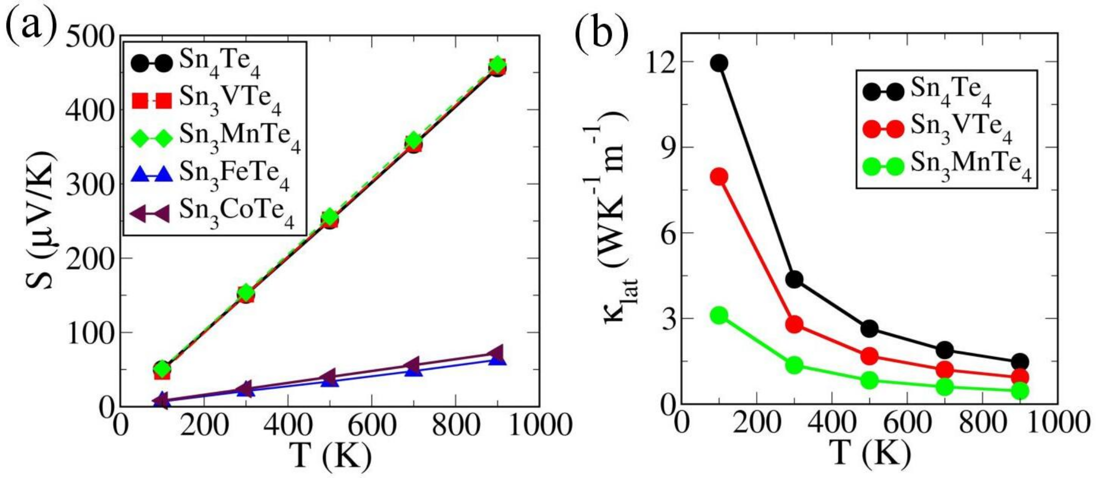

Figure 6.9: (a) Seebeck coefficient S as a function of temperatures. The estimated S for both V@SnTe and Mn@SnTe are slightly higher than pristine 2D SnTe. On the other hand, the Seebeck coefficient turns out to be very low for Fe- and Co-doped 2D SnTe due to the metallic nature of the electronic band structure. (b) the temperature dependent lattice thermal conductivity κ_{lat}.

power (S) is defined as the proportionality constant between the voltage difference to the temperature gradient in a semiconductor. In the present study, we calculate the Seebeck coefficient using equation (1.15) and have shown in Figure 6.9(a). The thermopower shows an increasing trend with higher temperatures. We estimate S to be 251 V/K, 353 V/K, 456 V/K at temperatures 500 K, 700 K, 900 K, respectively. For V and Mn doped systems, we could achieve a slightly higher Seebeck coefficient in the higher temperature limit. We compute S for the V@SnTe system to be 252 V/K, 354 V/K, 458 V/K at temperatures 500 K, 700 K, and 900 K, respectively. In fact, due to Mn doping in SnTe, we find S to be 256 V/K, 359 V/K, 461 V/K at temperatures 500 K, 700 K, and 900 K, respectively. The achievement of a slightly higher Seebeck coefficient is because of the contribution of the d orbitals of the 3d-TM, which appears near the Fermi level. In contrast, Fe and Co doping in SnTe give very low values of Seebeck coefficient even at higher temperatures.

Table 6.3: Deformation potential constant (eV), elastic modulus (Jm^{-2}), and effective mass (in unit of m_0) associated with the hole for pristine and doped SnTe are tabulated below.

Systems	Sn_4Te_4	Sn_3VTe_4	Sn_3MnTe_4	Sn_3FeTe_4	Sn_3CoTe_4
E_1	1.72	1.32	1.26	1.44	1.43
C_{2D}	12.00	9.34	12.19	66.00	43.00
m_x^*	0.22	0.50	0.62	0.66	0.57
m_y^*	0.23	0.50	0.62	0.66	0.57

6.3.5 Thermal transport properties

Other than electrical transport, thermoelectric properties also depend crucially on thermal transport. Lattice thermal conductivity can be evaluated using equation (1.16). Since lattice thermal conductivity has a direct dependence on phonon-phonon relaxation time, the relevant quantity to correctly estimate phonon relaxation time is computed. As can be observed, the phonon-phonon scattering strength gradually increases with V and Mn doping (e.g., 2.37 meV, 2.91 meV, and 3.34 meV for pristine, V@SnTe, and Mn@SnTe, respectively). Using scattering strength and elastic modulus, we can estimate relaxation time and lattice thermal conductivity. Figure 6.9(b) shows temperature-dependent thermal conductivity κ_{lat} for pristine and doped SnTe systems. We estimate lattice thermal conductivity to be 2.64 $WK^{-1}m^{-1}$, 1.89 $WK^{-1}m^{-1}$, 1.47 $WK^{-1}m^{-1}$ at temperatures 500 K, 700 K, and 900 K, respectively for pristine SnTe. Interestingly, our estimated results obtained by solving the Boltzmann transport equation correctly reproduce the earlier reported findings for monolayer SnTe. Now V and Mn doping in the Sn site further reduces the lattice thermal conductivity which has been shown in Figure 6.9(b). Importantly, we achieve quite low value of κ_{lat}, namely, 0.93 $WK^{-1}m^{-1}$ and 0.46 $WK^{-1}m^{-1}$ for V and Mn-doped SnTe systems at 900 K. The achievement of an ultralow lattice thermal conductivity is indeed beneficial for thermoelectricity.

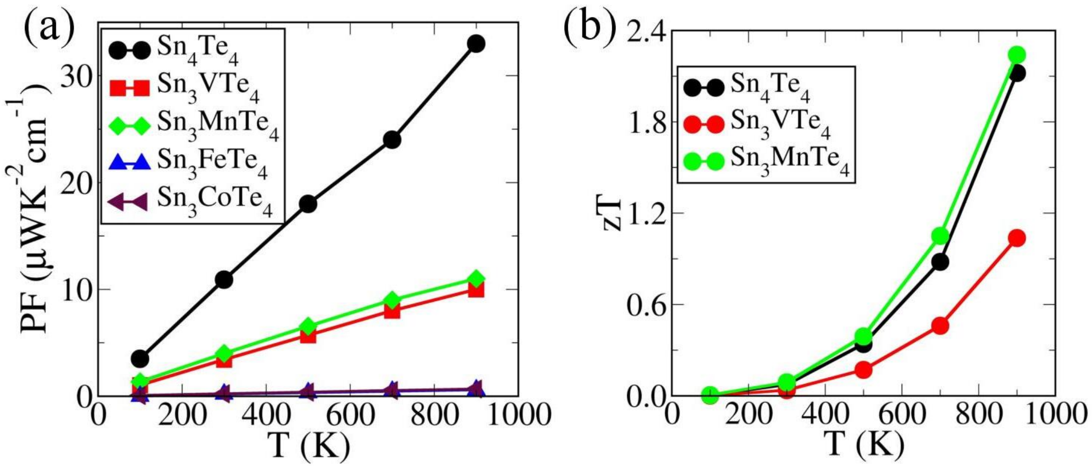

Figure 6.10: (a) power factor (PF) at temperature range (100-900K). We achieve moderate power factor for both V@SnTe and Mn@SnTe, while PF becomes a very small value over the temperature range (100-900K) in case of Fe@SnTe and Co@SnTe. (b) thermoelectric figure of merit (zT) at the temperature range (100-900K).

6.3.6 Power factor and figure of merit

Once electrical conductivity and thermopower are obtained, it is easy to estimate the power factor. We then calculate the thermoelectric figure of merit from the power factor and lattice thermal conductivity. From our estimation, the PF turns out to be 18 $WK^{-1}cm^{-1}$, 23 $WK^{-1}cm^{-1}$, and 33 $WK^{-1}cm^{-1}$ at temperatures 500 K, 700 K, and 900 K for 2D SnTe. The PF for 3d-TM substituted systems are shown in Figure 6.10(a). In fact, upon V and Mn substitution, we achieve moderate PF while it deteriorates upon Fe and Co substitution in Sn sites. The deterioration of PF happens because of the metallic nature of the electronic band structure for Fe and Co systems. Finally, we compute the thermoelectric figure of merit (zT) for pristine and doped SnTe at various temperatures (shown in Figure 6.10(b)). We achieve a very high zT value of 2.14 for 2D SnTe at T=900 K. In fact, V@SnTe and Mn@SnTe predict zT to be 1.04 and 2.24, respectively at T=900 K.

6.4 Conclusions

In summary, we have studied the thermoelectric efficiency of 3d transition metal doped two-dimensional SnTe using first-principles calculations together with Boltzmann transport theory. Analyzing the 3d-TM doped SnTe systems, V and Mn doping results in a very low formation energy and binding energy, thereby providing the possibility of spontaneous doping, while the formation energies and binding energy for the Fe and Co doping in SnTe are comparatively higher, which suggests that V and Mn doping form more stable structure than Fe and Co doping. Moreover, AIMD simulation along with lattice dynamics studies also confirm that pristine and doped SnTe systems are thermally as well as dynamically stable. The current study also suggests that 12.5% substitution of V, Mn even though affects the intrinsic carrier mobility due to increased carrier effective mass and lower elastic constant, that slightly enhances the Seebeck coefficient. On the contrary, Fe and Co substitution drastically reduces the Seebeck coefficient because of semiconductor to metallic transition. We also show that the V and Mn doping decreases the lattice thermal conductivity significantly. In fact, the substantial reduction in lattice thermal conductivity yields a significant enhancement ($\simeq$ 5-6%) in zT values for the Mn@SnTe system as compared to that of the pristine 2D β'-SnTe system. So, overall we can conclude that the Mn@SnTe as well as the V@SnTe systems can be successfully utilized as efficient thermoelectric materials.

6.5 References

[1] Ellabban, O.; Abu-Rub, H.; Blaabjerg, F. Renewable energy resources: Current status, future prospects and their enabling technology. Renewable and Sustainable Energy Reviews 2014, 39, 748-764.

[2] Banerjee, P.; Chakrabarty, S.; Thapa, R.; Das, G. P. Exploring the catalytic

activity of pristine T6[100] surface for oxygen reduction reaction: A first-principles study. Applied Surface Science 2017, 418, 56-63.

[3] Shakeel, S. R.; Takala, J.; Zhu, L.-D. Commercialization of renewable energy technologies: A ladder building approach. Renewable and Sustainable Energy Reviews 2017, 78, 855-867.

[4] Banerjee, P.; Thapa, R.; Rajkamal, A.; Chandrakumar, K. R. S.; Das, G. P. First-principles identification of the origin for higher activity of surface doped carbon nanohorn: Impact on hydrogen storage. International Journal of Hydrogen Energy 2019, 44, 23196-23209.

[5] Shi, X.-L.; Zou, J.; Chen, Z.-G. Advanced Thermoelectric Design: From Materials and Structures to Devices. Chemical Reviews 2020, 120, 7399-7515.

[6] Hao, S.; Dravid, V. P.; Kanatzidis, M. G.; Wolverton, C. Computational strategies for design and discovery of nanostructured thermoelectrics. npj Computational Materials 2019, 5, 58.

[7] Biswas, K.; He, J.; Blum, I. D.; Wu, C.-I.; Hogan, T. P.; Seidman, D. N.; Dravid, V. P.; Kanatzidis, M. G. High-performance bulk thermoelectrics with all-scale hierarchical architectures. Nature 2012, 489, 414-418.

[8] Tan, G.; Zhao, L.-D.; Kanatzidis, M. G. Rationally Designing High-Performance Bulk Thermoelectric Materials. Chemical Reviews 2016, 116, 12123-12149.

[9] Zhou, H.; Liu, P. High Seebeck Coefficient Electrochemical Thermocells for Efficient Waste Heat Recovery. ACS Applied Energy Materials 2018, 1, 1424-1428.

[10] Tritt, T.M. Thermoelectric phenomena, materials, and applications. Annual review of materials research 2011, 41, 433-448.

[11] Zhao, L.-D.; Lo, S.-H.; Zhang, Y.; Sun, H.; Tan, G.; Uher, C.; Wolverton, C.; Dravid, V. P.; Kanatzidis, M. G. Ultralow thermal conductivity and high thermoelectric figure of merit in SnSe crystals. Nature 2014, 508, 373-377.

[12] Luo, Y.; Hao, S.; Cai, S.; Slade, T. J.; Luo, Z. Z.; Dravid, V. P.; Wolverton, C.; Yan, Q.; Kanatzidis, M. G. High Thermoelectric Performance in the New

Cubic Semiconductor $AgSnSbSe_3$ by High-Entropy Engineering. Journal of the American Chemical Society 2015, 142, 15187-15198.

[13] Luo, Z. A.-O.; Cai, S. A.-O.; Hao, S. A.-O.; Bailey, T. A.-O. X.; Spanopoulos, I. A.-O.; Luo, Y. A.-O. X.; Xu, J. A.-O.; Uher, C. A.-O.; Wolverton, C. A.-O. X.; Dravid, V. A.-O.; Yan, Q. A.-O.; Kanatzidis, M. A.-O. Strong Valence Band Convergence to Enhance Thermoelectric Performance in PbSe with Two Chemically Independent Controls. Angewandte Chemie 2021, 133, 272-277.

[14] Roychowdhury, S.; Biswas, K. Effect of In and Cd co-doping on the thermoelectric properties of $Sn_{1-x}Pb_xTe$. Materials Research Express 2019, 6, 104010.

[15] Banik, A.; Shenoy, U. S.; Saha, S.; Waghmare, U. V.; Biswas, K. High Power Factor and Enhanced Thermoelectric Performance of SnTe-$AgInTe_2$: Synergistic Effect of Resonance Level and Valence Band Convergence. Journal of the American Chemical Society 2016, 138, 13068-13075.

[16] Pei, Y.; Shi, X.; LaLonde, A.; Wang, H.; Chen, L.; Snyder, G. J. Convergence of electronic bands for high performance bulk thermoelectrics. Nature 2011, 473, 66-69.

[17] Chang, C.; Wu, M.; He, D.; Pei, Y.; Wu, C.-F.; Wu, X.; Yu, H.; Zhu, F.; Wang, K.; Chen, Y.; Huang, L.; Li, J.-F.; He, J.; Zhao, L.-D. 3D charge and 2D phonon transports leading to high out-of-plane ZT in n-type SnSe crystals. Science 2018, 360, 778.

[18] Biswas, K.; He, J.; Blum, I. D.; Wu, C.-I.; Hogan, T. P.; Seidman, D. N.; Dravid, V. P.; Kanatzidis, M. G. High-performance bulk thermoelectrics with all-scale hierarchical architectures. Nature 2012, 489, 414-418.

[19] L-D. Zhao, S-H. Lo, Y. Zhang, H. Sun, G. Tan, C. Uher, C. Wolverton, V. P. Dravid, and M. G. Kanatzidis, Ultralow thermal conductivity and high thermoelectric figure of merit in SnSe crystals, Nature 508, 373-377 (2014).

[20] Zhao, L.-D.; Tan, G.; Hao, S.; He, J.; Pei, Y.; Chi, H.; Wang, H.; Gong, S.; Xu, H.; Dravid, V. P.; Uher, C.; Snyder, G. J.; Wolverton, C.; Kanatzidis, M.

G. Ultrahigh power factor and thermoelectric performance in hole-doped single-crystal SnSe. Science 2016, 351, 141.

[21] Tayari, V.; Senkovskiy, B. V.; Rybkovskiy, D.; Ehlen, N.; Fedorov, A.; Chen, C. Y.; Avila, J.; Asensio, M.; Perucchi, A.; di Pietro, P.; Yashina, L.; Fakih, I.; Hemsworth, N.; Petrescu, M.; Gervais, G.; Gruneis, A.; Szkopek, T. Quasi-two-dimensional thermoelectricity in SnSe. Physical Review B 2018, 97, 045424.

[22] Shafique, A.; Shin, Y. H. Thermoelectric and phonon transport properties of two-dimensional IV-VI compounds. Sci Rep 2017, 7, 506.

[23] Sharma, S.; Singh, N.; Schwingenschlogl, U. Two-Dimensional Tellurene as Excellent Thermoelectric Material. ACS Applied Energy Materials 2018, 1, 1950-1954.

[24] Askarpour, V.; Maassen, J. Unusual thermoelectric transport anisotropy in quasi-two-dimensional rhombohedral GeTe. Physical Review B 2019, 100, 075201.

[25] Chang, K.; Liu, J.; Lin, H.; Wang, N.; Zhao, K.; Zhang, A.; Jin, F.; Zhong, Y.; Hu, X.; Duan, W.; Zhang, Q.; Fu, L.; Xue, Q. K.; Chen, X.; Ji, S. H. Discovery of robust in-plane ferroelectricity in atomic-thick SnTe. Science 2016, 353, 274-278.

[26] Chang, K.; Kaloni, T. P.; Lin, H.; Bedoya-Pinto, A.; Pandeya, A. K.; Kostanovskiy, I.; Zhao, K.; Zhong, Y.; Hu, X.; Xue, Q. K.; Chen, X.; Ji, S. H.; Barraza-Lopez, S.; Parkin, S. A.-O. Enhanced Spontaneous Polarization in Ultrathin SnTe Films with Layered Antipolar Structure. Adv. Mater 2019, 1804428.

[27] Kooi, B. J.; Noheda, B., Ferroelectric chalcogenides–materials at the edge. Science 2016, 353, 221-222.

[28] Xu, L.; Yang, M.; Wang, S. J.; Feng, Y. P. Electronic and optical properties of the monolayer group-IV monochalcogenides MX (M = Ge, Sn; X = S, Se, Te). Physical Review B 2017, 95, 235434.

[29] Liu, Y.; Zhou, W.; Tang, G.; Yang, C.; Wang, X.; Hong, J. Coexistence of Magnetism and Ferroelectricity in 3d Transition-Metal-Doped SnTe Monolayer. The Journal of Physical Chemistry C 2019, 123, 28919-28924.

[30] Guo, H.; Jiang, W.; She, Q.; Fan, H.; He, X.; Tian, X. SnTe monolayer: Tuning its electronic properties with doping. Superlattices and Microstructures 2019, 130, 12-19.

[31] Li, Y.; Wu, M. N.; Ding, T.; Ma, K.; Liu, F. S.; Ao, W. Q.; Li, J. Q. Promising thermoelectric properties and anisotropic electrical and thermal transport of monolayer SnTe. Applied Physics Letters 2019, 114, 083901.

[32] Dong, B.; Wang, Z.; Hung, N. T.; Oganov, A. R.; Yang, T.; Saito, R.; Zhang, Z. New two-dimensional phase of tin chalcogenides: Candidates for high-performance thermoelectric materials. Physical Review Materials 2019, 3, 013405.

[33] Tominaga, J.; Kolobov, A. V.; Fons, P.; Nakano, T.; Murakami, S. Ferroelectric Order Control of the Dirac-Semimetal Phase in GeTe-Sb_2Te_3 Superlattices. Advanced Materials Interfaces 2014, 1, 1300027.

[34] Tominaga, J.; Kolobov, A. V.; Fons, P. J.; Wang, X.; Saito, Y.; Nakano, T.; Hase, M.; Murakami, S.; Herfort, J.; Takagaki, Y. Giant multiferroic effects in topological GeTe-Sb_2Te_3 superlattices. Science and Technology of Advanced Materials 2015, 16, 014402.

[35] Saito, Y.; Tominaga, J.; Fons, P.; Kolobov, A. V.; Nakano, T. Ab-initio calculations and structural studies of $(SiTe)_2(Sb_2Te_3)_n$ (n: 1, 2, 4 and 6) phase-change superlattice films. Phys. Status Solidi RRL 2014, 8, 302-306.

[36] Sa, B.; Sun, Z.; Wu, B. The development of two dimensional group IV chalcogenides, blocks for van der Waals heterostructures. Nanoscale 2016, 8, 1169-1178.

[37] Bader, R.F.W. Atoms in molecules - a quantum theory, oxford university press 1990, oxford.

[38] Hohenberg, P.; Kohn, W. Inhomogeneous Electron Gas. Physical Review 1964, 136, B864-B871.

[39] Kohn, W.; Sham, L. J. Self-Consistent Equations Including Exchange and Correlation Effects. Physical Review 1965, 140, A1133-A1138.

[40] Kresse, G.; Furthmuller, J. Efficiency of ab-initio total energy calculations for

metals and semiconductors using a plane-wave basis set. Computational Materials Science 1996, 6, 15-50.

[41] Kresse, G.; Hafner, J. Ab initio molecular-dynamics simulation of the liquid-metal–amorphous-semiconductor transition in germanium. Physical Review B 1994, 49, 14251-14269.

[42] Blochl, P. E. Projector augmented-wave method. Physical Review B 1994, 50, 17953-17979.

[43] Perdew, J. P.; Burke, K.; Ernzerhof, M. Generalized Gradient Approximation Made Simple. Phys. Rev. Lett. 1996, 77, 3865-3868

[44] Nose, S. A unified formulation of the constant temperature molecular dynamics methods. The Journal of Chemical Physics 1984, 81, 511-519.

[45] Monkhorst, H. J.; Pack, J. D. Special points for Brillouin-zone integrations. Physical Review B 1976, 13, 5188-5192.

[46] Grimme, S. Semiempirical GGA-type density functional constructed with a long-range dispersion correction. Journal of Computational Chemistry 2006, 27, 1787-1799.

[47] Momma, K.; Izumi, F. VESTA: a three-dimensional visualization system for electronic and structural analysis. Journal of Applied Crystallography 2008, 41, 653-658.

[48] Guo, S.; Zhu, Z.; Hu, X.; Zhou, W.; Song, X.; Zhang, S.; Zhang, K.; Zeng, H. Ultrathin tellurium dioxide: emerging direct bandgap semiconductor with high-mobility transport anisotropy. Nanoscale 2018, 10, 8397-8403.

[49] Lee, H. A Theoretical Model of Thermoelectric Transport Propertiesfor Electrons and Phonons. Journal of Electronic Materials 2016, 45, 1115-1141.

[50] Lee, H., Thermoelectrics: Design and Materials. John Wiley Sons 2016.

[51] Chen, Z.; Zhang, X.; Lin, S.; Chen, L.; Pei, Y. Rationalizing phonon dispersion for lattice thermal conductivity of solids. National Science Review 2018, 5, 888-894.

[52] Ziman, J. M., Principles of the theory of solids. University Press: Cambridge [Eng.], 1972.

[53] Cordero, B.; Gomez, V.; Platero-Prats, A. E.; Reves, M.; Echeverria, J.; Cremades, E.; Barragan, F.; Alvarez, S. Covalent radii revisited. Dalton Transactions 2008, 2832-2838.

[54] Tan, G.; Shi, F.; Hao, S.; Chi, H.; Bailey, T. P.; Zhao, L.-D.; Uher, C.; Wolverton, C.; Dravid, V. P.; Kanatzidis, M. G. Valence Band Modification and High Thermoelectric Performance in SnTe Heavily Alloyed with MnTe. Journal of the American Chemical Society 2015, 137, 11507-11516.

[55] Biswas, R.K.; Pati, S.K. Exploring a Superlattice of SnO-PbO: A New Material for Thermoelectric Applications. ACS Applied Energy Materials 2021, 4(3), 2081-2090.

7

High Thermoelectric Figure of Merit at Near-Room-Temperature in n-type Ag_2Se through Rashba Effect and Entropy Engineering

7.1 Introduction

Recent issues on rising temperature due to global warming emphasize the inhibition of carbon emissions and strengthen the energy management and sustainability measures to alleviate the effects of climate change.[1-2] Therefore, research on renewable energy sources such as wind, solar and geothermal energy sources have attracted much attention for the last two decades. Especially, geothermal energy is the internal heat generated in the Earth's interior near-room-temperature regime (150-400 ^{0}C), which can widely be used to recover waste heat and utilise it for power generation.[3-4] However, the extensive use of thermoelectric materials is limited by low thermoelectric efficiency. It is related to dimensionless quantity i.e. figure of merit $zT = \frac{\sigma S_b^2}{\kappa}T$, where S_b, σ, and T are the Seebeck coefficient, electrical conductivity, thermal conductivity, and absolute temperature, respectively.[5] Interestingly, the efficient way to enhance the zT value is determined by a combination of two major factors; electrical transport should be high, characterised by power factor ($S_b^2\sigma$) and glass-like thermal transport. Some of the compounds which demonstrate high zT at mid-range temperature have been achieved in lead chalcogenide, which not only contains toxic lead (Pb) but also encompasses less abundant tellurium (Te).[6] The scarcity of Te implies one has to search for new earth-abundant elements that could lead to large zT[7] near-room-temperature through innovative approaches such as defect structure engineering[8], band convergence[9], nano-structuring[10], and phonon glass electron-crystal[11].

Presently, entropy-engineering has become another unique strategy for the reduction of lattice thermal conductivity (κ_{lat}) of a crystalline solid by manipulating configurational entropies. Configurational entropy increases when multiple components occupy identical atomic sites inside the crystal. Multicomponent chalcogenide like $(\mathrm{SnTe})_{1\text{-}2x}$ $(\mathrm{SnSe})_x$ $(\mathrm{SnS})_x$, $(\mathrm{GeTe})_{1\text{-}2x}$ $(\mathrm{GeSe})_x(\mathrm{GeS})_x$ and $(\mathrm{PbTe})_{1\text{-}2x}$ $(\mathrm{PbSe})_x$ $(\mathrm{PbS})_x$ are very well known pseudoternary systems to exhibit low lattice thermal conductivity. It occurs because an increase in configurational entropy arises from point defect phonon scattering, mass fluctuation of different elements and strain (induced from atomic size mismatch.)[12-16] Additionally, the large atomic size mismatch between the constituent atoms could also lead to locally strained domains in the global structure. Moreover, the large size mismatch of Te and S atoms would generate off-centering of S atoms which introduces local dipole moment and soft phonon modes in the crystal. As a result, the soft phonons effectively scatter heat-carrying acoustics phonons and reduce lattice thermal conductivity significantly.[17] Along with entropy engineering, the Rashba effect has an additional effect in the fields of thermoelectricity through the spin-orbit coupling

(SOC) mechanism in the charge carrier transport phenomenon.[18] The Rashba spin splitting leads to a distinctive feature in the electronic density of states (DOS) due to the unique Fermi surface topology [19]. Consequently, the power factor ($S_b^2\sigma$) is found to be large because of the sharp peak in DOS [20]. Thus, the Rashba spin splitting can potentially be a very effective mechanism for thermoelectricity.

Chalcogenide families, such as, PbTe and its solid solution with PbSe and PbS are well known semiconductors to show excellent thermoelectric efficiency.[21] However, PbTe based materials are not eco-friendly because of the presence of Pb, and as a result, the use of PbTe remains unsuitable for mass-market applications. Various other thermoelectric materials, such as, SiGe,[22] skutterudites,[23] half-Heusler compounds,[24] colusites,[25] SnSe,[26] SnS,[27] Cu_2Se,[28] exhibit high zT (between 1.5-2.5 above T=500K). Interestingly, none of the above materials show zT above 1.0 at room temperature except Bi_2Te_3 [$zT \simeq$ 1.3-1.7]. Although the performance of Bi_2Te_3 has been strategically improved via various mechanisms, it indeed turns out to be p-type.[29] In Contrast, the n-type Bi_2Te_3 remains below $zT \simeq 1.0$ at room temperature.[30] Meanwhile, it has become imperative to explore new n-type thermoelectric materials that exhibit zT above unity near-room-temperature as maximum energy wastage in line with geothermal power generation occurs approximately in this temperature range.[31]

The current materials with high Thermoelectric (TE) performance working in near-room-temperature range mainly include Bi_2Te_3-based systems, Mg_3Sb_2, MgAgSb, Mg_2(Si, Sn), $AgSbTe_2$ and β-Ag_2Q (Q=Se, Te)[32-33]. Recently, there has been sustained research for quite some time, where β-Ag_2Q is considered as a promising candidate for thermoelectric application because of its intrinsic metal-like electrical conductivity and inherently glass-like thermal conductivity at room temperature.[32,34] Experimentally, Silver selenide specimens were prepared by a direct reaction of the source elements (6N purity) in evacuated ($\simeq 10^{-4}$ Torr) quartz tubes and the subsequent X-ray diffraction analysis confirmed the formation of β-Ag_2Se.[34] However, this material shows discrepancies in zT at the temperature range 300-400 K, which have been reported in the literature.[35-36] Subsequent efforts were attempted towards increasing the figure of merits of thermoelectric materials.[37] Finally, the achievement of a high $zT > 1.0$ at temperature range (300-375 K) has been demonstrated by improving charge carrier mobility along with tuning of the carrier concentration via the addition of minute anion excess.[38] In due course, the synthesis of solid solution, $Ag_2Se_{1\text{-}x}Te_x$ has been confirmed by X-ray diffraction data and Rietveld refinement.[39] In fact, Drymiotis et al. showed Ag_2Se-As_2Te phase diagram at different compositions using density functional theory (DFT) calculations. In the present study, we have further doped the Sulphur atom in the ternary phase and have examined the thermoelectric performance of the pseudoternary phase, Ag_2Se-Ag_2Te-Ag_2S. Our analysis encompasses the comprehensive understanding in calculating intrinsic carrier mobility, not only limited by longitudinal acoustics phonon scattering, rather governed by longitudinal optical phonons. Achieving the excellent thermoelectric performance at near-room-temperature range in an Ag_2Se-rich phase, $Ag_2\ Se_{1\text{-}2x}Te_x\ S_x$ by minimizing lattice thermal conductivity (κ_{lat}) using the mechanism, such as, configurational entropy engineering, is demonstrated. Furthermore, we will also discuss an increment of power factor due to the Rashba type of spin splitting which leads to a very high value of $zT \simeq 2.1$ at 400 K in $Ag_2Se_{0.5}Te_{0.25}S_{0.25}$.

7.2 Theoretical Section

7.2.1 First-principle formalism

First-principles based density functional theory calculations have been performed by a Quantum Espresso package[40] which employs the pseudopotential model considering the ion-electron interaction inside the material. We use full relativistic projected augmented wave(PAW) pseudopotentials[41-42] together with exchange-correlation energy of the electrons with generalized gradient approximated (GGA)[43] functional parametrized by Perdew, Burke, Erzenhoff (PBE).[44] The crystal structure is fully relaxed using the conjugate gradient scheme until the magnitude of Helmann-Fynman force becomes less than 0.025 eV/$\AA$. The electronic wave function and charge density cutoff are taken to be 70 Ry and 400 Ry, respectively. Brillouin zone integration of orthorhombic crystal structure is sampled on the uniform grid of 24 x 16 x 16 k-points. A strict energy convergence of 10^{-8} eV has been used to obtain phonon frequencies accurately. The sharp discontinuity of the electronic states near the Fermi level is smeared out with the Fermi-Dirac distribution function with a broadening of 0.003 Ry.

We consider the orthorhombic phase of Ag_2Se, β-Ag_2Se, that undergoes a first-order phase transition to a cubic phase around 407 K. The low-temperature phase is a narrow bandgap semiconductor with space group $P2_12_12_1$ and lattice parameters a=4.35 Å, b=7.07 Å and c=7.78 Å. [45,46] The unit cell of β-Ag_2Se consist of 12 atoms with four molecules of Ag_2Se totaling 8 Ag and 4 Se atoms. At high temperature above 407 K, it transforms to a cubic phase where the materials become metallic with Ag atoms becoming superionic in nature.[47] We also incorporate the spin-orbit coupling (SOC) effect while calculating band structure. It has been observed that the effect of SOC is very prominent for doped Ag_2Se. Pristine, S-doped, Te-doped and co-doped (Te & S) Ag_2Se have been simulated to obtain electronic band structure along the high symmetry points. Furthermore, phonon dispersion properties of pristine and doped Ag_2Se have been calculated using density functional perturbation theory (DFPT). Ag_2Se unit cell containing 12 atoms, is considered for phonon frequency calculation. A uniform grid of 2 x 2 x 2 q-mesh is taken into consideration. To deeply understand the origin of ultralow lattice thermal conductivity, we further focused on various branches in the phonon dispersion curve of both pristine and doped Ag_2Se. In addition to that, we have also computed the configurational entropy or mixing of entropy using the formula:

$$\Delta S_{max} = -nR(x_1 ln x_1 + x_2 ln x_2) \tag{7.1}$$

where x_1 and x_2 are mole fractions of species 1 and 2, respectively.

7.2.2 Formation energy (F.E) and Binding energy (B.E) calculations

$$F.E = E(Ag_2Se_{1-x}M_x) + E(Se) - E(Ag_2Se) - E(M) \tag{7.2}$$

$$B.E = E(Ag_2Se_{1-x}M_x) - E(Ag_2Se_{1-x}) - xE(M) \tag{7.3}$$

here, M = Te & S atoms. E(Se), E(Ag_2Se), E(M) are the single Se atom in the unit cell, Ag_2Se unit cell, and single M atom in the unit cell, respectively. On the other hand, E($Ag_2Se_{1-x}M_x$), E(Ag_2Se_{1-x}), E(M) are total energy of unit cell where one M atom substituted Se atom, one Se atom absent Ag_2Se_{1-x} unit cell, and single M atom unit cell, respectively.

7.2.3 Transport calculations

To calculate mode resolved intrinsic carrier mobility limited by longitudinal optical (LO) phonon, we recall that the small-momentum behaviour of the Fröhlich interaction is well described by the leading order in Vogl's model for 3D semiconductor[65]:

$$g^{3D}_{Fr}(q_p) = \frac{4\pi e^2}{V|q_p|\epsilon^q_p} \sum_a \frac{e_{qp}.Z^b_a.e_{qpLO}}{\sqrt{2M_a\omega_{qpLO}}} \tag{7.4}$$

where e is the electronic charge, V is the unit cell volume, ϵ^q_p is the bulk dielectric constant and $e_{qp} = \frac{q_p}{|q_p|}$. M_a is the atomic mass, Z_a^b is Born effective charge associated with a particular atom, a, q_{pLO} is the longitudinal optical phonon frequency at wave vector q_p. Thus the total scattering rates due to LO phonon can be written in terms of Fröhlich interaction as follows[66]:

$$\frac{1}{\tau_{LO}} = \frac{V}{4\pi^2}\frac{2\pi}{\hbar}\int_0^{2\pi} d\phi \int_{qmin}^{qmax} |g_{Fr}^{3D}(q_p)|^2 \frac{1}{\hbar\omega_{qp}} q_p(n_{\hbar\omega_{qp}} + \frac{1}{2} \mp \frac{1}{2})dq \tag{7.5}$$

Once we determine τ_{LO}, we can evaluate longitudinal optical phonon limited carrier mobility using the expression $\mu_{LO} = \frac{e\tau_{LO}}{m^*}$. Using Matthiessen's rule $\frac{1}{\mu} = \frac{1}{\mu_{LA}} + \frac{1}{\mu_{LO}}$, we obtain effective carrier mobility (μ). Finally, the electrical conductivity can be calculated using the Drude formula $\sigma = ne\mu$, where n: carrier concentration, e: electronic charge.

7.3 Results and Discussion

In this work, we have considered the orthorhombic phase of Ag_2Se (β-Ag_2Se) whose full description of its crystal structure was studied by Wiegers in 1971 based on X-ray powder diffraction data[55]. We notice that all of the crystallographic sites corresponding to Ag atoms are not equivalent. This particular phase contains crystallographically distinct two silver atoms, Ag1 is coordinated tetrahedrally, whereas Ag2 atoms are placed in an almost triangular symmetry [Shown in Figure 7.1]. Generally, Ag_2Se seems to be a non-stoichiometric compound at both low as well as in high-temperature phases. In fact, the low-temperature phase of Ag_2Se reveals not only excellent thermoelectric efficiency even at room temperature but rather is also an n-type semiconductor. Despite numerous research on thermoelectric properties of Ag_2Q (Q=Te, Se) reported previously,[32-35] to date, there is no significant studies on pseudoternary (Ag_2Se-Ag_2Te-Ag_2S) system for

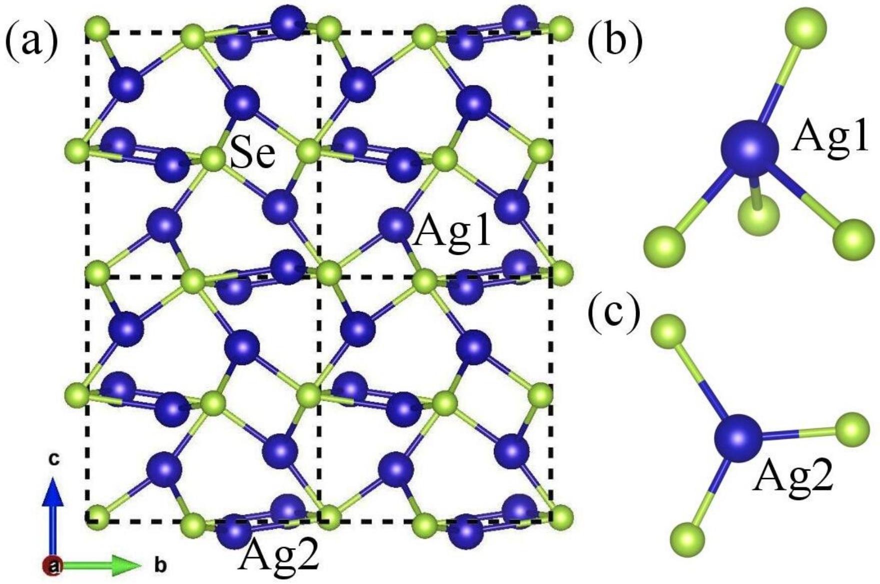

Figure 7.1: Crystal structure of Ag_2Se at room temperature. Silver atoms are shown in blue colours, selenium atoms in light green colours. (a) Ag_2Se crystal structure viewed from a-axis. Local atomic coordination of Ag atoms in the crystal structure where (b) Ag1 atoms are in tetrahedral geometry. (c) the coordination sphere of Ag2 is triangular geometry.

thermoelectric application because of its complex chemistry. Here, we discuss the structural, thermodynamical, chemical aspect and thermoelectric properties of the pseudoternary phases of Ag_2Se. Also, to verify our methods, we have calculated the Seebeck coefficients, electronic conductivity, thermal conductivity and zT values for Ag_2Se, Te doped Ag_2Se and these have been verified with corresponding experimental values for these systems. The theoretically calculated thermoelectric parameters such as μ, κ_{lat}, zT for Ag_2Se obtained solving BTE are 2457 S/cm, 1.01 $Wm^{-1}K^{-1}$, 1.05, respectively. These values match fairly well with experimental values of 2000 S/cm, 0.96 $Wm^{-1}K^{-1}$, 0.96, respectively. In fact, we also compared thermoelectric paremeters after Te doping in Ag_2Se. With Te doping, κ_{lat} decreases and reaches 0.6 $Wm^{-1}K^{-1}$ which is well consistent with the theoretically calculated value 0.63 $Wm^{-1}K^{-1}$.

Recently, ab-initio based density functional perturbation theory (DFPT) methods have become well-established techniques to investigate the structural stability

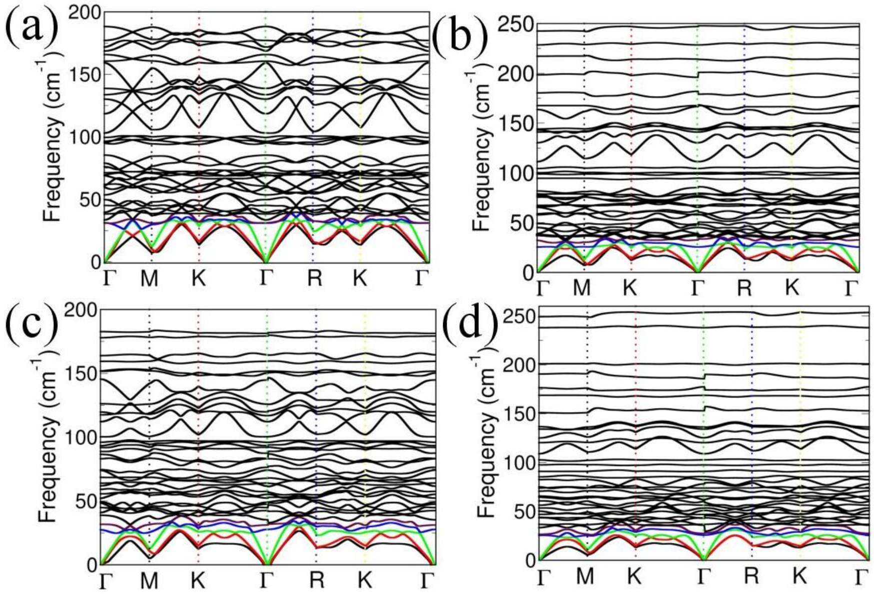

Figure 7.2: Phonon dispersion curve of (a) Ag_8Se_4, (b) Ag_8Se_3S, (c) Ag_8Se_3Te, (d) Ag_8Se_2TeS, have been calculated using DFPT and plotted as a function of q-point. The lattice dynamics curves signify both pristine and doped Ag_2Se are dynamically stable. The green and red color phonon band represent longitudinal and transverse acoustics mode, respectively. On the other hand, blue color phonon band signifies low energy optical phonon mode.

of various materials.[56,57] In this regard, our lattice dynamics study using phonon dispersion calculations reveal that pristine and doped Ag_2Se are dynamically stable. In phonon dispersion curves shown in Figure 7.2, we observe that all the vibrational modes are positive in magnitude which implies structural stability of both pristine and doped Ag_2Se crystal structures. Furthermore, thermodynamic stability is also examined performing formation energy and binding energy calculations for doped Ag_2Se. The estimated formation energies for S-doped, Te-doped and Te & S co-doped Ag_2Se are found to be -0.81 eV, -0.27 eV and -0.40 eV, respectively (Calculated using Equation 7.2). Moreover, binding energies are also calculated, which turns out to be -6.12 eV, -5.02 eV and -10.47 eV, respectively (Calculated using Equation 7.3). Interestingly, formation energy in combination with binding energy determines the chemical stability of these pseudobinary and pseudo-ternary phases of Ag_2Se.

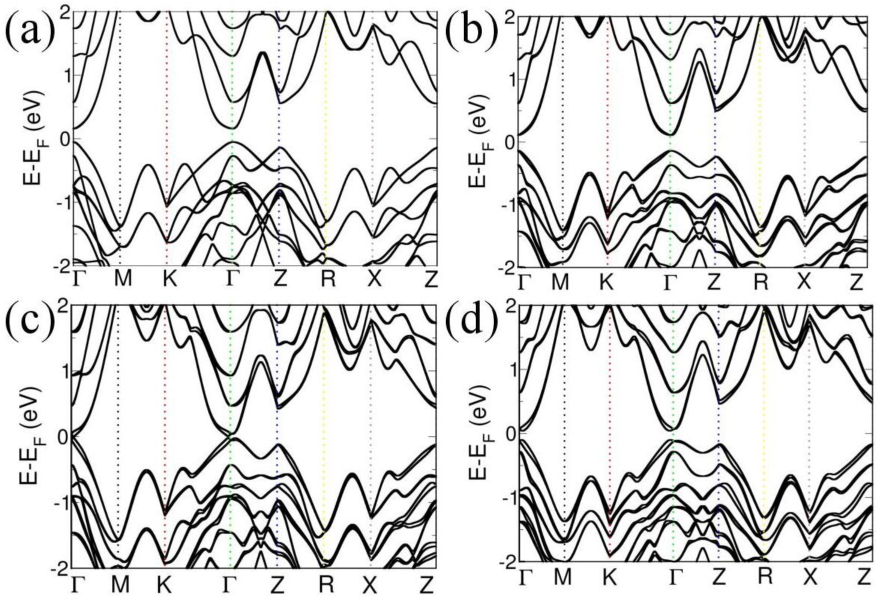

Figure 7.3: Electronic band structure of (a) Pristine, (b) S doped, (c) Te doped, (d) Te & S co-doped, Ag_2Se, along the high symmetry k-points. All the band dispersions are plotted including spin-orbit coupling (SOC) due to the presence of heavy metals in the unit cell. The Fermi level is considered as a reference for each figure.

In order to determine the electronic structure properties of all these systems, we use density functional theory (DFT) calculations. The calculations are carried out for Te and S co-doped Ag_2Se, Te-doped Ag_2Se, S-doped Ag_2Se and undoped Ag_2Se systems. Figure 7.3 represents electronic band dispersion of pristine, S-doped, Te-doped and Te & S co-doped, Ag_2Se, respectively along the high symmetry points. The bandgap estimated at the PBE level for pristine is well consistent with other theoretical calculations.[55] It is interesting to note that the sulphur doping widens the bandgap which is also shown in Figure 7.3(b). In contrast, the Te-doping narrows down the band gap between valence band maxima (VBM) and conduction band minima (CBM) and most importantly lifts the spin degeneracies due to spin-orbit coupling (SOC) originated because of the presence of heavy nuclei in the unit cell (See Figure 7.3(c)). Finally, Figure 7.3(d) indicates that Te & S co-doping serves the combined purpose simultaneously that not only opens up the

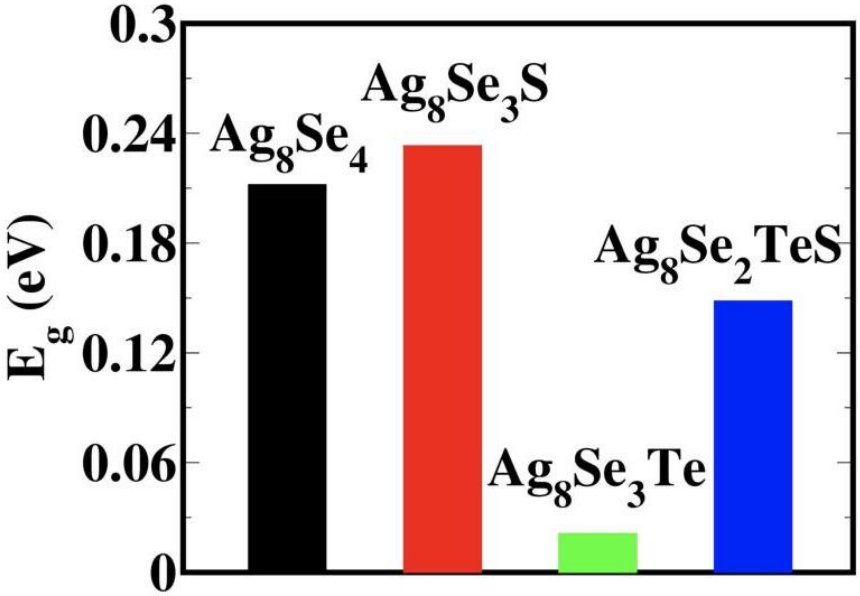

Figure 7.4: PBE-SOC band gap for pristine and doped Ag_2Se

band gap between VBM and CBM but also lifts spin degeneracy near the Fermi level which is effective to enhance electrical conductivity. In fact, we compare bandgap for pristine and doped Ag_2Se and shown in Figure 7.4.

Fundamentally, the SOC driven spin dependent band structure splitting is known as the Rashba effect. In fact, the indirect bandgap along with a larger number of energy bands near the Fermi level, originated due to the Rashba effect, would be beneficial for thermoelectric performance, as we will see later in this chapter. To understand the Rashba effect rigorously, we have calculated band structures for pristine, Ag_2Se and doped Ag_2Se, which are shown in Figure 7.5. The k-dependent spin-splitting of the conduction band shifts the band edge from the high symmetry Γ-point due to Tellurium doping along both K $\longrightarrow$ Γ and M $\longrightarrow$ Γ directions. The momentum offset, Δk, is the difference between the Γ-point and shifted band-extrema in k-space. For Te-doped Ag_2Se and Te & S co-doped Ag_2Se, Δk in the conduction band along M $\longrightarrow$ Γ high symmetry directions are 0.025 and 0.037 $\mathring{A}^{-1}$, respectively. Whereas, Δk for such splitting in its valence band is found to be the same as 0.025 $\mathring{A}^{-1}$ along the M $\longrightarrow$ Γ high symmetry directions for single doping and co-doping cases (see Figures 7.5(c) and 7.5(d)). Therefore, we conclude from the above discussions that the extent of momentum offset differing of Δk in the frontier bands create an indirect bandgap for co-doped (Te & S) Ag_2Se, leading directly to lowering of the electron-hole recombination rates. However, the extent of splitting in the conduction band for S-doped Ag_2Se along the K $\longrightarrow$ Γ and M $\longrightarrow$ Γ directions is quite small compared to the same for Te doped systems. Interestingly, the weak band-splitting observed for S-doped Ag_2Se actually does not arise due to SOC, rather it is due to the off-centering of S atoms from its equilibrium position(shown in Figure 7.6). In fact, due to off-centering (the S atom from its original position), the crystal structure further gains 2.09 meV of energy. The strength of the Rashba effect can be calculated using the parameter $\alpha = \frac{E_R}{2\Delta k}$, where E_R is the amplitude of the band splitting at the band edge in a particular direction. The estimated value for the co-doped Ag_2Se in the M $\longrightarrow$ Γ direction is 1.004 eV$\mathring{A}$ which is of the same order as those reported by previous computational studies on Ag_2Te.[55]

To further examine the consequence of the Rashba effect on electronic structure, we plot the density of states (DOS) in Figure 7.7(a). Surprisingly, we find that the total DOS shows a sharp peak near the Fermi level because of Te doping in the unit cell. In fact, pristine and S-doped Ag_2Se does not exhibit any such contribution near the Fermi level. Consequently, a sudden peak in the total DOS as a result of tellurium doping gives rise to increase in DOS effective mass, contributing to enhancement in the Seebeck coefficient. We have also studied the atomic orbital projected DOS (pDOS) to understand the orbital contribution due to the Rashba effect. In fact, it has been confirmed from the pDOS in Figure 7.7(b) that the tellurium ions have the highest orbital contribution near the Fermi level and consequently Te's are mainly responsible for Rashba types of effect.

Finally, we perform transport calculations based on favourable electronic band

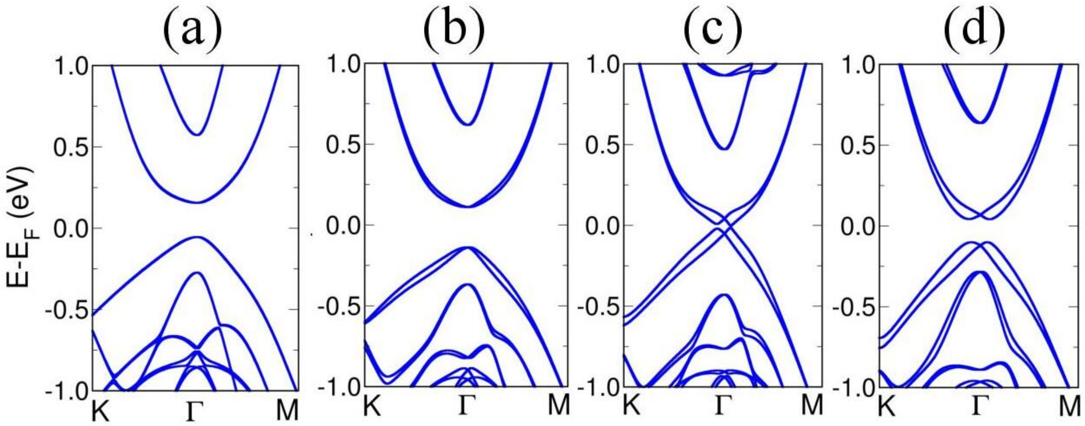

Figure 7.5: Rashba type effect in Ag_8Se_4. The PBE-SOC electronic band structure of (a) Ag_8Se_4, (b) Ag_8Se_3S, (c) Ag_8Se_3Te, (d) Ag_8Se_2TeS, have been plotted for a dense k-grid. The Rashba splitting for Ag_8Se_2TeS system in both VBM and CBM along the M $\longrightarrow \Gamma$ and K $\longrightarrow \Gamma$ directions are prominent. Interestingly, momentum offset (k) for co-doped systems are not equal for VBM and CBM which transform direct to indirect bandgap and effectively help to reduce electron-hole recombination rates.

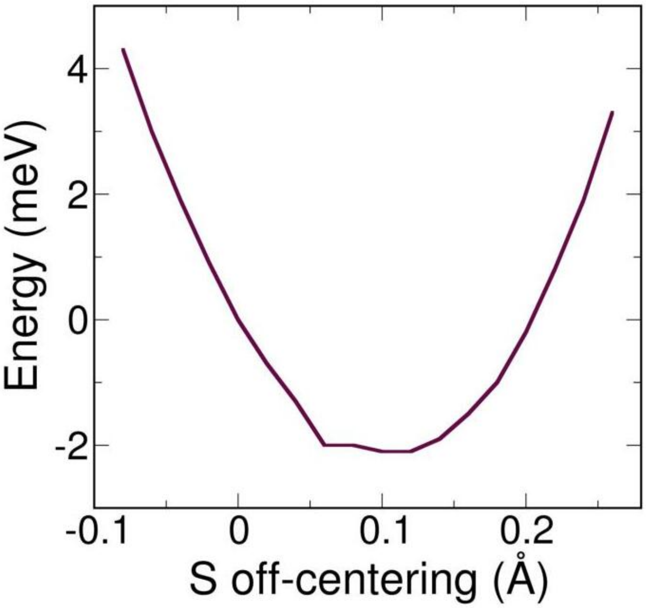

Figure 7.6: Energy profile vs. coordinate of displacement of sulphur (S) atom from its equilibrium position. Through the displacement (around 0.1 $\AA$) of the S atom, the crystal reduces energy by 2.09 meV.

structure to evaluate Seebeck coefficient (S_b), electrical conductivity (σ) and thermoelectric power factor ($S_b^2\sigma$) for pristine and doped Ag_2Se. As described in the computational section, we solve the Boltzmann transport equation (BTE) within relaxation time approximation (RTA) to estimate the Seebeck coefficient, (S_b) and mobility (μ). We compute S_b using equation (**1.12**), which is plotted in Figure 7.9(a) within the temperature range (100-400 K). Interestingly, the estimated Seebeck coefficient turns out to be negative which implies n-type carriers are the determining factor for transport in Ag_2Se. We now compare the calculated S_b for pristine Ag_2Se (197 μV/K at 200 K) with the experimentally measured Seebeck coefficient (175 μV/K at 200 K).[34] Accordingly, the S_b for Te-doped Ag_2Se has been calculated to be 155 μV/K at 400 K, which is slightly lower than pristine Ag_2Se. Therefore, we substitute Sulphur in place of Se and the estimated Seebeck coefficient turns out to be 525 μV/K, 292 μV/K at 400 K for S-doped and Te & S co-doped Ag_2Se, respectively. Importantly, as can be seen, the S_b (292 μV/K at 400 K) estimated in the case of co-doping is far more than Ag_2Te (150 μV/K at 400 K).[58]

We calculate intrinsic charge carrier mobility values, considering the fact that the carriers are not only scattered by longitudinal acoustic phonons but also limited by low energy longitudinal optical phonons. According to deformation potential theory (DPT), the charge carrier mobility, (μ_{LA}) largely depends on the carrier scattering information in combination with carrier effective mass and deformation potential constant (see Table 7.1). In fact, the carrier effective mass (m^*) has been derived from the 2nd order derivative of electronic band dispersion curves with momentum which is tabulated in Table 7.1. We further compare m^* for pristine Ag_2Se with other ab-initio results.[59] Using these parameters, we find temperature-dependent carrier mobility, (μ_{LA}) using equation (**1.10**). To incorporate the longitudinal optical (LO) phonon limited carrier transport, we use the Fröhlich interaction term which is described in equation (7.4). The carrier-optical

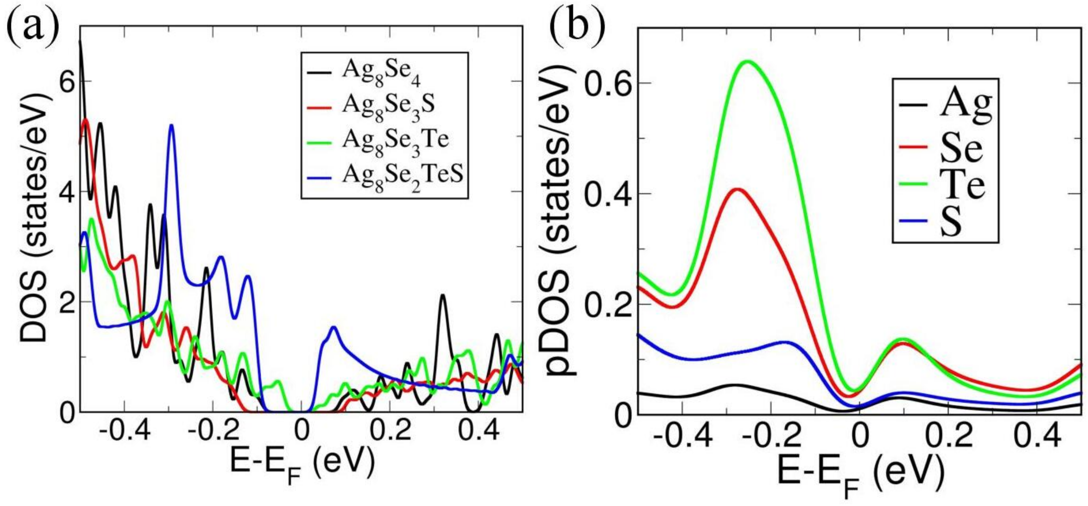

Figure 7.7: (a) Total density of states (DOS), (b) atom projected DOS (pDOS), have been plotted as a function of energy. Interestingly, we observe sharp peaks just near the Fermi level in DOS for the Ag_8Se_2TeS system (blue line). From pDOS, it is clear that the atom projected orbital arising near the Fermi level predominantly originated from the Te atom (represented by green colour). The Fermi level is considered as a reference for each figure.

phonon scattering strength, ($g^{3D}_{Fr}(q_p)$) depends upon Born effective charge (Z^b_a), bulk dielectric constant (ϵ^q_p) and magnitude of an optical phonon, ($\omega_{qp}LO$). These parameters can easily be obtained using density functional perturbation theory (DFPT) implemented in Quantum Espresso distribution. With these, the scattering rate can be computed using equation (7.5) and which can further be used to calculate the optical phonon limited intrinsic mobility, (μ_{OP}). Finally, the mode resolved carrier mobility is shown in Figure 7.8, which turns out to be of the order of 10^3 for doped Ag_2Se at temperature 400 K. The mobility for pristine Ag_2Se evaluated considering the scattering model driven by both acoustic as well as optical phonons, is eventually well consistent with experimental results (experimentally $\mu \simeq 2000$ S/cm at 300 K).[34] Once carrier mobility is known (shown in Figure 7.9(b)), we can calculate carrier electrical conductivity using the Drude formula $\sigma = ne\mu$ and are shown in Figure 7.9(c). Here, we find that carrier concentration is of the order of 10^{19} cm^{-3}. The estimated σ for pristine, S-doped, Te-doped, co-doped (Te & S) Ag_2Se are found to be 2457 S/cm, 432 S/cm, 7499 S/cm, 3160

S/cm, respectively, at room temperature. To validate DPT theory, we compare theoretically predicted σ for pristine Ag_2Se (2457 S/cm at 300 K) with experimental value (1988 S/cm at 300 K).[34] The enhancement of electrical conductivity in the case of Te-doping occurs due to the appearance of multiple levels near the Fermi energy as a consequence of the Rashba type spin splitting. Since carrier electrical conductivity increases due to Te doping, it has a direct impact on the thermoelectric power factor (PF). As a result, we achieve PF to be 152 $Wcm^{-1}K^{-2}$ for Te & S co-doped Ag_2Se at 300 K. The thermoelectric power factor for pristine and doped Ag_2Se are shown in Figure 7.9(d).

Table 7.1: Deformation potential constant, E_1 (eV), elastic modulus, C_{3D} ($10^{11}Jm^{-3}$), and effective mass, m^* (in unit of m_0) associated with the electron for pristine and doped Ag_2Se are tabulated below.

Systems	Ag_8Se_4	Ag_8Se_3S	Ag_8Se_3Te	Ag_8Se_2TeS
E_1	38.57	2.24	1.14	2.40
C_{3D}	119	2.74	3.57	1.47
m^*	0.28	0.36	0.21	0.14

Figure 7.10(a) displays magnitudes of soft vibrational modes at high symmetry M and K-points in the Brillouin zone. As can be seen, some of the modes have exceptionally low soft vibrational frequencies. The phonon frequency for pristine Ag_2Se at M-point (K-point) is found to be 7.60 cm^{-1} (13.65 cm^{-1}). For S-doped, Te-doped and Te & S co-doped Ag_2Se, phonon modes get further softer, which would eventually be effective for good thermoelectric performance. The observed phonon modes (cm^{-1}) at M-point (K-point) are found to be 6.82 (12.07), 4.40 (11.7), 4.31 (11.58) for S-doped, Te-doped and Te & S co-doped Ag_2Se, respectively. Interestingly, the frequency of the soft phonon mode at M-point for the co-doped system is in the same order of n-type BiSe.[60] To unravel the origin of such soft mode in the phonon spectra, we present phonon density of states (DOS), determined from first principles. Total phonon density of states (Figure 7.10(b)) of Te-doped

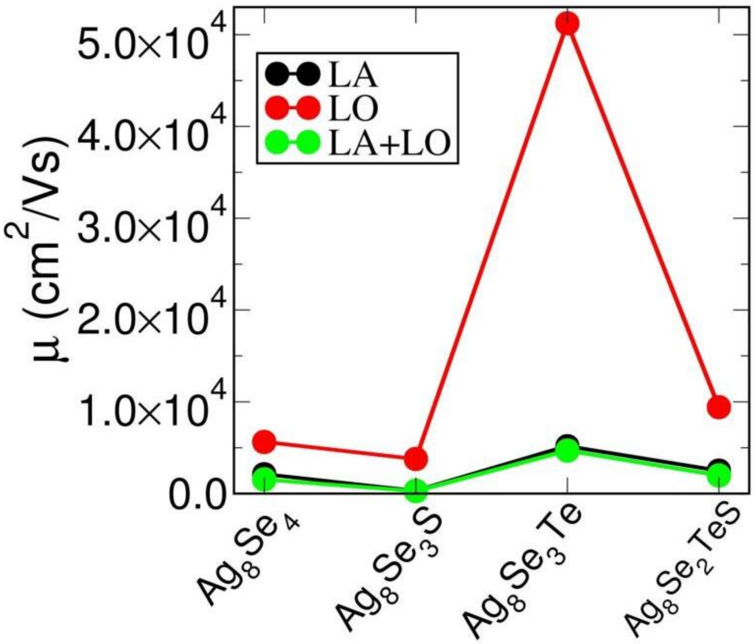

Figure 7.8: Mode resolved Carrier mobility.

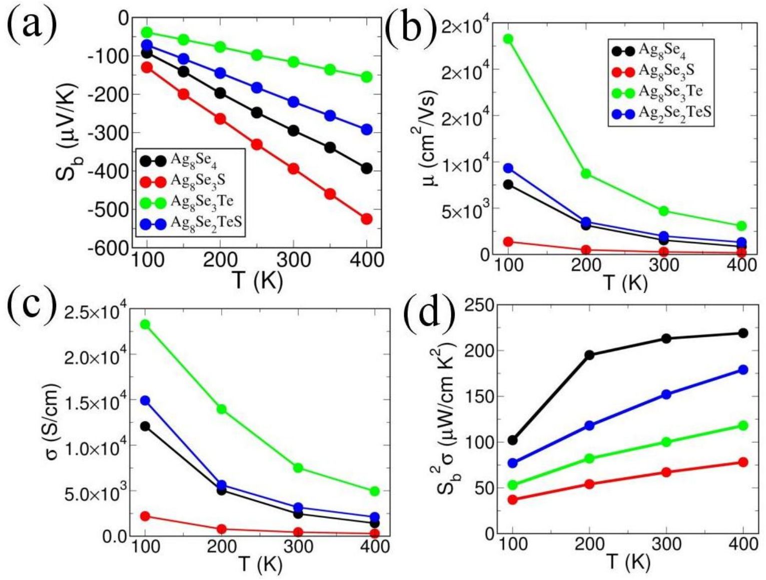

Figure 7.9: (a) Seebeck coefficient, (b) Mobility, (c) Electrical conductivity, (d) Power factor, have been shown in the temperature range (50-400 K). The Seebeck coefficient is derived from Boltzmann transport formalism. On the other hand, temperature-dependent mobility is calculated using acoustics phonon limited deformation potential theory. Finally, the Drude model gives the temperature-dependent electrical conductivity using the formula $\sigma = ne\mu$).

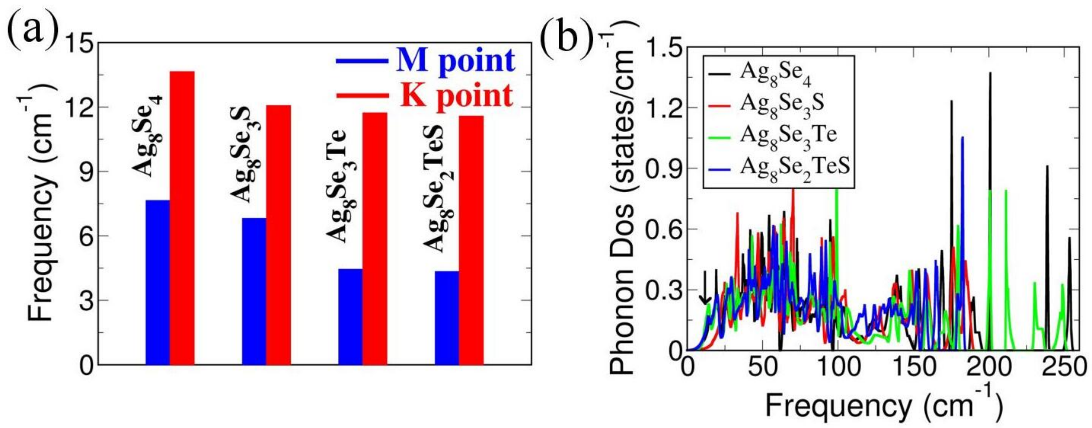

Figure 7.10: (a) Soft phonon modes observed at both M-point (blue bar) and K-point (red bar) for pristine and doped Ag_2Se in the Brillouin zone. Phonon frequency gradually decreases for Ag_8Se_4, Ag_8Se_3S, Ag_8Se_3Te, Ag_8Se_2TeS, respectively. (b) Phonon Dos for pristine and doped Ag_2Se. The sharp peak indicated by the black arrow signifies soft phonon modes at M and K points in the Brillouin zone for Ag_8Se_3Te (green line) and Ag_8Se_2TeS (blue line) systems.

and Te & S co-doped Ag_2Se clearly confirms the sharp peak arising because of Te doping in the low-energy phonon modes, which is highlighted by the black ellipse. As we will see below, these low energy acoustics modes are the reasons to achieve low lattice thermal conductivity in such a pseudo-ternary phase.

Additionally, entropy engineering is also utilized to modulate lattice thermal conductivity via Te and S doping at Se sites in Ag_2Se crystal. As calculated using equation (7.1), the configurational entropy (ΔS_{conf}) gradually increases with S-doping, Te-doping and Te & S co-doping, respectively. The calculated ΔS_{conf} are found to be 5.276 $JK^{-1}mol^{-1}$, 6.658 $JK^{-1}mol^{-1}$, 6.976 $JK^{-1}mol^{-1}$ for S-doped, Te-doped and co-doped Ag_2Se, respectively. In fact, the order of the (ΔS_{conf}) for doped cases is well consistent with another similar study, Te-doped in Cu_7P Se_6.[61] Eventually, the co-doping of Te and S in Ag_2Se increases the configurational entropy and point defects scattering which results in reducing lattice thermal conductivity significantly.

Both pristine and doped Ag_2Se have intrinsically low lattice thermal conductivity, (k_{lat}) at room temperature due to an increase in configurational entropy

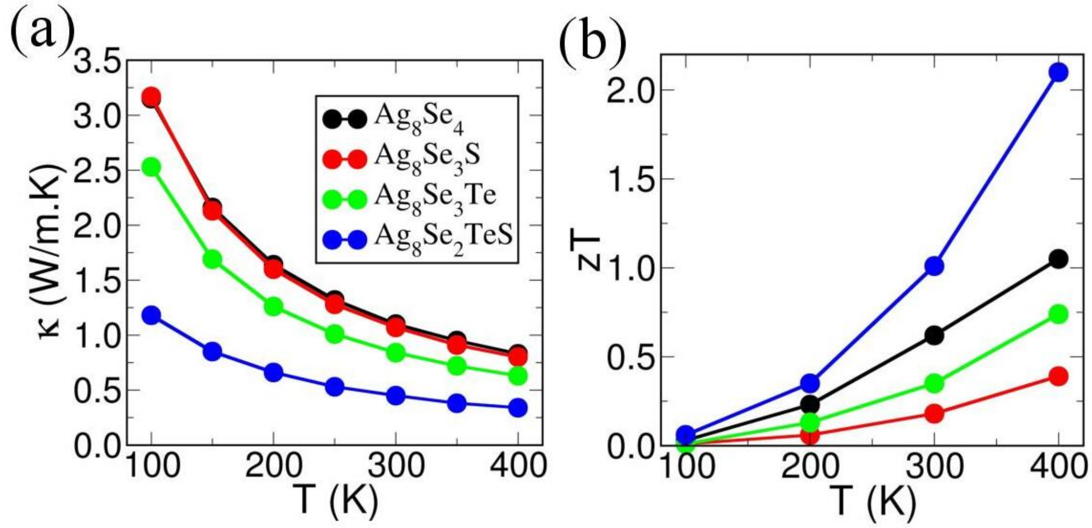

Figure 7.11: Temperature-dependent (a) Total lattice thermal conductivity (κ), (b) Figure of merit (zT), have been shown for pristine and doped Ag2Se. The pseudoternary phase (Ag_8Se_2TeS) shows very high $zT \simeq 2.1$ at 400 K.

dominated by point defect scattering.[62-63] Herein, we solve the Boltzmann transport equation to evaluate phonon relaxation time at temperature range (100-400 K). Pristine Ag_2Se seems to show $\kappa_{lat} \simeq 0.83$ $Wm^{-1}K^{-1}$ at 400 K which is well consistent with experiments.[34] Via Te and S doping at Se site in Ag_2Se crystal, the κ_{lat} gradually decreases. Note that, the κ_{lat} is calculated using the equation (**1.13**) for S-doped, Te-doped and co-doped (Te & S) Ag_2Se systems, which are found to be 0.8 $Wm^{-1}K^{-1}$, 0.63 $Wm^{-1}K^{-1}$, 0.34 $Wm^{-1}K^{-1}$, respectively at 400 K. The temperature-dependent κ_{lat} have been shown in Figure 7.11(a).

Finally, the dimensionless parameter, zT as a function of temperature have been computed and shown in Figure 7.11(b). The pristine Ag_2Se shows quite high zT value ($\simeq 1.05$) at 400 K which is also compared and found to be well consistent with other experimental and theoretical studies. [34,64] The zT is calculated for temperature up to 400 K because Ag_2Se crystal undergoes structural phase transition near 410 K.[64] In fact, we also estimate zT for Te-doped Ag_2Se, which is found to be 0.74 at 400 K. Finally, due to both S & Te doping, we achieve maximum zT around 2.1 at 400 K in co-doped (Te & S) Ag_2Se.

7.4 Conclusions

In conclusion, we have investigated the superlattice of $(Ag_2Se)_{1\text{-}2x}(Ag_2Te)_x(Ag_2S)_x$, where we have thoroughly analyzed the electronic as well as thermal transport behaviour of pseudo-ternary phase at near-room-temperature regime. This superlattice shows higher configurational entropy arising due to a large atomic size mismatch between Te & S atoms in Ag_2Se unit cell, which would lead to point defect scattering. Due to such defect scattering, we observe a very low value of lattice thermal conductivity (0.34 $Wm^{-1}K^{-1}$ at 400 K). This is because of the fact that the phonon scattering eventually occurs due to effective point defect scattering involving a broad range of mass fluctuation of constituting atoms (Se/Te/S). Additionally, the Rashba effect, the spin-split band dispersion appeared due to Te, introduces a sharp peak in the density of states near the conduction band region just above the Fermi level. Indeed, we find a moderately high thermoelectric power factor in the case of the co-doped superlattice. As a result of such relatively high PF and ultra-low lattice thermal conductivity, we achieve an exceptionally high zT (2.1 at 400 K) in n-type $Ag_2\,Se_{0.5}Te_{0.25}\,S_{0.25}$. In fact, the SOC driven spin split Rashba effect helps to greatly enhance the thermoelectric power factor and simultaneously enhancement of configurational entropy due to point defect scattering leads to reduction of lattice thermal conductivity. Eventually, these two combined effects synergistically increase the thermoelectric zT value in the pseudo-ternary phase operating in a near-room-temperature regime.

7.5 References

[1] Bell, L. E. Cooling, heating, generating power, and recovering waste heat with thermoelectric systems. Science 2008, 321, 1457-1461.

[2] Kajikawa, T. Thermoelectric power generation system recovering industrial waste heat. Thermoelectrics handbook: macro to nano, CRC/Taylor Francis., DM Rowe 2006, 50-1.

[3] Zhao, W.; Liu, Z.; Sun, Z.; Zhang, Q,; Wei, P.; Mu, X.; Zhou, H. Superparamagnetic enhancement of thermoelectric performance. Nature 2017, 549, 7671, 247-251.

[4] Zhao, W.; Liu, Z.; Wei, P.; Zhang, Q.; Zhu, W.; Su, X.; Tang, X. Magnetoelectric interaction and transport behaviours in magnetic nanocomposite thermoelectric materials. Nature nanotechnology 2017, 12, 55-60.

[5] Goldsmid, H. J. Conversion efficiency and figure-of-merit. In CRC Handbook of Thermoelectrics; Rowe, D. M., Ed.; CRC Press: Boca Raton 1995, 1926.

[6] Pei, Y.; LaLonde, A.; Iwanaga, S.; Snyder, G. J. High thermoelectric figure of merit in heavy hole dominated PbTe. Energy Environmental Science 2011, 4, 2085-2089.

[7] Ohno, S.; Aydemir, U.; Amsler, M.; Pöhls, J-H.; Chanakian, S.; Zevalkink, A.; White, M. A.; Bux, S. K.; Wolverton, C.; Snyder, G. J. Achieving zT > 1 in inexpensive Zintl phase $Ca_9Zn_{4+x}Sb_9$ by phase boundary mapping. Advanced Functional Materials 2017, 27, 1606361.

[8] Li, Z.; Xiao, C.; Zhu, H.; Xie, Y. Defect Chemistry for Thermoelectric Materials. J. Am. Chem. Soc. 2016, 138, 14810–14819.

[9] Pei, Y.; Wang, H.; Snyder, G. J. Band Engineering of Thermoelectric Materials. Adv. Mater. 2012, 24, 6125–6135.

[10] Lan, Y.; Minnich, A. J.; Chen, G.; Ren, Z. F. Enhancement of Thermoelectric Figure-of-Merit by a Bulk Nanostructuring Approach. Adv. Funct. Mater. 2010,

20, 357–376.

[11] Rowe, D. M. CRC Handbook of Thermoelectrics, CRC Press, New York, 1995.

[12] Roychowdhury, S.; Biswas, R. K.; Dutta, M.; Pati, S. K.; Biswas, K. Phonon Localization and Entropy-Driven Point Defects Lead to Ultralow Thermal Conductivity and Enhanced Thermoelectric Performance in $(SnTe)_{1-2x}(SnSe)_x(SnS)_x$. ACS Energy Letters 2019, 4, 1658-1662.

[13] Korkosz, R. J.; Chasapis, T. C.; Lo, S.-H.; Doak, J. W.; Kim, W. J.; Wu, C.-I.; Hatzikraniotis, E. High ZT in p-Type $(PbTe)_{1-2x}(PbSe)_x(PbS)_x$ Thermoelectric Materials. Journal of the American Chemical Society 2014, 136, 3225-3237.

[14] Ginting, D.; Lin, C.-C.; Lydia, R.; So, H. S.; Lee, H.; Hwang, J.; Kim, W.; Orabi, R.A.R.A; Rhyee, J. S. High thermoelectric performance in pseudo quaternary compounds of $(PbTe)_{0.95-x}(PbSe)_x(PbS)_{0.05}$ by simultaneous band convergence and nano precipitation. Acta Materialia 2017, 131, 98-109.

[15] Manettas, A.; Santos, R.; Ferreres, X. R.; Yamini, S. A. Thermoelectric performance of single phase p-type quaternary $(PbTe)_{0.65-x}(PbSe)_{0.35}(PbS)_x$ alloys. ACS Applied Energy Materials 2018, 1, 1898-1903.

[16] Samanta, M.; Biswas, K. Low thermal conductivity and high thermoelectric performance in $(GeTe)_{1-2x}(GeSe)_x$ $(GeS)_x$: competition between solid solution and phase separation. Journal of the American Chemical Society 2017, 139, 9382-9391.

[17] Doak, J. W.; Wolverton, C.; Ozoliņš, V. Vibrational contributions to the phase stability of PbS-PbTe alloys. Physical Review B 2015, 92, 174306.

[18] Wu, L.; Yang, J.; Wang, S.; Wei, P.; Yang, J.; Zhang, W.; Chen, L. Two-dimensional thermoelectrics with Rashba spin-split bands in bulk BiTeI. Physical Review B 2014, 90, 195210.

[19] Cappelluti, E.; Grimaldi, C.; Marsiglio, F. Topological change of the Fermi surface in low-density Rashba gases: application to superconductivity. Physical review letters 2007, 98, 167002.

[20] Singh, D.J. Electronic structure of $NaCo_2O_4$. Physical Review B 2000, 61,

13397.

[21] Biswas, K.; He, J.; Blum, I. D.; Wu, C.-I.; Hogan, T. P.; Seidman, D. N.; Dravid, V. P.; Kanatzidis, M. G. High-performance bulk thermoelectrics with all-scale hierarchical architectures. Nature 2012, 489, 414-418.

[22] Minnich, A . J.; Dresselhaus, M. S.; Ren Z. F.; Chen, G. Bulk nanostructured thermoelectric materials: current research and future prospects. Energy Environ. Sci. 2009, 2, 466–479.

[23] Shi, X.; Yang, J.; Wu, L.; Salvador, J. R.; Zhang, C.; Villaire, W. L.; Haddad, D.; Yang, J.; Zhu, Y.; Li, Q. Band Structure Engineering and Thermoelectric Properties of Charge-Compensated Filled Skutterudites. Sci. Rep. 2015, 5, 14641.

[24] Liu, Y.; Xie, H.; Fu, C.; Snyder, G. J.; Zhao, X.; Zhu, T. Demonstration of a phonon-glass electron-crystal strategy in (Hf,Zr)NiSn half-Heusler thermoelectric materials by alloying. J. Mater. Chem. A 2015, 3, 22716–22722.

[25] Bourg‘es, C.; Bouyrie, Y.; Supka, A. R.; Orabi, R. A. R. A.; Lemoine, P.; Lebedev, O. I.; Ohta, M.; Suekuni, K.; Nassif, V.; Hardy, V.; Daou, D.; Miyazaki, Y.; Fornari M.; Guilmeau, E. High-Performance Thermoelectric Bulk Colusite by Process Controlled Structural Disordering. J. Am. Chem. Soc. 2018, 140, 2186–2195.

[26] Chen, Z.-G.; Shi, X.; Zhao, L. D.; Zou, J. High-performance SnSe thermoelectric materials: progress and future challenge. Prog. Mater. Sci. 2018, 97, 283–346.

[27] He, W.; Wang, D.; Wu, H.; Xiao, Y.; Zhang, Y.; He, D.; Feng, Y.; Hao, Y. J.; Dong, J. F.; Chetty, R.; Hao, L.; Chen, D.; Qin, J.; Yang, Q.; Li, X.; Song, J.-M.; Zhu, Y.; Xu, W.; Niu, C.; Li, X.; Wang, G.; Liu, C.; Ohta, M.; Pennycook, S. J.; He, J.; Li, J.-F.; Zhao, L.-D. High thermoelectric performance in low- cost $SnS_{0.91}Se_{0.09}$ crystals. Science 2019, 365, 1418–1424.

[28] Liu, H.; Yuan, X.; Lu, P.; Shi, X.; Xu, F.; He, Y.; Tang, Y.; Bai, S.; Zhang, W.; Chen, L.; Lin, Y.; Shi, L.; Lin, H.; Gao, X.; Zhang, X.; Chi, H.; Uher, C. Ul-

trahigh Thermoelectric Performance by Electron and Phonon Critical Scattering in $Cu_2Se_{1-x}I_x$. Adv. Mater. 2013, 25, 6607–6612.

[29] Poudel, B.; Hao, Q.; Ma, Y.; Lan, Y.; Minnich, A.; Yu, B.; Yan, X.; Wang, D.; Muto, A.; Vashaee, D.; Chen, X.; Liu, J.; Dresselhaus, M. S.; Chen, G.; Ren, Z. High- Thermoelectric Performance of Nanostructured Bismuth Antimony Telluride Bulk Alloys. Science 2008, 320, 634–638.

[30] Snyder, G. J.; Toberer, E. S. Complex thermoelectric materials. Nat. Mater. 2008, 7, 105.

[31] Shindo, T.; Nakatani, Y.; Oishi, T. Thermoelectric Generating System for Effective Use of Unutilized Energy. Toshiba Rev. 2008, 63, 7–10.

[32] Simon, R.; Bourke, R. C.; Lougher, E. H. Preparation and thermoelectric properties of β-Ag2Se. Advanced Energy Conversion 1963, 3, 481-505.

[33] Pei, Y.; Heinz, N. A.; Snyder, G. J. Alloying to increase the band gap for improving thermoelectric properties of Ag_2Te. Journal of Materials Chemistry 2011, 21, 18256-18260.

[34] Ferhat, M.; Nagao, J. Thermoelectric and transport properties of β-Ag_2Se compounds. Journal of Applied Physics 2000, 88, 813-816.

[35] Day, T.; Drymiotis, F.; Zhang, T.; Rhodes, D.; Shi, X.; Chen, L.; Snyder, G. J. Evaluating the potential for high thermoelectric efficiency of silver selenide. Journal of Materials Chemistry C 2013, 1, 7568-7573.

[36] Mi, W.; Qiu, P.; Zhang, T.; Lv, Y.; Shi, X.; Chen, L. Thermoelectric transport of Se-rich Ag_2Se in normal phases and phase transitions. Applied Physics Letters 2014, 104(13), 133903.

[37] Conn, J.B.; Taylor, R.C. Thermoelectric and crystallographic properties of Ag_2Se. Journal of The Electrochemical Society 1960, 107(12), 977.

[38] Jood, P.; Chetty, R.; Ohta, M. Structural stability enables high thermoelectric performance in room temperature Ag_2Se. Journal of Materials Chemistry A 2020, 8(26), 13024-13037.

[39] Drymiotis, F.; Day, T.W.; Brown, D.R.; Heinz, N.A.; Jeffrey Snyder, G. Enhanced thermoelectric performance in the very low thermal conductivity $Ag_2Se_{0.5}Te_{0.5}$. Applied Physics Letters 2013, 103, 143906.

[40] http://www.quantum-espresso.org and http://www.pwscf.org.

[41] Blochl, P. E. Projector Augmented-Wave Method. Phys. Rev. B: Condens. Matter Mater. Phys. 1994, 50, 1795317979.

[42] Kresse, G.; Joubert, D. From Ultrasoft Pseudopotentials to the Projector Augmented-Wave Method. Phys. Rev. B: Condens. Matter Mater. Phys. 1999, 59, 17581775.

[43] Hua, X.; Chen, X.; Goddard, W.A. Generalized generalized gradient approximation: An improved density-functional theory for accurate orbital eigenvalues. Physical Review B 1997, 55(24), 16103.

[44] Perdew, J.P.; Burke, K.; Ernzerhof, M. Generalized gradient approximation made simple. Physical review letters 1996, 77(18), 3865.

[45] Ferhat, M.; Nagao, J. Thermoelectric and transport properties of β-Ag_2Se compounds. Journal of Applied Physics 2000, 88, 813-816.

[46] Pei, Y.; Heinz, N.A.; Snyder, G.J. Alloying to increase the band gap for improving thermoelectric properties of Ag_2Te. Journal of Materials Chemistry 2011, 21(45), 18256-18260.

[47] Kobayashi, M. Review on structural and dynamical properties of silver chalcogenides. Solid State Ionics 1990, 39, 121-149.

[48] Lee, H. A theoretical model of thermoelectric transport properties for electrons and phonons. Journal of Electronic Materials 2016, 45, 1115-1141.

[49] Lee, H. Thermoelectrics: design and materials. John Wiley Sons 2016.

[50] Bardeen, J.; Shockley, W. Deformation potentials and mobilities in non-polar crystals. Physical review 1950, 80, 72.

[51] Vogl, P., 1976. Microscopic theory of electron-phonon interaction in insulators or semiconductors. Physical Review B, 13(2), p.694.

[52] Cheng, L.; Liu, Y. What limits the intrinsic mobility of electrons and holes in two dimensional metal dichalcogenides?. Journal of the American Chemical Society 2018, 140(51), 17895-17900.

[53] Ziman, J. M. Principles of the Theory of Solids, Cambridge University Press 1972.

[54] Chen, Z.; Zhang, X.; Lin, S.; Chen, L.; Pei, Y. Rationalizing phonon dispersion for lattice thermal conductivity of solids. National Science Review 2018, 5, 888-894.

[55] Noor-A-Alam, M.; Lee, M.; Lee, H.J.; Choi, K.; Lee, J.H. Switchable Rashba effect by dipole moment switching in an Ag_2Te monolayer. Journal of Physics: Condensed Matter 2018, 30, 385502.

[56] Giannozzi, P., Baroni, S., Bonini, N., Calandra, M., Car, R., Cavazzoni, C.; Ceresoli, D.; Chiarotti, G.L.; Cococcioni, M.; Dabo, I.; Dal Corso, A. QUANTUM ESPRESSO: a modular and open-source software project for quantum simulations of materials. Journal of physics: Condensed matter 2009, 21(39), 395502.

[57] Malakkal, L.; Szpunar, B.; Zuniga, J.C.; Siripurapu, R.K.; Szpunar, J.A. First principles calculation of thermo-mechanical properties of thoria using Quantum ESPRESSO. International Journal of Computational Materials Science and Engineering 2016, 5(02), 1650008.

[58] Taylor, P.F.; Wood, C. Thermoelectric properties of Ag_2Te. Journal of Applied Physics 1961, 32(1), 1-3.

[60] Samanta, M.; Pal, K.; Pal, P.; Waghmare, U.V.; Biswas, K. Localized vibrations of bilayer leading to ultralow lattice thermal conductivity and high thermoelectric performance in weak topological insulator n-type BiSe. Journal of the American Chemical Society 2018, 140(17), 5866-5872.

[61] Chen, R.; Qiu, P.; Jiang, B.; Hu, P.; Zhang, Y.; Yang, J.; Ren, D.; Shi, X.; Chen, L. Significantly optimized thermoelectric properties in high-symmetry cubic Cu_7PSe_6 compounds via entropy engineering. Journal of Materials Chemistry A

2018, 6(15), 6493-6502.

[62] Drymiotis, F.; Day, T.W.; Brown, D.R.; Heinz, N.A.; Jeffrey Snyder, G. Enhanced thermoelectric performance in the very low thermal conductivity $Ag_2Se_{0.5}Te_{0.5}$. Applied Physics Letters 2013, 103(14), 143906.

[63] Wang, H.; LaLonde, A.D.; Pei, Y.; Snyder, G.J. The criteria for beneficial disorder in thermoelectric solid solutions. Advanced Functional Materials 2013, 23(12), 1586-1596.

[64] Lee, C.; Park, Y.H.; Hashimoto, H. Effect of nonstoichiometry on the thermoelectric properties of a Ag_2Se alloy prepared by a mechanical alloying process. Journal of applied physics 2007, 101(2), 024920.

[65] Vogl, P., 1976. Microscopic theory of electron-phonon interaction in insulators or semiconductors. Physical Review B, 13(2), p.694.

[66] Cheng, L.; Liu, Y. What limits the intrinsic mobility of electrons and holes in two dimensional metal dichalcogenides?. Journal of the American Chemical Society 2018, 140(51), 17895-17900.

8

Summary & Outlook

The central theme of this dissertation is to elucidate the role of charge and phonon transport in electronic and thermoelectric applications in layered as well as in bulk materials. We have employed a combination of first-principles based density functional theory coupled with Boltzmann transport equation theory throughout working chapters and for analysis purposes. Three major topics of research are mainly discussed in this thesis, namely, understanding the strain-induced transport anisotropy in charge carrier mobility in layered semiconductors, studying phonon dynamics in bulk and monolayer systems along with manifestation of avoided crossing in thermodynamic properties and finally realizing charge and phonon dynamics in modulating inter-dependent thermoelectric parameters with innovative computational strategies to design better thermoelectric materials.

In Chapter 2, we have elaborately discussed about the ab-initio based deformation potential theory to study strain-induced anisotropy in the carrier mobility in β-TeO$_2$. We have analyzed carrier mobility at various compressive as well as tensile strain. At 3% compressive strain along the x-direction, we achieve increment in hole mobility (39500 cm^{2}V^{-1}s^{-1}) that occurs because of the lowering of both hole-phonon coupling strength and effective mass. We also find a sharp peak in the electron mobility (17500 cm^{2}V^{-1}s^{-1}) at 4% compressive strain along the y-direction. The enhancement of such large carrier mobility is attributed to higher carrier relaxation time along the $\Gamma \longrightarrow$ Y direction. This wider bandgap material coupled with ultrahigh carrier mobility could be utilized for next-generation nano-electronics and power electronics applications.

In the next chapter (Chapter 3), we have compared and contrasted phonon dispersions of SnO and PbO in their single layer and bulk forms using density functional perturbation theory (DFPT) implemented in Quantum Espresso. We obtain good agreement of Raman and IR active modes between our theory and the available experimental data. Interestingly, we notice strong avoided crossing in both monolayer and bulk SnO and only in bulk PbO along the high symmetry points, which has a direct consequence in reducing phonon contribution to vibrational entropy. Our study on abrupt change in phonon group velocity further confirms the appearance of Landau quasi-degeneracy or avoided crossing in bulk and monolayer form of SnO and only in bulk PbO. Interestingly, we do not observe any avoided crossing for monolayer PbO which is additionally validated by the appearance of kink in $C_v(T)$ determined by the energy fluctuations. This chapter mainly encompasses the detailed understanding of the vibrational spectra of MO and provides new insight in thermodynamic parameters, which is crucial to the development of better thermoelectric materials.

In chapter 4, 5, 6 and 7, we have developed Boltzmann transport equation mechanism in deformation potential limit and have studied carrier (charge and phonon) transport properties in designing better thermoelectric materials. We have modelled a superlattice of SnO-PbO in chapter 4 which could be used as a thermoelectric (TE) oxides. Our result indicates that this complex is dynamically as well as thermodynamically stable at both ambient and high temperatures. This superlattice shows higher Seebeck coefficient and low thermal conductivity, compared to its component oxides (SnO & PbO). Moreover, the localized lone pair induced charge anisotropy and bonding inhomogeneity are the reasons for the reduction of the lattice thermal conductivity in this air-stable TE oxides. In Chapter 5, we have shown Gd doping introduces a non-interacting flat conduction band in n-type PbTe which increases its effective mass (m^*). The presence of this nearly flat conduction band distorts the electronic DOS which is beneficial for enhancing the Seebeck coefficient in n-type PbTe. Gd is found to be favorable when it is locally off-centered from its parent position by ≈ 0.21 $\mathring{A}$ along [111] crystallographic direction in the PbTe lattice, which creates significant lattice anharmonicity. Phonon dispersion revealed the presence of low frequency nearly flat optical phonon mode which plays a pivotal role in scattering the heat carrying acoustic phonons, thus lowering its κ_{lat}. The high thermoelectric figure of merit in Gd doped PbTe is due to the high power factor arising due to distortion of electronic DOS and simultaneous low thermal conductivity due to Gd off-centering and enhanced scattering due to formation of low energy localized phonon modes.

We have also studied the thermoelectric efficiency of 3d transition metal incorporated Pb-free ecofriendly two-dimensional SnTe in chapter 6. This chapter suggests 12.5% substitution of V and Mn increase the thermodynamic efficiency. In fact, although these doping affects the intrinsic carrier mobility due to increased carrier effective mass and lower elastic constant, the Seebeck coefficient in turn increases slighly. On the contrast, Fe and Co substitution drastically reduce the Seebeck coefficient because of semiconductor to metal transition. In fact, the substantial reduction in lattice thermal conductivity yields a significant enhancement ($\approx$ 5-6%) in zT values for the Mn doped SnTe system as compared to that of the pristine 2D β'-SnTe system.

In the last working chapter (Chapter 7), we investigated the superlattice of $(Ag_2Se)_{1-2x}(Ag_2Te)_x(Ag_2S)_x$ where we have thoroughly analyzed electronic as well as thermal transport behaviour of pseudo-ternary phase at near-room-temperature. This superlattice shows higher configurational entropy arising due to a large atomic size mismatch between Te & S atoms in Ag_2Se unit cell, which would lead to lowering of lattice thermal conductivity. Additionally, the Rashba effect, spin-split band dispersion appeared due to Te, introduces a sharp peak in the density of states which moderately enhances the thermoelectric power factor in case of the co-doped superlattice. As a result, we achieve an exceptionally high zT (2.1 at 400 K) in $Ag_2Se_{0.5}Te_{0.25}S_{0.25}$.

In brief, we have established a comprehensive microscopic understanding of their inter-dependent complex relationship of charge and phonon transport in periodic systems to determine the electronic as well as thermoelectric properties throughout the thesis. Most importantly, such studies provide access to atomistic details which is not readily accessible to experimentalists. Recently, the experimental advancement makes available a library of new low-dimensional to bulk materials which can be utilized as next generation nano-electronics, photovoltaic solar cells, FETs and thermoelectric devices.

We already have developed in-house codes based on Boltzmann transport equation for all the descriptors that are required to obtain thermoelectric efficiency and also for thermodynamic quantities. In fact, our developed methodology would be able to predict microscopic details of the systems listed in the libraries for their applications in advanced devices. In near future, we are interested in developing machine learning algorithms by which we would be able to predict many more new energy materials with exotic properties that benefit the experimentalists for synthesizing advanced materials for applications in advanced devices and in particular in thermoelectric devices.

Other works by Author

ACS Energy LETTERS

Cite This: ACS Energy Lett. 2019, 4, 1658−1662

http://pubs.acs.org/journal/aelccp

Phonon Localization and Entropy-Driven Point Defects Lead to Ultralow Thermal Conductivity and Enhanced Thermoelectric Performance in $(SnTe)_{1-2x}(SnSe)_x(SnS)_x$

Subhajit Roychowdhury,[†] Raju K. Biswas,[‡] Moinak Dutta,[†] Swapan K. Pati,[‡,§] and Kanishka Biswas*[,†,§]

[†]New Chemistry Unit, Jawaharlal Nehru Centre for Advanced Scientific Research (JNCASR), Jakkur P.O., Bangalore 560064, India

[‡]Theoretical Sciences Unit, Jawaharlal Nehru Centre for Advanced Scientific Research (JNCASR), Jakkur P.O., Bangalore 560064, India

[§]School of Advanced Materials and International Centre of Materials Science, Jawaharlal Nehru Centre for Advanced Scientific Research (JNCASR), Jakkur P.O., Bangalore 560064, India

Supporting Information

ABSTRACT: **Understanding of phase stability, chemical bonding, and phonon transport are essential to realize ultralow thermal conductivity in crystalline solids for designing high-performance thermoelectric (TE) materials. Pristine SnTe, a homologue of PbTe, exhibits poor TE performance primarily because of high lattice thermal conductivity, κ_{lat}. Herein, the amorphous limit of κ_{lat} is achieved via engineering configurational and vibrational entropies in pseudoternary $(SnTe)_{1-2x}(SnSe)_x(SnS)_x$. Density functional theory calculations and synchrotron X-ray pair distribution function analysis reveal that S atoms are locally off-centered in global cubic SnTe, resulting in a low-energy localized optical phonon which strongly couples with heat-carrying acoustic phonons. Additionally, substitution of Se and S in SnTe increases the configurational entropy and point defects, resulting in an ultralow κ_{lat} of 0.52 W/mK. Finally, improvement of the Seebeck coefficient is achieved via the synergistic effect of resonant doping (In) and valence band convergence (Ag), which lead to a high TE figure of merit, zT, of ∼1.3 at 854 K.**

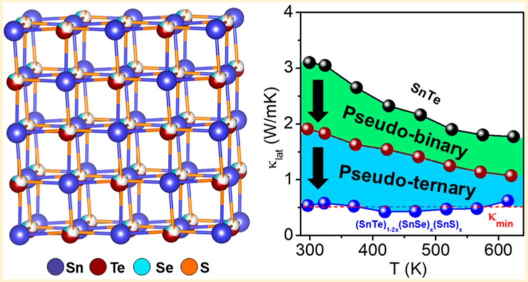

Entropy is a measure of the number of microscopic configurations present in the macrostate of a material.[1] Introduction of extensive alloying/point defects (site or size disorder) increases the configurational entropy of the system and simultaneously decreases the lattice thermal conductivity, κ_{lat}, providing the opportunity to realize better thermoelectric (TE) performance, which is important for future energy management as TE materials can convert waste heat to electricity.[2−9]

We present a unique strategy for the reduction of κ_{lat} of a crystalline solid to its amorphous limit by engineering its vibrational and configurational entropies simultaneously. In alloys, vibrational entropy is used to calculate the solubility of the second phase in the host matrix.[10] The large size mismatch between the constituent atoms may generate locally strained regions in the global structure. Recently, the effect of large size mismatch between Te and S was theoretically predicted in PbTe−PbS where S atoms are off-centered from their ideal crystallographic position, resulting in local dipole moments and soft phonon modes which scatter heat-carrying acoustic phonons effectively.[11] On the other hand, configurational entropy arises because of the occupation of multiple elements in a particular crystallographic site.[1] Multicomponent chalcogenides such as $(PbTe)_{1-2x}(PbSe)_x(PbS)_x$ and $(GeTe)_{1-2x}(GeSe)_x(GeS)_x$ are known to show low thermal conductivity due to increase in configurational entropy-driven point defect phonon scattering, resulting from strong strain and mass fluctuations between different components.[8,9]

Pristine SnTe exhibits κ_{lat} of ∼3.1 W/mK at 300 K, which is significantly higher than its theoretical limit of minimum κ_{lat} ($\kappa_{min} \approx 0.5$ W/mK).[12,13] Recently, thermal conductivity of SnTe has been significantly reduced via multielement alloy scattering (∼0.8 W/mK at 300 K)[14] and introducing matrix-

Received: May 20, 2019
Accepted: June 17, 2019
Published: June 17, 2019

DOI: 10.1021/acsenergylett.9b01093
ACS Energy Lett. 2019, 4, 1658−1662

encapsulated layered intergrowth compounds (~0.67 W/mK at 300 K).[12] The measured κ_{lat} values are still far from the theoretical limit of SnTe. The decrease of the κ_{lat} without degrading the carrier mobility has recently been demonstrated in SnTe via engineering ferroelectric instability which effectively scatters heat-carrying acoustic modes and results in low thermal conductivity (~0.67 W/mK at 300 K).[15] We envisaged that the synergistic effects of configurational entropy engineering and the introduction of phonon localization via off-centering of the selective atom would be a promising approach to realize the κ_{min} of SnTe via coalloying SnSe and SnS.

We report an ultralow κ_{lat} of ~0.52 W/mK and high thermoelectric performance in $(SnTe)_{1-2x}(SnSe)_x(SnS)_x$ [x = 0−0.10] via a three-step process. Initially, we used the self-compensation in SnTe, i.e., $Sn_{1.03}Te$, to optimize the excess hole carrier concentration. Subsequently, the reduction of κ_{lat} of $Sn_{1.03}Te$ is achieved via coalloying SnSe and SnS. Configurational entropy for the pseudoternary $(SnTe)_{1-2x}(SnSe)_x(SnS)_x$ system is significantly higher compared to the conventional binary systems SnTe−SnSe or SnSe−SnS, which enhances the point defect phonon scattering markedly. Using first-principles density functional theory (DFT) calculations and synchrotron X-ray pair distribution function (PDF) analysis, we discover that S atoms are off-centered in cubic $(SnTe)_{1-2x}(SnSe)_x(SnS)_x$, resulting in local strain and strong overlap between heat-carrying acoustic and low-energy optical phonons, which reduces κ_{lat} significantly. Finally, improvement of the Seebeck coefficient is achieved via codoping of In and Ag in $(SnTe)_{1-2x}(SnSe)_x(SnS)_x$, where In and Ag act as a resonant dopant and valence band convergent, respectively. Consequently, a peak zT of ~1.3 at 854 K can be achieved for p-type $Sn_{1.03}Te_{0.85}Se_{0.075}S_{0.075}$ − 2 mol % Ag and 2 mol % In sample, which is markedly higher compared to that of pristine SnTe.

First, we synthesized SnTe samples with slight excess Sn, i.e., $Sn_{1.03}Te$,[16,17] by sealed tube melting and spark plasma sintering, which exhibits lower p-type carrier concentration (1.08×10^{20} cm^{-3}) compared to that of pristine SnTe (4.5×10^{20} cm^{-3}). Despite the research on thermoelectric properties of pseudobinary SnTe−SnSe and SnSe−SnS systems reported previously,[18−20] to date, there is no report on the pseudoternary SnTe−SnSe−SnS system for thermoelectrics because of its complex chemistry. Here, we describe the structure, thermodynamical aspect, and thermoelectric properties of the SnTe-rich $Sn_{1.03}Te_{1-2x}Se_xS_x$ system in detail.

Room-temperature powder XRD patterns (Figure S1a, Supporting Information, SI) for $Sn_{1.03}Te_{1-2x}Se_xS_x$ (x = 0−0.10) samples have been indexed based on cubic SnTe (space group $Fm\bar{3}m$). However, XRD of higher SnSe/SnS concentration ($x \geq 0.05$) in $Sn_{1.03}Te$ show additional weak reflections of SnS, indicating the lower solubility limit of SnS in the SnTe matrix compared to that of SnSe, which is further confirmed via backscattered field emission scanning electron microscopy (FESEM; Figure S2) and vibrational entropy calculation (Table S1).

Se and S substitution in SnTe reduces the κ_{lat} enormously throughout the measured temperature range compared to that of controlled $Sn_{1.03}Te$ sample (Figure 1a). Typically, $Sn_{1.03}Te_{0.85}Se_{0.075}S_{0.075}$ sample exhibits a κ_{lat} value of 0.52 W/mK at room temperature, which is significantly lower than that of other reported SnTe-based samples (Figure 1b),[12,14,15,18,21−24] and reaches to the κ_{min} of SnTe (0.5 W/mK). The $Sn_{1.03}Te_{0.85}Se_{0.075}S_{0.075}$ sample possesses extensive solid solutions and big SnS-rich precipitates (~20 μm, Figure S2). Micrometer sized SnS precipitates are formed in the SnTe matrix because of the large miscibility gap between SnTe and SnS due to the significant difference in atomic radii between Te (1.40 Å) and S (1.00 Å). The big SnS precipitates do not affect much in phonon scattering because the mean free path of heat-carrying phonons in SnTe lies in the 2−20 nm range.[25] We have also performed transmission electron microscopy (TEM) experiments on the $Sn_{1.03}Te_{0.85}Se_{0.075}S_{0.075}$ sample to confirm the absence of any nanoscale precipitate (Figure S3) in the matrix.

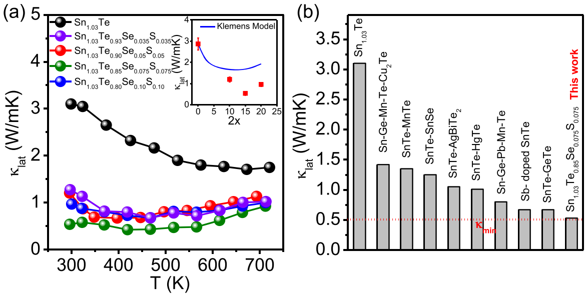

Figure 1. (a) Temperature-dependent lattice thermal conductivity (κ_{lat}) for $Sn_{1.03}Te_{1-2x}Se_xS_x$ (x = 0−0.10) samples. Inset in panel a: Room-temperature κ_{lat} as a function of total Se and S concentration. The solid blue line is a solid solution line predicted by the Klemens model. (b) κ_{lat} at room temperature in this work in comparison with previously reported SnTe samples.[12,14,15,18,21−24]

To find the fundamental reason for the ultralow κ_{lat} in $Sn_{1.03}Te_{0.85}Se_{0.075}S_{0.075}$ sample, we have calculated configurational entropy, vibrational entropy, and phonon dispersion via first-principles density functional perturbation theory (DFPT). Configurational entropy increases when several initially separated systems of different atoms are mixed without chemical reaction. Configurational entropy for pseudoternary system, $SnTe_{1-2x}Se_xS_x$ (2.8 J/K/mol) is significantly higher compared to that of the pseudobinary phase, $SnTe_{1-2x}Se_x$ (0.55 J/K/mol) and $SnTe_{1-2x}S_x$ (0.95 J/K/mol) (Table S1). It is worth noting that multicomponent thermoelectric materials are capable of scattering phonons extensively because of highly tunable configurational entropy, resulting from complex crystal structure and bond inhomogeneity.[8,9] The $Sn_{1.03}Te_{0.85}Se_{0.075}S_{0.075}$ sample exhibits ultralow κ_{lat}, especially from room temperature to 600 K, compared to that of the controlled pseudobinary systems (Figure S5b). Thus, low κ_{lat} in the pseudoternary system can be attributed to the entropy-driven point defect phonon scattering due to enhanced mass fluctuation as several anions occupying the same position within the lattice. Similarly, configurational entropy plays an important role in decreasing the κ_{lat} in previously reported Pb/Ge-based pseudoternary systems,[8,9] but none of those systems were able to reach their κ_{min} unlike the present case. This hints about the presence of additional phonon scattering mechanisms operating in tandem with the point defect scattering to bring the κ_{lat} of SnTe down to its amorphous limit. The Klemens model was calculated to understand the effect of point defect scattering on κ_{lat} of the $Sn_{1.03}Te_{1-2x}Se_xS_x$ system (inset of Figure 1a). However, experimental κ_{lat} values for all the samples lie far below the theoretical line, which gives further indication of the additional mechanism which is complementary to the point defect phonon scattering.

DOI: 10.1021/acsenergylett.9b01093
ACS Energy Lett. 2019, 4, 1658−1662

Phonon dispersion of pristine rock salt SnTe exhibits imaginary modes (instability) with frequency of 36i cm^{-1} at the Γ point (Figure 2a), resulting from the rhombohedral distortion in the global cubic structure via Sn off-centering.[26] However, there is an appearance of flat bands in imaginary modes of frequency 117i cm^{-1} at Γ point for Sn_8Te_6SeS (Figure 2b). The imaginary localized mode originates from S atoms in Sn_8Te_6SeS, which was visualized from the analysis of Eigen vectors (Figure S8). The high-energy optical modes also show flat behavior. A significant band overlap between acoustic modes and low-energy optical modes is obtained which, scatters heat-carrying acoustics phonons and reduces the κ_{lat} in the $SnTe_{1-2x}Se_xS_x$ system. The reason for the band to be flat is the off-centering of S atoms in the global cubic Sn_8Te_6SeS lattice. The phonon dispersion of Sn_8Te_6SeS is analogous to that of the $BaTiO_3$, where the unstable localized mode originated because of off-centering of Ti atoms along the Ti−O−Ti chain.[27]

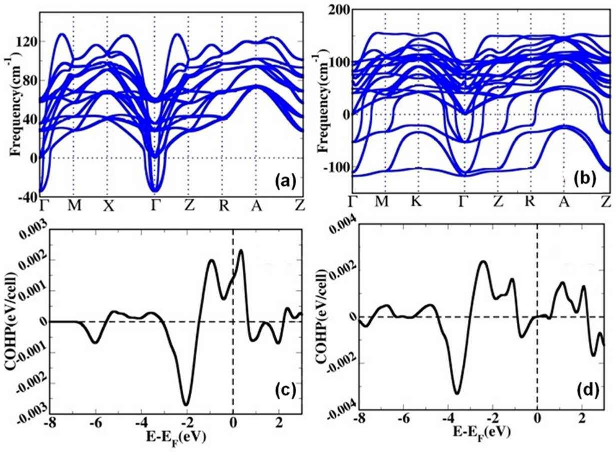

Figure 2. Phonon dispersion of (a) Sn_8Te_8 and (b) Sn_8Te_6SeS as a function of q-points. Crystal orbital Hamiltonian analysis (COHP) of (c) Sn 5s and off-centered S 3p orbitals and (d) Sn 5s and regular site S 3p orbitals.

The crystal orbital Hamiltonian population (COHP) analysis further confirms that the strong interactions between Sn 5s and S 3p are bonding in nature with the S off-center configuration (Figure 2c), whereas the antibonding nature appears when S is placed in its regular crystallographic site (Figure 2d). We thus understand there is a driving force on the S atom to off-center toward the Sn, making the bonding stronger between them and stabilizing the structure. Therefore, thermal energy could displace the S atom from one potential well to another in a dynamic fashion, which has a strong consequence in phonon scattering. Similar behavior has been recently observed in a PbSe−GeSe system where Ge off-centers from its position to stabilize the structure and reduces thermal conductivity significantly.[28] Further, the lower values of the calculated sound velocity (Table S2) can be attributed to the lower thermal conductivity of $SnTe_{1-2x}Se_xS_x$.

Although the theoretical calculation indicated toward bonding heterogeneity and S atom off-centering instability, a concomitant experimental proof was obtained using X-ray PDF analysis (Figure 3). Full range X-ray PDF data of $Sn_{1.03}Te_{0.85}Se_{0.075}S_{0.075}$ at 300 K fits well with the rock salt cubic structure (Figure 3a). To understand the chemical bonding of nearest atom−atom correlation in $Sn_{1.03}Te_{0.85}Se_{0.075}S_{0.075}$, we have analyzed critically the first peak in the PDF (Figure 3b) and tried to rationalize the data using a distorted model, i.e., by off-centering the S atom (Figure 3c). We have observed that off-centering the S atom by 0.12 Å in the [111] direction at 300 K properly describes the nearest-neighbor correlation (R_w = 6.97%, Figure 3c). Although the global structure of $Sn_{1.03}Te_{0.85}Se_{0.075}S_{0.075}$ fits well with cubic rock salt structure, the first PDF peak cannot be well accounted for by simple rock salt model (R_w = 9.83%, Figure 3b). The off-centering of S further increases to 0.14 Å at 500 K (Figures 3d and S12). The off-centering of S from its mean position suggests a bonding heterogeneity, wherein a stronger bonding interaction between Sn and S acts as a catalyst for the S-off centering. Similar local cationic distortion results in the depletion of the thermal conductivity of few solids.[15,28] Thus, the local S off-centering in global cubic $SnTe_{0.85}Se_{0.075}S_{0.075}$ is an important cause that inhibits the propagation of acoustic phonons and thereby decreases the κ_{lat} of the system.

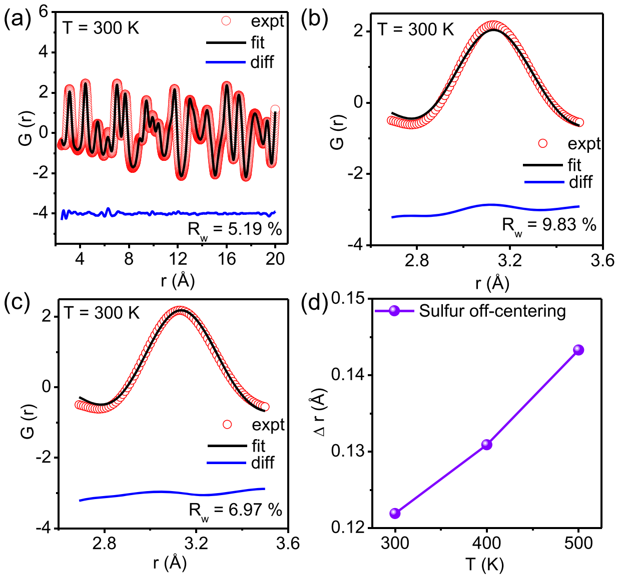

Figure 3. (a) Global fit of X-ray PDF with cubic structure in $Sn_{1.03}Te_{0.85}Se_{0.075}S_{0.075}$ at 300 K. Fit of X-ray PDF for the nearest-neighbor atomic correlation with (b) cubic structure and (c) S off-centering along the [111] direction in $Sn_{1.03}Te_{0.85}Se_{0.075}S_{0.075}$ at 300 K. (d) Off-centering of S atom in $Sn_{1.03}Te_{0.85}Se_{0.075}S_{0.075}$ as obtained from temperature-dependent X-ray PDF analysis.

In the next step, we focused on the modification of the electronic structure of the $Sn_{1.03}Te_{0.85}Se_{0.075}S_{0.075}$ sample to enhance the Seebeck coefficient. Here, we choose a Ag and In codoping strategy to further improve the thermoelectric performance in the $Sn_{1.03}Te_{0.85}Se_{0.075}S_{0.075}$ sample. Substitution of Ag and In together decreases the electrical conductivity, especially at room temperature, because of the significant reduction in carrier mobility for all the samples due to resonant carrier scattering (Figure 4a and Table S4). The Seebeck coefficients for $Sn_{1.03}Te_{0.85}Se_{0.075}S_{0.075}$ − y% Ag and y% In (y = 1−3) samples are significantly higher over the entire temperature range compared to the controlled singly Ag- and In-doped $Sn_{1.03}Te_{0.85}Se_{0.075}S_{0.075}$ sample (Figures 4b and S16). Typically, the Seebeck value for the $Sn_{1.03}Te_{0.85}Se_{0.075}S_{0.075}$ −

DOI: 10.1021/acsenergylett.9b01093

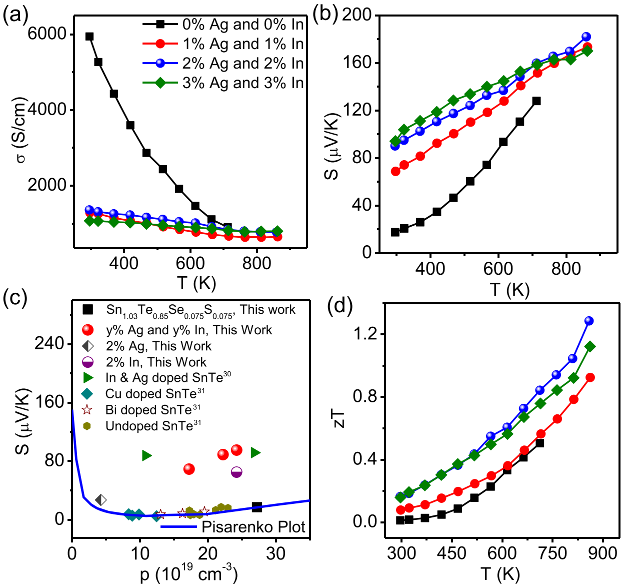

Figure 4. Temperature-dependent (a) electrical conductivity (*σ*) and (b) Seebeck coefficient (*S*) for $\mathbf{Sn_{1.03}Te_{0.85}Se_{0.075}S_{0.075}}$ − *y* % Ag and *y*% In (*y* = 0−3) samples. (c) Room-temperature *S* vs carrier concentration (*p*) plot of the present $\mathbf{Sn_{1.03}Te_{0.85}Se_{0.075}S_{0.075}}$ and $\mathbf{Sn_{1.03}Te_{0.85}Se_{0.075}S_{0.075}}$ − *y*% Ag and *y*% In samples.[29−31] (d) Temperature-dependent thermoelectric figure of merit (zT) for $\mathbf{Sn_{1.03}Te_{0.85}Se_{0.075}S_{0.075}}$ − *y*% Ag and *y*% In (*y* = 0−3), samples.

2% Ag and 2% In sample is 90 μV/K at room temperature, which further increases linearly to 180 μV/K at 856 K.

We compared the room-temperature Seebeck coefficient of $Sn_{1.03}Te_{0.85}Se_{0.075}S_{0.075}$ − *y*% Ag and *y*% In (*y* = 0−3) samples as a function of carrier concentration with the well-known Pisarenko line of SnTe.[29−31] Interestingly, $Sn_{1.03}Te_{0.85}Se_{0.075}S_{0.075}$ − *y*% Ag and *y*% In codoped samples exhibit a Seebeck coefficient that is much higher than that of monodoped Ag and In samples, which confirms that Ag and In synergistically enhance the Seebeck coefficient in $Sn_{1.03}Te_{0.85}Se_{0.075}S_{0.075}$ − *y*% Ag and *y*% In codoped samples, where In acts a resonant dopant and Ag increases the valence band convergence.[29,30] Moreover, the detailed electronic structure of Ag and In codoped $SnTe_{1-2x}Se_xS_x$ samples calculated by DFT confirms the valence band convergence and resonance state formation (Figure S18).

The $Sn_{1.03}Te_{0.85}Se_{0.075}S_{0.075}$ − 2% Ag and 2% In sample exhibits the highest zT of ∼1.3 at 854 K (Figure 4d), which is significantly higher than that of pristine SnTe and the previously reported Ag and In codoped SnTe sample (zT ≈ 1 at 856 K).[30]

Although the scope of the investigations in $(SnTe)_{1-2x}(SnSe)_x(SnS)_x$ system is huge because of the possibility of vast compositional variation and complexity, here we have limited our investigation to study the thermoelectric properties of SnTe-rich compositions with an equal fraction of SnSe and SnS. While with lower concentrations of SnSe and SnS, the system $(SnTe)_{1-2x}(SnSe)_x(SnS)_x$ ($x = 0.05$) represents solid solution, but with $x > 0.05$, the system exhibits coexistence of solid solution and phase separation of $SnS_{1-x}Se_x$-rich precipitates (∼20 μm) in a $SnTe_{1-x}Se_x$-rich matrix. The $(SnTe)_{1-2x}(SnSe)_x(SnS)_x$ is significantly point defect rich because of high configurational entropy. Sulfur atoms locally off-center in global rock salt lattice of $(SnTe)_{1-2x}(SnSe)_x(SnS)_x$ because of covalent bonding between Sn and S, resulting in local instability that induces coupling between optical and acoustic phonons. The synergistic effect of enhanced configurational entropy and S off-centering in pseudoternary system reduces the κ_{lat} to its amorphous limit ($\kappa_{min} \approx 0.5$ W/mK). Further, Ag and In codoping in $Sn_{1.03}Te_{0.85}Se_{0.075}S_{0.075}$ significantly enhances the Seebeck coefficient because of the synergistic effect of resonance level formation and valence band convergence, respectively. As a result, the highest zT ≈ 1.3 is achieved in the $Sn_{1.03}Te_{0.85}Se_{0.075}S_{0.075}$ − 2% Ag and 2% In sample at 854 K.

■ ASSOCIATED CONTENT

Supporting Information

The Supporting Information is available free of charge on the ACS Publications website at DOI: 10.1021/acsenergylett.9b01093.

> Methods; PXRD, lattice parameter, and electronic spectra of $Sn_{1.03}Te_{1-2x}Se_xS_x$ (Figure S1); BSE-FESEM (Figure S2); TEM (Figure S3); heat capacity (Figure S4); κ_{tot} and additional κ_{lat} of controlled samples (Figure S5); κ_{el} (Figure S6); phonon dispersion (Figure S7); visualization of Eigen vectors (Figure S8); electronic DOS and COHP (Figure S9); strain−phonon coupling (Figure S10); temperature-dependent lattice parameter and U_{iso} (Figure S11); PDF at 500 K (Figure S12); *σ* and *S* of $Sn_{1.03}Te_{1-2x}Se_xS_x$ (Figure S13); PXRD and BSE-FESEM of Ag−In codoped samples (Figure S14); σS^2 of Ag−In codoped samples (Figure S15); comparison of *σ*, *S*, and σS^2 of In, Ag, In, and Ag codoped samples (Figure S16); electronic structure (Figures S17 and S18); κ_{tot}, κ_{el}, and κ_{lat} of In and Ag codoped samples (Figure S19); change in entropy (Table S1); phonon group velocity and Debye temperature (Table S2); elemental qualification of $Sn_{1.03}Te_{0.85}Se_{0.075}S_{0.075}$ sample (Table S3); carrier concentration and mobility (Table S4); densities (Table S5) (PDF)

■ AUTHOR INFORMATION

Corresponding Author

*E-mail: kanishka@jncasr.ac.in.

ORCID

Swapan K. Pati: 0000-0002-5124-7455
Kanishka Biswas: 0000-0001-9119-2455

Notes

The authors declare no competing financial interest.

■ ACKNOWLEDGMENTS

This work was partially supported by DST (DST/TMD/MES/2k17/24) and Sheikh Saqr Laboratory, JNCASR. S.R. thanks CSIR for a fellowship. R.K.B. and M.D. thank UGC for fellowships. The synchrotron X-ray experiment was carried out at the light source PETRA III of DESY, a member of the Helmholtz Association (HGF). We thank Dr. J. C. Bednarcik for assistance at beamline P02.1. Financial support by the DST (Govt. of India) provided within the framework of the India@DESY collaboration is gratefully acknowledged.

REFERENCES

(1) Fultz, B. Vibrational thermodynamics of materials. *Prog. Mater. Sci.* **2010**, *55*, 247−352.

(2) Tan, G.; Zhao, L. D.; Kanatzidis, M. G. Rationally designing high-performance bulk thermoelectric materials. *Chem. Rev.* **2016**, *116*, 12123−12149.

(3) Sootsman, J.; Chung, D. Y.; Kanatzidis, M. G. New and old concepts in thermoelectric materials. *Angew. Chem., Int. Ed.* **2009**, *48*, 8616−8639.

(4) Jana, M. K.; Biswas, K. Crystalline solids with intrinsically low lattice thermal conductivity for thermoelectric energy conversion. *ACS Energy Lett.* **2018**, *3*, 1315−1324.

(5) Chang, C.; Wu, M.; He, D.; Pei, Y.; Wu, C. F.; Wu, X.; Yu, H.; Zhu, F.; Wang, K.; Chen, Y.; Huang, L.; Li, J.-F.; He, J.; Zhao, L.-D. 3D charge and 2D phonon transports leading to high out-of-plane ZT in n-type SnSe crystals. *Science* **2018**, *360*, 778−783.

(6) Chandra, S.; Banik, A.; Biswas, K. *n*-Type ultrathin few-layer nanosheets of Bi-doped SnSe: synthesis and thermoelectric properties. *ACS Energy Lett.* **2018**, *3*, 1153−1158.

(7) Roychowdhury, S.; Panigrahi, R.; Perumal, S.; Biswas, K. Ultrahigh thermoelectric figure of merit and enhanced mechanical stability of p-type $AgSb_{1-x}Zn_xTe_2$. *ACS Energy Lett.* **2017**, *2*, 349−356.

(8) Samanta, M.; Biswas, K. Low thermal conductivity and high thermoelectric performance in $(GeTe)_{1-2x}(GeSe)_x(GeS)_x$: Competition between solid solution and phase separation. *J. Am. Chem. Soc.* **2017**, *139*, 9382−9391.

(9) Korkosz, R. J.; Chasapis, T. C.; Lo, S.; Doak, J. W.; Kim, Y. J.; Wu, C.; Hatzikraniotis, E.; Hogan, T. P.; Seidman, D. N.; Wolverton, C.; Dravid, V. P.; Kanatzidis, M. G. High ZT in p-Type $(PbTe)_{1-2x}(PbSe)_x(PbS)_x$ thermoelectric materials. *J. Am. Chem. Soc.* **2014**, *136*, 3225−3237.

(10) Mao, Z.; Seidman, D. N.; Wolverton, C. The effect of vibrational entropy on the solubility and stability of ordered Al_3Li phases in Al-Li alloys. *APL Mater.* **2013**, *1*, 042103.

(11) Doak, J. W.; Wolverton, C.; Ozoliņs, V. Vibrational contributions to the phase stability of PbS-PbTe alloys. *Phys. Rev. B: Condens. Matter Mater. Phys.* **2015**, *92*, 174306.

(12) Banik, A.; Vishal, B.; Perumal, S.; Datta, R.; Biswas, K. The origin of low thermal conductivity in $Sn_{1-x}Sb_xTe$: phonon scattering *via* layered intergrowth nanostructures. *Energy Environ. Sci.* **2016**, *9*, 2011−2019.

(13) Li, W.; Wu, Y.; Lin, S.; Chen, Z.; Li, J.; Zhang, X.; Zheng, L.; Pei, Y. Advances in environment friendly SnTe thermoelectrics. *ACS Energy Lett.* **2017**, *2*, 2349−2355.

(14) Hu, L.; Zhang, Y.; Wu, H.; Li, J.; Li, Y.; Mckenna, M.; He, J.; Liu, F.; Pennycook, S. J.; Zeng, X. Entropy engineering of SnTe: Multi-principal-element alloying leading to ultralow lattice thermal conductivity and state-of-the-Art thermoelectric performance. *Adv. Energy Mater.* **2018**, *8*, 1802116.

(15) Banik, A.; Ghosh, T.; Arora, R.; Dutta, M.; Pandey, J.; Acharya, S.; Soni, A.; Waghmare, U. V.; Biswas, K. Engineering ferroelectric instability to achieve ultralow thermal conductivity and high thermoelectric performance in $Sn_{1-x}Ge_xTe$. *Energy Environ. Sci.* **2019**, *12*, 589−595.

(16) Tan, G.; Zhao, L. D.; Shi, F.; Doak, J. W.; Lo, S. H.; Sun, H.; Wolverton, C.; Dravid, V. P.; Uher, C.; Kanatzidis, M. G. High thermoelectric performance of p-type SnTe via a synergistic band engineering and nanostructuring approach. *J. Am. Chem. Soc.* **2014**, *136*, 7006−7017.

(17) Banik, A.; Shenoy, U. S.; Anand, S.; Waghmare, U. V.; Biswas, K. Mg alloying in SnTe facilitates valence band convergence and optimizes thermoelectric properties. *Chem. Mater.* **2015**, *27*, 581−587.

(18) Banik, A.; Biswas, K. Lead-free thermoelectrics: promising thermoelectric performance in p-type $SnTe_{1-x}Se_x$ system. *J. Mater. Chem. A* **2014**, *2*, 9620−9625.

(19) Zhang, Q.; Chere, E. K.; Sun, J.; Cao, F.; Dahal, K.; Chen, S.; Chen, G.; Ren, Z. Studies on thermoelectric properties of n-type polycrystalline $SnSe_{1-x}S_x$ by iodine doping. *Adv. Energy Mater.* **2015**, *5*, 1500360.

(20) Lin, C.-C.; Lydia, R.; Yun, J. H.; Lee, H. S.; Rhyee, J. S. Extremely low lattice thermal conductivity and point defect scattering of phonons in Ag-doped $(SnSe)_{1-x}(SnS)_x$ compounds. *Chem. Mater.* **2017**, *29*, 5344−5352.

(21) Tan, G. J.; Shi, F. Y.; Doak, J. W.; Sun, H.; Zhao, L. D.; Wang, P. L.; Uher, C.; Wolverton, C.; Dravid, V. P.; Kanatzidis, M. G. Extraordinary role of Hg in enhancing the thermoelectric performance of p-type SnTe. *Energy Environ. Sci.* **2015**, *8*, 267−277.

(22) Wu, H.; Chang, C.; Feng, D.; Xiao, Y.; Zhang, X.; Pei, Y.; Zheng, L.; Wu, D.; Gong, S.; Chen, Y.; He, J.; Kanatzidis, M. G.; Zhao, L.-D. Synergistically optimized electrical and thermal transport properties of SnTe *via* alloying high-solubility MnTe. *Energy Environ. Sci.* **2015**, *8*, 3298−3312.

(23) Tang, J.; Gao, B.; Lin, S.; Li, J.; Chen, Z.; Xiong, F.; Li, W.; Chen, Y.; Pei, Y. Manipulation of band structure and interstitial defects for improving thermoelectric SnTe. *Adv. Funct. Mater.* **2018**, *28*, 1803586.

(24) Tan, G.; Shi, F.; Sun, H.; Zhao, L.-D.; Uher, C.; Dravid, V. P.; Kanatzidis, M. G. SnTe−$AgBiTe_2$ as an efficient thermoelectric material with low thermal conductivity. *J. Mater. Chem. A* **2014**, *2*, 20849−20854.

(25) Lee, S.; Esfarjani, K.; Luo, T.; Zhou, J.; Tian, Z.; Chen, G. Resonant bonding leads to low lattice thermal conductivity. *Nat. Commun.* **2014**, *5*, 3525.

(26) Aggarwal, L.; Banik, A.; Anand, S.; Waghmare, U. V.; Biswas, K.; Sheet, G. Local ferroelectricity in thermoelectric SnTe above room temperature driven by competing phonon instabilities and soft resonant bonding. *J. Materiomics* **2016**, *2*, 196−202.

(27) Baroni, S.; de Gironcoli, S.; Dal Corso, A.; Giannozzi, P. Phonons and related properties of extended systems from density-functional perturbation theory. *Rev. Mod. Phys.* **2001**, *73*, 515−562.

(28) Luo, Z.-Z.; Hao, S.; Zhang, X.; Hua, X.; Cai, S.; Tan, G.; Bailey, T. P.; Ma, R.; Uher, C.; Wolverton, C.; Dravid, V. P.; Yan, Q.; Kanatzidis, M. G. Soft phonon modes from off-center Ge atoms lead to ultralow thermal conductivity and superior thermoelectric performance in n-type PbSe−GeSe. *Energy Environ. Sci.* **2018**, *11*, 3220−3230.

(29) Zhang, Q.; Liao, B.; Lan, Y.; Lukas, K.; Liu, W.; Esfarjani, K.; Opeil, C.; Broido, D.; Chen, G.; Ren, Z. High thermoelectric performance by resonant dopant indium in nanostructured SnTe. *Proc. Natl. Acad. Sci. U. S. A.* **2013**, *110*, 13261−13266.

(30) Banik, A.; Shenoy, U. S.; Saha, S.; Waghmare, U. V.; Biswas, K. High power factor and enhanced thermoelectric performance of SnTe-$AgInTe_2$: synergistic effect of resonance level and valence band convergence. *J. Am. Chem. Soc.* **2016**, *138*, 13068−13075.

(31) Brebrick, R. F.; Strauss, A. J. Anomalous thermoelectric power as evidence for two valence bands in SnTe. *Phys. Rev.* **1963**, *131*, 104−110.

THE JOURNAL OF
PHYSICAL CHEMISTRY C

pubs.acs.org/JPCC Article

Broadband Colossal Dielectric Constant in the Superionic Halide $RbAg_4I_5$: Role of Intercluster Ag^+ Diffusion

Paribesh Acharyya, Tanmoy Ghosh, Shidaling Matteppanavar, Raju K. Biswas, Premakumar Yanda, Srinivasa R. Varanasi, Dirtha Sanyal, A. Sundaresan, Swapan K. Pati, and Kanishka Biswas*

Cite This: *J. Phys. Chem. C* 2020, 124, 9802−9809

Read Online

ACCESS | Metrics & More | Article Recommendations | Supporting Information

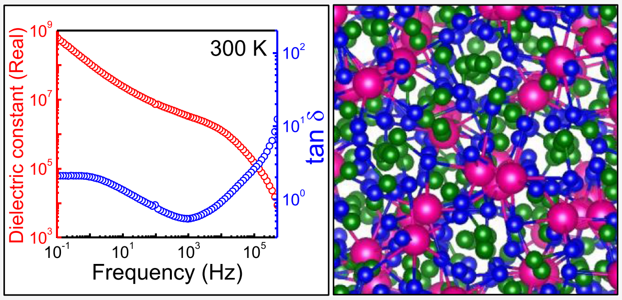

ABSTRACT: Materials with ultrahigh dielectric constants and a low value of dielectric loss are important for energy storage and electronic devices. Traditionally, high dielectric constant is found in ferroelectric complex oxides, but they exhibit high dielectric loss as well. Herein, a broadband colossal dielectric constant in a superionic halide, $RbAg_4I_5$, with a low dielectric loss is presented. The real part of the dielectric constant, ε', increases by 10^2 orders of magnitude as $RbAg_4I_5$ goes through a superionic transition at 121 K. At room temperature, $\varepsilon' > 10^6$ in the frequency range 10^{-1} to 10^4 Hz with a low dielectric loss, which ranges between 2.03 and 0.53. The maximum of ε' reaches a colossal value of 6.4×10^8 at 0.1 Hz at 300 K. The molecular dynamics simulation reveals the presence of Ag^+ clusters with a broad size distribution. The intercluster diffusion of Ag^+ causes significant instantaneous charge separation and a consequent large fluctuation in the dipole moments. The fluctuating dipoles, in turn, result in the colossal dielectric constant in $RbAg_4I_5$.

■ INTRODUCTION

The development of materials with a colossal dielectric constant (CDC) is an integral part of advancing the modern electronics, sensors, and energy-storage devices.[1−6] Traditionally, high dielectric constant is associated with ferroelectric oxides across their paraelectric to ferroelectric transition, where $\varepsilon' \approx 10^3$ to 10^4 can be easily achieved.[7−12] Recently, few complex oxides have also emerged as nonferroelectric high dielectric constant materials where high ε' arises either from polarization relaxation and polar fluctuations in nanosize domains or from Maxwell−Wagner polarization in the grain boundaries.[13−18] One of the most notable examples is the double-perovskite $CaCu_3Ti_4O_{12}$ (CCTO) in which CDC with $\varepsilon' \approx 10^4$ to 10^5 has been achieved over a broad temperature and frequency range, although the exact origin of the CDC in CCTO is still under debate.[19−22] However, most of these oxides have a high dielectric loss, tan δ, as well. Low-dimensional systems with a charge density wave also show a high dielectric constant; however, the associated tan δ is high.[23,24] Recently, another intriguing category of materials, called superionic conductors, are emerging as high dielectric constant materials with a low tan δ.[25−27] The perovskite oxide superionic conductor $Rb_2Ti_2O_5$ exhibited a dielectric constant $\varepsilon' \approx 10^9$ at 0.01 Hz at 300 K.[25]

Superionic conductors are solid materials with a high ionic conductivity ($\sigma > 10^{-3}$ S/cm; in ordinary solid $\sigma \approx 10^{-8}$ S/cm).[28,29] For example, the room-temperature ionic conductivities of the superionic compounds $Rb_2Ti_2O_5$ and $RbAg_4I_5$ are $\sim 10^{-3}$ and ~ 0.2 S/cm, respectively.[25,30] Such a high ionic conductivity is, in general, thought to be detrimental to achieving CDC in a material. One of the requirements for observing CDC in superionic conductors is that the material must have very low electronic conductivity. For example, $Rb_2Ti_2O_5$ has room-temperature electronic conductivity $\sim 10^{-8}$ S/cm.[25] The room-temperature electronic conductivity of the present $RbAg_4I_5$ is $\sim 10^{-9}$ S/cm, which satisfies the required condition.[31,32] Superionicity in a material is induced when highly disordered cation sites are present along with polar states.[33] The polar states are created by the charge transfer due to ion migrations to the interstices. Consequently, these ionic migrations may create dipoles in the lattice, which is probably important to have a high dielectric constant. $RbAg_4I_5$ exhibits a complex crystal structure[34−36] with a large number of Ag^+ present in the lattice, which migrate to the interstitial positions in its superionic phase, and therefore, $RbAg_4I_5$ is expected to show CDC.

Herein, we have demonstrated a broadband CDC with a low dielectric loss in superionic $RbAg_4I_5$, which is synthesized by a

Received: March 10, 2020
Revised: April 11, 2020
Published: April 14, 2020

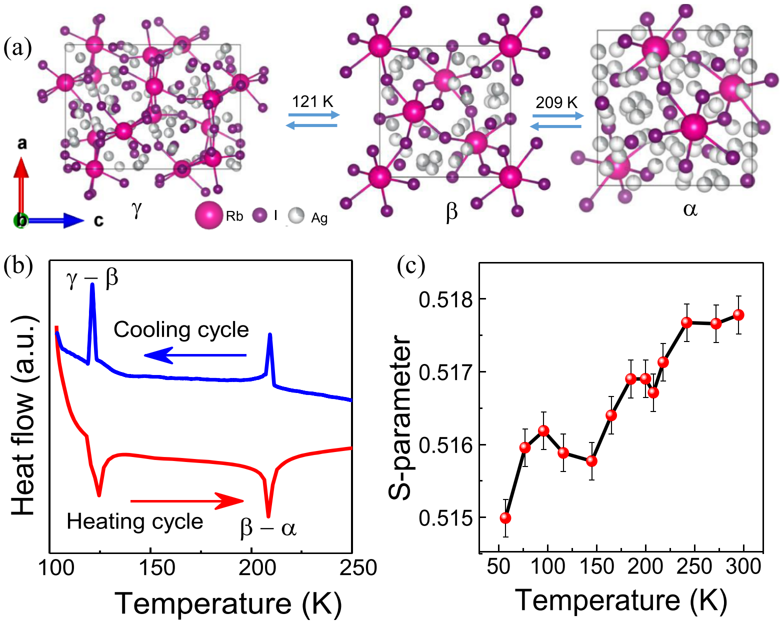

Figure 1. (a) Cubic α-phase, rhombohedral β-phase, and trigonal γ-phase of $RbAg_4I_5$. (b) DSC signal showing the structural phase transitions in $RbAg_4I_5$. (c) Temperature dependence of the S-parameter obtained from PAL spectroscopy.

facile, solvent-free mechanochemical synthesis at room temperature. The presence of two structural phase transitions with decreasing temperature, α (cubic, space group $P4_332$; Figure 1a) $\rightarrow \beta$ (rhombohedral, space group R32; Figure 1a) at 209 K and $\beta \rightarrow \gamma$ (trigonal, space group $P321$; Figure 1a) at 121 K, has been confirmed via temperature-dependent powder X-ray diffraction (PXRD) and differential scanning calorimetry (DSC). The temperature-dependent positron annihilation lifetime (PAL) spectroscopy and coincidence Doppler broadening (CDB) spectra evidence the presence of charged vacancies associated with the diffusion of Ag^+. We have shown that ε' increases by 10^2 orders of magnitude as $RbAg_4I_5$ goes through the $\gamma \rightarrow \beta$ superionic phase transition from the low-temperature side, and ε' reaches a giant value $\sim 6.4 \times 10^8$ at 0.1 Hz in the room-temperature superionic α phase. The molecular dynamics (MD) simulation shows charge density fluctuation within Ag^+ clusters because of intercluster Ag^+ diffusion. This causes fluctuation in the instantaneous dipole moments associated with Ag^+ clusters and results in the experimentally observed CDC in the room-temperature superionic phase of $RbAg_4I_5$.

■ METHODS

Experimental Section. *Starting Materials.* Rubidium (I) iodide (RbI, 99.5%) and silver (I) iodide (AgI, 99.999%) were purchased from Sigma Aldrich and used without further purification during synthesis.

Methods of Synthesis. For the $RbAg_4I_5$ synthesis, 939 mg of AgI (4 mmol) and 212.4 mg (1 mmol) of RbI were taken as precursors in a mortar and pestle. The precursors were mechanically ground and mixed thoroughly in the mortar and pestle for about 2 h under inert condition (N_2-filled glove bag).

The following scheme is implemented to synthesize high-quality polycrystals of $RbAg_4I_5$

$$\text{RbI} + 4\text{AgI} \xrightarrow{\text{mechanochemistry}} \text{RbAg}_4\text{I}_5$$

The polycrystalline pellets of $RbAg_4I_5$ (Figure S1, Supporting Information) were obtained thorough spark plasma sintering (SPS) using a SPS211-LX, Dr. Sinter Lab SPS machine. SPS was carried out at 120 °C under an applied pressure of 50 MPa for 20 min. The SPS-processed sample was polished and used for PAL spectroscopy and dielectric measurements.

PXRD. A Rigaku Smart Lab X-ray diffractometer equipped with a Cu Kα (wavelength = 1.54059 Å) X-ray source was used to acquire the temperature-dependent PXRD patterns of as-synthesized $RbAg_4I_5$ at 80, 180, and 300 K.

DSC. Finely ground powder samples were used for DSC measurements, in which the data were collected in a wide temperature range from 100 to 300 K by using a METTLER TOLEDO differential scanning calorimeter (DSC 822 e) at a fixed heating/cooling rate of 1 K/min.

PAL and CDB Spectroscopies. The PAL spectra was measured by the standard fast γ−γ coincidence technique by utilizing two BaF_2 ultrafast scintillators coupled with a XP2020Q photomultiplier tube. An approximately 10 μCi ^{22}NaCl positron-emitting source sealed in a thin mylar foil was sandwiched between two identical pellets of the $RbAg_4I_5$ sample. The specific experimental setup can be found in an earlier report.[37] The acquired life-time spectrum has been deconvoluted to reveal the lifetime values by the computer program, PATFIT-88,[38] after considering proper source correction.

An HPGe detector was exploited for the detection of Doppler broadening, originating from the positron annihilation γ-ray of 511 keV. An energy resolution of 1.15 from ^{85}Sr at 514 keV possesses an efficiency equivalent to 12% (model number PGC 1216sp of DSG, Germany). The details of the experimental setup are described in an earlier report.[39]

The CDB spectroscopic method was employed to recognize either the chemical features of the defect or the potential rationale for the enhancement in the S-parameter. The CDB experiments were carried out by using two analogous HPGe detectors of 12% efficiency with the model number PGC 1216sp of DSG, Germany. The peak to background ratio for the present CDB setup with ± ΔE selection is better than 105:1. Details of the experimental setup are depicted in an earlier report.[39]

S-Parameter can be designated as the ratio of the counts within the energy range of $|511\text{ keV} - E| \leq 0.85$ keV to the total counts within the energy range of $|511\text{ keV} - E| \leq 4.25$ keV under the photopeak of 511 keV.

Dielectric Measurements. The temperature- and frequency-dependent dielectric properties were determined in a physical property measurement system (Quantum Design, USA) using an Agilent E4980A LCR meter within the frequency range of 20 Hz to 200 kHz. The room-temperature dielectric properties were obtained using a Solartron 1260A impedance analyzer from the frequency of 0.1 Hz to 500 kHz. These measurements were conducted in the parallel plate geometry, in which Pelco high-performance silver paste from TED PELLA was coated on either side of the disk-shaped pellet sample.

I−V Measurement. The room-temperature $I-V$ curve of $RbAg_4I_5$ (Figure S2, Supporting Information) was measured using a rectangular bar of dimensions ∼2 × 2 × 8 mm, which was obtained after polishing an SPS processed pellet specimen in a ULVAC-RIKO ZEM-3 instrument.

Theoretical Section. *MD Simulation.* The interactions between Ag^+-Ag^+, Ag^+-I^-, Ag^+-Rb^+, and I^--I^- have been modeled using the Vasishta−Rahman potential.[40]

$$\phi_{ab}^{VR} = \frac{Z_a Z_b e^2}{r_{ab}} + \frac{A(\sigma_a + \sigma_b)^{n_{ab}}}{r_{ab}^{n_{ab}}} - \frac{w_{ab}}{r_{ab}^{6}} - \frac{(\alpha_a {Z_b}^2 + \alpha_b {Z_a}^2)/2}{r_{ab}^{4}} \qquad (1)$$

where r_a, r_b, and r_{ab} are the positions of the ions a and b and the distance between them, respectively. A is the repulsive strength; σ_a and σ_b are the ionic radii; α_a and α_b are the electronic polarizabilities; and Z_a and Z_b are the fractional charges on the ions a and b, respectively. Electronic polarizabilities of Ag^+ and Rb^+ have been taken to be zero since they are relatively smaller in size than I^-. n_{ab} is the degree of hardness of the repulsive interaction between the ions a and b.

The interaction between Rb^+-Rb^+ and Rb^+-I^- has been modeled with the Born−Mayer potential[40]

$$\phi_{ab}^{BM} = \frac{Z_a Z_b e^2}{r_{ab}} + B_{ab} e^{-\gamma r_{ab}} - \frac{C_{ab}}{r_{ab}^{6}} - \frac{D_{ab}}{r_{ab}^{8}} \qquad (2)$$

where the first and second terms emerged from the Coulomb interactions between two point charges and the overlap between the outer shell electrons of corresponding ions, respectively. Furthermore, the third and fourth terms appeared due to van der Waals interactions. The parameters related to the above-mentioned interaction potentials have been extracted from the work of Tahara and Fukami.[40]

We have taken the crystal structure of α-$RbAg_4I_5$ as our starting configuration, and the unit cell has been replicated three times in each direction to form a larger cubic simulation box. The simulation box contains 2560 atoms in total. MD simulations were performed in the NPT ensemble under ambient conditions for about 3 ns to obtain an equilibrated volume of the simulation cell. A time step of 1 fs was used in the velocity form of Verlet integrator. We implemented the simulation in the microcanonical (NVE) ensemble for about 3 ns to equilibrate the system at 298 K. After achieving the equilibration, further MD simulation was executed for 10 ns during which the trajectories were stored every 10 fs. In order to calculate the electrostatic interactions, Ewald summation technique was utilized. All interactions were truncated using a cutoff distance of 1.8 nm. Periodic boundary conditions were employed in all directions in order to ensure that there are no surface effects at the boundaries.

Connectivity Analysis and Cluster Size Estimation. Further to study the ordering arrangement of Ag^+ ions, connectivity analysis was carried out on the equilibrated atomic configurations procured from the MD simulations. In the connectivity analysis, we considered that the neighboring atoms formed clusters of various sizes within the first correlation length, corresponding to the first peak position in $g_{ab}(r)$. The dimensions of such cluster sizes are estimated by the number of ions present in the cluster within the first peak in the radial distribution function. The size distributions of these clusters were estimated by considering an average of 25 atomic configurations, each of which was obtained after consecutive 2000 MD time steps.

Diffusion Coefficient Calculation. To further validate our results, we investigated the dynamical properties of Ag^+, which correspond to the time correlation functions. These functions are further associated with the values obtained on different time scales (t) by assuming that the system is in equilibrium as well as independent of the choice of origin. The time evolution of ionic configurations in the simulation cell was implemented to calculate the physical quantity equivalent of the ionic transport properties, which is as follows. The following equation of mean square displacement (MSD) can be expressed as

$$\langle {r_a}^2(t) \rangle = \frac{1}{N_a} \sum_{i_a=1}^{N_a} \langle |r_{i_a}(t) - r_{i_a}(0)|^2 \rangle \qquad (3)$$

where the total number of a-type ions can be denoted by the N_a term. MSD curves plotted as a function of MD time steps for Rb^+, Ag^+, and I^- are shown in Figure S3, Supporting Information. We notice that the diffusive behavior of Ag^+ is more prominent compared to all other types of ions. Once MSD is calculated, the diffusion coefficient (D) can be estimated from the linear regime in the MSD curve of Ag^+ ions at $t \to \infty$, that is,

$$D = \lim_{t \to \infty} \frac{{r_a}^2(t)}{6t} \qquad (4)$$

Dipole Moment Calculation. The dipole moment (M) of component x at time step t of a MD simulation trajectory is calculated by the expression[41]

$$M_{x,t} = \sum_{k=1}^{N} q_k r_{k,t} \qquad (5)$$

where r_k, N, and q_k are the position coordinate of atom k, the total number of atoms in the simulation box, and the charges, respectively. It is important to mention that the calculation of the dipole moment relied on the choice of the basis of the coordinate system. For our model, the dipole moment was evaluated in respect of the center of mass of the system. The static dielectric constant of a material follows the expression:[42]

$$\varepsilon = \frac{\langle M^2 \rangle - \langle M \rangle^2}{3V\varepsilon_0 k_B T} + 1 \qquad (6)$$

where V, k_B, ε_0, and T are the volume of the supercell, the Boltzmann constant, the permittivity of free space, and the absolute temperature, respectively.

RESULTS AND DISCUSSION

$RbAg_4I_5$ is a well-known prototypical superionic conductor with a very high ionic conductivity of ~0.2 S/cm at room temperature.[30] The room-temperature superionic phase (α-phase) has a complex cubic crystal structure with four $RbAg_4I_5$ units in the unit cell.[34−36] Three types of crystallographically nonequivalent sites are present for Ag^+: one eight-fold (Ag-c sites) and two 24-fold sets (Ag−I and Ag-II sites). The superionicity in $RbAg_4I_5$ arises from the fast diffusion of Ag^+ (diffusion coefficient $\sim 10^{-6}$ cm^2 s^{-1}) in a β-Mn-type rigid iodide sublattice.[34−36,43,44] The iodide substructure contains 56 iodide tetrahedra in which 16 Ag^+ are randomly distributed in the interstitial positions. The tetrahedral framework is arranged in such a fashion that they create a network of passageways for the diffusion of Ag^+. The room-temperature cubic α-phase of $RbAg_4I_5$ is preceded by two structural phase transitions with decreasing temperature: a weak first-order $\alpha \rightarrow \beta$ phase transition at 209 K and a first-order $\beta \rightarrow \gamma$ phase transition at 121 K.[35,45−48] Remarkably, the iodide substructure remains almost intact, suffering only minor distortions to accommodate the partial ordering of Ag^+ at specific sites, across all these phase transitions.[35] The partial ordering of Ag^+ in the β phase restricts the movement of Ag^+ along the crystallographic c-axis, which decreases the ionic conductivity. Interestingly, Ag^+ remains partially disordered in the lowest temperature γ phase; however, the Ag^+ ionic diffusion occurs only within isolated clusters.[36]

Here, we have carried out a facile solvent-free mechanochemical synthesis of $RbAg_4I_5$ at room temperature (see details in experimental section). The presence of two sharp peaks in the DSC signal (Figure 1b) confirms the presence of two structural phase transitions at 209 and 121 K in the mechanochemically synthesized $RbAg_4I_5$. The temperature-dependent PXRD patterns at 300, 180, and 80 K are shown in Figure S4, Supporting Information. The Rietveld refinements of the temperature-dependent PXRD patterns confirm the room-temperature cubic (space group $P4_332$), mid-temperature rhombohedral (space group R32), and low-temperature trigonal (space group $P321$) structures corresponding to α, β, and γ phases, respectively. The two superionic α and β phases are differentiated only by a small distortion in the iodide sublattice. The obtained crystal structure parameters (Tables S1−S4, Supporting Information) for all three phases agree well with the previous reports.

The diffusion of Ag^+ creates charged vacancies in the system, which have been experimentally probed using PAL and CDB spectroscopies. The fitting of PAL spectra at 300 K (Figure S5a, Supporting Information) yields a short lifetime of 180 ± 2 ps of 20 ± 1% intensity and a longer component of 341 ± 5 ps with 80 ± 1% intensity. The positron trapped in a cation defect elapses for a longer time.[49] Therefore, the short lifetime component (180 ± 2 ps) has been assigned to the free annihilation of positrons, whereas the longer lifetime component (341 ± 5 ps) has been assigned to the positron annihilation at the vacancy sites.[49] The high intensity of the PAL component at the vacancy sites indicates the strong ionic character of the material as these charged vacancies are created because of the diffusion of Ag^+. The ionic conductivity of $RbAg_4I_5$ increases with increasing temperature because of increased diffusion of Ag^+.[43,44] As a result, charged vacancies also increase, and this is reflected in the gradual increase of the Doppler broadening S-parameter with increasing temperature (Figure 1c). Two anomalies corresponding to the $\gamma \rightarrow \beta$ and $\beta \rightarrow \alpha$ phase transitions with increasing temperature are also evident in the temperature variation of the S-parameter. The area-normalized ratio curve of the CDB spectra at 300 K with respect to the 50 K CDB spectra (Figure S5b, Supporting Information) shows a broad dip at the momentum value $\sim 19 \times 10^{-3}$ m °c. The corresponding energy value is 92 eV which is very close to the binding energy of the 4 s electron of Ag. This indicates that the positrons are less annihilating with the core electrons of Ag^+ at 300 K.

The experimentally measured temperature variations of the dielectric constant (ε') and dielectric loss (tan δ) at different frequencies ranging between 1 and 200 kHz are shown in Figures 2 and S6, Supporting Information. The presence of two phase transitions, $\gamma \rightarrow \beta$ and $\beta \rightarrow \alpha$, with increasing temperature is evident from the temperature variations of ε' and tan δ. From the low-temperature side, ε' steeply increased by 10^1 to 10^2 orders of magnitude at the first-order superionic $\gamma \rightarrow \beta$ phase transition. For example, ε' at 1 kHz increases from 16.5 at 110 K to 3096 at 125 K. Correspondingly, tan δ exhibits a peak, which shifts to higher temperature with increasing frequency. ε' continues to increase gradually after the superionic $\gamma \rightarrow \beta$ phase transition with increasing temperature, except for a weak anomaly across the $\beta \rightarrow \alpha$ phase transition at 209 K. $RbAg_4I_5$ emerges to the superionic phase at the first structural transition ($\gamma \rightarrow \beta$ at ~121 K); therefore, the dielectric constant changes drastically across this transition. However, $RbAg_4I_5$ is already in the superionic regime when the second phase transition ($\beta \rightarrow \alpha$) occurs at ~209 K, and as a result, the change in dielectric response is not as dramatic as the one observed across the first structural transition ($\gamma \rightarrow \beta$) at ~121 K.

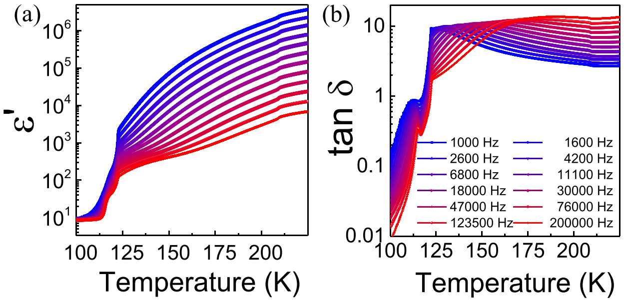

Figure 2. Temperature and frequency dependences of the (a) dielectric constant (ε') and (b) dielectric loss (tan δ) for $RbAg_4I_5$.

The experimentally obtained frequency dependence of the dielectric constant (ε') at 150 and 300 K corresponding to the superionic β and α phases, respectively, is shown in Figure 3a. At 300 K, ε' has a broadband colossal value $>10^6$ in the frequency range 10^{-1} to 10^4 Hz, with the maximum value reaching $\sim 6.4 \times 10^8$ at 0.1 Hz. The corresponding dielectric loss (tan δ) in the frequency range 10^{-1} to 10^4 varies between 2.03 and 0.53, which is low (Figure 3b). A comparison of the room-temperature dielectric properties of $RbAg_4I_5$ with other high dielectric constant materials is listed in Table S5, Supporting Information. Ag^+ diffusion dominates the transport behavior of $RbAg_4I_5$ at 300 K. For such diffusion-dominated behavior, log|Z| (|Z| is the impedance magnitude) varies linearly with log f in the low-frequency region and has a slope −1/2 or −1/4.[50] This linear relationship between log|Z| and log f is evident in the low-frequency region at room temperature (Figure 3c). The

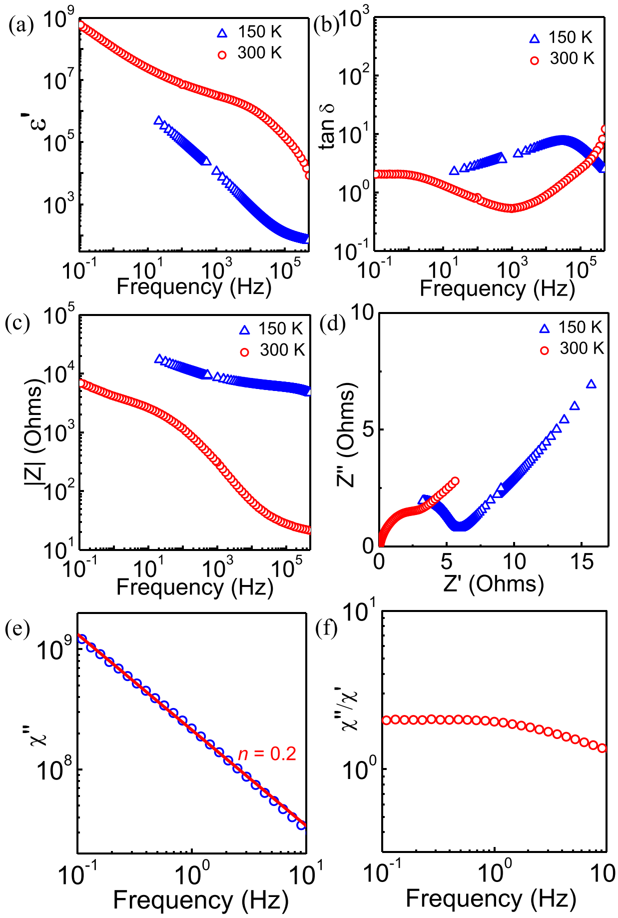

Figure 3. Frequency dependences of (a) the dielectric constant (ε'), (b) the dielectric loss ($\tan\delta$), (c) |Z|, and (d) Nyquist plots at 150 and 300 K. Room-temperature (e) $\chi''(\omega)$ and (f) $\chi''(\omega)/\chi'(\omega)$ exhibiting the universal dielectric response according to Jonscher's theory.

obtained slope is −0.234(2) in the frequency region 1−0.1 Hz. Furthermore, the Nyquist plot (Figure 3d) also shows a linear relationship between the real and imaginary parts of impedance, Z' and Z'', respectively, in the low-frequency region, indicating the diffusion-dominated behavior.

The observed dielectric properties of $RbAg_4I_5$ can also be reconciled with the universal dielectric response (UDR), as put forward by Jonscher.[51,52] According to the Jonscher's theory, the dielectric response of most materials follows a universal pattern, which in the frequency domain can be expressed as follows: (i) the frequency dependence of the imaginary part of complex susceptibility (χ) follows a sublinear power law, that is, $\chi''(\omega) \propto \omega^{n-1}$ with $0 < n < 1$ and (ii) the ratio $\chi''(\omega)/\chi'(\omega)$ is constant and independent of the frequency. In the case of ionic conductors, n has low values so that the exponent $(n - 1)$ is close to unity, which is often called as low-frequency dispersion (LFD). The frequency dependences of room-temperature $\chi''(\omega)$ and $\chi''(\omega)/\chi'(\omega)$ are shown in Figure 3e,f, respectively, which evidence that LFD of $RbAg_4I_5$ is in accordance with UDR with $n \approx 0.2$.

MD simulation was carried out in order to understand the origin of the experimentally observed broadband CDC behavior in the superionic $RbAg_4I_5$. The calculated partial radial pair distribution function $g_{ab}(r)$, which has been defined as $g_{ab}(r) = \frac{N_{ab}(r)}{4\pi r^2 \Delta r \rho_b}$ where $N_{ab}(r)$ is the number of b-type ions at a distance between r and $r + \Delta r$ from the central a-type ion and ρ_b is the mean number density of the b-type ions, from the equilibrated atomic configuration in the MD simulation cell at 298 K is shown in Figures 4a and S7a, Supporting Information. The partial radial distribution functions calculated from our model match reasonably well with those from other previous studies.[40,42] The first sharp peak in $g_{ab}(r)$ for the I^-—I^- pair at ∼4.28 Å and a deep minimum at ∼5.76 Å (Figure 4a) correspond to the first coordination between the I^-—I^- pair and indicates the structural ordering of I^-. Further, the presence of well-defined second and third peaks at ∼7.30 and ∼8.60 Å,

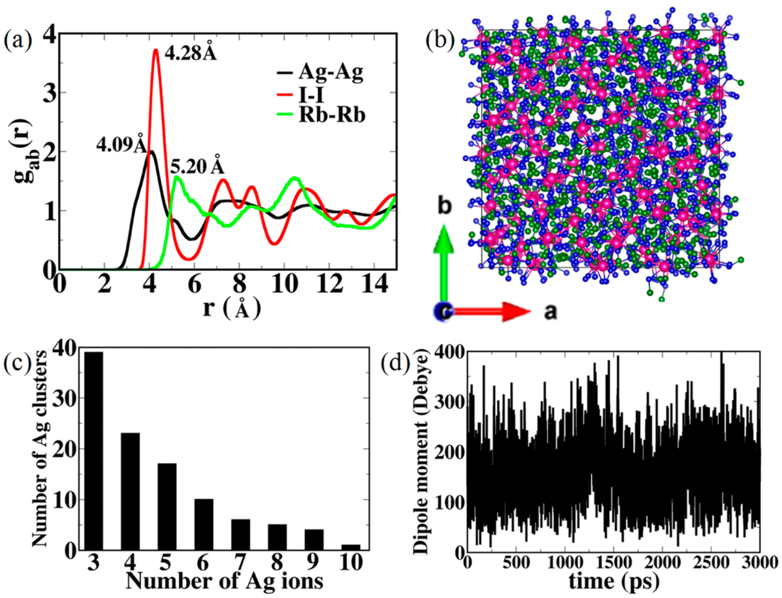

Figure 4. (a) Partial radial pair distribution function $g_{ab}(r)$ vs radial distance r between Ag^+—Ag^+, Rb^+—Rb^+, and I^-—I^- and (b) snapshot of the $RbAg_4I_5$ supercell obtained from MD simulation at 298 K; Ag, green; Rb, magenta; and I, blue. (c) Histogram showing the distribution of the Ag cluster. (d) Fluctuation in dipole moments at 298 K.

respectively, in $g_{ab}(r)$ indicates the long-range ordering of I^-. The presence of the first sharp peak in $g_{ab}(r)$ corresponding to the first neighbor coordination for the Ag^+-I^- pair at ~2.62 Å (Figure S7a, Supporting Information) further indicates the ordered arrangement of I^- around Ag^+ throughout the solid. The first peak in $g_{ab}(r)$ for the Rb^+-I^- pair at ~3.30 Å (Figure S7a, Supporting Information) is also sharp, but the magnitude is lower than that of the Ag^+-I^- pair, which suggests that a greater number of Ag^+ are present in the surrounding of I^- than Rb^+. This particular arrangement formed by I^- enforces Ag^+ to come close to each other and make a collection of Ag^+ as a cluster. A similar signature is observed in $g_{ab}(r)$ for the Ag^+-Ag^+ pair (Figure 4a). Instead of complete randomness, $g_{ab}(r)$ for the Ag^+-Ag^+ pair shows a broad peak at ~4.10 Å corresponding to the nearest neighbor coordination; however, the long-range coordination peaks, such as for the second and third coordinations, are not well defined, which indicate clustering of Ag^+. Ag^+ accumulation within the network of channels created by I^- and the formation of Ag^+ clusters are evident from the snapshot of the $RbAg_4I_5$ supercell obtained from MD simulation (Figures 4b and S7b, Supporting Information). Rb^+, because of its large size, facilitates smooth conduction pathways for Ag^+ to hop from one cluster to another, which consequently results in the high diffusion coefficient. The calculated diffusion coefficient 0.383×10^{-5} cm^2/s (see Methods for the diffusion coefficient calculation) agrees well with the experimental reports.[43] This intercluster ionic diffusion leads to a broad size distribution of the clusters (Figure 4c) and large charge separations, which, in turn, lead to large fluctuations in the instantaneous dipole moments in the range between 25 and 300 Debye (see Methods for dipole moment calculation) (Figure 4d). Consequently, these large fluctuating dipole moments result in the high dielectric constant as observed in the experiment.

CONCLUSIONS

In conclusion, we have demonstrated an extremely high room-temperature ε' in the superionic halide $RbAg_4I_5$, which reaches a maximum value of $\sim 6.4 \times 10^8$ at 0.1 Hz. This colossal ε' persists over a wide frequency range along with a low dielectric loss. The frequency dependence of impedance indicates that ionic diffusion has the dominating contribution, which results in such a giant ε'. MD simulation further established that this colossal ε' arises because of intercluster Ag^+ diffusion, which causes a large charge separation and an associated fluctuation in the instantaneous dipole moments. The observed broadband colossal ε' in this nonoxide superionic solid opens up new opportunities in dielectric investigations and structure−property relationship in new halides.[53]

ASSOCIATED CONTENT

Supporting Information

The Supporting Information is available free of charge at https://pubs.acs.org/doi/10.1021/acs.jpcc.0c02118.

Refinement of X-ray diffraction, additional PAL and dielectric data, and additional MD results (PDF)

AUTHOR INFORMATION

Corresponding Author

Kanishka Biswas − *New Chemistry Unit and School of Advanced Materials and International Centre of Materials Science, Jawaharlal Nehru Centre for Advanced Scientific Research (JNCASR), Bangalore 560064, India;* orcid.org/0000-0001-9119-2455; Email: kanishka@jncasr.ac.in

Authors

Paribesh Acharyya − *New Chemistry Unit, Jawaharlal Nehru Centre for Advanced Scientific Research (JNCASR), Bangalore 560064, India*

Tanmoy Ghosh − *New Chemistry Unit, Jawaharlal Nehru Centre for Advanced Scientific Research (JNCASR), Bangalore 560064, India*

Shidaling Matteppanavar − *New Chemistry Unit, Jawaharlal Nehru Centre for Advanced Scientific Research (JNCASR), Bangalore 560064, India*

Raju K. Biswas − *Theoretical Sciences Unit, Jawaharlal Nehru Centre for Advanced Scientific Research (JNCASR), Bangalore 560064, India*

Premakumar Yanda − *Chemistry and Physics of Materials Unit, Jawaharlal Nehru Centre for Advanced Scientific Research (JNCASR), Bangalore 560064, India*

Srinivasa R. Varanasi − *Theoretical Sciences Unit, Jawaharlal Nehru Centre for Advanced Scientific Research (JNCASR), Bangalore 560064, India*

Dirtha Sanyal − *Variable Energy Cyclotron Centre, Kolkata 700064, India;* orcid.org/0000-0003-2490-3610

A. Sundaresan − *Chemistry and Physics of Materials Unit and School of Advanced Materials and International Centre of Materials Science, Jawaharlal Nehru Centre for Advanced Scientific Research (JNCASR), Bangalore 560064, India;* orcid.org/0000-0002-1613-3030

Swapan K. Pati − *Theoretical Sciences Unit and School of Advanced Materials and International Centre of Materials Science, Jawaharlal Nehru Centre for Advanced Scientific Research (JNCASR), Bangalore 560064, India;* orcid.org/0000-0002-5124-7455

Complete contact information is available at: https://pubs.acs.org/10.1021/acs.jpcc.0c02118

Notes

The authors declare no competing financial interest.

ACKNOWLEDGMENTS

This work was supported by the DST (DST/TMD/MES/2k17/24). P.A. acknowledges the UGC and Diptikanta Swain, IISc for PXRD measurements. R.K.B. acknowledges the UGC. S.K.P. acknowledges the SERB, J C Bose Fellowship and DST for the financial support.

REFERENCES

(1) Kingon, A. I.; Maria, J.-P.; Streiffer, S. K. Alternative dielectrics to silicon dioxide for memory and logic devices. *Nature* **2000**, *406*, 1032−1038.

(2) Wang, Y.; Jie, W.; Yang, C.; Wei, X.; Hao, J. Colossal permittivity materials as superior dielectrics for diverse applications. *Adv. Funct. Mater.* **2019**, *29*, 1808118.

(3) Yim, K.; Yong, Y.; Lee, J.; Lee, K.; Nahm, H.-H.; Yoo, J.; Lee, C.; Seong Hwang, C.; Han, S. Novel high-κ dielectrics for next-generation electronic devices screened by automated ab initio calculations. *NPG Asia Mater.* **2015**, *7*, e190.

(4) Hao, X. A review on the dielectric materials for high energy-storage application. *J. Adv. Dielectr.* **2013**, *03*, 1330001.

(5) Palumbo, F.; Wen, C.; Lombardo, S.; Pazos, S.; Aguirre, F.; Eizenberg, M.; Hui, F.; Lanza, M. A review on dielectric breakdown in thin dielectrics: silicon dioxide, high-k, and layered dielectrics. *Adv. Funct. Mater.* **2019**, DOI: 10.1002/adfm.201900657.

(6) Roscow, J. I.; Bowen, C. R.; Almond, D. P. Breakdown in the case for materials with giant permittivity? *ACS Energy Lett.* **2017**, *2*, 2264−2269.

(7) Kim, B.-G.; Cho, S. M.; Kim, T.-Y.; Jang, H. M. Giant dielectric permittivity observed in Pb-based perovskite ferroelectrics. *Phys. Rev. Lett.* **2001**, *86*, 3404−3406.

(8) Pecharromán, C.; Esteban-Betegón, F.; Bartolomé, J. F.; López-Esteban, S.; Moya, J. S. New Percolative $BaTiO_3$−Ni Composites with a high and frequency-independent dielectric constant ($\epsilon_r \approx 80000$). *Adv. Mater.* **2001**, *13*, 1541−1544.

(9) Yan, Y.; Zhou, J. E.; Maurya, D.; Wang, Y. U.; Priya, S. Giant piezoelectric voltage coefficient in grain-oriented modified $PbTiO_3$ material. *Nat. Commun.* **2016**, *7*, 13089.

(10) Yu, J.; Ishikawa, T.; Arai, Y.; Yoda, S.; Itoh, M.; Saita, Y. Extrinsic origin of giant permittivity in hexagonal $BaTiO_3$ single crystals: Contributions of interfacial layer and depletion layer. *Appl. Phys. Lett.* **2005**, *87*, 252904.

(11) Wang, Z.; Chen, X. M.; Ni, L.; Liu, X. Q. Dielectric abnormities of complex perovskite $Ba(Fe_{1/2}Nb_{1/2})O_3$ ceramics over broad temperature and frequency range. *Appl. Phys. Lett.* **2007**, *90*, 022904.

(12) Haeni, J. H.; Irvin, P.; Chang, W.; Uecker, R.; Reiche, P.; Li, Y. L.; Choudhury, S.; Tian, W.; Hawley, M. E.; Craigo, B.; et al. Room-temperature ferroelectricity in strained $SrTiO_3$. *Nature* **2004**, *430*, 758.

(13) Sarkar, S.; Jana, P. K.; Chaudhuri, B. K.; Sakata, H. Copper (II) oxide as a giant dielectric material. *Appl. Phys. Lett.* **2006**, *89*, 212905.

(14) Wu, J.; Nan, C.-W.; Lin, Y.; Deng, Y. Giant dielectric permittivity observed in Li and Ti doped NiO. *Phys. Rev. Lett.* **2002**, *89*, 217601.

(15) Krohns, S.; Lunkenheimer, P.; Kant, C.; Pronin, A. V.; Brom, H. B.; Nugroho, A. A.; Diantoro, M.; Loidl, A. Colossal dielectric constant up to gigahertz at room temperature. *Appl. Phys. Lett.* **2009**, *94*, 122903.

(16) Park, T.; Nussinov, Z.; Hazzard, K. R. A.; Sidorov, V. A.; Balatsky, A. V.; Sarrao, J. L.; Cheong, S.-W.; Hundley, M. F.; Lee, J. S.; Jia, Q. X.; et al. Novel dielectric anomaly in the hole-doped $La_2Cu_{1-x}Li_xO_4$ and $La_{2-x}Sr_xNiO_4$ insulators: signature of an electronic glassy state. *Phys. Rev. Lett.* **2005**, *94*, 017002.

(17) Hu, W.; Liu, Y.; Withers, R. L.; Frankcombe, T. J.; Norén, L.; Snashall, A.; Kitchin, M.; Smith, P.; Gong, B.; Chen, H.; et al. Electron-pinned defect-dipoles for high-performance colossal permittivity materials. *Nat. Mater.* **2013**, *12*, 821.

(18) Liu, J.; Duan, C. G.; Yin, W. G.; Mei, W. N.; Smith, R. W.; Hardy, J. R. Large dielectric constant and Maxwell-Wagner relaxation in $Bi_{2/3}Cu_3Ti_4O_{12}$. *Phys. Rev. B: Condens. Matter Mater. Phys.* **2004**, *70*, 144106.

(19) Adams, T. B.; Sinclair, D. C.; West, A. R. Giant barrier layer capacitance effects in $CaCu_3Ti_4O_{12}$ ceramics. *Adv. Mater.* **2002**, *14*, 1321−1323.

(20) Lunkenheimer, P.; Fichtl, R.; Ebbinghaus, S. G.; Loidl, A. Nonintrinsic origin of the colossal dielectric constants in $CaCu_3Ti_4O_{12}$. *Phys. Rev. B: Condens. Matter Mater. Phys.* **2004**, *70*, 172102.

(21) Subramanian, M. A.; Li, D.; Duan, N.; Reisner, B. A.; Sleight, A. W. High dielectric constant in $ACu_3Ti_4O_{12}$ and $ACu_3Ti_3FeO_{12}$ phases. *J. Solid State Chem.* **2000**, *151*, 323−325.

(22) Ramirez, A. P.; Subramanian, M. A.; Gardel, M.; Blumberg, G.; Li, D.; Vogt, T.; Shapiro, S. M. Giant dielectric constant response in a copper-titanate. *Solid State Commun.* **2000**, *115*, 217−220.

(23) Staresinic, D.; Lunkenheimer, P.; Hemberger, J.; Biljakovic, K.; Loidl, A. Giant dielectric response in the one-dimensional charge-ordered semiconductor $(NbSe_4)_3I$. *Phys. Rev. Lett.* **2006**, *96*, 046402.

(24) Blumberg, G.; Littlewood, P.; Gozar, A.; Dennis, B. S.; Motoyama, N.; Eisaki, H.; Uchida, S. Sliding density wave in $Sr_{14}Cu_{24}O_{41}$ ladder compounds. *Science* **2002**, *297*, 584−587.

(25) Federicci, R.; Hole, S.; Popa, A. F.; Brohan, L.; Baptiste, B.; Mercone, S.; Leridon, B. $Rb_2Ti_2O_5$: Superionic conductor with colossal dielectric constant. *Phys. Rev. Mater.* **2017**, *1*, 032001.

(26) Ahmad, M. M.; Yamada, K. Superionic PbSnF4: A giant dielectric constant material. *Appl. Phys. Lett.* **2007**, *91*, 052912.

(27) Ahmad, M. M.; Yamane, Y.; Yamada, K. Structure, ionic conduction, and giant dielectric properties of mechanochemically synthesized $BaSnF_4$. *J. Appl. Phys.* **2009**, *106*, 074106.

(28) Karamov, F. A. *Superionic conductors: heterostructures and elements of functional electronics based on them*; Cambridge International Science Publishing: Cambridge, U.K., 2008.

(29) Boyce, J. B.; Huberman, B. A. Superionic conductors: transitions, structures, dynamics. *Phys. Rep.* **1979**, *51*, 189−265.

(30) Owens, B. B.; Argue, G. R. High-conductivity solid electrolytes: MAg_4I_5. *Science* **1967**, *157*, 308−310.

(31) Boris, A.; Bredikhin, S. I. Interface charge transport and the electronic conductivity of $RbAg_4I_5$ solid electrolytes. *Solid State Ionics* **1990**, *40-41*, 269−271.

(32) Bredikhin, S.; Bondarev, V. N.; Boris, A. V.; Pikhitsa, P. V.; Weppner, W. Electronic conductivity and current instability in superionic crystals. *Solid State Ionics* **1995**, *81*, 19−28.

(33) Lidorenko, N. S.; Zil'bervarg, V. E.; Nagaev, E. L. Dielectric constants of solid electrolytes and transition to superionic state. *Sov. Phys. JETP* **1980**, *51*, 89−93.

(34) Geller, S. Crystal Structure of the Solid Electrolyte, $RbAg_4I_5$. *Science* **1967**, *157*, 310−312.

(35) Geller, S. Low-temperature phases of the solid electrolyte $RbAg_4I_5$. *Phys. Rev. B: Condens. Matter Mater. Phys.* **1976**, *14*, 4345−4355.

(36) Funke, K.; Banhatti, R. D.; Wilmer, D.; Dinnebier, R.; Fitch, A.; Jansen, M. Low-Temperature Phases of Rubidium Silver Iodide: Crystal structures and dynamics of the mobile silver ions. *J. Phys. Chem. A* **2006**, *110*, 3010−3016.

(37) Sarkar, A.; Chakrabarti, M.; Ray, S. K.; Bhowmick, D.; Sanyal, D. Positron annihilation lifetime and photoluminescence studies on single crystalline ZnO. *J. Phys.: Condens. Matter* **2011**, *23*, 155801.

(38) Kirkegaard, P., Pedersen, N. J.; Eldroup, M. *Report of Riso National Lab (Riso-M2740)*, 1989.

(39) Luitel, H.; Sanyal, D.; Gogurla, N.; Sarkar, A. Defect generation and recovery in polycrystalline ZnO during annealing below 300 °C as studied by in situ positron annihilation spectroscopy. *J. Mater. Sci.* **2017**, *52*, 7615−7623.

(40) Tahara, S.; Fukami, T. Anion polarization effects on static structure and ionic transport in superionic melt of $RbAg_4I_5$. *J. Phys. Soc. Jpn.* **2015**, *84*, 024602.

(41) Floros, S.; Liakopoulou-Kyriakides, M.; Karatasos, K.; Papadopoulos, G. E. Detailed study of the dielectric function of a lysozyme solution studied with molecular dynamics simulations. *Eur. Biophys. J.* **2015**, *44*, 599−611.

(42) Matsunaga, S. Structural features of superionic phase in AgBr-CuBr system by molecular dynamics simulation. *J. Phys.: Conf. Ser.* **2009**, *144*, 012011.

(43) Looser, H.; Mali, M.; Roos, J.; Brinkmann, D. Ag diffusion constant in $RbAg_4I_5$ and KAg_4I_5 determined by pulsed magnetic gradient NMR. *Solid State Ionics* **1983**, *9−10*, 1237−1240.

(44) Bentle, G. G. Silver diffusion in a high-conductivity solid electrolyte. *J. Appl. Phys.* **1968**, *39*, 4036−4038.

(45) Lederman, F. L.; Salamon, M. B.; Peisl, H. Evidence for an order-disorder transformation in the solid electrolyte $RbAg_4I_5$. *Solid State Commun.* **1976**, *19*, 147−150.

(46) Brinkmann, D.; Freudenreich, W.; Arend, H.; Roos, J. Evidence for a first-order phase transition at 209 K in the superionic conductor $RbAg_4I_5$. *Solid State Commun.* **1978**, *27*, 133−135.

(47) Gallagher, D. A.; Klein, M. V. Raman scattering studies in the solid electrolytes of the $RbAg_4I_5$ family. *Phys. Rev. B: Condens. Matter Mater. Phys.* **1979**, *19*, 4282.

(48) Vargas, R.; Coronel, G. W. First-order behavior of the 209 K phase transition of $RbAg_4I_5$. *Solid State Ionics* **1995**, *81*, 69−72.

(49) Dhar, J.; Sil, S.; Dey, A.; Ray, P. P.; Sanyal, D. Positron Annihilation Spectroscopic Investigation on the origin of temperature-dependent electrical response in methylammonium lead iodide perovskite. *J. Phys. Chem. Lett.* **2017**, *8*, 1745−1751.

(50) Sharon, M. *An introduction to the physics and electrochemistry of semiconductors: fundamentals and applications*; Wiley, 2016.

(51) Jonscher, A. K. The "universal" dielectric response. *Nature* **1977**, *267*, 673−679.

(52) Jonscher, A. K. Dielectric relaxation in solids. *J. Phys. D: Appl. Phys.* **1999**, *32*, R57−R70.

(53) Mohanty, A.; Swain, D.; Govinda, S.; Row, T. N. G.; Sarma, D. D. Phase diagram and dielectric properties of $MA_{1-x}FA_xPbI_3$. *ACS Energy Lett.* **2019**, *4*, 2045−2051.

https://dx.doi.org/10.1021/acs.jpcc.0c02118
J. Phys. Chem. C 2020, 124, 9802−9809

ACS OMEGA

http://pubs.acs.org/journal/acsodf Article

Elusive Co_2O_3: A Combined Experimental and Theoretical Study

Pavitra N. Shanbhag, Raju K. Biswas, Swapan K. Pati,* Athinarayanan Sundaresan,*
and Chinthamani Nagesa Ramachandra Rao

Cite This: ACS Omega 2020, 5, 29009−29016 Read Online

ACCESS | Metrics & More | Article Recommendations | Supporting Information

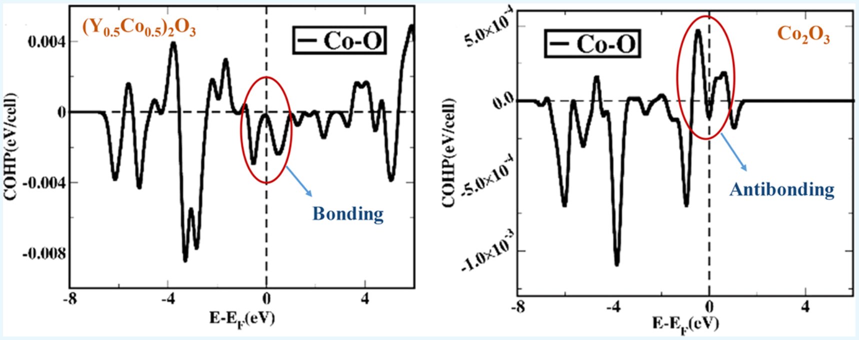

ABSTRACT: Despite several oxides with trivalent cobalt ions are known, the sesquioxide M_2O_3 with Co^{3+} ions remains elusive. Our attempts to prepare Co_2O_3 have failed. However, 50% of Co^{3+} ions could be substituted for Ln^{3+} ions in Ln_2O_3 (Ln = Y and Lu) with a cubic bixbyite structure where the Co^{3+} ions are in the intermediate-spin state. We have therefore examined the structural stability of Co_2O_3 and the special features of solid solutions $(Ln_{0.5}Co_{0.5})_2O_3$ (Ln = Y and Lu). The experimental results are interpreted in the context of ab initio-based density functional theory, molecular dynamics (AIMD), and crystal orbital Hamiltonian population (COHP) analysis. Our AIMD study signifies that Co_2O_3 in a corundum structure is not stable. COHP analysis shows that there is instability in Co_2O_3 structures, whereas Co and O have a predominantly bonding character in the bixbyite structure of the solid solution $(Y_{0.5}Co_{0.5})_2O_3$.

1. INTRODUCTION

Among the transition metal oxides, cobalt oxides are of special interest because of the existence of cobalt in different oxidation as well as spin states, i.e., low-spin, high-spin, and intermediate-spin states.[1] Among these, Co^{2+} generally has octahedral coordination and is in the high-spin state ($t_{2g}^5e_g^2$, $S = 3/2$); Co^{4+} exists in the low-spin state ($t_{2g}^5e_g^0$, $S = 1/2$). Unlike these two, Co^{3+} can exist in high-spin (HS, $t_{2g}^4e_g^2$), low-spin (LS, $t_{2g}^6e_g^0$), and intermediate-spin (IS, $t_{2g}^5e_g^1$) states. Existence of the intermediate-spin state arises since the crystal field splitting energy is of the same order as the pairing energy.[1,2] Many compounds containing cobalt ions in different oxidation states are known. However, CoO and Co_3O_4 are the only known binary oxides with Co^{2+} and Co^{2+}/Co^{3+} states, respectively.[3,4] This is unlike the neighboring Fe, which forms FeO, Fe_2O_3, and Fe_3O_4.[5] It is somewhat intriguing that it has not been possible to form pure Co_2O_3. Since many of the transition metal oxides in which metal in the +3 state form sesquioxides in the corundum structure, one would expect Co_2O_3 to occur in this structure. The only report on Co_2O_3 is by Chenavas et al.[6] who reported a high-pressure synthesis of the oxide with Co^{3+} in the low-spin state, which transforms to the high-spin state on heating. We have tried to prepare Co_2O_3 by high-pressure synthesis and other methods and failed to obtain the oxide. In view of this, we sought to investigate $(Ln_{0.5}Co_{0.5})_2O_3$ (Ln = Y and Lu) solid solutions with composition similar to the $LnCoO_3$ perovskites, wherein it appears to occur in the C-type rare earth oxide structure.

Perovskite oxides of the formula, $LnCoO_3$ (Ln: Y or rare earth) show interesting electronic and magnetic properties. These perovskites are prepared by a solid-state reaction by heating the precursors in air (Ln = Y, La, Pr, Tb, and Dy) under 200 bar oxygen pressure (Ln = Ho, Er) and 20 kbar hydrostatic pressure (Ln = Tm, Yb, and Lu) above 900 °C.[7] Some of the heavy rare earths, Ln = Y, Dy, Er, and Yb give rise to a solid solution of Ln_2O_3 with Co_2O_3 when the reaction is carried out at lower temperatures (500−600 °C).[8] Here, we have carried out a detailed experimental investigation on the bixbyite form of $((Ln_{0.5}Co_{0.5})_2O_3)$ (Ln = Y and Lu) by substituting Ln_2O_3 by 50% Co where cobalt exists in a trivalent

Received: July 15, 2020
Accepted: August 28, 2020
Published: November 2, 2020

https://dx.doi.org/10.1021/acsomega.0c03397
ACS Omega 2020, 5, 29009−29016

state. Our experimental results are well supported with the theoretical approach using the first principle-based DFT calculations and AIMD simulations.

2. RESULTS AND DISCUSSION

2.1. Experimental Studies. All our attempts to prepare Co_2O_3 have resulted in the formation of CoO and Co_3O_4 phases with no traces of the Co_2O_3 phase. We have therefore examined the structural aspects of Co_2O_3 present in the solid solution $(Ln_{0.5}Co_{0.5})_2O_3$ (Ln = Y and Lu). Rietveld refined powder X-ray diffraction profiles of $(Y_{0.5}Co_{0.5})_2O_3$ at two different temperatures (600 and 920 °C) and $(Lu_{0.5}Co_{0.5})_2O_3$ at 600 °C are shown in Figure 1a, b, and c, respectively. XRD profiles fitted using the pseudo-Voigt function revealed that both solid solutions prepared at 600 °C crystallize in the cubic bixbyite structure with an $Ia\bar{3}$ space group. Heating a $(Y_{0.5}Co_{0.5})_2O_3$ solid solution to 920 °C in oxygen gave rise to perovskite $YCoO_3$ crystallizing in orthorhombic symmetry with a *Pbnm* space group, and the corresponding crystal structure is shown in the Figure 2a. Unlike $(Y_{0.5}Co_{0.5})_2O_3$, a $(Lu_{0.5}Co_{0.5})_2O_3$ solid solution at 800 °C decomposed into cubic Lu_2O_3 and Co_3O_4 phases. Refined structural parameters for perovskite $YCoO_3$ and solid solutions, $(Ln_{0.5}Co_{0.5})_2O_3$ (Ln = Y and Lu) are given in the Table 1. The crystal structure of $YCoO_3$ consists of distorted CoO_6 octahedra where Co is situated at the center surrounded by six oxygen ions. Oxygen occupies two different sites in the crystal structure. Y resides in the voids created by the surrounding CoO_6 octahedra.[9]

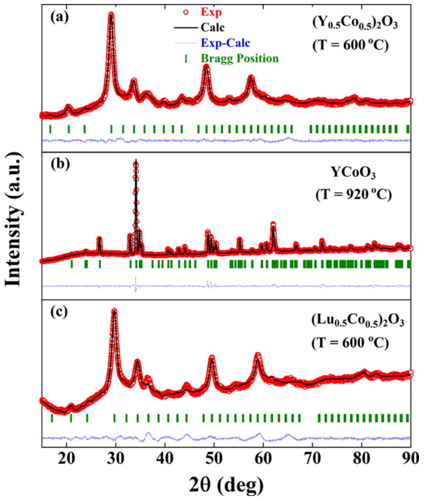

Figure 1. Rietveld refined X-ray diffraction profiles of (a) $(Y_{0.5}Co_{0.5})_2O_3$ (600 °C), (b) $YCoO_3$ (920°C), and (c) $(Lu_{0.5}Co_{0.5})_2O_3$ (600 °C).

The crystal structure of solid solutions $(Ln_{0.5}Co_{0.5})_2O_3$ (Ln = Y and Lu) is shown in the Figure 2b, which consists of two octahedral cation sites where eight Co atoms occupy *8b* and other eight occupy *24d* Wyckoff site, whereas Y or Lu occupies *24d* Wyckoff sites. The octahedra LnO_6 (Ln = Y and Lu) and CoO_6 are highlighted in Figure 2c and d, respectively. The lattice constants of different cubic (C-type) $(Ln_{0.5}Co_{0.5})_2O_3$ (Ln = Y, Er, Yb, and Lu) solid solutions were plotted against corresponding lanthanide radii as shown in Figure 3. The lattice parameters of $(Ln_{0.5}Co_{0.5})_2O_3$ (Ln = Er and Yb) are taken from ref 8. The linear nature of the plot confirms that the system follows Vegard's law,[10] which is attributed to the contraction of the unit cell of the $(Ln_{0.5}Co_{0.5})_2O_3$ solid solution with decreasing size of lanthanide ions. Being the smallest lanthanide, Lu^{3+} forms a unit cell of volume, $V \sim 1122.2$ Å^3, which is 7% smaller than that of Y.

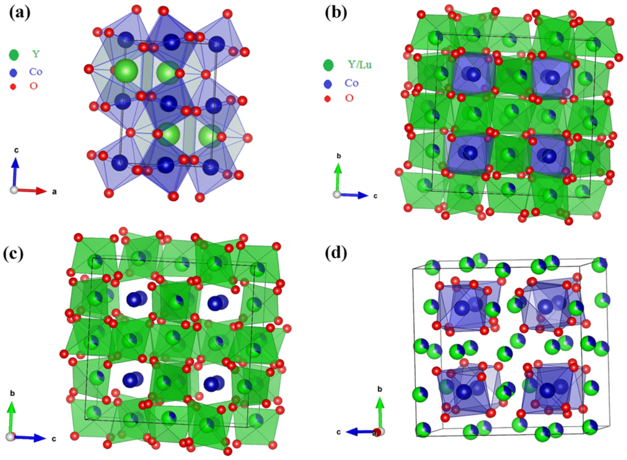

Figure 2. Crystal structure of (a) perovskite $YCoO_3$ (b) bixbyite $(Ln_{0.5}Co_{0.5})_2O_3$ (Ln = Y and Lu), (c) octahedra of Y/Lu (green colored) in $(Ln_{0.5}Co_{0.5})_2O_3$(Ln = Y and Lu), and (d) highlighted (blue colored) CoO_6 octahedra.

Our XPS study reveals the oxidation state of cobalt in perovskite $YCoO_3$ as well as $(Ln_{0.5}Co_{0.5})_2O_3$ (Ln = Y and Lu) solid solutions. The core level spectra of cobalt for $YCoO_3$ and $(Ln_{0.5}Co_{0.5})_2O_3$ (Ln = Y and Lu) are shown in Figure 4. The four signals due to cobalt in Figure 4a−c, correspond to energy levels Co $2p_{3/2}$, Co $2p_{1/2}$, and their satellites confirming the presence of trivalent cobalt ions.[11]

The temperature-dependent field-cooled (FC) magnetic susceptibility for $YCoO_3$ and $(Y_{0.5}Co_{0.5})_2O_3$ was measured under an applied DC field of 100 Oe in the temperature range 2−390 K as shown in Figure 5. We find that perovskite $YCoO_3$ shows a low-spin state ($t_{2g}^6e_g^0$) from low temperature 2 to 390 K. $(Y_{0.5}Co_{0.5})_2O_3$ on the other hand shows an intermediate-spin state ($t_{2g}^5e_g^1$) with $\mu_{eff} \sim 2.13\ \mu_B$. Spin state transitions of trivalent cobalt is well known in the perovskites $LnCoO_3$ (Ln = La, Y, Pr, Nd, and Eu).[12−14] Anomaly observed at $T_N \sim 32$ K in the magnetic susceptibility curve of $(Y_{0.5}Co_{0.5})_2O_3$ is attributed to antiferromagnetic ordering of Co^{3+} ions, which is further evidenced by a negative θ_{CW} value (Table 2). Similarly, $(Lu_{0.5}Co_{0.5})_2O_3$ shows antiferromagnetic ordering below $T_N \sim 25$ K with $\mu_{eff} \sim 2.68\ \mu_B$, indicating the existence of Co^{3+} in the intermediate-spin state ($t_{2g}^5e_g^1$).

To explore the effect of pressure on the magnetic interaction of Co^{3+} ions in these solid solutions of Co_2O_3, a high pressure (1.5 GPa) was applied on $(Ln_{0.5}Co_{0.5})_2O_3$ (Ln = Y and Lu) at room temperature for 1 hr, and the magnetic susceptibilities of the so-obtained $(Ln_{0.5}Co_{0.5})_2O_3$ are compared with that of ambient pressure samples as shown in Figure 6a,b. There is no change observed in the phase of the high-pressure treated samples, and their XRD profiles are shown in Figure S1 (Supporting Information).

Temperature-dependent inverse magnetic susceptibility is fitted using the Curie−Weiss law for ambient and high-pressure samples of $(Ln_{0.5}Co_{0.5})_2O_3$ (Ln = Y and Lu) and are shown in Figure S2 (Supporting Information). μ_{eff} and θ_{CW} values for $(Ln_{0.5}Co_{0.5})_2O_3$ (Ln = Y and Lu) for ambient pressure and high-pressure treated samples are listed in Table

Table 1. Structural Parameters Obtained by Rietveld Refined XRD for $YCoO_3$and $(Ln_{0.5}Co_{0.5})_2O_3$(Ln = Y and Lu)

compound	space group : *Pbnm* (orthorhombic); $\alpha = \beta = \gamma = 90°$				
	$a = 5.14519(22)$, $b = 5.42765(24)$, $c = 7.37531(33)$ Å; $\chi^2 = 3.2\%$				
$YCoO_3$	*x*	*y*	*z*	B_{iso}	Occ.
Y (*4c*)	−0.0157(6)	−0.0678(3)	0.25	0.028(16)	1.0
Co (*4b*)	0.5	0.0	0.0	0.158(11)	1.0
O1 (*4c*)	0.0970(18)	0.5229(17)	0.25	1.0	1.0
O2 (*8d*)	−0.1918(15)	0.1996(15)	0.0479(11)	1.0	1.0
	space group : $Ia\bar{3}$ (cubic); $\alpha = \beta = \gamma = 90°$				
	$a = b = c = 10.6303(12)$ Å; $\chi^2 = 1.72\%$				
$(Y_{0.5}Co_{0.5})_2O_3$	*x*	*y*	*z*	B_{iso}	Occ.
Y (*24d*)	−0.0271(1)	0.0	0.25	0.422(32)	0.333
Co1 (*24d*)	−0.0271(1)	0.0	0.25	0.422(32)	0.167
Co2 (*8b*)	0.25	0.25	0.25	0.471(28)	0.167
O (*48e*)	0.3962(8)	0.1550(6)	0.3812(9)	1.0	1.0
	$a = b = c = 10.3916(18)$ Å; $\chi^2 = 3.1\%$				
$(Lu_{0.5}Co_{0.5})_2O_3$	*x*	*y*	*z*	B_{iso}	Occ.
Lu (*24d*)	−0.02537(2)	0.0	0.25	0.183(1)	0.333
Co1 (*24d*)	−0.02537(2)	0.0	0.25	0.183(1)	0.167
Co2 (*8b*)	0.25	0.25	0.25	0.164(1)	0.167
O (*48e*)	0.4086(11)	0.1506(12)	0.3484(19)	1.0	1.0

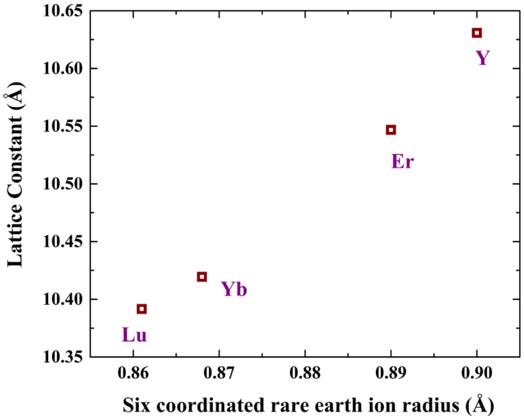

Figure 3. Variation of lattice parameters of $(Ln_{0.5}Co_{0.5})_2O_3$ (Ln = Y, Er, Yb, and Lu) solid solutions with Ln^{3+} radius.

2. Even though Co^{3+} ions are existing in the intermediate-spin state in both the $(Ln_{0.5}Co_{0.5})_2O_3$ (Ln = Y and Lu) solid solutions, $(Lu_{0.5}Co_{0.5})_2O_3$ has a high effective magnetic moment than that of $(Y_{0.5}Co_{0.5})_2O_3$. This is attributed to the chemical pressure due to Lu^{3+} ions. On the other hand,

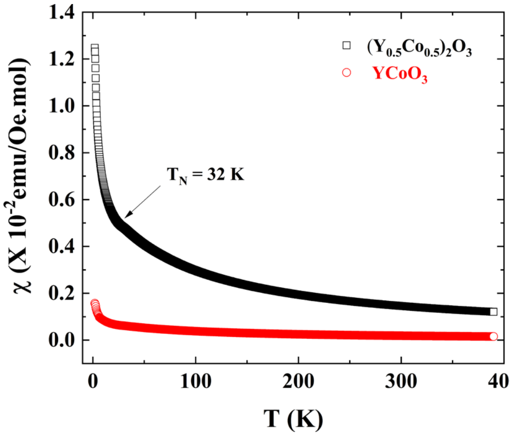

Figure 5. Comparative temperature-dependent field-cooled (FC) magnetic susceptibility curves of $(Y_{0.5}Co_{0.5})_2O_3$ and $YCoO_3$ perovskites.

external pressure increases the μ_{eff} in both the solid solutions and is more significant in $(Y_{0.5}Co_{0.5})_2O_3$ than $(Lu_{0.5}Co_{0.5})_2O_3$.

2.2. Theoretical Studies. Ab initio-based density functional theory (DFT) methods have become well-established

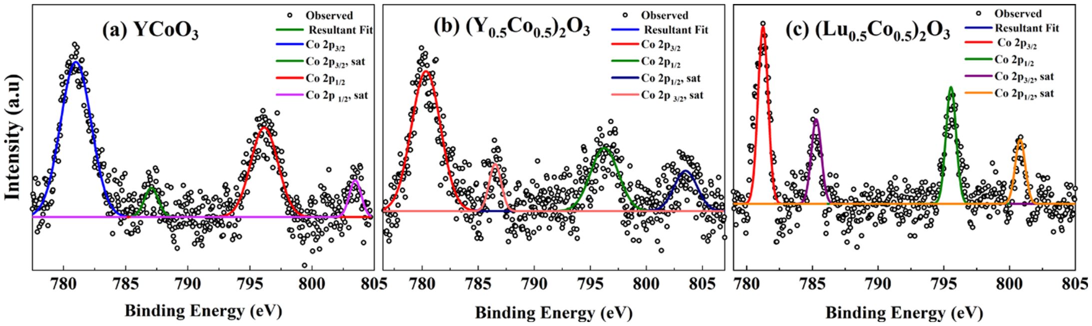

Figure 4. Co 2p core level XPS spectra of (a) $YCoO_3$, (b) $(Y_{0.5}Co_{0.5})_2O_3$, and (c) $(Lu_{0.5}Co_{0.5})_2O_3$.

Table 2. μ_{eff} and θ_{CW} Values for $(Y_{0.5}Co_{0.5})_2O_3$ and $(Lu_{0.5}Co_{0.5})_2O_3$

	$(Y_{0.5}Co_{0.5})_2O_3$		$(Lu_{0.5}Co_{0.5})_2O_3$	
	μ_{eff}	θ_{CW}	μ_{eff}	θ_{CW}
Ambient pressure	2.13 μ_B	−91 K	2.68 μ_B	−90 K
High pressure (1.5 GPa)	2.84 μ_B	−93 K	2.79 μ_B	−82 K

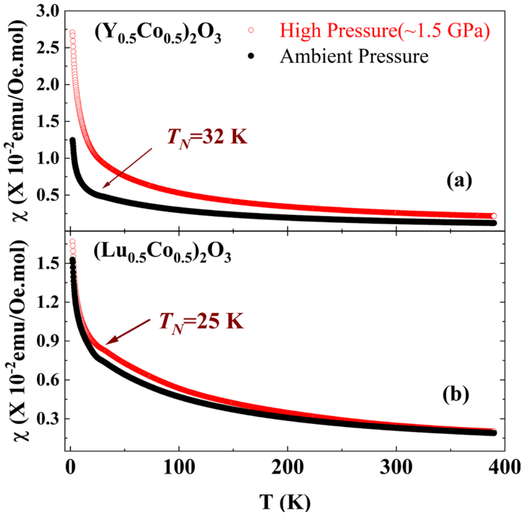

Figure 6. Comparative temperature-dependent field-cooled (FC) magnetic susceptibility curves of (a) $(Y_{0.5}Co_{0.5})_2O_3$ and (b) $(Lu_{0.5}Co_{0.5})_2O_3$ synthesized in ambient pressure and high pressure (1.5 GPa).

techniques to study structural and chemical properties of various materials. Our computational methodology provides comprehensive understanding related to the structural stability and chemical bonding analysis of a well-known Al_2O_3 corundum structure followed by hypothetical Co_2O_3 crystal in the corundum phase. In order to further investigate the chemical aspects of Co^{3+} ions in the chemical environment, we study the bonding characteristics of Y_2O_3 with different doping concentrations of Co^{3+} ions. Our theoretical analysis based on first principles calculation supported by experimental findings will be discussed to interpret structural stability and chemical aspects more rigorously.

2.2.1. Al_2O_3. In the optimized structure of Al_2O_3, the DOS and the PDOS have been calculated (Figure 7a,b). From the DOS plot, it is clear that Al_2O_3 is an insulator with a DFT band gap of 3.4 eV. From the projected DOS, we find that interestingly the low-energy valence bands are dominated exclusively by the oxygen 3p orbitals with very small electronic contributions from Al orbitals. On the other hand, low-energy conduction bands remain almost empty and only at some high energy, it has small contributions from both the Al and O atomic orbitals. Moreover, we emphasize that the lack of overlap between Al and O orbitals in the valence band lead to very small orbital overlapping and less degree of covalence. In contrast, the charge transfer mechanism effectively dominates to form ionic bonds between Al and O atoms in stabilizing Al_2O_3 crystals in the corundum phase.

To further understand the bonding characteristics, we study crystal orbital Hamiltonian population (COHP)[15] analysis between Al and O orbitals (Figure 7c). The COHP is described as the negative of DOS multiplied by the corresponding Hamiltonian matrix elements. The negative and positive values of COHP suggest bonding and antibonding interaction between the electronic states, respectively. The negative value of COHP indicates bonding interactions between Al 3s−Al 3p and O 2p orbitals in the valence bands, which stabilizes the corundum structure of Al_2O_3.

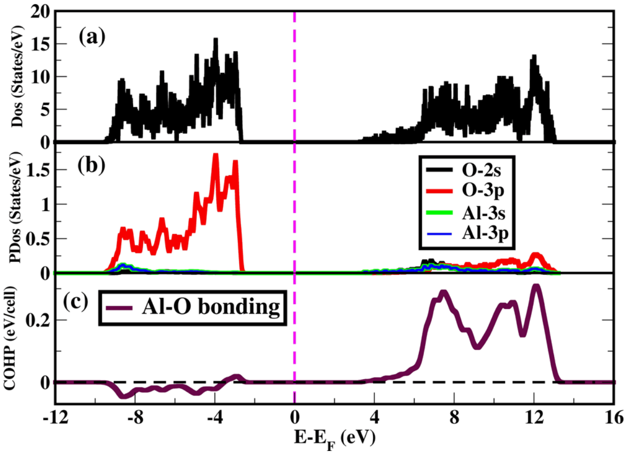

Figure 7. (a) Density of states (DOS) of Al_2O_3; (b) projected DOS on relevant orbitals; (c) COHP is shown as a function of energy for the Al−O bond. PDOS indicates less orbital overlapping between Al and O atoms below the Fermi level although there is significant orbital overlapping above the Fermi level. Negative value of COHP below the Fermi level shows that Al_2O_3 is electronically stable. In figures, Fermi levels are considered as a reference.

2.2.2. Co_2O_3. To understand why there is no stable structure of Co_2O_3, we have carried out a series of optimizations of the corundum structures of Cr_2O_3 and Fe_2O_3 and obtained the M−M and M−O distances. Interestingly, in relaxed crystal structures of all of these oxides, there is no direct M−M bond. In fact, the distances between M−M are 2.60 Å (2.66 Å) and 2.93 Å (2.88 Å), respectively (the numbers in brackets are distances obtained from experiments). Expectedly, we find that all these oxides in their 3+ state show a high spin atomic ground state with varying magnetic moments and antiferromagnetic orders as found experimentally.

We started the optimization studies with the corundum structure of the Fe_2O_3 and substituted Fe atoms with Co atoms. The crystal structure has been relaxed using a fully variable cell and BFGS algorithm, and we find that Co^{3+} forms a low-spin atomic ground state with $t_{2g}^6e_g^0$ configuration. The relaxed (but unstable) structure shows that the distance between two Co atoms decreases compared to the Fe−Fe distance in the Fe_2O_3 corundum structure. The shorter Co−Co distance introduces strain in the system due to the repulsive e−e interaction between two octahedra. Because of the shorter distance between the Co atoms, bonding characteristics between Co and O atoms get influenced quite strongly. As a result, the bond length between Co and O decreases considerably (much shorter compared to other M−O bonds (Table 3) that leads to the large crystal field octahedral gap leading to $S = 0$ ground state for Co^{3+} ions. Our electronic density of states (Figure 8a) confirms that Co_2O_3 forms low-spin states. Energy levels below Fermi level spread from −8 to 0 eV, and the conduction bands spread from 0.6 to 2.5 eV. We also calculated projected density of states (PDOS) of Co 3d orbitals and O 2p orbitals in Figure 8b. From PDOS calculations, it is confirmed that there is significant orbital

Table 3. M−M and M−O Bond Length for the M_2O_3 Given Below for Antiferromagnetic Crystal Structure and Compared with the Experimental Value

crystal structure	M−M distance (Å)	M−O distance (Å)	M−M expt. (Å)	M−O expt. (Å)	Angle M−O−M
Cr_2O_3	2.60	2.00	2.66[16]	1.98	82.12
Fe_2O_3	2.93	2.16	2.88[16]	2.02	87.00
Co_2O_3	2.76	1.90	-	-	82.73

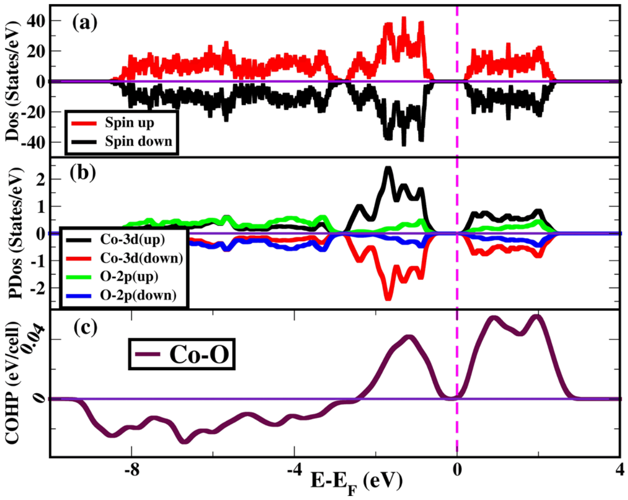

Figure 8. (a) Electronic density of states of spin-up (red) and spin-down (black) of the relaxed but unstable crystal structure of Co_2O_3. Here, zero energy level is considered as Fermi level. (b) Projected density of states of Co 3d and O 2p orbitals where states above the x axis are the contribution from spin up states, and states below is the contribution from spin down states. (c) Crystal orbital Hamiltonian population (COHP) of a Co−O bond (Co:4s Co:3d and O:2s O:2p).

overlapping between Co 3d and O 2p orbitals in the valence band as well as in the conduction band.

The COHP has been plotted in Figure 8c, where we have considered strong interaction between Co:4s, Co:3d and O:2s, O:2p in the unstable relaxed structure of Co_2O_3. Our results show that COHP value is positive near the Fermi level, which signifies that the strong interaction between Co:4s, Co:3d and O:2s, O:2p are antibonding in nature below and above the Fermi level. Interestingly, the interaction between Co and O are antibonding from −2.5 to −0.4 eV in the valence band and from 0.2 to 3 eV in the conduction band, suggesting that Co_2O_3 is least favorable in corundum or any other structure unlike other transition metal oxides (Fe_2O_3, V_2O_3, and Cr_2O_3). Antibonding nature of Co:4s, Co:3d and O:2s, O:2p partly destabilizes the structure of Co_2O_3. Interestingly, due to such partially destabilized bonding, the octahedral crystal field gives complete filling of t_{2g}^6 electrons with no unpaired electrons in Co^{3+} for bonding. Also, since 3d orbitals form narrow band semiconductors, this leads to such a small and almost overlapping bond distance between two octahedral Co ions, where we find highly unstable phonon modes (shown in Figure 9). Unstable phonon modes that are characterized by negative values of the frequencies in a phonon dispersion curve at any wave vector leads to dynamical instability in the crystal structure.

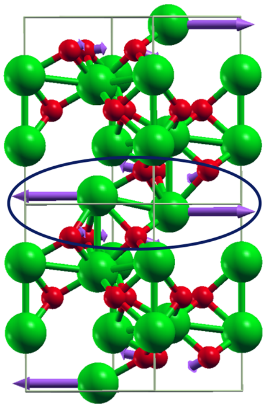

Figure 9. Unstable relaxed corundum crystal structure of Co_2O_3 is calculated using PBE functional. Here, 'green' color balls represent Co atoms and 'red' color balls represent oxygen atoms. Purple arrows in a circle indicate unstable phonon mode of frequency -51 cm^{-1}, which has been obtained performing phonon mode calculations through DFPT at Γ (Gamma) point.

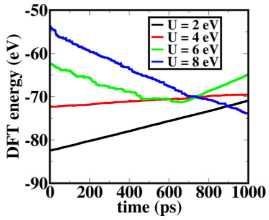

Figure 10. DFT energies have been plotted considering different U values as a function of AIMD time steps. Our computed plot shows significant drift, which further signifies that a Co_2O_3 corundum crystal structure remains unstable for different values of U.

We have also performed ab initio molecular dynamics[17,18] study considering different U values to find the structural stability of a Co_2O_3 crystal. In the simulation, we have plotted DFT energies or electronic energies for different values of U (U = 2, 4, 6, and 8 eV) up to 1000 ps and that have been shown in Figure 10. Interestingly, we find that DFT energies obtained using AIMD studies show considerable drift during the AIMD time steps. The drift in the DFT energies corresponding to different U values would certainly lead to structural instability of the Co_2O_3 corundum structure. To find the microscopic reasons for the structural instability, we have further analyzed the vibrational spectra of the system after 70 ps of AIMD run. These have been analyzed from the dynamical matrix of the force constants. Interestingly, we observe negative phonon mode at the high symmetry Γ point, which suggest that the Co_2O_3 corundum structure is unstable due to constrained geometry of the two octahedra wherein the two corner sharing Co^{3+} ions come at a distance of 2.78 Å. The structure without external pressure and with external pressure (80 kbar) are shown in Figure 11a,b, respectively, where we have marked the unstable phonon modes and the constrained geometry.

2.2.3. Y_2O_3. To elucidate microscopic reasons more rigorously, we consider Y_2O_3 unit cell in the cubic bixbyite structure. The unit cell contains 80 atoms (32 Y atoms and 48 O atoms). We notice that all of the crystallographic sites corresponding to Y atoms are not equivalent. There are 8 numbers of Y atoms (b sites) and 24 numbers of Y atoms (d sites). In the b site, Y atoms are present in the octahedral

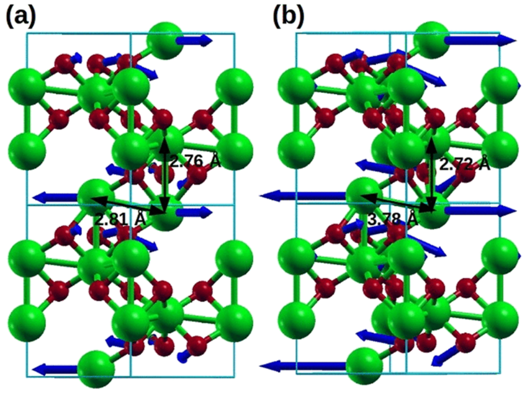

Figure 11. (a) Co_2O_3 crystal structure without external pressure and (b) Co_2O_3 crystal structure with external pressure. Due to applied hydrostatic external pressure on the unit cell, Co−Co distances along the c axis and along in-plane directions decreases as shown in Figure 11b. Blue arrows shown in the figure indicate unstable phonon modes, and the length of the arrows signifies the amount of force acting on the individual atoms introducing dynamical instability.

symmetry, and in the d site, Y atoms are placed in distorted octahedral symmetry. After optimizing the crystal, we perform electronic structure calculations and compute COHP for Y−O bonds. After that, we substitute 50% of Y with Co atoms and optimize the structure. Interestingly, we find that Co occupies eight numbers of b sites and eight numbers of d sites that are energetically favorable. As a result, 50% Co-doped Y_2O_3 stabilizes the crystal in the cubic form. The stability of 50% Co-doped Y_2O_3 has also been confirmed by COHP analysis and experiments.

Presence of bonding between Y−O orbitals (negative value of COHP in the valence band region) implies that the Y_2O_3 crystal structure is electronically stable) shown in Figure 12a. On the other hand, 50% of Co-doping in Y_2O_3 introduces that Co−O orbital interactions are bonding in nature near the Fermi level in the valence band, and it leads to a stable 50% Co-doped Y_2O_3 structure. In the special case, when we replace all the Y atoms by Co atoms in the Y_2O_3 cubic structure, we find the positive value of COHP close to the Fermi level in the valence band region, and the bonding characteristics are highly antibonding in nature, which essentially partly destabilizes the crystal. Experimentally, it has also been found that the Y_2O_3 crystal with all Y atoms doped by Co atoms is not stable. Finally, to quantify the degree of structural stability, we have tabulated ICOHP values for different orbitals and shown in Table S3 (Supporting Information). Such analysis would help to compare the bonding strength between the orbitals and determine the structural stability for different materials considered in this work.

We have also calculated the magnetic moments of individual Co atoms and find that Co ions in different crystallographic sites have different magnetic moments due to the difference in symmetry leading to crystal field splitting. Interestingly, we find the total number of unpaired spins of Co in a site and b site to be 2.2 and 1.92 μ_B, respectively. Experimentally, it has been found that Co has an intermediate-spin state with a spin-only value, 2.13 μ_B. The main point in the overall studies involving experimental and computational results is that Co_2O_3 with $3d^6$ Co^{3+} ions with $S = 0$ neither stabilizes in corundum nor in cubic form, while other systems with $S = 0$ (Y^{3+}: $4d^0$ and Al^{3+}: valence orbitals are 3s and 3p) stabilize in cubic and corundum crystal respectively, which is highly significant.

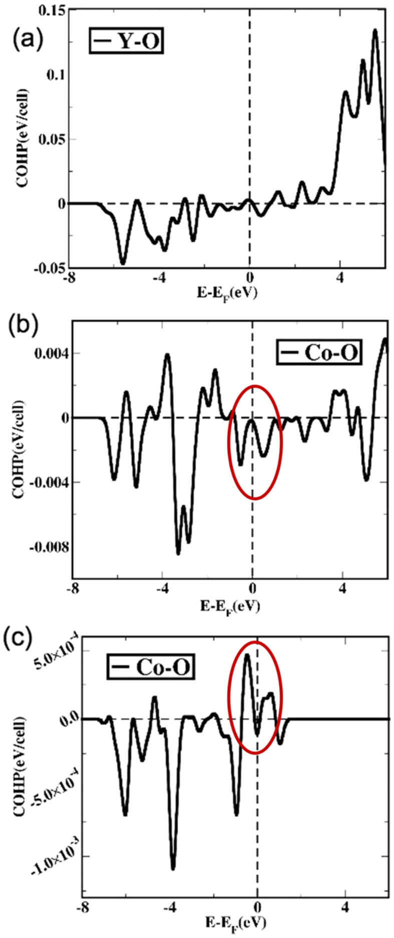

Figure 12. (a) COHP of cubic Y_2O_3 has been mentioned. Negative COHP values between Y and O atomic orbitals imply that the Y_2O_3 crystal stabilizes in a cubic form. (b) COHP after the insertion of Co (50%) in place of Y atoms in Y_2O_3. (c) COHP has been calculated for the cubic phase of Y_2O_3 with all the Y atoms replaced by Co atoms.

3. CONCLUSIONS

Based on the studies, it seems apparent that Co_2O_3 itself does not exist but forms stable solid solutions with Y_2O_3 and Lu_2O_3 in the cubic bixbyite structure. The solid solutions are formed at lower temperatures than the perovskites $Y(Lu)CoO_3$. Co^{3+} ions in the solid solution are in the intermediate-spin state. The difficulty with Co_2O_3, unlike sesquioxides of other transition metals, is that interactions between Co:4s−Co:3d and O:2s−O:2p are antibonding in nature in the corundum structure, while it essentially has a bonding character in the bixbyite structure. This finding would be of interest in understanding the chemistry of transition metal oxides.

4. EXPERIMENTAL AND THEORETICAL METHODS

4.1. Synthesis and Characterization. We have attempted to synthesize Co_2O_3 at high pressures and temperatures using different precursors. In the first attempt, $LiCoO_2$ and CoF_3 were mixed and heated to high temperatures (900−1000°C) under high pressure (4.5 GPa). Again, the reaction was carried out using the precursor mixture of CoO and

$KClO_3$ under high pressure and temperature. Solid solutions of $(Ln_{0.5}Co_{0.5})_2O_3$ (Ln = Y and Lu) were prepared by nitrate−citrate sol−gel combustion method as mentioned in a report[8] in which lanthanide nitrate, cobalt nitrate, and citric acid in 1:1:10 stoichiometric ratio were dissolved in distilled water. This solution was heated to 80 °C with constant stirring until it forms a gel. The obtained gel was heated in an oven at 200°C for 12 h to give rise to a porous powder, which was later heated at 600 °C for 12 h in oxygen to remove carbonaceous content.

The phase purity was confirmed by carrying out X-ray diffraction measurements using a Bruker D8 Advance diffractometer where the sample was subjected to Cu $K\alpha$ radiation in the range of Bragg angle ($10° \leq 2\theta \leq 120°$) under θ-2θ scan. XRD data have been analyzed by the Rietveld method[19] using FullProf Suite software.[20] X-ray photoelectron spectra (XPS) were recorded using an Omicron Nanotechnology spectrometer with a monochromatic Mg $K\alpha$ radiation as the X-ray source with energy E = 1253.6 eV. All the individual core level spectra are corrected using the C 1s level signal (284.6 eV). Cubic multianvil high-pressure apparatus was used to apply high pressure on polycrystalline powder of solid solutions. The pressure on the sample was increased to 1.5 GPa and maintained for 1 h at room temperature. DC magnetic measurements are done in SQUID VSM (Quantum Design, USA) in vibrating sample mode.

4.2. Theoretical Calculations.

First principle-based density functional theory (DFT), as implemented in the Quantum Espresso package, has been used to calculate electronic structure properties. Projected augmented plane wave[21] and a generalized gradient approximated (GGA) exchange−correlation energy[22] with parameterized functional of Perdew, Burke, and Ernzerhof (PBE) are used. An energy cutoff of 50 Ry to truncate the plane wave basis states in representing the Kohn−Sham wave functions and an energy cutoff of 500 Ry for the basis states to represent charge density are used. The crystal structures are fully relaxed using the Broyden−Fletcher−Goldfarb−Shanno (BFGS) algorithm technique to minimize the energy until the magnitude of Hellman−Feynman force on each atom is less than 0.025 eV/Å. A uniform grid of 12 × 12 × 6 k-mesh in the Brillouin zone was used for relaxing the corundum crystal structure of M_2O_3. To include the effect of Coulomb interaction beyond GGA at transition metal sites, we consider GGA + U correction in Hamiltonian. Moreover, to incorporate the effect of Hubbard U in the calculation, we executed variable cell relaxation with different U values. After full relaxation of the crystal structure, we performed self-consistent calculations with the final optimized crystal coordinates. Besides, we have also studied density functional perturbation theory (DFPT)[23] to calculate phonon modes at the zone center Gamma point to confirm the dynamical stability. We adopt U = 3.5 eV for our calculations, which is taken from the previous studies of a similar crystal structure.[24,25] To justify the selection of U, we have also tested our calculations for other various U values (U = 2, 4, 6, and 8). Interestingly, we observe that although the magnitude of phonon eigenvalues varies with different U values, a few of the phonon eigenvalues still remain negative [shown in Table S1]. Negative eigenvalue of phonon signifies that the crystal structure is unstable with regards to small perturbation of atoms along the crystallographic directions. We have also analyzed the phonon eigenvectors associated with each eigenvalue for different U values. The imaginary eigenvectors do not show any drastic change in their directions, and the overall nature of phonons do not change with U values. Furthermore, we have plotted COHP for various U values to analyze bonding characteristics for better understanding of realistic chemical bonding picture in the framework of COHP methodology [shown in Table S2]. We find that there is no significant variation in COHP for different U values. In fact, we find an appearance of unstable antibonding characteristics in COHP below the Fermi level. The "degree of bonding" or bonding strength has been computed by integrating the COHP values below the Fermi level from −5.0 eV to Fermi energy (at 0.0 eV; all energy are scaled). The "degree of bonding" also suggests that with the increase in electronic correlations, the corundum structure becomes more and more unstable.

To further investigate the effect of external pressure at room temperature as well as at higher temperature, we perform ab initio molecular dynamics (AIMD) as implemented in Vienna ab initio package (VASP).[26,27] The plane wave basis set, scalar relativistic pseudopotentials, and projected augmented wave (PAW)[28] methods were employed for molecular dynamics simulations. The Nose−Hoover thermostat and barostat[29,30] were used to evaluate the equilibrium dynamics under the NPT ensemble. Equilibrium dynamics were maintained for 1000 ps with a time step of 1 fs after the equilibrium spanning of the first 20 ps. We also consider Y_2O_3 unit cell in cubic form and optimize the structure using the Broyden−Fletcher−Goldfarb−Shannon (BFGS) algorithm to minimize the energy until the magnitude of Hellman−Feynman force on each atom is less than 0.025 eV/Å. We consider similar exchange−correlation functional as have been taken for the Co_2O_3 corundum structure with a uniform grid of 6 × 6 × 6 k-mesh and an energy cutoff of 50 Ry.

■ ASSOCIATED CONTENT

Supporting Information

The Supporting Information is available free of charge at https://pubs.acs.org/doi/10.1021/acsomega.0c03397.

> Additional results including X-ray diffraction profiles of high-pressure treated samples and temperature-dependent inverse magnetic susceptibility curves fitted with the Curie−Weiss law, variation of phonon eigenvalues at Γ point as a function of Hubbard U, variation of integrated COHP (ICOHP)1-2 for Co−O bonding with the increasing values of Hubbard U, and integrated COHP (ICOHP) in eV/atoms for different materials (PDF)

■ AUTHOR INFORMATION

Corresponding Authors

Swapan K. Pati − *Theoretical Sciences Unit, School of Advanced Materials, Jawaharlal Nehru Centre for Advanced Scientific Research, Bangalore 560064, India;* orcid.org/0000-0002-5124-7455; Email: pati@jncasr.ac.in

Athinarayanan Sundaresan − *Chemistry & Physics of Materials Unit, School of Advanced Materials, Jawaharlal Nehru Centre for Advanced Scientific Research, Bangalore 560064, India;* orcid.org/0000-0002-1613-3030; Email: sundaresan@jncasr.ac.in

Authors

Pavitra N. Shanbhag − *Chemistry & Physics of Materials Unit, School of Advanced Materials, Jawaharlal Nehru Centre for Advanced Scientific Research, Bangalore 560064, India*

Raju K. Biswas − *Theoretical Sciences Unit, School of Advanced Materials, Jawaharlal Nehru Centre for Advanced Scientific Research, Bangalore 560064, India*

Chinthamani Nagesa Ramachandra Rao − *New Chemistry Unit, School of Advanced Materials, Jawaharlal Nehru Centre for Advanced Scientific Research, Bangalore 560064, India;* orcid.org/0000-0003-4088-0615

Complete contact information is available at:
https://pubs.acs.org/10.1021/acsomega.0c03397

Notes

The authors declare no competing financial interest.

ACKNOWLEDGMENTS

The authors would like to thank the International Centre for Materials Science and Sheikh Saqr Laboratory at Jawaharlal Nehru Centre for Advanced Scientific Research for providing experimental facilities. A.S. acknowledges, SERB, DST, and the government of India for financial support. P.N.S acknowledges Jawaharlal Nehru Centre for Advanced Scientific Research for providing a research fellowship (JNC/S0484). R. K. B. thanks the UGC and the government of India, and S. K. P. acknowledges SERB, DST, and the government. of India for financial support.

REFERENCES

(1) Raveau, B.; Seikh, M., *Cobalt oxides: from crystal chemistry to physics;* John Wiley & Sons: 2012.

(2) Maekawa, S.; Tohyama, T.; Barnes, S. E.; Ishihara, S.; Koshibae, W.; Khaliullin, G., *Physics of transition metal oxides*. Springer Science & Business Media: 2013; Vol. *144*.

(3) Tombs, N. C.; Rooksby, H. P. Structure of monoxides of some transition elements at low temperatures. *Nature* **1950**, *165*, 442.

(4) Roth, W. The magnetic structure of Co_3O_4. *J. Phys. Chem. Solids* **1964**, *25*, 1−10.

(5) Cornell, R. M.; Schwertmann, U., *The iron oxides: structure, properties, reactions, occurrences and uses*; John Wiley & Sons 2003.

(6) Chenavas, J.; Joubert, J. C.; Marezio, M. Low-spin to high-spin state transition in high pressure cobalt sesquioxide. *Solid State Commun.* **1971**, *9*, 1057−1060.

(7) Alonso, J. A.; Martínez-Lope, M. J.; de La Calle, C.; Pomjakushin, V. Preparation and structural study from neutron diffraction data of $RCoO_3$ (R= Pr, Tb, Dy, Ho, Er, Tm, Yb, Lu) perovskites. *J. Mater. Chem.* **2006**, *16*, 1555−1560.

(8) Naidu, B. S.; Gupta, U.; Maitra, U.; Rao, C. N. R. Visible light induced oxidation of water by rare earth manganites, cobaltites and related oxides. *Chem. Phys. Lett.* **2014**, *591*, 277−281.

(9) Mehta, A.; Berliner, R.; Smith, R. W. The structure of yttrium cobaltate from neutron diffraction. *J. Solid State Chem.* **1997**, *130*, 192−198.

(10) Denton, A. R.; Ashcroft, N. W. Vegard's law. *Phys. Rev.A* **1991**, *43*, 3161.

(11) Naumkin, A. V.; Kraut-Vass, A.; Gaarenstroom, S. W.; Powell, C. J., *NIST X-ray photoelectron spectroscopy database, NIST standard reference database 20*, version 4.1. US Department of Commerce, Washington 2012.

(12) Knížek, K.; Jirák, Z.; Hejtmánek, J.; Veverka, M.; Maryško, M.; Hauback, B. C.; Fjellvåg, H. Structure and physical properties of $YCoO_3$ at temperatures up to 1000 K. *Phys. Rev. B* **2006**, *73*, 214443.

(13) Rao, C. N. R.; Seikh, M. M.; Narayana, C., Spin-state transition in $LaCoO_3$ and related materials. In *Spin Crossover in Transition Metal Compounds II*; Springer: 2004; pp. 1−21, DOI: 10.1007/b95410.

(14) Berggold, K.; Kriener, M.; Becker, P.; Benomar, M.; Reuther, M.; Zobel, C.; Lorenz, T. Anomalous expansion and phonon damping due to the Co spin-state transition in R CoO_3 (R= La, Pr, Nd, and Eu). *Phys. Rev. B* **2008**, *78*, 134402.

(15) Deringer, V. L.; Tchougréeff, A. L.; Dronskowski, R. Crystal orbital Hamilton population (COHP) analysis as projected from plane-wave basis sets. *J. Phys. Chem. A* **2011**, *115*, 5461−5466.

(16) Finger, L. W.; Hazen, R. M. Crystal structure and isothermal compression of Fe_2O_3, Cr_2O_3, and V_2O_3 to 50 kbars. *J. Appl. Phys.* **1980**, *51*, 5362−5367.

(17) Hafner, J. Materials simulations using VASP—a quantum perspective to materials science. *Comput. Phys. Commun.* **2007**, *177*, 6−13.

(18) Hafner, J. Ab-initio simulations of materials using VASP: Density-functional theory and beyond. *J. Comput. Chem.* **2008**, *29*, 2044−2078.

(19) Rietveld, H. A profile refinement method for nuclear and magnetic structures. *J. Appl. Crystallogr.* **1969**, *2*, 65−71.

(20) Rodríguez-Carvajal, J., Recent developments of the program FULLPROF. *Commission on powder diffraction (IUCr);* Newsletter 2001, *26*, 12−19.

(21) Blöchl, P. E. Projector augmented-wave method. *Phys. Rev. B* **1994**, *50*, 17953.

(22) Perdew, J. P.; Burke, K.; Ernzerhof, M. Generalized gradient approximation made simple. *Phys. Rev. Lett.* **1996**, *77*, 3865.

(23) Baroni, S.; De Gironcoli, S.; Dal Corso, A.; Giannozzi, P. Phonons and related crystal properties from density-functional perturbation theory. *Rev. Mod. Phys.* **2001**, *73*, 515.

(24) Gray, C.; Lei, Y.; Wang, G. Charged vacancy diffusion in chromium oxide crystal: DFT and DFT+ U predictions. *J. Appl. Phys.* **2016**, *120*, 215101.

(25) Huang, X.; Ramadugu, S. K.; Mason, S. E. Surface-specific DFT + U approach applied to α-Fe_2O_3 (0001). *J. Phys. Chem. C* **2016**, *120*, 4919−4930.

(26) Kresse, G.; Hafner, J. Ab initio molecular dynamics for liquid metals. *Phys. Rev. B* **1993**, *47*, 558−561.

(27) Kresse, G.; Hafner, J. Ab initio molecular-dynamics simulation of the liquid-metal–amorphous-semiconductor transition in germanium. *Phys. Rev. B* **1994**, *49*, 14251−14269.

(28) Kresse, G.; Joubert, D. From ultrasoft pseudopotentials to the projector augmented-wave method. *Phys. Rev. B* **1999**, *59*, 1758−1775.

(29) Nosé, S. A unified formulation of the constant temperature molecular dynamics methods. *J. Chem. Phys.* **1984**, *81*, 511−519.

(30) Hoover, W. Canonical dynamics: method for simulations in the canonical ensemble. *Phys. Rev. A* **1985**, *31*, 1695−1697.